Title
Permanent Deformation of Asphalt Concrete Pavements: A Nonlinear Viscoelastic Approach to Mix Analyses and Design

Author
Long, Fenella Margare

Publication Date
2001

Permanent Deformation of Asphalt Concrete Pavements: A Nonlinear Viscoelastic Approach to Mix Analyses and Design

by

Fenella Margaret Long

B.S. (University of Cape Town) 1992
M.S. (University of California, Berkeley) 1996

A dissertation submitted in partial satisfaction of the
requirements for the degree of
Doctor of Philosophy

in

Engineering - Civil and Environmental Engineering
in the
GRADUATE DIVISION
of the
UNIVERSITY OF CALIFORNIA, BERKELEY

Committee in charge:

Professor Carl L. Monismith, Chair
Professor Sanjay Govindjee
Professor John T. Harvey
Professor Panayiotis Papadopoulos

Spring 2001

Permanent Deformation of Asphalt Concrete Pavements: A Nonlinear Viscoelastic Approach to Mix Analyses and Design

by

Fenella Margaret Long

Abstract

Permanent Deformation of Asphalt Concrete Pavements: A Nonlinear Viscoelastic Approach to Mix Analyses and Design

by

Fenella Margaret Long

Doctor of Philosophy in Engineering - Civil and Environmental Engineering

University of California, Berkeley

Professor Carl L. Monismith, Chair

Because pavements are being subjected to increasingly heavy loads, many mix design procedures currently in use may not adequately prevent permanent deformation (rutting) in asphalt concrete. This dissertation describes the development of a nonlinear viscoelastic constitutive model that can be used in mix analyses to design rut-resistant mixes.

Shear deformation is the dominant cause of rutting in asphalt concrete, a nonlinear viscoelastic material. To determine the viscoelastic shear properties simple shear frequency sweep tests at constant height were run. The test results indicated that the mix behavior depends on both strain level and temperature. Master curves of the laboratory data were then shifted horizontally and vertically to create a single master curve from which to extract the viscoelastic material properties. These horizontal and vertical shift factors were used to develop shift factor functions dependent on temperature and strain.

The constitutive model was formulated from the basis of linear viscoelasticity and extended to incorporate the horizontal and vertical shift factors. The strain in the shift factors was the maximum strain experienced in the time history. The model was implemented in a finite element code and the solution was calculated in discrete time steps. The maximum strain and, hence, the shift factors were updated in each time step.

Simulations of the repeated load simple shear test at constant height (RSST-CH) and of pavement structures were performed to validate the model. The RSST-CH simulations matched the laboratory data fairly well. The average shapes of the rutting profiles in the pavement simulations compared favorably with those observed in the Heavy Vehicle Simulator Rutting Study, including the "humps" apparent at the edge of the wheel tracks. Thus, despite limitations in the model, including its inability to account for densification of the mix, the nonlinear viscoelastic model captures the permanent deformation behavior of asphalt concrete reasonably well.

Simulations with the constitutive model were used to evaluate the relationship between rut depth in the field and shear strain in the RSST-CH utilized in the SHRP A003A mix design procedure. The results also demonstrated the usefulness of the model in quantifying the effect of tire type on rutting.

Professor C. L. Monismith

To my parents -

for encouraging me to try

TABLE OF CONTENTS

LIST OF TABLES

LIST OF FIGURES

Acknowledgements

To Professor Carl Monismith, I am indebted to you for your guidance, encouragement, inspiration, and unwavering support during my time at Berkeley. I am deeply appreciative of the opportunities you created for me and am honored and privileged to have been able to work so closely with you. Thank you for sharing your passion for engineering and for teaching me the "test of reasonableness."

To Professor Sanjay Govindjee, I am grateful for your patience and willingness to teach me, starting from the fundamentals. Thank you to Professor John Harvey for your many valuable suggestions and support over the years. Thank you also to Professor Panos Papadopoulos for reviewing my dissertation.

Funding for my graduate studies have been provided by Transportek, CSIR, the University of California Transportation Center, the Association of Asphalt Paving Technologists, the Konosuke Matshushita Fund, the Tsuneo Sekine Fund, and the Robert Horonjeff Fund. I gratefully acknowledge these organizations and funds. Thank you to Transportek, CSIR for granting me a leave of absence to complete this degree and for supporting me throughout the process.

Thank you to my friends and colleagues from the Pavement Research Center at the Richmond Field Station, UC Berkeley. Each of you contributed to making the PRC a challenging and fun place to work. Special thanks to Maggie Paul and David Kim for

administrative support, Dave Hung, Hector Matha, and Ed Diaz for assistance with specimen preparation, and Irwin Guada for performing laboratory tests. Thanks are also due to my office mates, Louw du Plessis, Andrew Heath, Lorina Popescu, and Clark Scheffy for sharing the laughter and the tears. Thank you to Dr Ronald Blab for willingly sharing your time and knowledge both during your stay at UC Berkeley and at the Technical University of Vienna, Austria. I am also grateful for the mentoring provided by Mr Bill Nokes and Dr Nick Coetzee.

Life in Berkeley would not have been the same experience without my many friends, especially my roommates, Erica Adelsheimer, Sarah de Forest, Krista Jeannotte, and Karen Smilowitz. Erica, you were there for every step, right up to your enthusiastic and thorough editing of my dissertation.

Finally, thank you to Mom, Dad and Royce for always offering your unconditional support and encouragement. Without ever pressuring me you have taught me how to challenge myself.

CHAPTER 1

INTRODUCTION

Permanent deformation (rutting) in asphalt concrete pavements manifests itself as longitudinal depressions in the wheel paths. The action of traffic loading displaces the asphalt concrete by pushing it away from the loaded area. This results in depressions and humps in and along the sides of the wheelpaths. Figure 1.1, a photograph of an in-service pavement, shows this type of rutting. Permanent deformation predominantly occurs under the action of heavy vehicles in high temperature areas and in areas of slow moving traffic, such as at intersections. Rutting is usually found in the upper layers of the pavement near the loaded areas.

Rutting is a serious safety issue for road users for two reasons: (1) steering in the ruts is difficult and, (2) if water pools in the ruts at a depth of 5 mm or greater, hydroplaning may occur.*(1)*

Rutting failures occur early in the life of a pavement, typically in the first five years after construction. In later years, a pavement mix develops a greater resistance to rutting

through aging and densification caused by environmental influences. However, in the early years the material is more susceptible to deformation. In some extreme cases in hot areas with very heavy truck traffic, rutting can occur in a matter of days.

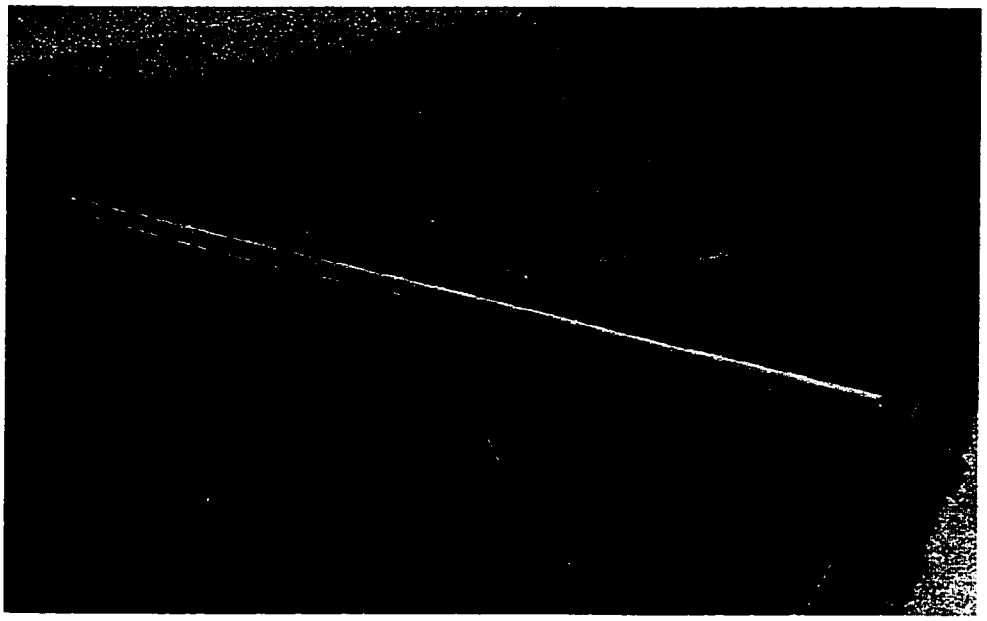

Figure 1.1 Permanent Deformation (Rutting) in Wheelpaths

Terminal rut depths in highway pavements are usually approximately 12.5 mm. When rutting exceeds the terminal rut depths, the pavement needs to be overlaid or removed and replaced to restore the smooth surface profile. Both solutions are very costly and are particularly onerous when required so soon after the initial laying of the pavement.

The trucking industry is continually trying to increase the legal axle loads and tire pressures of trucks, and larger aircraft are being used, for example, the Boeing 747 and

the Boeing 777. Pavement design procedures need to ensure that pavements will be able to withstand these heavier loads to prevent excessive rutting. Many of the mix design procedures used in practice may not be able to provide mixes that are sufficiently rut resistant under these heavier loads. Additionally, these procedures may not adequately account for the inclusion of new materials, such as asphalt-rubber or polymer modified binders.

This dissertation develops a constitutive model that describes the permanent deformation behavior of asphalt concrete. The model is used to evaluate a mix analysis and design procedure. Such evaluations can be used to more confidently design mixes that can withstand the increased traffic demands without premature and costly rutting failures.

1.1 Scope of Dissertation

Chapter 2 describes the rutting behavior of mixes and identifies the properties of the mix and its constituents that are important for rutting. A variety of laboratory tests used to determine the rutting potential of mixes are summarized, and the appropriate test from which to develop the constitutive model is selected. Available methods for predicting rutting are also discussed.

In Chapter 3 laboratory data from the simple shear at constant height frequency sweep test are described, including the materials used in the mixes tested and the specimen

preparation. The results of the laboratory tests are presented and the variability inherent to asphalt concrete is discussed.

Chapter 4 uses the laboratory test data and other available data to discern an appropriate constitutive model. The data are also used to develop the components of the model using time-temperature-strain superpositioning. The constitutive model is formulated in Chapter 5, and the model is implemented in a finite element code. The material properties are determined from the data analyses reported in Chapter 4, and limitations in the model and the implications thereof are discussed.

Chapter 6 presents the results of finite element simulations of the repeated load simple shear test at constant height (RSST-CH) and of accelerated pavement tests to evaluate the ability of the constitutive model to capture the permanent deformation behavior of asphalt concrete. A previously developed performance based mix design procedure is discussed in Chapter 7, and the nonlinear viscoelastic model developed herein is used to evaluate some aspects of this mix design procedure.

Finally, Chapter 8 presents conclusions drawn from the results and offers recommendations for future work.

CHAPTER 2

BACKGROUND

Permanent deformation of asphalt concrete pavements is known to occur primarily in hot areas. Rutting is often found in areas of slow moving traffic, for example, at intersections, but can occur on highways with high-speed traffic. Properties of the asphalt, and the aggregate, and their combined effect in the mix influence the rutting characteristics of asphalt concrete. Laboratory tests are available for determining the mix properties, and these test data are used to evaluate the permanent deformation potential of asphalt concrete pavements.

This chapter discusses the asphalt, aggregate, and mix properties that are important for rutting and identifies and describes permanent deformation behavior, specifically the relative contribution of shear and volumetric deformation. Available laboratory tests are discussed, including the physical test configuration and the modes of loading, and the advantages, disadvantages and limitations of each are identified. Finally, a brief literature review on methods currently used for estimating and modeling permanent deformation of asphalt concrete is presented.

2.1 Asphalt Concrete Properties Important to Rutting

Asphalt concrete mixtures are composed of asphalt, aggregate, and air-voids. The aggregate, and asphalt, and the relative proportions of each in the mix have direct effects on the permanent deformation behavior of the mix. This section describes these effects and thereby identifies which components need to be carefully controlled in mix design and included in models.

2.1.1 Asphalt

Asphalt (binder) is a viscoelastic material and exhibits dependence on the rate of loading and on temperature. Conventional binders are typically considered thermorheologically simple. However at higher strain levels binder behavior is nonlinear, indicating thermorheological complexity.*(2, 3)*

The addition of materials, such as asphalt-rubber from recycled tires and polymers, to the conventional binder change the binder properties, thereby improving the resistance of the binder to distress. These modified binders show larger deviations from thermorheological simplicity, which makes estimation of the mix properties complex.*(4)*.

The more viscous and less temperature-susceptible a conventional binder, the better the mix rutting performance at high temperatures.

2.1.2 Aggregate

The aggregate plays a major role in rutting resistance. Aggregates with rough surface textures and angular rather than rounded shapes show improved rutting resistance. Crushed aggregates are, therefore, better than natural gravels. Dense gradations also typically perform better than open or gap graded mixes. For well-compacted mixes, dense gradations result in mixes with more contact points for load distribution.*(1)*

2.1.3 Asphalt-Aggregate Mixes

The proportions of the aggregate, asphalt, and air-void content in an asphalt concrete mix are critical determinants of the permanent deformation behavior. For conventional binders, the rut resistance of a mix is dependent on the mix stiffness; a stiffer mix provides more resistance. For well-proportioned mixes, the stiffness of the mix will improve with increased compaction effort.

As the binder content of a mix increases, the mix becomes increasingly prone to rutting. The coefficient of thermal expansion of the binder is approximately an order of magnitude higher than the aggregate. In some hot temperature environments the binder may expand due to the heat, and if the binder content is high and the air-void content is low, the binder can bleed through to the surface of the pavement. This significantly reduces the skid resistance of the pavement, which is potentially very dangerous.

Too low a binder content, however, results in a mix that has low workability, and as a result the mix can be difficult to compact, resulting in a high air-void content. A high air-void content increases the propensity of the mix to densify to a more stable state and results in less shear resistance because the binder can easily move into the air-voids. For good rut resistance a low air-void content is preferable. In addition, a low binder content and high air-void content compromise the durability and fatigue cracking resistance of a mix.

However, a low air-void content as a result of a high asphalt content will increase the propensity for rutting.*(1)* It has been found that for asphalt concrete mixes, below a threshold, an increase in density can result in a decrease in stability, i.e., a decrease in the rut resistance. From experimental data of triaxial tests, Monismith and Vallerga *(5)* determined that an air-void content in the mix of less than three percent increases the rutting propensity of the mix. This is illustrated in Figure 2.1, where the line representing a three percent air-void content is plotted on a stress at 2 percent strain and bulk specific gravity graph. A three percent air-void content therefore represents a "*...reasonable boundary between a condition above which the mix can carry the expected traffic with little permanent deformation and below which the potential for excessive rutting exists.*"*(4)*

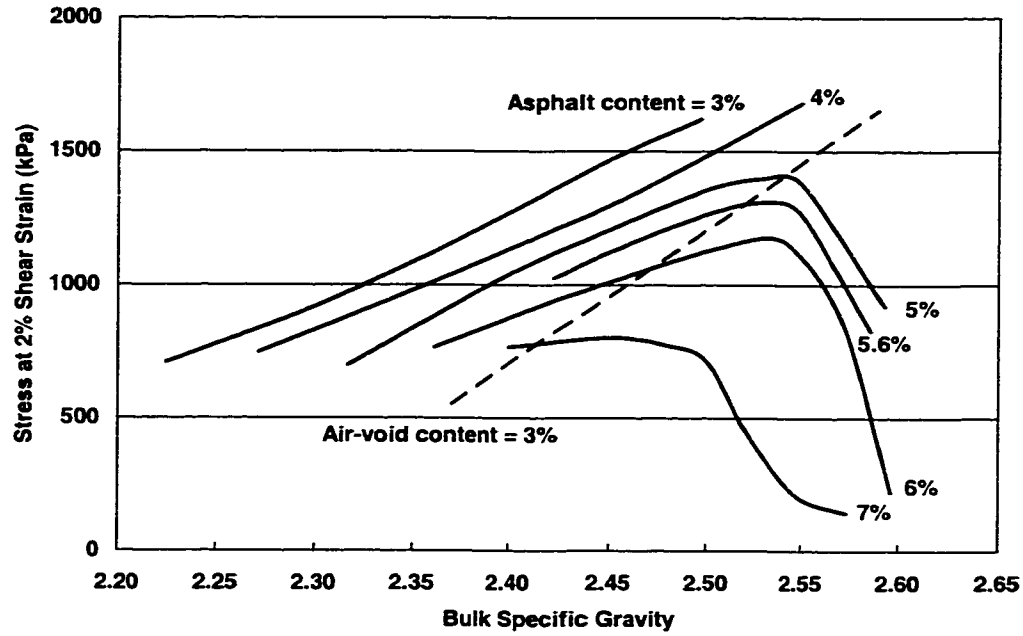

Figure 2.1 Relationship between Bulk Specific Gravity and Stress at 2% Strain for a Fixed Asphalt Content *(5)*

In summary, a rut resistant mix should have a low binder content, but not so low as to compromise the fatigue resistance, durability and workability. The in situ mix should be compacted to a low air-void content, but not below 3 percent.

2.2 Permanent Deformation Behavior

It is widely accepted that the dominant material behavior causing permanent deformation of asphalt concrete is shear deformation.*(1, 4, 6)* Densification of the mix under the action of a load does occur, but in a well-compacted mix this densification is small compared to the shear deformation. Figure 2.2 shows the profile of a Heavy Vehicle

Simulator (HVS) rutting test section after accelerated loading. This test, 508RF, was performed on an asphalt concrete pavement with an asphalt-rubber hot mix (ARHM) overlay of 61 mm. A 40 kN load was applied with a single wide-base tire with a tire pressure of 760 kPa in a channelized mode. The test was run at a temperature of 50°C at a depth of 50 mm.*(7)* The shear deformations or "humps" at the edges of the wheel path are clearly visible. These humps would not appear if the rutting were due to densification only.

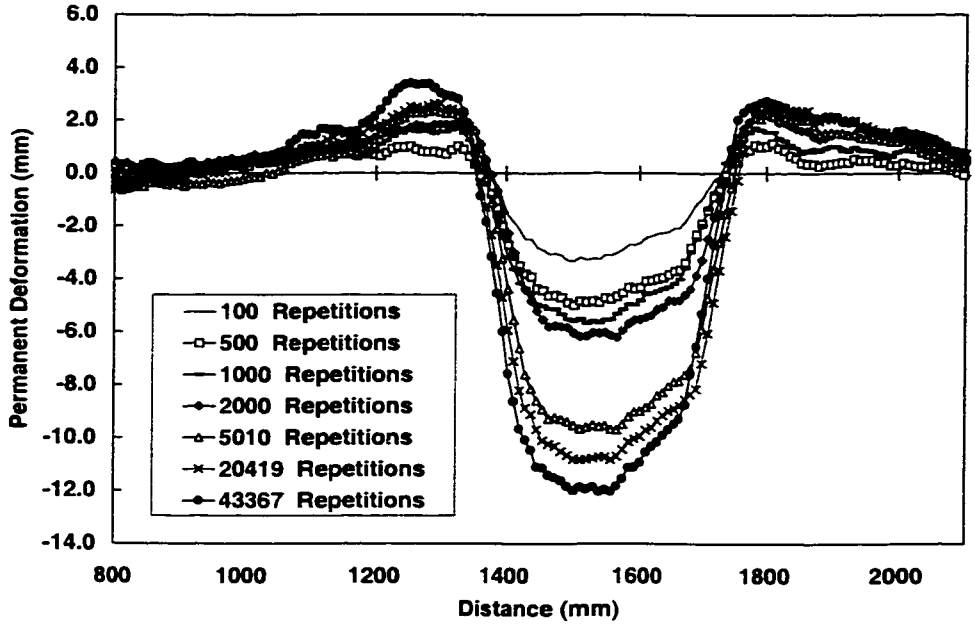

Figure 2.2 HVS Rutting Test Section (508RF) Profile

2.2.1 Shape Distortion and Volume Change

Asphalt concrete mixes, at the high temperatures at which rutting typically occurs, exhibit large differences between volume change and shape distortion (shear) modes of deformation. This is because of the sensitivity of these modes to temperature, the rate of loading, and the amount of residual deformation after a load is removed. Asphalt concrete also shows markedly different behavior in tension and compression.*(6, 8)*
Much of the discussion in this section is based primarily on material contained in References *(6, 9, 10)* from work by Weissman.

Deformation of materials can be attributed to the combination of volume change and shape distortion. Volume change is defined as deformation in which the change in the three principal strains are equal, i.e., the shape remains the same, but the volume changes, as shown in Figure 2.3. The bulk modulus, K, controls volume change (bulk deformation). Shape distortion, shear or deviatoric deformation is defined as an isochoric (volume-preserving) deformation where the shape changes but the volume remains constant, as illustrated in Figure 2.3. Shape distortion is controlled by the shear modulus, G.

An investigation of 15 mixes used in the Strategic Highway Research Program (SHRP) study showed that the shear deformation of asphalt concrete at the temperatures critical to rutting is considerably greater than the volumetric deformation.*(4, 6)* Two laboratory

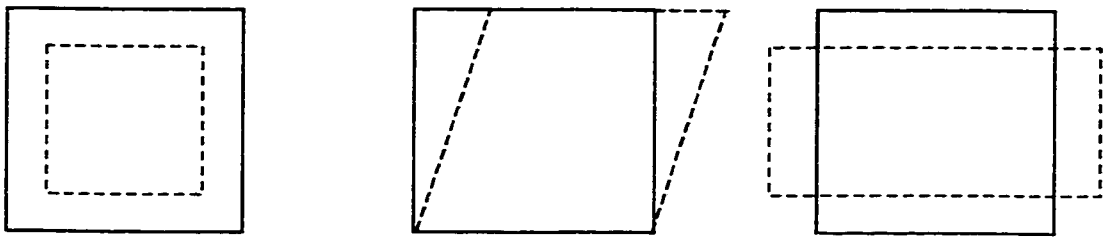

Figure 2.3 Modes of Deformation

tests were performed, a simple shear creep test and a hydrostatic pressure creep test. Neither of these tests gives a pure measure of the volume change or shape distortion because it is difficult to perform pure tests in the laboratory, because asphalt concrete mixes are very heterogeneous, and because separation of the two modes is difficult. Because it is difficult to separate the deformation modes, the data underestimate the differences. However, the data do provide good approximations to the relative differences between shape distortion and volume change.

Both types of tests were performed at 50°C on specimens 150 mm in diameter and 50 mm high. A 69 kPa shear stress was used and a 690 kPa hydrostatic stress. The loading was increased at a steady rate from 0 to the peak value in 10 seconds, maintained for 100 seconds and then reduced to 0 in 10 seconds at a constant rate. Measurements continued for an additional 120 seconds after the load was removed.

Figure 2.4 shows the strain history results of these tests. The results are averaged for the 15 mixes. The first figure, Figure 2.4 (a), demonstrates the deformation in shear is considerably larger than the volumetric deformation, especially considering the hydrostatic load is ten times larger than the shear load. And, from the slopes of the curves, it can be inferred that the bulk modulus is significantly larger than the shear modulus. The same data have been normalized in Figure 2.4 (b) to highlight the amount of recovery that each test experiences after the load is removed. The shear deformation of the mix recovers much less than the volumetric deformation, indicating that the residual deformation, which causes rutting in the pavement, is predominantly due to the shear deformation.*(6)*

2.2.2 Location of Asphalt Concrete Pavement Rutting and Tire Contact Stresses

It has been observed in rutted pavements in high temperature areas that most of the permanent deformation occurs in the upper 100 to 150 mm of the pavement under the tires. Analyses have shown the critical depth for the maximum shear stresses is approximately 50 mm or less.*(6, 7)* In addition, surface tractions can cause significant shear stresses at the tire-pavement interface. Tire-contact stresses therefore have a large influence on the rutting, and to accurately model permanent deformation, it is important to use loading that best represents field conditions.

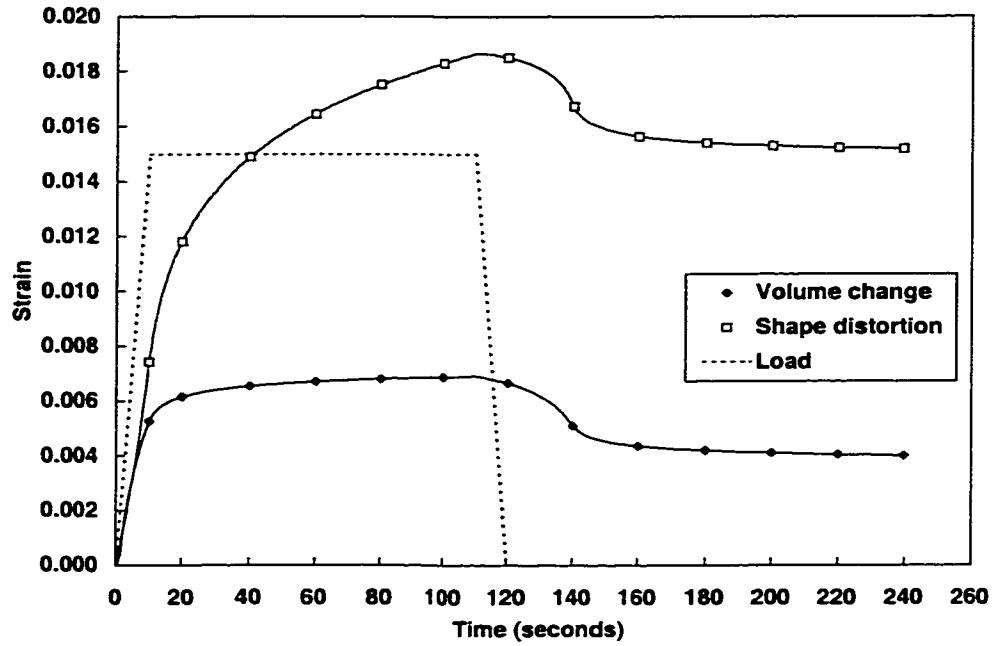

(a)

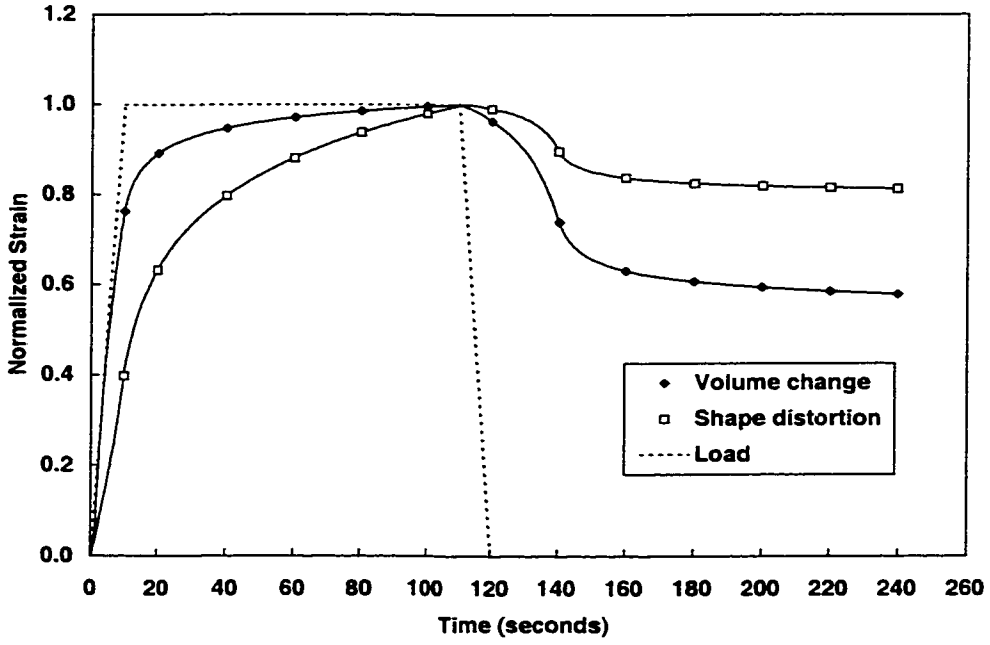

(b)

Figure 2.4 Average Strain History for 15 Different Mixes *(6)*

Measurements of tire contact stresses have been made with the Vehicle-Road-Surface-Pressure-Transducer-Array (VRSPTA).*(11)* This device records the vertical, lateral, and longitudinal displacement as the tire moves slowly over the measuring pad. The VRSPTA is shown in Figure 2.5. The lighter colored pins contain the measuring devices. Although the measurements are not an exact measure of the contact stresses due to some limitations in the physical configuration of the device, the results aid in quantification of the effect of overloaded wheels, under- and over-inflated tires, and different tire types. The contact stresses vary widely for the different loading conditions.*(11)* By utilizing these data, which can be transformed to load tables for input into software codes, the effect of tire-contact stresses can be accounted for in rutting analyses.*(12)*

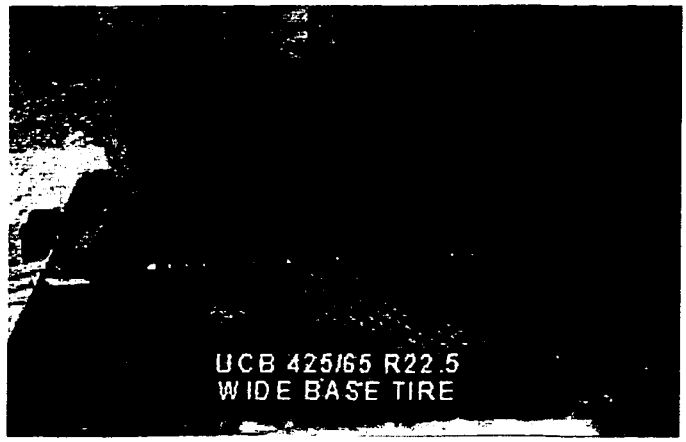

Figure 2.5 Vehicle Road Surface Pressure Transducer Array (VRSPTA)

2.3 Asphalt Concrete Permanent Deformation Laboratory Tests

Various laboratory tests are used to characterize the rutting potential of asphalt concrete mixes. This section describes and highlights the advantages and disadvantages of a number of tests used in recent years, including: uniaxial, triaxial, hollow cylinder, and simple shear tests. The differences between creep and repeated loading are also discussed.

2.3.1 Uniaxial and Triaxial Tests

Uniaxial and triaxial tests are widely used for permanent deformation testing of asphalt concrete.*(13, 14, 15, 16, 17, 18)* In these types of tests, an asphalt concrete specimen with flat, parallel ends is placed between two steel platens. The load is applied through the platens, and in triaxial tests a lateral (confining) pressure is applied. Temperatures are controlled in the tests, but it is difficult to perform the triaxial test at temperatures greater than 40°C with confinement, and it is almost impossible to perform the test without confinement.

The physical configuration of the triaxial test imposes imperfections in the test. Friction between the platens and the specimen restricts lateral movement of the specimen, which introduces a localized state of stress near the platens. In compression tests, lubrication of the end plates reduces the effect of the friction, but it cannot be eliminated. In an

extension test it is necessary to glue the platens to the specimen, resulting in a large friction effect. Because of the end effects, when the length over height ratio is insufficient, a larger modulus value is measured as compared to the actual value.*(9)*

Typical specimens are cylindrical in shape, with a diameter of 100 to 150 mm and a height of 150 to 300 mm. To decrease the end effects due to the friction, and to have a good aspect ratio in the test to allow reasonable measurements, large specimens are necessary. The height of these specimens may exceed the thickness of asphalt concrete layers, which makes the testing of field specimens infeasible.

Repeated or dynamic load tests allow the application of repeated tensile or compressive axial and lateral stress pulses of any shape and duration. Vertical and horizontal strains or deformations are measured on the specimen, from which various quantities can be determined, for example, Young's modulus (E) or the complex equivalent (E*), Poisson's ratio, and plastic strains.*(1)*

An advantage of the triaxial test is the wide range of stress states that can be achieved by varying the confining and axial pressures. Shear components can be introduced, although a state of pure shear is only produced by triaxial extension tests. Indirectly measuring the shear components with compression tests requires the conversion of the measured properties to shear properties. The simple linear elastic relationships are not applicable

because of the nonlinear nature of asphalt concrete mixes, especially at high temperatures and strain levels.*(6, 9, 19, 20)* In addition, it has been reported that the shear stress components that can be produced in the triaxial test are not large enough to represent field conditions and should therefore not be relied on for permanent deformation prediction.*(1)*

2.3.2 Hollow Cylinder Tests

Hollow cylinder tests utilize hollow, cylindrical specimens, and data have been reported using specimens 200 mm high with inner and outer diameters of 90 and 115 mm, respectively.*(19)* In the tests, torque and/or axial loads are applied and the internal and external radial pressures are controlled. Because of the symmetrical specimen, the normal and shear stresses are uniformly applied. With this loading, controlled changes in the magnitude and direction of the principal stresses can be achieved, which is impossible in most other laboratory tests.*(19)*

This test is difficult to perform as the equipment is sophisticated and therefore cannot be easily standardized for routine applications.*(1)* The test also uses large specimens which are difficult to cut in the laboratory, and it is not possible to obtain field specimens. A further disadvantage of the test is the size of the specimen wall, typically 12.5 mm. With this small width, a large aggregate may have a significant influence on the measurements.

Despite this disadvantage, Alavi reported high repeatability in the measurements. *(19)* It is also difficult to perform the tests at high temperatures.

2.3.3 Simple Shear Tests

The simple shear test allows the direct measurement of shear properties. Currently, the simple shear test is performed on cylindrical specimens 150 mm in diameter and 50 mm high glued between two steel platens as shown in Figure 2.6. Tractions are applied to the top and bottom face of the specimen. The physical constraints of the test do not permit the application of tractions on the leading and trailing edge of the specimen, as shown by the dotted lines on Figure 2.7. The missing tractions cause boundary layers near the edges of the specimen, the width of which is independent of the specimen length.*(6)* Much of the industry criticism of the simple shear test has focused on this non-uniform stress state.*(14)* Research has shown that if the specimen length-to-height ratio is greater than three the effect of the missing traction is considerably reduced.*(6)*

The simple shear test is performed in various configurations. The most common is the simple shear test at constant height in which an axial force is applied to the specimen to maintain a constant height in an attempt to obtain a constant volume during the test. In this configuration the stress state in the specimen is close to a state of pure shear. Another configuration is a field state of stress test in which a constant ratio is maintained between the normal and shear stresses. The state of stress near the edge of a truck tire

can be simulated in this test.*(4)* The ability of the constant height test to obtain a condition close to pure shear is a major advantage, and the test is easy to perform. The simple shear test cannot measure the deviatoric component of the normal strains.*(1)* The tests can be performed with creep or repeated loading.

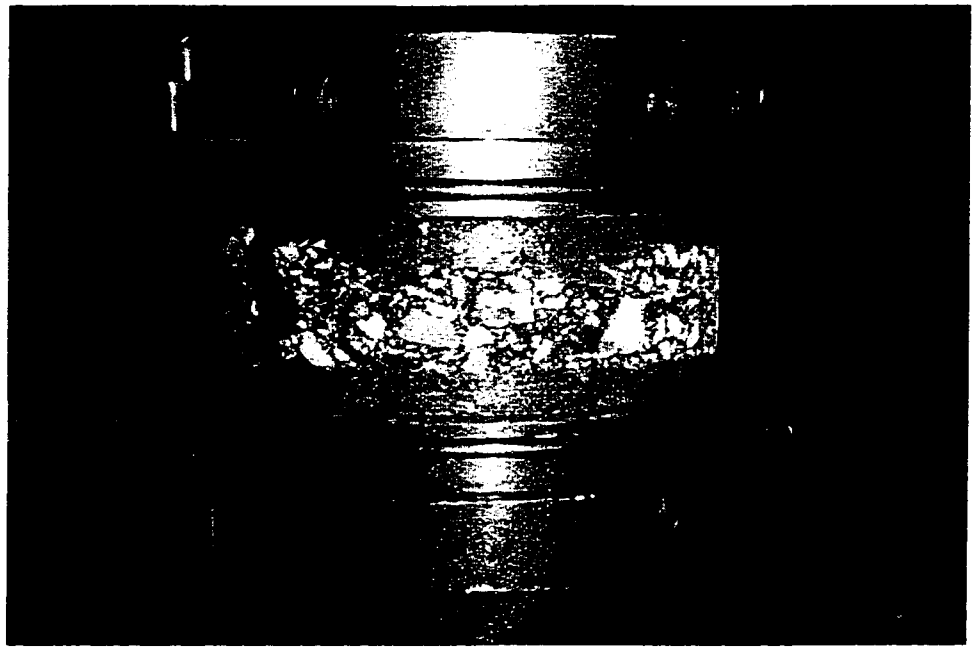

Figure 2.6 Simple Shear Test Specimen, 150 mm Specimen Glued Between Platens

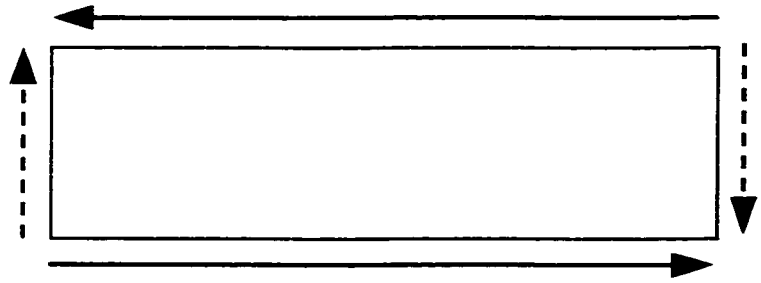

Figure 2.7 Simple Shear Test, Missing Traction on Leading and Trailing Edges

The need to apply an axial load to maintain the constant height was attributed to the specimen dilating.*(4)* However, more recent work attributes part of this change in axial load to the different behavior of asphalt concrete in tension and compression.*(6)*

The most frequent use of the simple shear test is the repeated load simple shear test at constant height (RSST-CH). A detailed description of this test is given in Chapter 6 and the test is used in the performance-based mix design procedure discussed in Chapter 7. Simple shear frequency sweep tests at constant height can be used to obtain the viscoelastic shear properties of asphalt concrete mixes. A description of this test is given in Chapter 3.

Cylindrical specimens are not the perfect specimen shape for this test. At the edges of the specimen, where the length-to-height ratio is small, large errors may be induced by the boundary layers. It has been recommended that rectangular parallelepiped specimens are used.*(9)* These specimens are more difficult to obtain from in-service pavements, and existing testing machines may need modification.

Simple shear test results currently exhibit large variability.*(21)* Most highway and airfield paving mixes have a 19 mm nominal maximum aggregate size, and for these mixes the current specimens (150 mm diameter and 50 mm tall) may be too small to accurately measure the mix response. This specimen size is likely below the

representative volume element (RVE), which is defined as "*...the smallest material volume large enough so that global characteristics of the material remain constant, regardless of the location of the RVE".(6, 9)* It has therefore been recommended that in addition to using rectangular parallelepiped specimens the dimensions of the specimens should be increased.

The accuracy of the measured shear modulus is also a function of the length-to-height ratio of the specimen. Analyses have shown that the error in measuring the shear modulus is reduced by increasing the length-to-height ratio. The analyses showed that smaller length-to-height ratios underestimate the modulus values. Therefore the error is conservative.*(6, 10)*

2.3.4 Creep and Repeated Loading

Both creep and repeated loading have been used with most of the laboratory tests that define the permanent deformation response characteristics of asphalt concrete mixes. It is widely reported that creep tests do not sufficiently differentiate between mixes.*(22, 23, 24, 25)*

In the Shell pavement design procedure *(13)* the permanent deformation characteristics of different mixes are measured using creep loading. Using these data the rutting is estimated, and those mixes for which the estimated rutting does not exceed a terminal

value are selected for use. This Shell method is discussed in more detail in Section 2.4.1. While this approach has worked satisfactorily for mixes containing conventional asphalt contents, Valkering *(23)* reports that when the procedure is used for mixes containing non-conventional binders "*a correction is required to take account of the different relationship between rutting and binder viscosity. The dynamic creep test has shown potential for a more universal applicability, extending to include those asphalts based on a* modified *binder...The great suitability of the dynamic test for rating the effect of the binder modification is ascribed to the recovery effects of the test.*" Furthermore, the use of creep test data may overpredict rutting for mixes containing some modified binders.*(15)*

The research of Tanco *(24)* on the permanent deformation response of conventional and modified asphalt-aggregate mixes under simple and compound loading conditions supports the conclusions of the Shell investigators. He found that repeated load tests were more responsive to the presence of modified binders in AC mixes than static load (creep) tests. Tayebali reports similar results.*(22, 25)* Both Tanco and Tayebali presented convincing evidence that a conventional test like the Hveem Stabilometer *(26)*, while adequate for mix design with conventional asphalt binders, is not suitable for mixes containing modified binders. The test utilizes a slow, controlled rate of deformation, and has no provision to measure the recovery properties of the mix. Subsequent work comparing a conventional binder (AR-8000) with a polymer modified binder (PBA-6A)

further demonstrated this point.*(27)* Hveem Stabilometer tests suggest the mixes with the conventional binder have greater rutting resistance, whereas RSST-CH tests suggest the mixes with the modified binder have greater rutting resistance.

All of these results stress the importance of using a dynamic or repeated load test rather than a static test to measure the permanent deformation characteristics of mixes. Relaxation tests are very difficult to perform in the laboratory, and therefore the viscoelastic properties of mixes are best obtained from frequency sweep tests.

2.3.5 Selection of Appropriate Laboratory Test for Characterizing Rutting

As indicated in Section 2.2, following the discussion in Section 2.3, the dominant material response for permanent deformation distress is shear deformation. The most appropriate test for characterizing permanent deformation is therefore a test that directly measures the shear response of the material. As described above, suitable tests are the simple shear and hollow cylinder tests. The simple shear test is easier to perform and therefore recommended for characterizing the material and for mix design purposes. Testing should also utilize repeated rather than creep loading.

2.4 Estimation of Permanent Deformation

The total amount of permanent deformation experienced at the surface of the pavement is the sum of the permanent deformation in each layer of the pavement. This research focuses on rutting in the asphalt concrete layers only, but for full predictive capacity it is necessary to consider the permanent deformation contributions from the whole pavement structure. Much of the previous research on permanent deformation of flexible pavements has focused on rutting in the unbound layers. Major work in this area was first published by Peattie *(28)* and Dorman *(29)* and is implemented in many pavement design procedures, for example, The Asphalt Institute *(30)*, Shell *(13)* and South African Mechanistic *(31)* Design Methods.

To date most of the research on the estimation of permanent deformation of asphalt concrete has been based on a layer strain approach and, to a lesser extent, on the viscoelastic nature of the material. Various implementations of these approaches have been summarized previously.*(1)* Some research has been performed on developing a viscoelastoplastic constitutive relationship for asphalt concrete, and these types of more complex constitutive relationships are currently being developed in numerous projects.

This section presents some of the methods of permanent deformation analysis and prediction. The advantages and limitations of each approach are discussed.

2.4.1 Layer Strain Approach

The layer strain approach was first proposed by Barksdale *(32)* and Romain *(33)* and is included in the Shell Pavement Design Manual.*(13)* Each layer of the pavement is subdivided into thinner layers and the stresses and strains are calculated at the center of each layer. The layer strain approach typically uses linear elastic layer theory. Laboratory tests are used to establish a relationship between the plastic and elastic strains. With this relationship and the calculated stiffness at the center of the sublayer, the axial plastic strain, ε_i^p, is determined for each sublayer with thickness Δz_i. The total permanent deformation, Δp, is calculated using Equation (2.1).

$$\Delta p = \sum_{i=1}^{n} \varepsilon_i^p \bullet \Delta z_i \qquad (2.1)$$

This approach only considers the area under the center of the tire and typically uses axial compression laboratory tests in the creep loading mode to determine the relationship between the elastic and plastic strains. The shear response of the pavement under the edge of the tires is ignored, and hence the method is unable to predict the "humps" that appear along the sides of the ruts. In addition, linear elasticity does not capture some of the essential behavior causing rutting, such as the shear flow at the edge of the tires and the permanent deformations that occur after the load is removed. Modeling the asphalt concrete as a linear elastic material therefore limits the ability to predict permanent deformation.

2.4.2 Mechanistic-Empirical Approach

An alternative to the layer strain approach was recently used to describe the rutting behavior of the Westrack test sections.*(34)* In this approach, the pavement is modeled as a multi-layered elastic system, with the asphalt concrete modulus determined from RSST-CH tests. The rutting is assumed to be controlled by shear deformations. The accumulation of permanent shear strain at a 50 mm depth beneath the edge of the tire is assumed to fit the relationship shown in Equation (2.2)

$$\gamma^i = a \exp(b\tau)\gamma^e n^c \qquad (2.2)$$

where γ^i is the permanent (inelastic) shear strain at a 50 mm depth, τ is the shear stress at the same depth determined with elastic analyses, γ^e the elastic shear strain, n the number of load repetitions and a, b and c are regression coefficients obtained from field data, RSST-CH laboratory test data and the elastic simulations.

The accumulation of the inelastic shear strains is calculated on an hourly basis, using a time-hardening principle. The corresponding rut depth for this inelastic shear strain is calculated using Equation (2.3)

$$\text{Rut depth} = K \cdot \gamma^i_j \qquad (2.3)$$

where γ^i_j is the inelastic shear strain at the j^{th} hour and K is a constant.

This method has significant advantages over the layer strain approach in that it considers the shear deformation under the edge of the tires, however it is still based on linear elasticity. In addition, the method has not been calibrated with a large data set.

2.4.3 Viscoelastic Approach

This approach attempts to account for the viscoelastic properties of asphalt concrete in determining permanent deformation. Moving wheel loads and the time-dependent nature of asphalt concrete are both accounted for by considering the material as either some configuration of Maxwell and/or Kelvin elements or by using generalized compliance relationships.*(1)* Burger's model is often used to characterize asphalt.*(3)* Both linear and nonlinear viscoelasticity have been considered although nonlinear viscoelasticity has usually been considered prohibitive in terms of laboratory and computational requirements.

A software program, VESYS, for viscoelastic modeling of pavements assumes the pavement is a linear elastic layered structure.*(35)* The material constants used by the program are the viscous equivalents of Young's modulus and Poisson's Ratio, and the viscoelastic correspondence principle is used.*(36)* VESYS was used to predict rutting in the asphalt concrete layer in a study by Collop and Cebon, et al.*(3)* The viscoelastic properties were estimated from creep compliance data, assuming Burger's model. The rheological properties of the asphalt-aggregate mix were assumed to be the same as for

the asphalt. Some assumptions, which are not based on experimental data, are made, to relate the mix stiffness to the binder stiffness. The results showed the prediction of shear deformations, or "humps," and the predicted residual deformation is realistic. However, it is reported that in the early stages of a test, the predicted deformation does not fit the measured field deformation. Deformation under the first few wheel loads is usually attributed to densification, which linear viscoelasticity is unable to reproduce.

Research for the Shell Pavement Design Manual reports that considering the viscoelastic properties of asphalt is not sufficient for rutting prediction because the large influence of the aggregate and the asphalt-aggregate interaction in the mix is not considered.*(15)*

Viscoelasticity is an obvious approach for permanent deformation prediction of asphalt concrete. However, to date, it has received limited use with relatively unsuccessful results. Most of the work reported only considers the viscoelastic properties of the asphalt and/or obtains and uses the viscoelastic properties of the mix indirectly.

2.4.4 Viscoelastoplastic Approach

As part of the Strategic Highway Research Program (SHRP) a constitutive model was developed to characterize permanent deformation of asphalt concrete.*(4)* Initially, a viscoelastic model with damage was developed, but this was not adequate to describe the response. The viscoelastic model was then enhanced with an elastoplastic component.

From laboratory tests and observed performance it was deemed necessary for the model to incorporate the following characteristics: dilation under shear loading; increase in stiffness with an increase in hydrostatic pressure; negligible volumetric creep; residual permanent deformation on removal of the load; and temperature and rate of loading dependence.*(4)*

The viscoelastic component of the model consists of several three-dimensional Maxwell elements in parallel. In each Maxwell element both the spring and the dashpot are nonlinear. The viscoelastic component of the model represents the rate and temperature dependent binder.

The elastoplastic component of the model represents the aggregate in an asphalt concrete mix. Rate-independent J_2 plasticity, which consists of an elastic component, the von Mises plasticity model with an associative flow rule, and linear isotropic and kinematic hardening laws, was adopted.

The viscoelastic model alone was not adequate to describe the behavior of asphalt concrete. Under cyclic loading most of the strain was recovered during unloading, which did not match test data. Even though the inclusion of the plastic component was an improvement, this particular model did not provide a good fit to the test data. Simulations of the repeated load simple shear test at constant height also did not fit the

data well. Furthermore, for some data, the response of the mix is insensitive to the air-void content, and such a response does not match field or laboratory data.

2.4.5 Current Research

The development of a constitutive model to characterize asphalt concrete rutting behavior is receiving widespread attention. Symplectic Engineering Corporation is working on a finite deformation viscoelastoplastic model.*(37)* A small deformation version of the model was used in a study to predict the differences between channelized and wandering traffic. The model predicts temperature and rate dependencies, large residual strains, Bauschinger-type effects for the rate-independent plastic component, and different behavior in tension and compression. The yield surface is a sphere in stress space. The model successfully predicts most of the permanent deformation behavior, although for some pavement structures the channelized traffic resulted in less rutting than the wandering traffic, which is not typically observed in the field.*(38)*

The Superpave Models Contract Team is identifying a simple performance test for characterizing asphalt concrete. Although the contract is not complete, early reports indicate their recommendation is the triaxial test. The project is also developing a constitutive model for asphalt concrete that will describe rutting, fatigue cracking, reflection cracking, and thermal cracking. The constitutive model will be based on

Shapery's continuum damage model for viscoelasticity and viscoplasticity *(39)*, Desai's Disturbed State Concept *(40)*, and fracture mechanics concepts.*(18)*

The Delft University of Technology in the Netherlands is developing a constitutive model to describe asphalt concrete behavior for both fatigue and rutting distress.*(17)* This model is also based on Desai's Disturbed State Concept model and will primarily use uniaxial compression and tension tests to determine the parameters for the model, although triaxial tests will also be performed to facilitate complete definition of the failure envelope.

2.5 Findings

This discussion on asphalt concrete properties, laboratory tests, and the methods of estimating permanent deformation summarizes the work to date on this subject and provides a starting point for the work described in this dissertation. The deformation of asphalt concrete is dependent on temperature and on the rate of loading, and the development of rutting is primarily a result of shear deformation. The appropriate laboratory test for characterizing the permanent deformation is therefore some form of shear test. At this time the repeated load simple shear test at constant height is a practical and feasible test. Creep tests have been shown to not adequately distinguish between mixes, therefore repeated loading tests are preferable.

The layer strain approach for estimating permanent deformation does not result in accurate predictions, primarily because the region of analysis is directly under the tire and because linear elasticity is used.

Attempts to use viscoelasticity to predict permanent deformation of asphalt concrete have typically obtained the viscoelastic properties indirectly or used a quasi-elastic approach with limited success and have often not considered the important effects of the aggregates in the mix. Because asphalt concrete exhibits largely viscoelastic behavior, measuring the viscoelastic properties directly and using them in a viscoelastic material model has the potential to predict permanent deformation accurately. Furthermore, the behavior at high strains is nonlinear and therefore accounting for these nonlinearities should improve prediction capabilities.

CHAPTER 3

LABORATORY TEST DATA

The discussion in Chapter 2 highlights some essential properties which need to be incorporated in a constitutive model for asphalt concrete, namely the viscoelastic nature of mixes and the nonlinear response of mixes at high strains and temperatures. In this chapter, these two properties are investigated in the laboratory, and the data are used to develop the constitutive model in Chapters 4 and 5.

A dense graded asphalt concrete and a gap-graded mix modified with asphalt-rubber are tested using the simple shear test at constant height in the frequency sweep mode. The data show some variability, and reasons for this are discussed.

3.1 Materials and Mix Design

This section discusses the materials, mix designs, and specimen preparation of the mixes used to develop the constitutive model.

3.1.1 Mix Design

The asphalt concrete mix used in the laboratory testing was obtained from the pavements constructed for Goal 3 of the Caltrans Accelerated Pavement Testing Program (CAL/APT) at the Richmond Field Station, University of California at Berkeley. The objective of the Goal 3 testing was to compare the performance of a gap-graded asphalt-rubber hot mix (ARHM) overlay and a conventional dense graded asphalt concrete (DGAC) overlay. The overlays were placed over an existing asphalt concrete pavement. Further details on the construction of the tests and the test results are contained in references *(7)* and *(41)*. The majority of laboratory testing was performed on the DGAC. Some testing was performed on the ARHM material for model development and to evaluate the applicability of the model to modified binders.

The asphalt used in the DGAC mix was an AR-4000 asphalt binder produced by Huntway Refining and the modified asphalt-rubber used in the ARHM consisted of 78 percent AR-4000, 2 percent extender oil, and 20% crumb rubber. The crumb rubber contained 75 percent ground tire rubber and 25 percent natural rubber. Specifications for the AR-4000 asphalt used in the DGAC and in the ARHM are shown in Table 3.1. Specifications for the blended asphalt-rubber binder used in the ARHM are shown in Table 3.2.

Table 3.1 Asphalt Properties for AR-4000 in DGAC and ARHM *(41)*

Property	AASHTO Method	Range	Report
Tests on Original Asphalt (Caltrans Specifications)			
Flash Point	T48	> 225°C	> 293°C
Solubility in TCE	T44	> 99 %	99.8+ %
Tests on Residue from RTFO AR 4000 (AASHTO T240)			
Asphalt Viscosity at 60°C (poises)	T202	4000 ± 1000	4907
Kinematic Viscosity at 135°C (poises)	T201	> 275	425
Penetration at 25°C 100g /5 sec (dmm)	T49	> 25	36
Percent of original penetration	T49	> 45 %	62 %
Ductility at 25 cm	T51	> 75	100+

Table 3.2 Specifications for Blended Asphalt-Rubber Binder in ARHM *(41)*

Property	ASTM Method	Range
Cone Penetration at 25°C	D217	25 – 70
Resilience at 25°C percent rebound	D3407	<18
Field softening point (°C)	D36	52 – 74
Viscosity at 190°C (centipoise)	Haake Viscometer	1900 - 3500

The aggregates for the mix were obtained from various sources, including the Point Richmond Quarry, Lone Star Clayton, and Tidewater sand. The DGAC gradation meets the Caltrans Standard Specifications for a 19mm Type A coarse gradation asphalt concrete and the ARHM gradation meets the Caltrans Standard Special Provisions for 12.5 mm Type 2 gap-graded asphalt concrete.*(42)* These gradations are shown in Table 3.3 and Figures 3.1 and 3.2.

Table 3.3 Aggregate Gradation *(41)*

	Dense Graded Asphalt Concrete (DGAC)		Asphalt-Rubber Hot Mix (ARHM)	
Sieve Size	**Specification**	**Mix Design**	**Specification**	**Mix Design**
19 mm (3/4 in.)	90 – 100[1]	100	100	100
12.5 mm (1/2 in.)		93	90 – 100	98
9.5 mm (3/8 in.)	60 – 75	73	80 – 90	85
4.75 mm (No. 4)	45 – 55	50	23 – 38	33
2.36 mm (No. 8)	31 – 41	39	18 – 26	23
1.18 mm (No. 16)		27		15
0.6 mm (No. 30)	13 – 23	18	6 – 14	10
0.3 mm (No. 50)		11		6
0.15 mm (No. 100)		6		4
0.075 mm (No. 200)	3 – 7	5	3 – 7	3

1 Percent passing

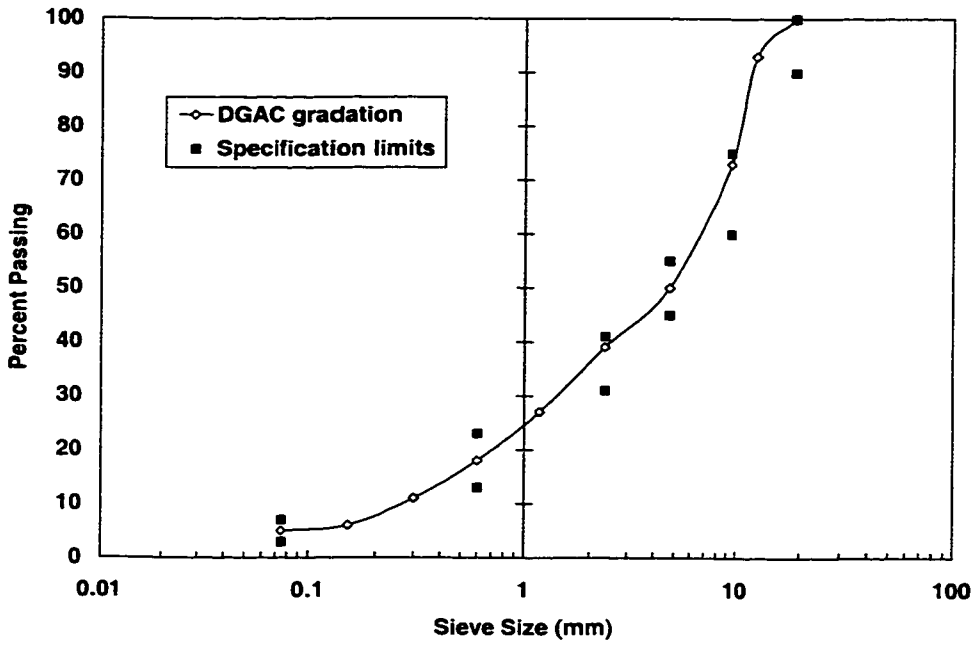

Figure 3.1 DGAC Aggregate Gradation

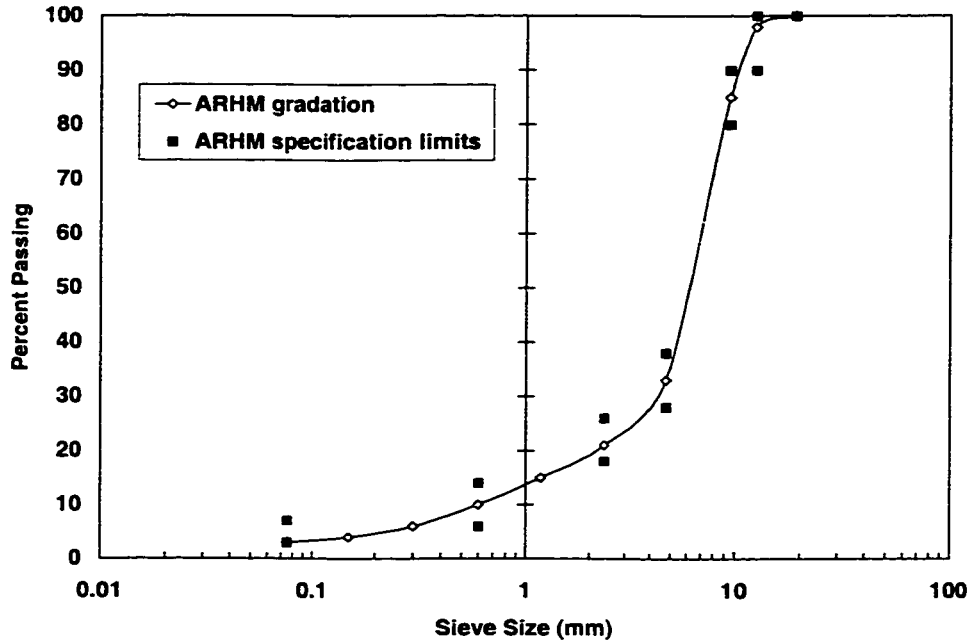

Figure 3.2 ARHM Aggregate Gradation

The recommended asphalt content range is 5.0 to 5.3 percent and 7.6 to 7.9 percent by weight of aggregate for the DGAC and ARHM respectively, as determined by the Caltrans Mix Design Procedure (Hveem Procedure).*(26, 41)* The detailed mix design is contained in reference *(41)*.

3.1.2 Specimen Preparation

The specimens were obtained from the pavement, either cored directly or cored from slabs cut from the pavement. All the specimens were therefore "field mix, field compacted." DGAC specimens numbered 25 to 43 were cored from the pavement in October 1997 and tested in December 1997. Specimens numbered 53 to 59 were also

cored from the pavement in October 1997 and stored in a room in which the temperature was maintained at 20°C until testing. Specimens numbered 80 to 97 were obtained from slabs cut from the pavement in October 1997 and stored in closed wooden boxes until coring in March 2000. Specimens numbered 98 to 131 were cored from the pavement in April 2000. Specimens numbered 53 to 59 and 80 to 87 were tested in March 2000, and those numbered 89 to 131 were tested in April and May 2000.

All the ARHM specimens were cored from the test sections in October 1997, stored at 20°C, and tested in either August 1998 or October 2000.

The specimens tested in 2000 were either those cored previously and stored at 20°C, those obtained from slabs stored in a closed wooden box under cover, or those obtained from the CAL/APT test sections. The test sections were located inside a building, and therefore the difference in aging between these specimens and specimens tested in 1997 and 1998 is negligible.

The air-void content of the specimens was determined in the laboratory using AASHTO Test Methods T-209-94, T-275-91 Method A, and AASHTO T166-93 to obtain the theoretical maximum specific gravity and the bulk specific gravity.*(43)* For some of the later specimens, the saturated, surface dry specimens were obtained by drying in a

dessicator, rather than drying the surface with an air gun. Both methods produce the same results.

Specimens were 150 mm in diameter and 50 mm in height. All edges had cut faces. The specimens were glued to platens for securing in the testing machine, as shown in Figure 3.3. Linear variable displacement transducers (LVDT), also shown in Figure 3.3, were mounted on the specimen to measure changes in the vertical height and the horizontal displacement. The shear strain was calculated from the LVDT data. Changes in height were measured from platen to platen (50 mm) to obtain an average result and avoid localized effects. The vertical LVDT was used to control the axial actuator which maintains the constant height in the test. The gage length was considered to be 37 mm to account for the effects of the rigid glue.

3.2 Laboratory Test and Program

Shear frequency sweep tests were performed according to AASHTO TP7-00.*(44, 45)* These tests are strain controlled with the strain imposed as a sine wave, and the resulting stress measured. The peak stress lags the peak strain by the phase angle. This is shown in Equations (3.1) and (3.2).

$$\varepsilon(t) = \varepsilon_0 \sin(\omega t) \tag{3.1}$$

$$\sigma(t) = \sigma_0 \sin(\omega t + \delta) \tag{3.2}$$

In these equations, $\varepsilon(t)$ and $\sigma(t)$ are the strain and stress at time t; ε_0 and σ_0 are the peak stress and strain; ω is the frequency in radians per second; and δ is the phase angle in radians.

Figure 3.3 Simple Shear Test Specimen with LVDTs Mounted

Five temperatures and seven strain levels were used for the DGAC mix, as shown in the test program in Table 3.4. Limited testing was performed on the ARHM. The temperatures and strain levels used are shown in Table 3.5. The air-void contents of the specimens are shown in parentheses.

Table 3.4 Laboratory Test Program, Dense Graded Asphalt Concrete (DGAC)[1]

Strain Level (%)	Temperature (°C)				
	20	30	40	50	57
0.01	31 CA[2] (7.73)[3] 33 CA (7.99) 35 CA (8.38)	102DA (7.74) 112DA (5.29) 112DA (6.10)	25 BA (9.04) 40 BA (7.77) 43 BA (8.52) 129 BA (5.35)	105 EA (7.51) 111 EA (5.53) 113 EA (6.49) 131 EA (5.49)	29 AA (8.40) 39 AA (7.76) 42 AA (8.52) 86 AA (6.88)
0.05	31 CB (7.73) 33 CB (7.99) 35 CB (8.38)	102DB (7.74) 112DB (5.29) 112DB (6.10)	25 BB (9.04) 40 BB (7.77) 43 BB (8.52) 129 BB (5.35)	105 EB (7.51) 111 EB (5.53) 113 EB (6.49) 131 EB (5.49)	29 AB (8.40) 39 AB (7.76) 42 AB (8.52) 86 AB (6.88)
0.10	31 CC (7.73) 33 CC (7.99) 35 CC (8.38)	102DC (7.74) 112DC (5.29) 112DC (6.10)	25 BC (9.04) 40 BC (7.77) 43 BC (8.52) 129 BC (5.35)	105 EC (7.51) 111 EC (5.53) 113 EC (6.49) 131 EC (5.49)	29 AC (8.40) 39 AC (7.76) 42 AC (8.52) 86 AC (6.88)
0.50		104DD (7.74) 123DD (5.95) 124DD (6.76)	93 BD (7.41) 126 BD (6.13) 132 BD (5.22)	92 ED (7.46) 98 ED (8.09) 120 ED (6.14)	53 AD (6.13) 55 AD (5.99) 81 AD (7.82)
1.00		95 DE (7.48) 103 DE (7.66) 108 DE (6.41)	91BE (7.98) 118 BE (5.31) 125 BE (6.65)	100 EE (7.77) 107 EE (6.54) 117 EE (6.01)	56 AE (6.37) 59 AE (5.73) 83 AE (8.66)
1.50			90 BF (7.17) 96 BF (7.89) 128 BF (5.34)	94 EF (6.90) 97 EF (7.55) 115 EF (6.06) 121 EF (6.80)	85 AF (6.20) 87 AF (6.15)
2.00				89 EG (7.33) 106 EG (7.93) 109 EG (6.30)	80 AG (7.07) 84 AG (7.63)

1 Specimens prefixed with G3 in text and charts
2 The first letter denotes the temperature and the second the strain level
3 Air-void content

When the first series of tests were performed in December 1997, the maximum temperature that could be maintained by the testing machine was 57°C; for consistency, the 57°C temperature was used for the second series of testing on the DGAC. The ARHM was tested at 60°C in both series of tests.

Table 3.5 Laboratory Test Program, Asphalt-Rubber Hot Mix (ARHM)[1]

Strain level (%)	Temperature (°C)		
	20	40	60
0.01	12 CA[2] (14.70)[3] 15 CA (14.62) 28 CA (14.82)	3 BA (14.83) 4 BA (14.60) 8 BA (14.75)	35 AA (14.82) 45 AA (14.84) 93 AA (14.78)
0.05	12 CB (14.70) 15 CB (14.62) 28 CB (14.82)	3 BB (14.83) 4 BB (14.60) 8 BB (14.75)	35 AB (14.82) 45 AB (14.84) 93 AB (14.78)
0.10	12 CC (14.70) 15 CC (14.62) 28 CC (14.82)	3 BC (14.83) 4 BC (14.60) 8 BC (14.75)	35 AC (14.82) 45 AA (14.84) 93 AC (14.78)
0.50		6 BD (14.17) 11 BD (15.03)	1 AD (14.40) 7 AD (14.18) 14 AD (15.11)
1.50		10 BF (15.37) 17 BF (14.21) 24 BF (14.40)	
2.00			31 AG (14.49) 37 AG (15.18) 38 AG (14.34)

1 Specimens prefixed with AR in text and charts
2 The first letter denotes the temperature and the second the strain level
3 Air-void content

No tests were performed at the higher strain levels for the lower temperatures because it is difficult for the testing machine to adequately control the test. The three lowest strain levels impose relatively little damage to the specimen, and it is standard practice to use one specimen for all three strain levels.*(44, 45, 46)* However, at the higher strain levels the specimen was damaged during testing. Therefore, a new specimen was used for each strain level above 0.1 percent strain.

The test method specifies preconditioning for the tests. The preconditioning performed varied between the tests. The specimens tested at the 0.01, 0.05 and 0.1 percent strain

levels at 30°C and 50°C, and DGAC specimens 129 and 86 were preconditioned before the 0.01 percent test only. The 0.05 and 0.1 percent tests immediately followed the first test. The remaining specimens were preconditioned before each test. Comparisons made between the different preconditioning methods indicated small, but relatively insignificant differences.

The temperature during a test was controlled within ±1°C of the target temperature.

The test programs in Tables 3.4 and 3.5 show the specimens that were used in the data analyses. Three or four specimens were tested in each cell. The tests on the stiff mixes require large loads to achieve the specified strain, and the rapid application of these large loads, especially at the higher frequencies, can cause problems with the feedback control, which induces resonance in the machine. This occurred on many specimens, especially those tested at the higher strain levels. In some extreme cases, the bond between the specimen and the platen broke. Most of the specimens that exhibited resonance did not give reasonable results, and were therefore omitted from further analyses. Appendix 1 contains a brief discussion of the raw data from these tests and the problems associated with the specimens that exhibited resonance.

Two data files were obtained for each test. One file contained the raw data and the other contained processed data. The processed data file included the shear stress (σ^0) and shear

strain (γ^0) amplitudes, the magnitude of the complex shear modulus (|G*|), and the shear phase angle (δ) for each frequency (f). The data were obtained with the ATS software *(47)*, which performs a fast Fourier transform to represent the laboratory data with sine curves. After the data are transformed, the peak values and phase angle are extracted. Only one value for each parameter estimated is reported per frequency, therefore it was not possible to determine the standard error of the estimates or other statistical measures. In Appendix 1, a set of raw data was used to obtain an indication of the variability of the reported parameters. The phase angle is the most difficult parameter to measure precisely. For the range of phase angle values obtained, the magnitude of the loss modulus is more sensitive to the phase angle than the storage modulus. Therefore, often the loss modulus values are more variable, and are sometimes unreasonable.

3.3 Laboratory Test Results

The most useful of using way of using the laboratory data to develop the constitutive model is to calculate the storage (G') and loss (G") moduli, as shown in Equations (3.3) and (3.4).

$$G' = \frac{\sigma^0}{\varepsilon^0}\cos(\delta) \tag{3.3}$$

$$G'' = \frac{\sigma^0}{\gamma^0}\sin(\delta) \tag{3.4}$$

Data from the laboratory testing are shown in Figures 3.4 to 3.15 for the DGAC mix and Figures 3.16 to 3.23 for the ARHM. Figures 3.4 to 3.13 and 3.16 to 3.21 show either the storage or the loss modulus versus frequency (radians per second), for each temperature, over a range of strains. Figures 3.14, 3.15, 3.22 and 3.23 show the results of tests at 0.1 percent strain for a range of temperatures.

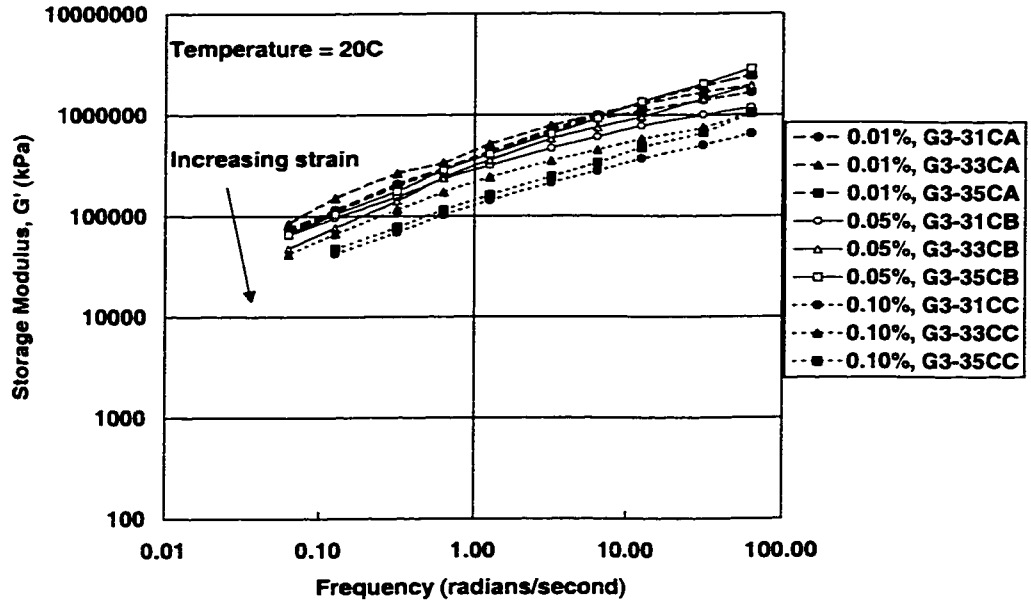

Figure 3.4 Storage Modulus Master Curves at 20°C, DGAC

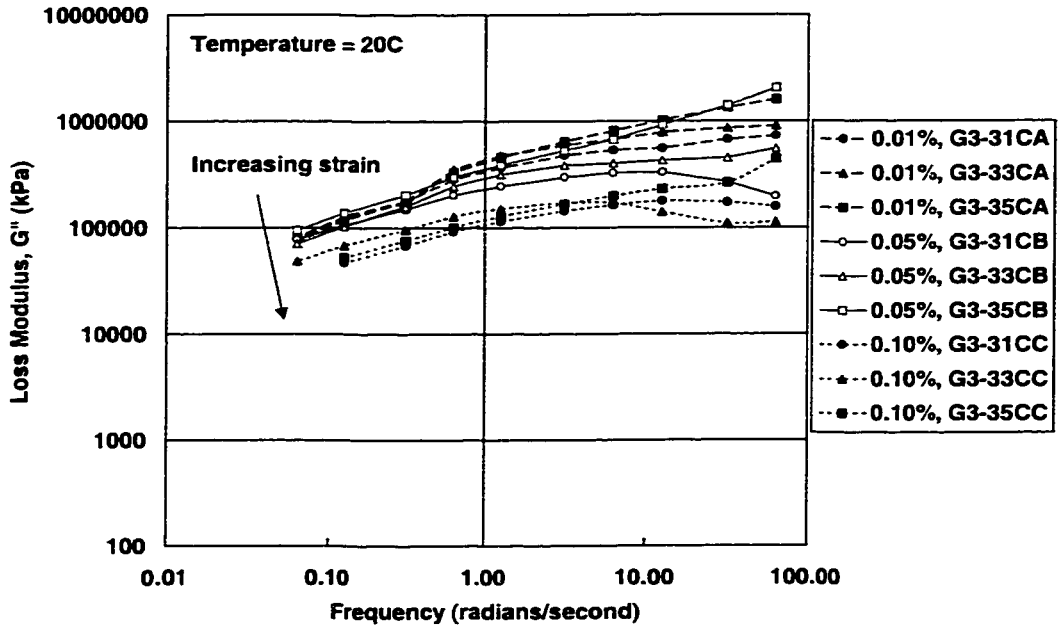

Figure 3.5 Loss Modulus Master Curves at 20°C, DGAC

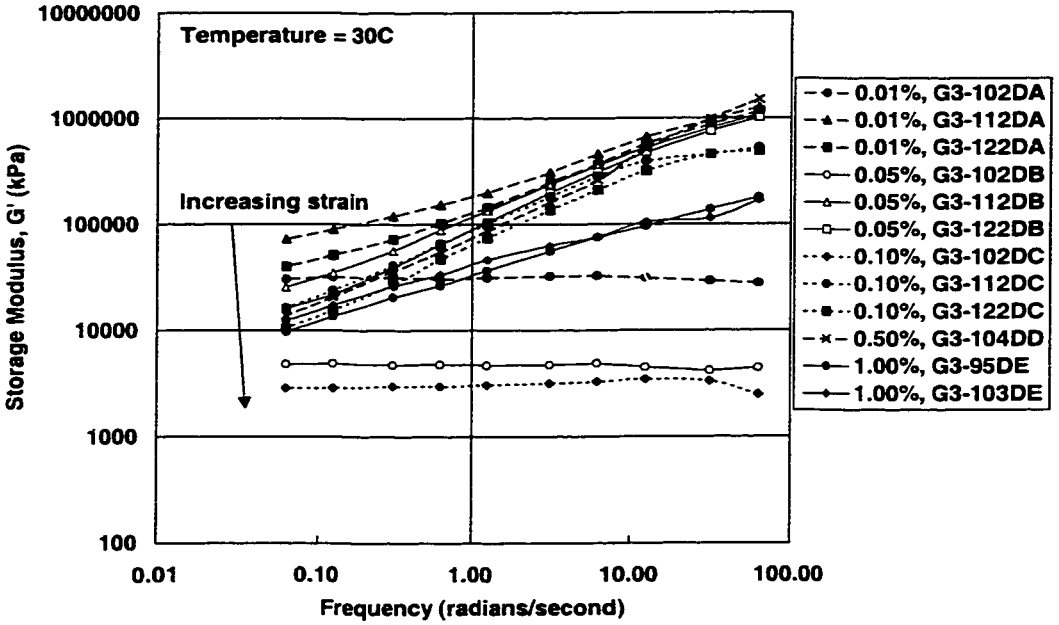

Figure 3.6 Storage Modulus Master Curves at 30°C, DGAC

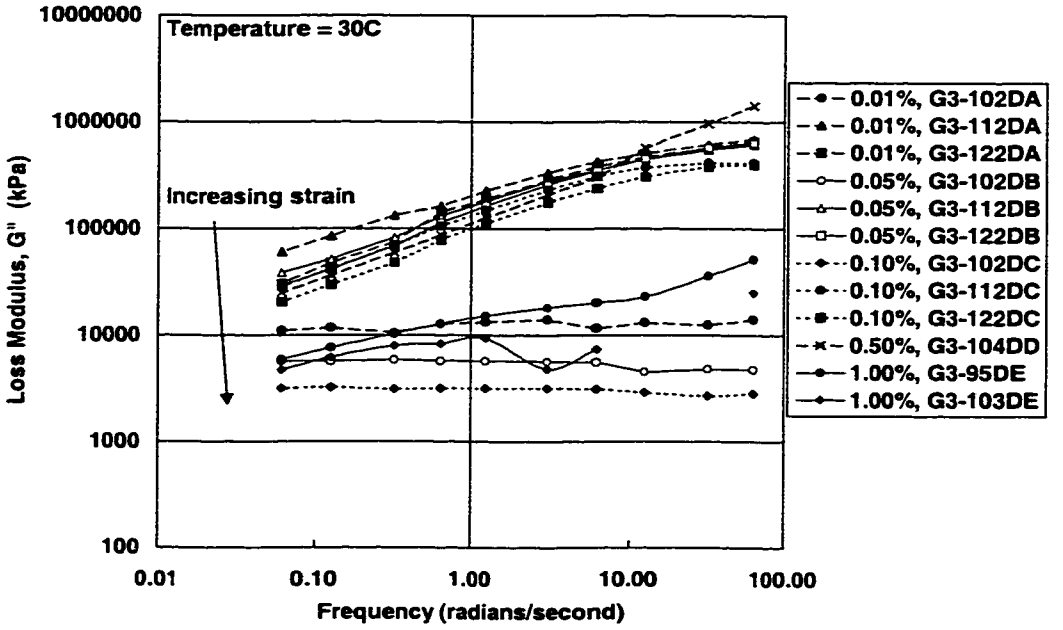

Figure 3.7 Loss Modulus Master Curves at 30°C, DGAC

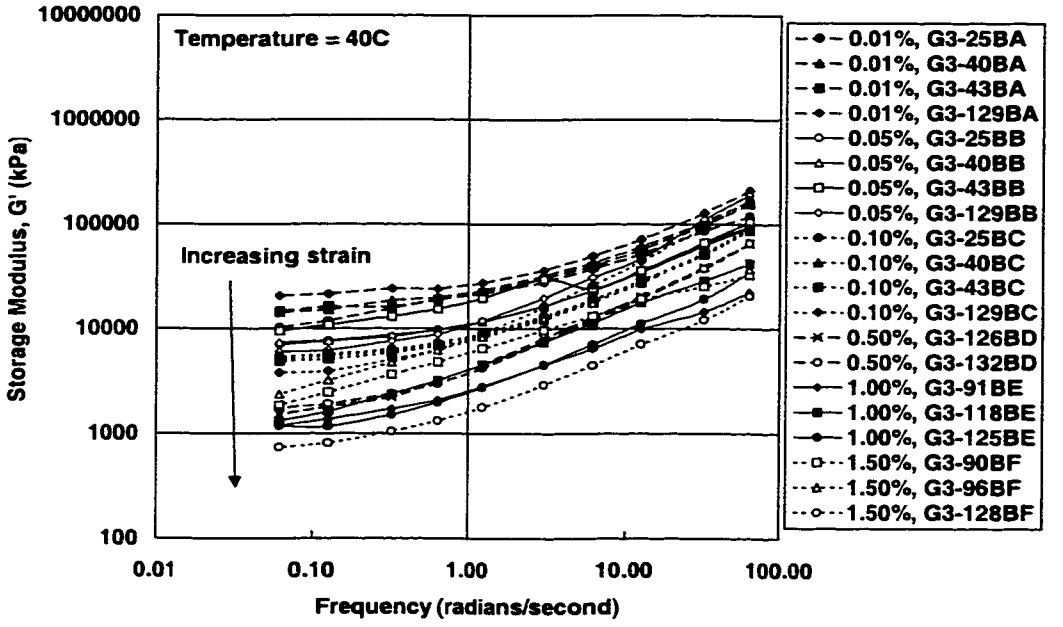

Figure 3.8 Storage Modulus Master Curves at 40°C, DGAC

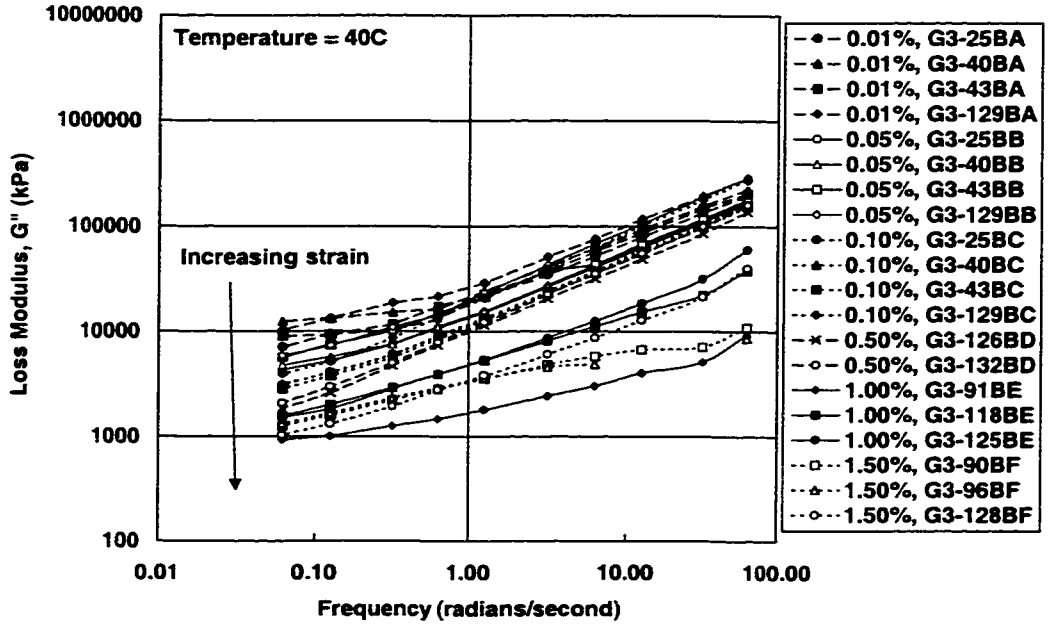

Figure 3.9 Loss Modulus Master Curves at 40°C, DGAC

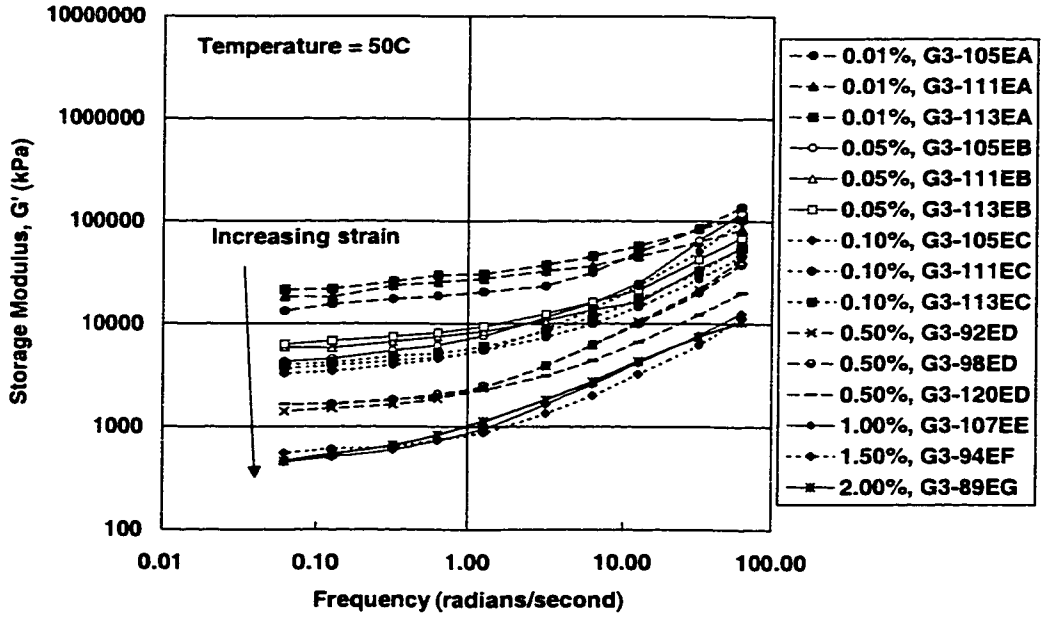

Figure 3.10 Storage Modulus Master Curves at 50°C, DGAC

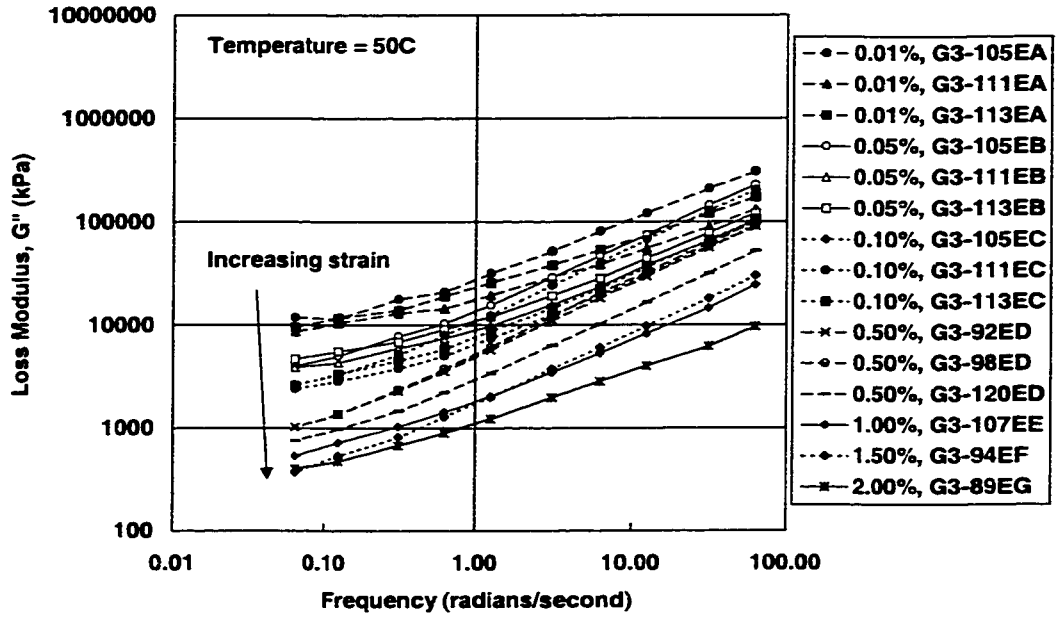

Figure 3.11 Loss Modulus Master Curves at 50°C, DGAC

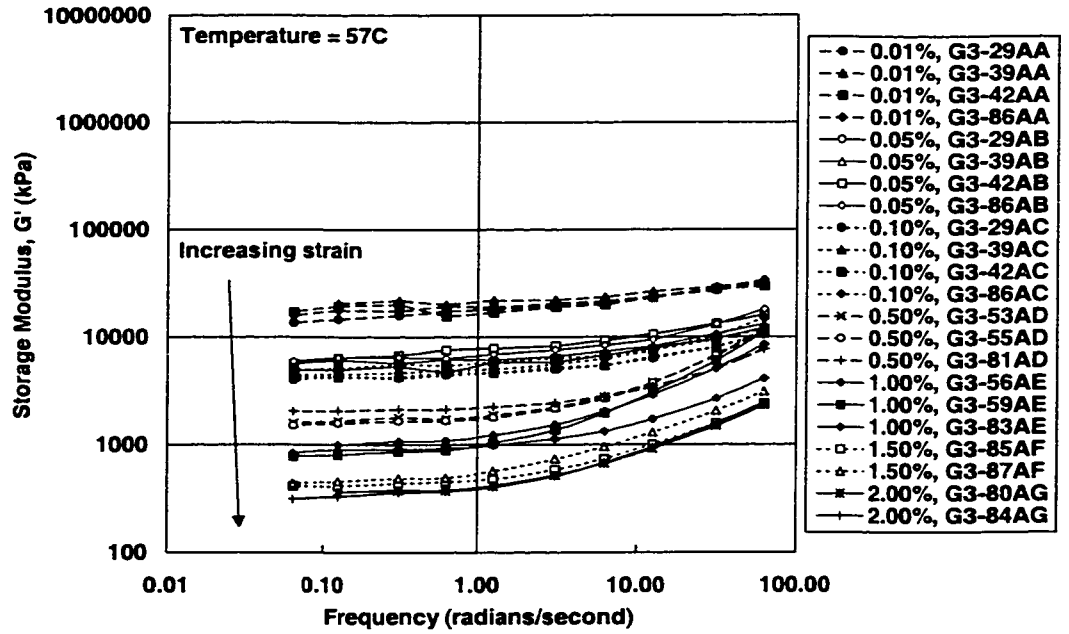

Figure 3.12 Storage Modulus Master Curves at 57°C, DGAC

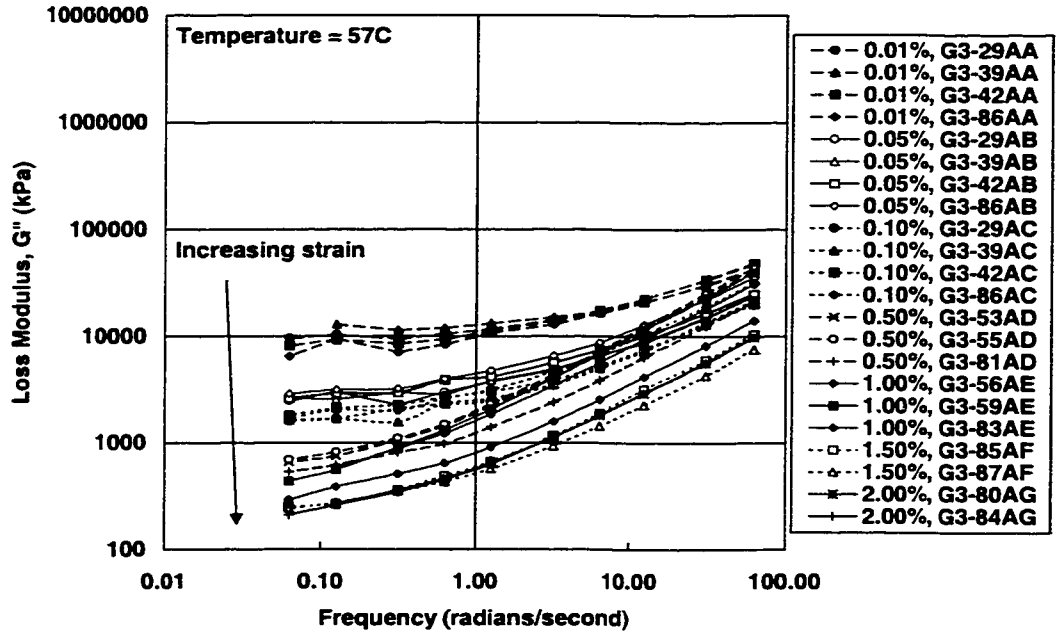

Figure 3.13 Loss Modulus Master Curves at 57°C, DGAC

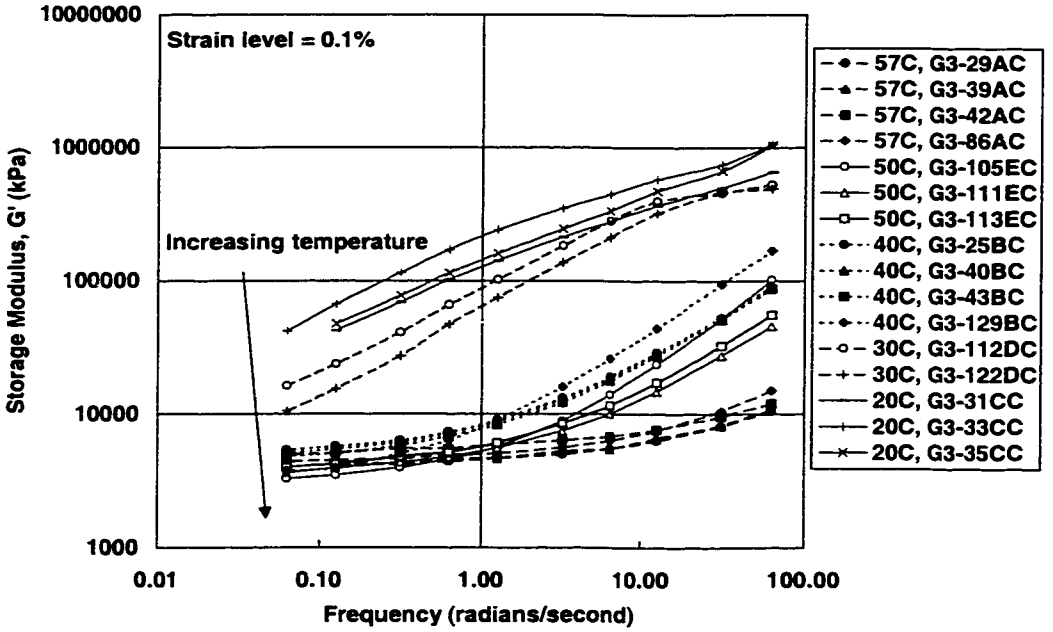

Figure 3.14 Storage Modulus Master Curves for 0.1% Shear Strain, DGAC

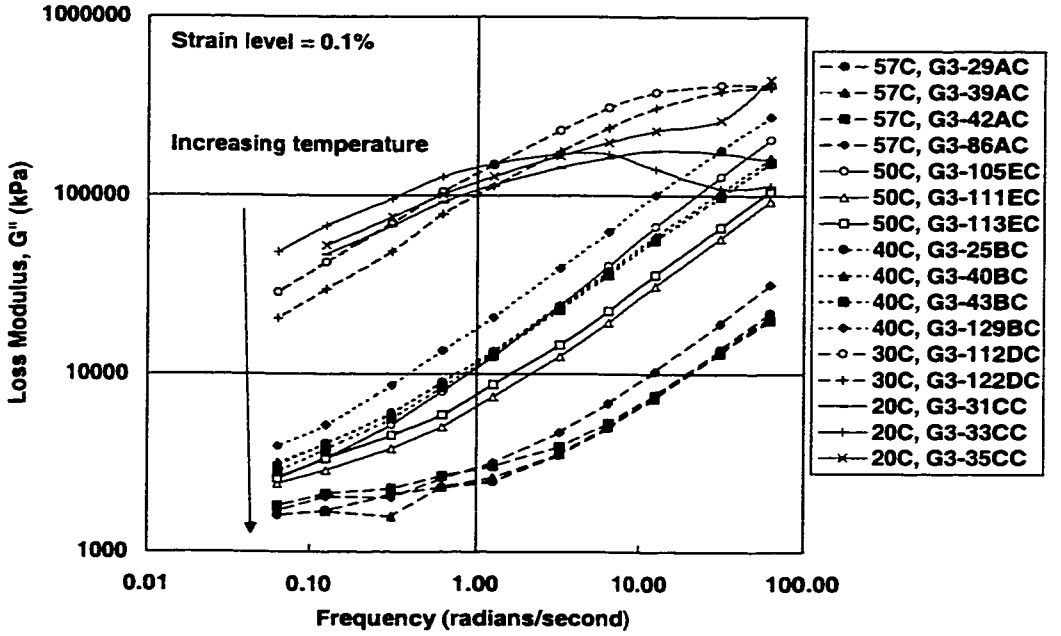

Figure 3.15 Loss Modulus Master Curves for 0.1% Shear Strain, DGAC

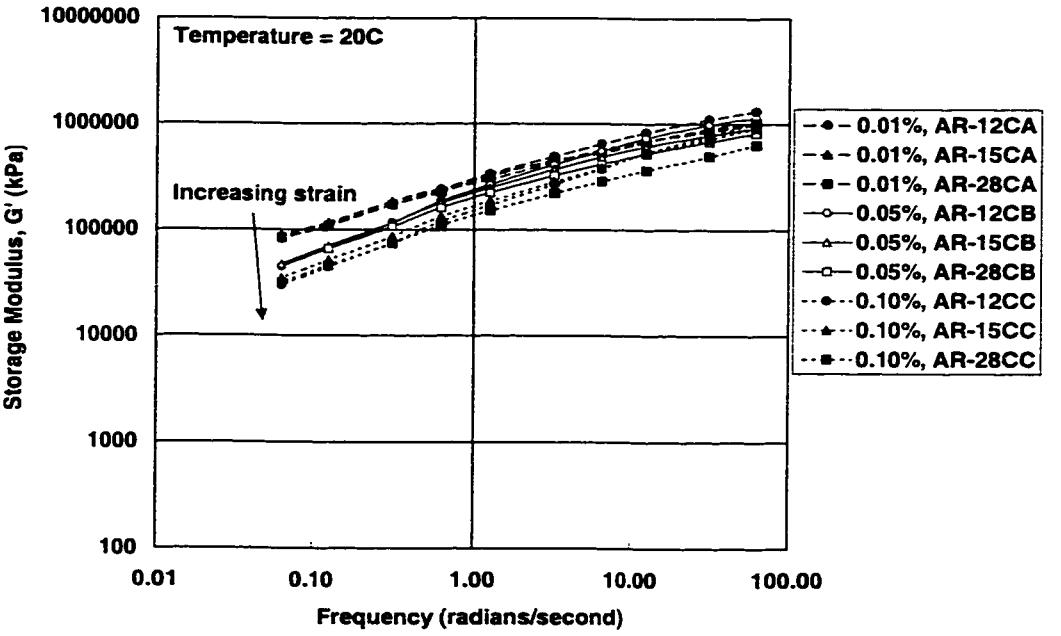

Figure 3.16 Storage Modulus Master Curves at 20°C, ARHM

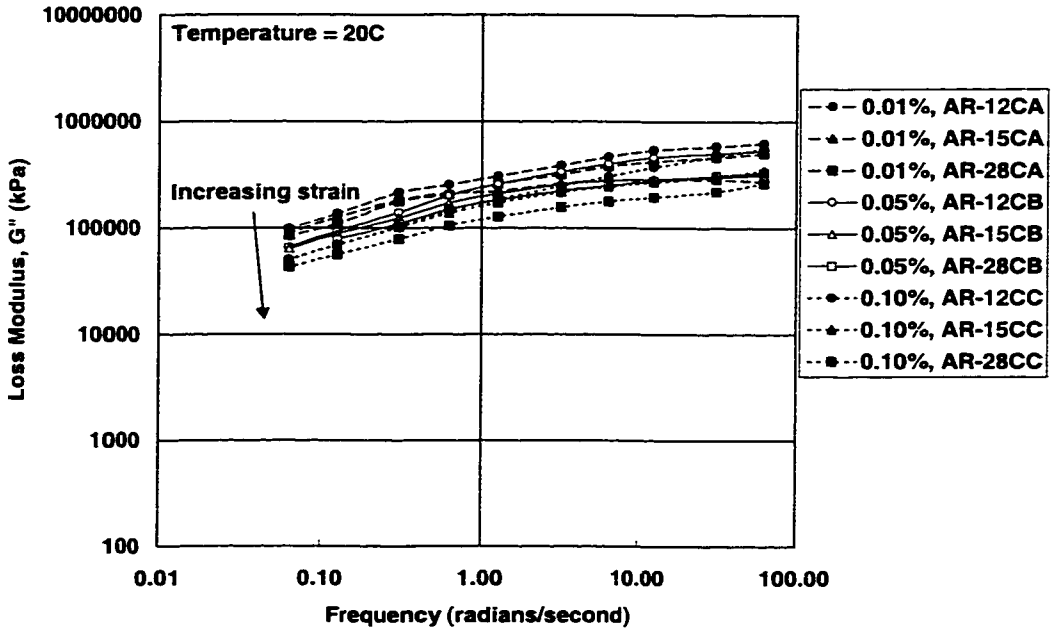

Figure 3.17 Loss Modulus Master Curves at 20°C, ARHM

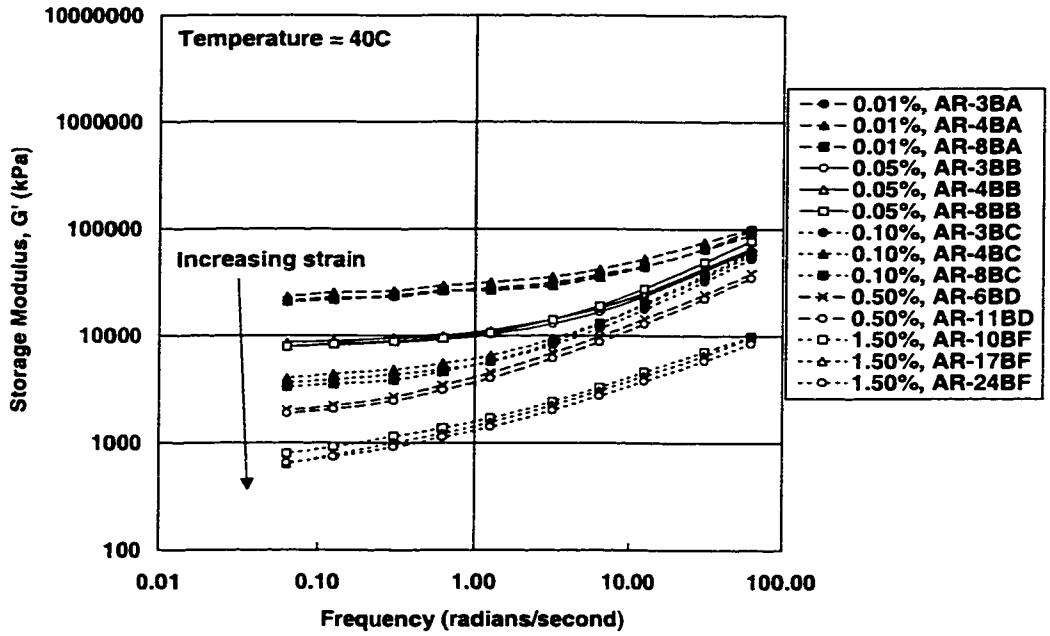

Figure 3.18 Storage Modulus Master Curves at 40°C, ARHM

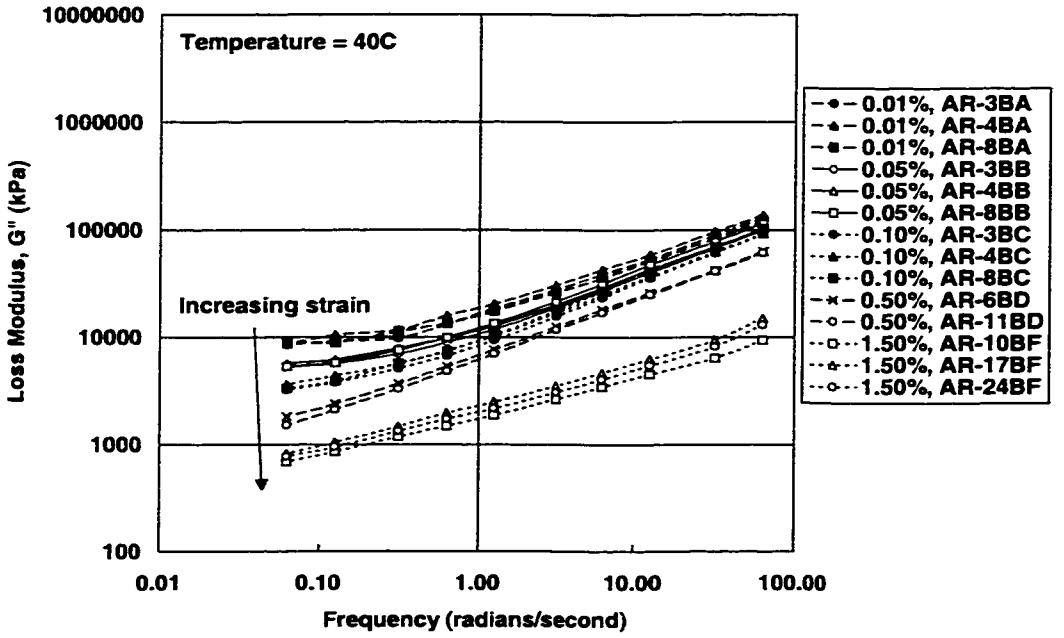

Figure 3.19 Loss Modulus Master Curves at 40°C, ARHM

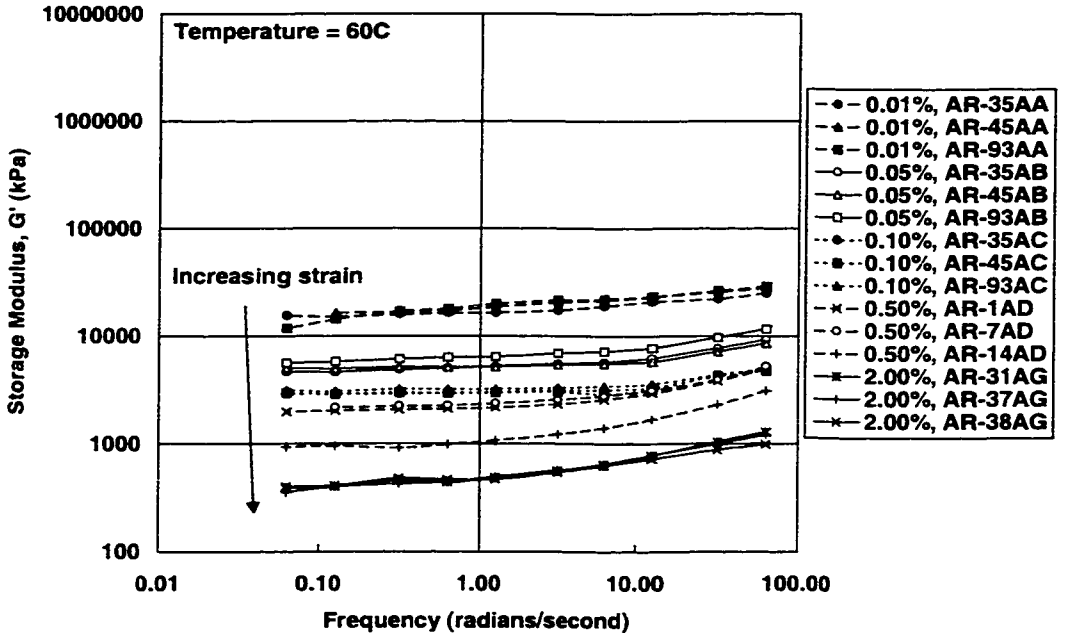

Figure 3.20 Storage Modulus Master Curves at 60°C, ARHM

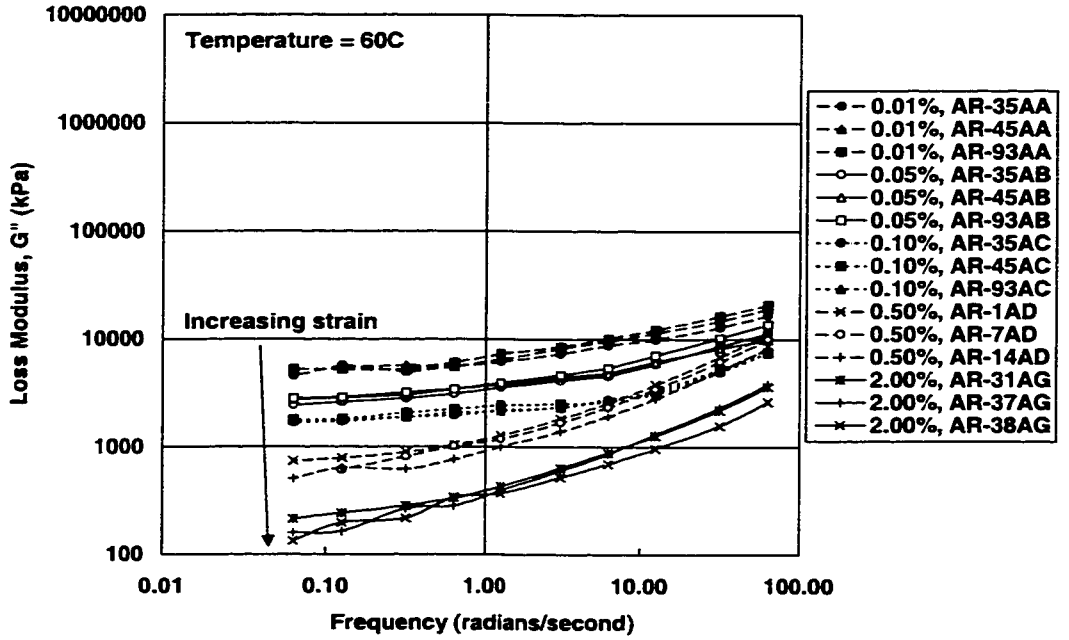

Figure 3.21 Loss Modulus Master Curves at 60°C, ARHM

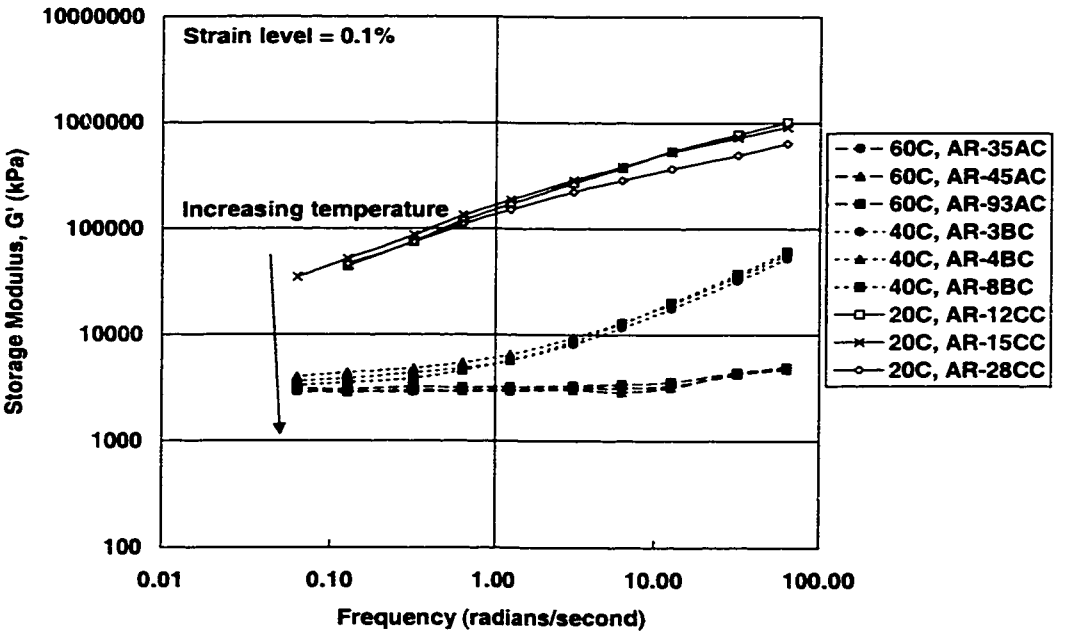

Figure 3.22 Storage Modulus Master Curves for 0.1% Shear Strain, ARHM

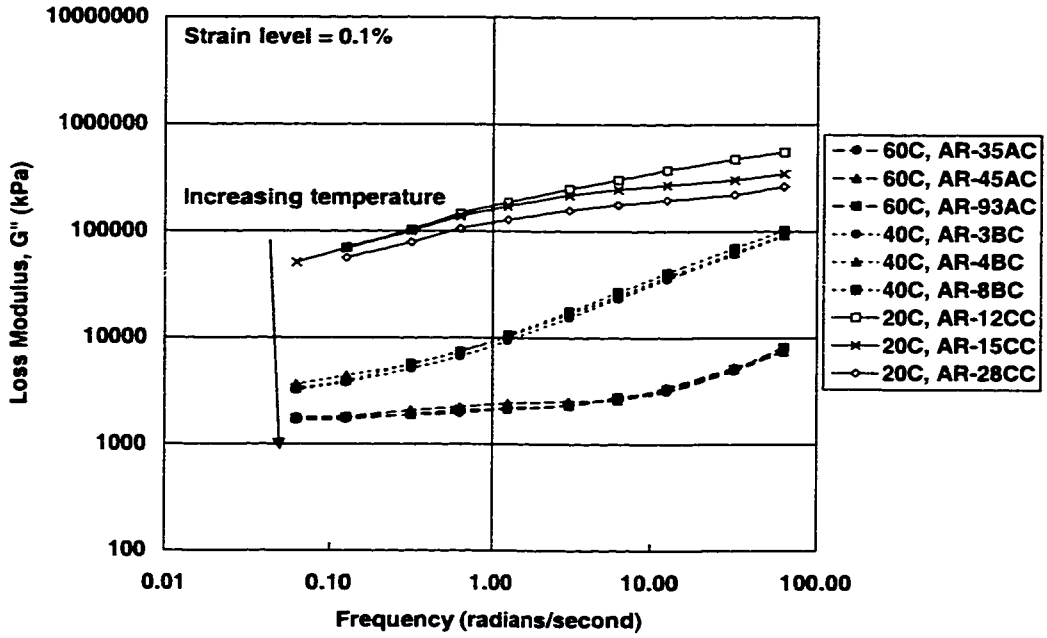

Figure 3.23 Loss Modulus Master Curves for 0.1% Shear Strain, ARHM

3.3.1 Variability in Laboratory Test Data

The laboratory test results show some variability. Specifically, the response between two specimens differed when the same testing conditions, test parameters, and materials were used. Asphalt concrete is a highly variable material composed of asphalt and aggregate, both naturally occurring materials. These materials have inherent variability in their properties, which contributes to the variability in the asphalt concrete properties. In addition, the composition of the mixes (proportion of aggregate sizes, asphalt, and air) in specimens obtained from the same batch or the same pavement also showed some variability, which affected the variability of the properties measured in the laboratory.

The size of the specimens used in the laboratory tests also contributed to the variability. The maximum size aggregate used in the DGAC mix was 19 mm, and the height of the specimen was 50 mm. The relatively small ratio of the specimen height to the maximum aggregate size can result in one aggregate dominating the response of the specimen. Much work is being done to investigate the optimum specimen size for laboratory testing, and some of the early work is discussed in references *(6), (9)* and *(21)*. The purpose behind optimum specimen size selection is to ensure the specimen is larger than the representative volume element (RVE) defined in Chapter 2.*(6)*

Because asphalt concrete is such a highly variable material, it is almost impossible to obtain laboratory test results that do not have significant variability. In comparison to other laboratory tests, for example, the repeated simple shear test at constant height (RSST-CH), the amount of variability shown in these frequency sweep tests is fairly small.

3.3.2 Discussion of Results

Although the data exhibit variability, clear trends were observed. The moduli were affected by both temperature and frequency, which is typical of a viscoelastic material. The DGAC and ARHM results are very similar, and showed the same trends. For these data, the moduli also showed a strong dependence on the strain level. The results show the typical behavior of a viscoelastic material. The moduli, plotted with frequency, lie on

a "S-curve" with the moduli increasing as the frequency increases. The temperature and strain level determine which part of the "S-curve" the data represents.

As expected, as the temperature increases the moduli decreases. Data at the high temperature of 57°C, lie on the flatter, bottom part of the "S-curve", and the 40°C and 50°C data on the steeper portion. At 20°C and 30°C for the higher strain levels, the data are flattening off, representing the upper portion of the "S-curve" (Figure 3.12). The ARHM shows the same behavior.

Although the air-void content of a mix is known to have an influence on the behavior, this is not apparent for these data. The air-void range was fairly small for both mixes, and because the dependencies on frequency, temperature, and strain are dominant within this air-void content range, it is difficult to quantify the effect. The moduli of asphalt concrete mixes typically increase with a decrease in air-void content, as discussed in Chapter 2.

If all the sections of the S-curve are available, it is possible to shift the data horizontally and vertically to obtain one master curve. A material that can be horizontally shifted on the frequency scale in this manner is known as thermorheologically simple, whereas a material which also requires vertical shifting to produce one master curve is thermorheologically complex.*(48)* This is discussed in more detail in Chapter 4, where

horizontal and vertical shifting for both temperature and strain are performed to create storage and loss moduli master curves from which the constitutive model is developed.

3.4 Summary

This chapter presents the laboratory test data that are used in Chapter 4 to develop the constitutive model. The data were obtained from shear frequency sweep tests at constant height. The data show the DGAC and ARHM are viscoelastic and the properties of the material are dependent on both temperature and strain level.

CHAPTER 4

CONSTITUTIVE MODEL DEVELOPMENT

Under the action of loading, asphalt concrete mixes exhibit a largely viscoelastic response. However, the development of rutting indicates the material is not fully viscoelastic. After the loads are removed, the mix does not recover to its undeformed state but rather shows permanent deformation. Linear viscoelastic materials do eventually recover to their original state after removal of the load. Thus, this kind of material model does not adequately describe the rutting behavior of asphalt concrete. As discussed in Chapter 2, previous research has shown that a linear viscoelastic material model is not adequate.

On the other hand, a viscoelastoplastic material model may give an improved description of the rutting behavior of a mix because of the inclusion of the non-recoverable deformation in the plasticity component. However, to determine the plasticity component of a viscoelastoplastic constitutive model for mix behavior would involve

extensive laboratory testing to allow the data to characterize the plasticity model. Such an approach would be difficult and complex.

This chapter discusses the development of a nonlinear constitutive model that describes the permanent deformation behavior of asphalt concrete mixes. The justification for using a nonlinear viscoelastic model is discussed, followed by the development of the components of the model for both the DGAC and ARHM. The constitutive model selected is derived in Chapter 5, using the developments presented in this Chapter.

4.1 Justification for a Nonlinear Viscoelastic Model

To determine and justify the selection of an appropriate constitutive model for modeling the permanent deformation behavior of asphalt concrete, laboratory test data that identify some of the critical material behavior were investigated.

Test data from a compound loading repeated load simple shear test at constant height give some insight.*(4)* The loading sequence used in this particular test included:

400 cycles at 14 kPa (2 psi)

600 cycles at 28 kPa (4 psi)

800 cycles at 41 kPa (6 psi)

1000 cycles at 55 kPa (8 psi)

This loading cycle (termed a sweep) was repeated three times. The load was ramped to the peak stress and then reduced back to zero in 0.1 seconds, with a rest period of 0.9 seconds. Figure 4.1 shows the complete test, where each data point is a hysteresis loop responding to the application and removal of the load. The magnitude of the accumulation of the residual deformation masks the hysteresis loops. The residual deformation that occurs in the first sweep is considerably greater than those of the second and third sweeps, especially for the 14, 28 and 41 kPa loading. A plasticity model could describe this: once the yield surface has been reached and possibly expanded and moved due to kinematic or isotropic hardening, subsequent deformation under the same load levels should be recoverable/elastic. However, for a purely plastic material, no further permanent deformation should occur after the first sweep because the maximum loads have been applied.

Figure 4.2 shows a few of the hysteresis loops from the first few periods at 55 kPa in the first sweep. The hysteresis loops have almost exactly the same shape and would plot on top of one another if it were not for the residual strain. The residual strain after each load application was small compared to the peak strain during the load application. It therefore seems that the viscoelastic response is dominant, but because of the residual strain, linear viscoelasticity alone cannot adequately describe the material behavior.

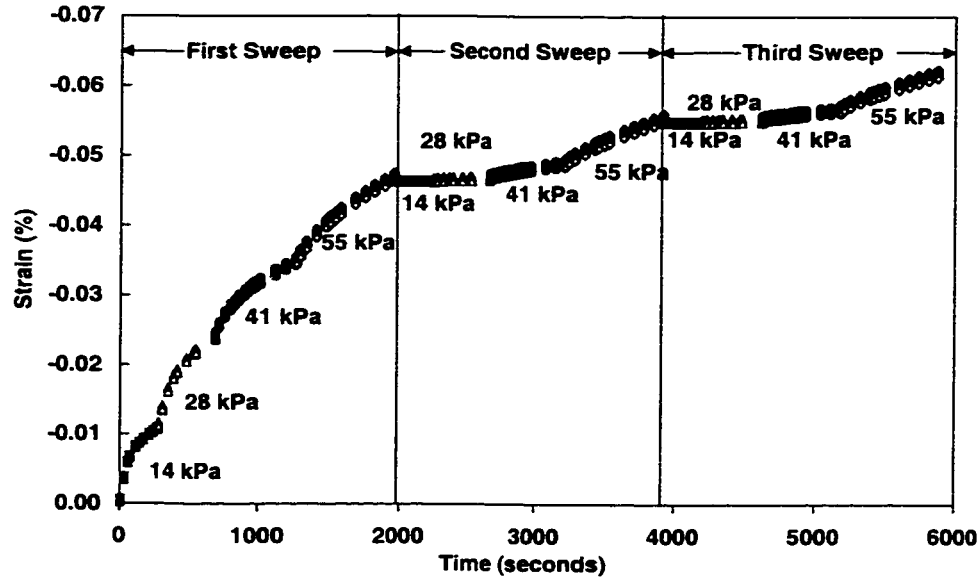

Figure 4.1 Compound Loading RSST-CH

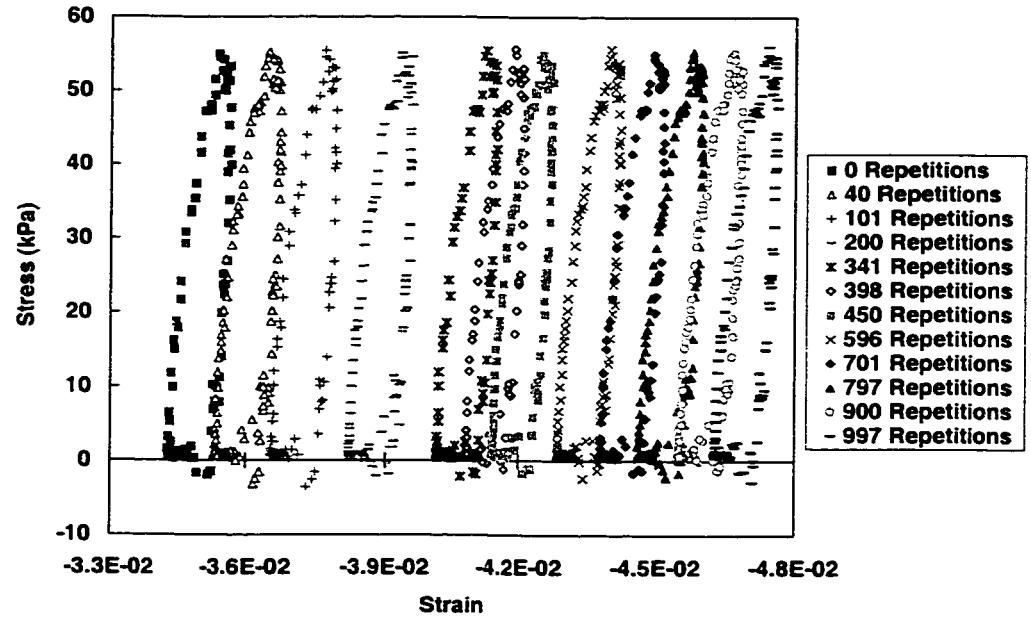

Figure 4.2 Compound loading, RSST-CH Hysteresis Loops

If the material data is investigated within a plasticity framework, it is obvious that the initial yield stress is small and the hardening laws need to be very carefully defined. This would require an extensive and difficult laboratory test program.

Both viscoelasticity and plasticity are material models used to describe material behavior. Elements from both may be adjusted to essentially give the same result, regardless of the approach. In other words, a viscoelastic model can be derived that provides a similar response as a plasticity model. One method is for the relaxation times to be dependent on the stress or strain. As the load is applied or removed, the relaxation times depend on the current deformation. If the relaxation times are shorter for higher strains, then the material will exhibit accelerated relaxation while the load is still being applied. When the load is removed, the material has already relaxed and therefore the recovery to the initial, undeformed state is significantly retarded, if not prevented, resulting in permanent deformations. These concepts are discussed in references *(49)*, *(50)* and *(51)*.

The laboratory test data presented and discussed in Chapter 3 show that the mix response is clearly dependent on the strain level. It was therefore feasible to investigate the strain dependent, nonlinear viscoelastic behavior of asphalt concrete mixes and to develop a constitutive model that describes and predicts this response and its contribution to rutting.

A non-linear viscoelastic model can be implemented as a stand-alone model or incorporated into viscoelastoplastic models. This research is therefore complementary to other research on viscoelastoplastic models currently underway.

A common method of describing material behavior in a constitutive model is to decompose the response into shear and volumetric components. The remainder of this chapter discusses the development of both the shear and volumetric components of the model. More focus is placed on the shear response because, as identified in Chapter 2, the shear behavior of asphalt concrete is critical to permanent deformation.

4.2 Shear Component: Time-Temperature-Strain Superpositioning

This section discusses the shear component of the model. Traditional methods of accounting for temperature in a viscoelastic material were extended to account for the dependency on strain level. This involved superpositioning of the master curves for time, temperature and strain. The resulting superpositioned master curve could then be used to determine the viscoelastic properties. The shift factors used to superpose the curves were used in the implementation of the model to account for the temperature and strain dependency.

4.2.1 Theoretical Background

Superpositioning of master curves is widely used for many viscoelastic materials.*(48)* A benefit of superpositioning master curves is that it is only necessary to test within a small frequency range. Shifting the master curves by superposition expands the master curve to include parts of the frequency range where it is not possible to physically perform a test. In addition, physical testing can be performed at temperatures at which it is easy to test. Then, the curves can be shifted to higher or lower temperatures at which testing is more difficult. This reduces the amount of testing necessary and provides a more extensive master curve from which to extract the viscoelastic material properties.

Time-temperature superpositioning is performed by shifting the data along the frequency axis. To include the dependency on strain level, a vertical shift along the modulus axis is necessary.

4.2.1.1 Horizontal Shifting for Temperature Dependence

Viscoelastic materials usually exhibit a strong dependency on temperature, which is widely discussed in the literature, for example *(48)*, *(52)*, *(53)*, and *(54)*. Materials in which the modulus can be horizontally shifted along the frequency scale in a modulus versus frequency graph by a constant factor depending on the reference and actual temperature are thermorheologically simple. Conventional asphalt concrete is typically considered to be thermorheologically simple for small deformations. *(20, 55)*

Horizontal shifting is performed by plotting the frequency and modulus data on a log-log plot and then shifting the resulting curve along the frequency (horizontal) axis by a constant factor, as shown in Equation (4.1)

$$\omega_{ref} = a_T \omega \tag{4.1}$$

where ω_{red} is the frequency (radians per second) shifted (reduced) to the reference temperature, ω is the original frequency (radians per second) and a_T is the temperature shift factor. The frequency in radians per second is calculated from the frequency in Hertz (f) using Equation (4.2).

$$\omega = 2\pi f \tag{4.2}$$

This procedure is demonstrated in Figure 4.3 for the shear storage modulus laboratory data. Data from laboratory tests performed at 20°C and 57°C are reduced to 40°C. The shift factor for the 20°C data is greater than one, shifting the curve to the right along the frequency scale. The 57°C shift factor is less than one, shifting the curve left to the lower frequencies.

One method of horizontal shifting for temperature is the Williams, Landel, and Ferry (WLF) equation shown in Equation (4.3), where a_T is the horizontal shift factor, T is the temperature, T_{ref} is the reference temperature, and C_1 and C_2 are material constants.*(48)* The material constants are determined using data from the shifting procedure.

$$\log a_T = -\frac{C_1 (T - T_{ref})}{C_2 + T - T_{ref}} \tag{4.3}$$

This expression is implemented by relating the time at the temperature (t) to the equivalent time at the reference temperature (t_{ref}) using Equation (4.4). The reduced or intrinsic time, $\xi(t)$, is defined in Equation (4.5) where T is the temperature.

$$t = \frac{a_T}{t_{ref}} \tag{4.4}$$

$$\xi(t) = \int_{-\infty}^{t} \frac{1}{a_T(T(s))} ds \tag{4.5}$$

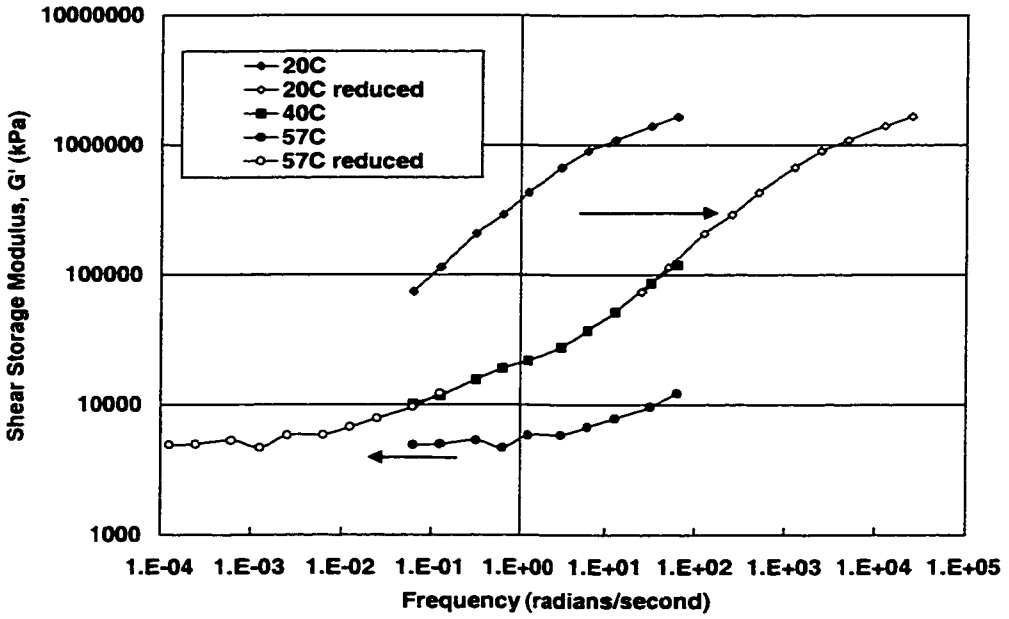

Figure 4.3 Horizontal Shifting for Temperature

4.2.1.2 Vertical Shifting for Strain Dependence

Asphalt concrete mixes also show a strong dependency on the strain or stress level at which they are loaded, as demonstrated in Chapter 3. Many viscoelastic materials exhibit similar behavior and, in the literature, these nonlinearities have been incorporated by either modifying the horizontal shift or including a vertical shift factor. *(54, 56, 57, 58, 59, 60)* The vertical shift factor is sometimes referred to as a damping function. The laboratory test data indicate a vertical shift is appropriate to incorporate the strain dependence of asphalt concrete. This is discussed further in the next section.

The shift factor for a vertical shift is determined in the same manner as the temperature shift. In this case, the relevant original modulus is multiplied by the shift factor to obtain the reduced modulus, as shown in Equation (4.6), for the storage modulus (G'). G" replaces G' in Equation (4.6) for the loss modulus calculations. The vertical shift factor is represented by a_V. A shift factor less than one decreases the modulus, resulting in a less stiff material.

$$G'_{ref} = G' \cdot a_V \tag{4.6}$$

4.2.2 Investigation of Appropriate Method of Shifting Laboratory Data

The data presented in Chapter 3 are used to determine the appropriateness of horizontal shifting for temperature and vertical shifting for strain level. The first approach considers

the temperature shift to be on the frequency (horizontal) scale only, and the strain shift to be on the modulus (vertical) scale only. Figure 4.3 shows that a frequency (horizontal) shift is adequate to account for different temperatures at the same strain level.

Figure 4.4 shows storage modulus data at 40°C from DGAC specimen 40 for the 0.01, 0.05, and 0.10 percent strain levels. The original data are the solid lines and the dashed lines represent the data shifted on the modulus (vertical) scale. It is clear that a vertical shift alone does not adequately reduce the curves at either 0.01 percent or 0.05 percent strain to the reference curve at 0.10 percent strain.

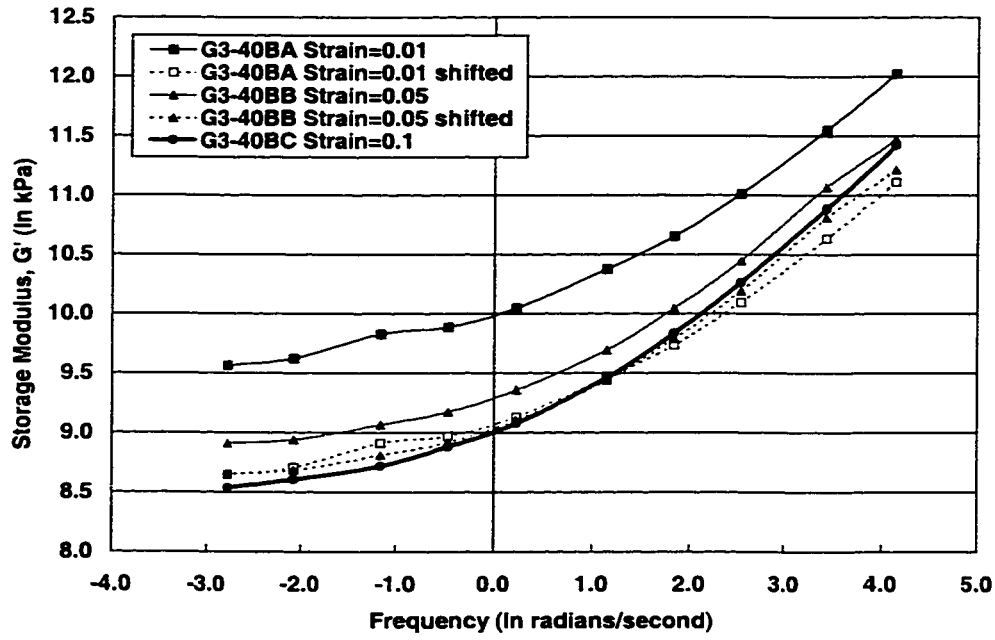

Figure 4.4 Constant Vertical Shift for Strain, DGAC Specimen 40, 40°C

However, in Figure 4.4, a small horizontal shift in addition to the vertical shift would give a much-improved reduction to the reference curve. This was the second approach evaluated to determine the shift factors. Figure 4.5 shows the same data from Figure 4.4, but a horizontal shift has been included to improve the reduction to the reference data. The vertical and horizontal shift factors are both less than one in this case. This small horizontal shift considerably improves the fit to the reference data. Similarly, Figure 4.6 shows storage and loss modulus data from DGAC specimen 80AG tested at 57°C and 2.0 percent strain reduced to 40°C and 0.1 percent strain. Again, these data show that both shifts result in a reasonable reduction to the master curve.

Based on this investigation, the approach of shifting vertically and horizontally for both strain and temperature was used to reduce all the laboratory data to obtain an extended master curve.

4.2.3 Time-Temperature-Strain Superpositioning of Laboratory Data

The data from the shear frequency sweep tests for all the specimens shown in Table 3.4 (DGAC) and Table 3.5 (ARHM) were reduced to a reference curve specific to each mix using vertical and horizontal shifting.

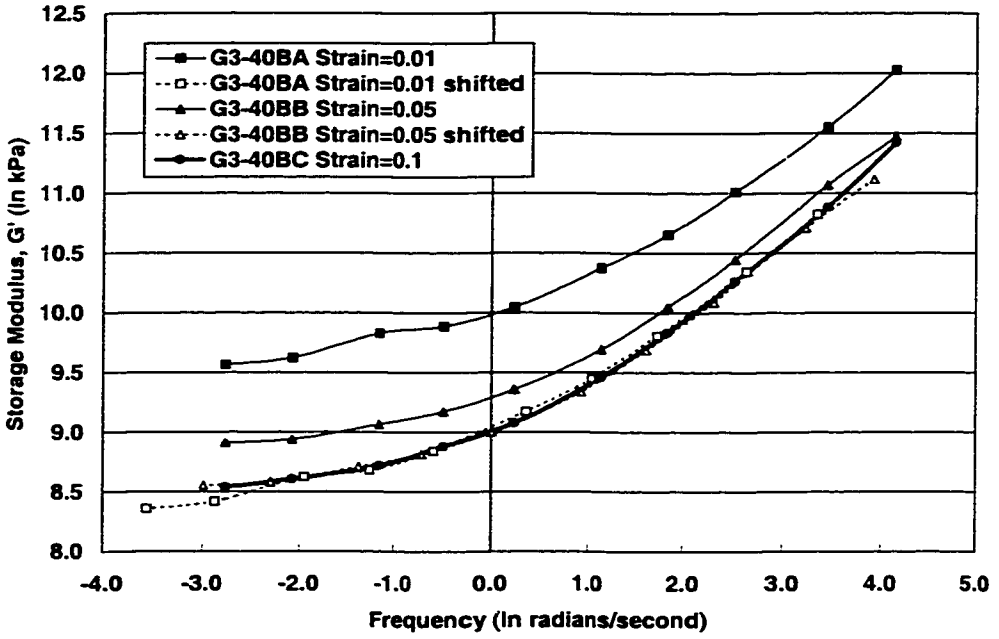

Figure 4.5 **Vertical and Horizontal Shifts for Strain, DGAC Specimen 40, 40°C and 0.01% and 0.05% Strain, Shifted to 40°C and 0.1% Strain, DGAC Specimen 40BC**

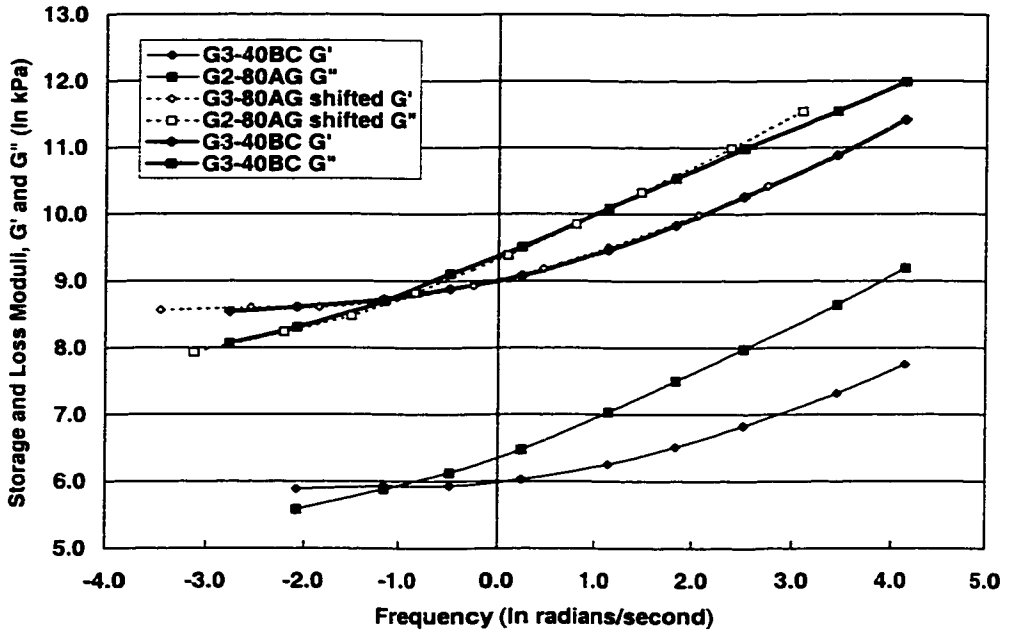

Figure 4.6 **Vertical and Horizontal Shifts for Strain and Temperature, DGAC Specimen 80AG, 57°C and 2.0% Strain, Shifted to 40°C and 0.10% Strain, DGAC Specimen 40BC**

A specimen at 40°C and 0.1 percent was used as the reference curve because the temperature and strain were in the middle of the temperature and strain ranges respectively. It was important to select a reference in the middle of the data set to give sufficient overlap between the original and reference data. Otherwise it would be very difficult, if not impossible, to determine the magnitude of the shift. Specimen 40BC for the DGAC and specimen 4BC for the ARHM at 40°C and 0.1 percent were chosen as the reference master curves. The data for these specimens appeared to not have any obvious errors or inexplicable behavior.

4.2.3.1 Procedure for Shifting Laboratory Test Data

Each specimen was individually shifted to the reference curve, to provide as much data as possible from which to develop the shift factor functions. Both the storage and loss moduli are shifted. The data were plotted with the natural log of the frequency (radians/second) and the natural log of the storage or loss modulus, as shown in Figures 4.4, 4.5 and 4.6. For each specimen, the storage and loss moduli were shifted to the reference curve individually using Equations (4.1) and (4.6), creating four shift factors, $a_{H,G'}$, $a_{H,G''}$, $a_{V,G'}$ and $a_{V,G''}$ where the subscripts H and V represent the horizontal or vertical shift, and G' and G" the storage or loss modulus. The symbol a_T from Equation (4.1) is replaced with a_H to represent "horizontal" rather than "temperature", because the horizontal shift accounts for both temperature and strain. The shift factors were adjusted

until the curves lined up to the reference curve with the best visual fit, as shown in Figures 4.5 and 4.6.

The storage and loss moduli were shifted separately because improved fits were obtained from shifting the curves separately. When the same shift factor was used, the curves often did not adequately reduce to the master curve. Theoretically, the same shift factors should be used for both the storage and loss moduli. The differences in the shift factors necessary for a good reduction to the reference data are most likely due to the variability in the test data. It was decided to shift the moduli separately to give more data from which to develop expressions for determining the shift factor. These expressions, described in Section 4.3, give one horizontal and one vertical shift factor for each strain and temperature condition, so when the expressions are implemented, the storage and loss moduli would be shifted with the same shift factors. This is important for implementation of the reduced time concept in the viscoelasticity theory.

4.2.3.2 Shift Factor Results

Tables 4.1 and 4.2 summarize the shift factor values obtained from the shifting procedure described above for the DGAC and ARHM respectively. Figures 4.7 to 4.12 (DGAC) and 4.13 to 4.16 (ARHM) present the data graphically. These plots give an idea of how well the data were reduced to the reference data to produce the master curve. Most of the curves shifted fairly well. A few specimens were impossible to shift and were excluded from the data set. The shift functions for the DGAC and ARHM were very similar.

Table 4.1 Shift Factors Used to Shift to 40°C and 0.1% Strain, DGAC

Specimen	Temperature (°C)	Strain (%)		Air-Void Content (%)	Shift Factor			
		Average	Exact		a_H, G'	a_H, G''	a_V, G'	a_V, G''
G3-29AA	57	0.01	0.0077	8.40	0.011	0.236	0.008	0.180
G3-39AA			0.0065	8.76	0.008	0.205	0.005	0.150
G3-42AA			0.0079	8.52	0.002	0.265	0.009	0.175
G3-86AA			0.0088	6.88	0.002	0.260	0.010	0.188
G3-29AB	57	0.05	0.0491	8.40	0.040	0.900	0.030	0.750
G3-39AB			0.0493	8.76	0.035	0.810	0.030	0.730
G3-42AB			0.0496	8.52	0.040	0.640	0.025	0.610
G3-86AB			0.0517	6.88	0.060	0.790	0.045	0.640
G3-29AC	57	0.10	0.1011	8.40	0.040	1.090	0.070	1.450
G3-39AC			0.1013	8.76	0.040	1.060	0.050	1.220
G3-42AC			0.1012	8.52	0.030	0.840	0.030	0.910
G3-86AC			0.1038	6.88	0.070	1.030	0.100	1.270
G3-53AD	57	0.51	0.5130	6.13	0.200	3.450	0.800	5.000
G3-55AD			0.5139	5.99	0.300	3.500	0.800	4.500
G3-81AD			0.5149	7.82	0.090	2.425	0.400	5.200
G3-56AE	57	1.03	1.0369	6.37	0.400	5.600	0.850	6.100
G3-59AE			1.0319	5.73	0.800	8.000	1.800	8.800
G3-83AE			1.0281	8.66	0.150	5.900	0.550	9.750
G3-85AF	57	1.54	1.5473	6.20	0.210	12.500	0.400	11.000
G3-87AF			1.5405	6.15	0.310	11.200	0.200	9.200
G3-80AG	57	2.06	2.0612	7.07	0.250	14.500	0.350	10.500
G3-84AG			2.0597	7.63	0.300	15.500	0.475	12.750
G3-105EA	50	0.01	0.0077	7.51	0.450	0.350	0.420	0.275
G3-111EA			0.0076	5.53	0.090	0.200	0.040	0.150
G3-113EA			0.0075	6.49	0.130	0.175	0.025	0.085
G3-105EA	50	0.05	0.0487	7.51	1.000	1.150	1.000	0.825
G3-111EA			0.0487	5.53	0.350	0.790	0.200	0.560
G3-113EA			0.0484	6.49	0.400	0.725	0.150	0.410
G3-105EA	50	0.10	0.0985	7.51	1.500	1.720	1.700	1.450
G3-111EA			0.1010	5.53	0.550	1.300	0.500	1.190
G3-113EA			0.1005	6.49	0.650	1.250	0.400	0.920
G3-92ED	50	0.50	0.4976	7.46	1.500	3.900	2.750	4.300
G3-98ED			0.5025	8.09	1.500	3.900	4.500	5.500
G3-120ED			0.4937	6.14	0.600	3.200	1.300	4.500
G3-107EE	50	1.01	1.0113	6.54	2.200	12.400	0.600	5.000
G3-94EF	50	1.50	1.4959	6.90	1.200	10.200	3.000	13.000
G3-89EG	50	2.01	2.0064	7.33	2.300	11.400	0.050	2.400
G3-25BA	40	0.01	0.0092	9.04	0.500	0.340	0.400	0.410
G3-40BA			0.0092	7.77	0.500	0.310	0.400	0.350
G3-43BA			0.0090	8.52	0.500	0.330	0.200	0.250
G3-129BA			0.0079	5.34	0.500	0.260	0.700	0.400
G3-25BB	40	0.05	0.0505	9.04	0.750	0.700	0.450	0.580
G3-40BB			0.0514	7.77	0.700	0.670	0.700	0.690
G3-129BB			0.0478	5.34	2.000	0.950	1.000	0.570

Table 4.1 continued Shift Factors Used to Shift to 40°C and 0.1% Strain, DGAC

Specimen	Temperature (°C)	Strain (%)		Air-Void Content (%)	Shift Factor			
		Average	Exact		a_H, G'	a_H, G''	a_V, G'	a_V, G''
G3-25BC	40	0.10	0.1042	9.04	0.900	0.940	0.850	0.940
G3-40BC			0.1042	7.77	1.000	1.000	1.000	1.000
G3-43BC			0.1042	8.52	1.000	1.050	1.000	1.070
G3-129BC			0.0987	5.34	4.000	1.750	2.000	0.970
G3-126BD	40	0.50	0.5025	6.13	5.000	4.150	4.000	2.900
G3-132BD			0.5010	5.22	3.500	3.500	3.500	2.450
G3-118BE	40	1.01	1.0070	5.31	5.000	4.500	0.050	0.580
G3-125BE			1.0175	6.65	3.000	5.300	0.200	1.100
G3-128BF	40	1.53	1.5297	5.34	3.000	8.000	0.200	1.550
G3-112DA	30	0.01	0.0078	5.29	2.000	0.065	200.000	1.100
G3-122DA			0.0077	6.10	7.000	0.160	9.000	0.300
G3-112DB	30	0.05	0.0470	5.29	16.000	0.310	22.000	0.500
G3-122DB			0.0475	6.10	30.000	0.620	30.000	0.680
G3-112DC	30	0.10	0.0974	5.29	20.000	0.480	25.000	0.670
G3-122DC			0.0975	6.10	42.000	1.040	45.000	1.300
G3-104DD	30	0.38	0.3803	7.74	55.000	1.020	47.000	1.100
G3-31CA	20	0.008	0.0085	7.73	600.000	0.850	300.000	1.000
G3-33CA			0.0081	7.99	500.000	0.600	200.000	0.750
G3-35CA			0.0083	8.38	500.000	0.800	350.000	1.000
G3-31CA	20	0.05	0.0475	7.73	1100.00	0.350	280.000	1.150
G3-33CB			0.0469	7.99	400.000	0.960	200.000	0.900
G3-35CB			0.0457	8.38	450.000	0.820	400.000	1.030
G3-31CC	20	0.10	0.0980	7.73	230.000	1.300	180.000	2.100
G3-33CC			0.0955	7.99	430.000	1.200	490.000	2.300
G3-35CC			0.0986	8.38	260.000	1.300	240.000	2.200

Table 4.2 Shift Factors Used to Shift to 40°C and 0.1% Strain, ARHM

Specimen	Temperature (°C)	Strain (%)		Air-Void Content (%)	Shift Factor			
		Average	Exact		a_H, G'	a_H, G''	a_V, G'	a_V, G''
AR-35AA	60	0.01	0.0093	14.82	0.010	0.215	0.008	0.410
AR-45AA			0.0083	14.64	0.009	0.185	0.009	0.370
AR-93AA			0.0089	14.78	0.120	0.190	0.010	0.360
AR-35AB	60	0.05	0.0507	14.82	0.030	0.800	0.020	0.890
AR-45AB			0.0505	14.64	0.020	0.780	0.010	0.720
AR-93AB			0.0503	14.78	0.030	0.630	0.025	0.830
AR-35AC	60	0.10	0.0980	14.82	0.030	1.450	0.025	1.730
AR-45AC			0.0994	14.64	0.030	1.500	0.030	1.750
AR-93AC			0.0993	14.78	0.023	1.300	0.040	1.900
AR-1AD	60	0.50	0.5033	14.40	0.050	1.900	0.300	4.800
AR-7AD			0.5187	14.18	0.050	1.800	0.220	4.500
AR-14AD			0.5088	15.11	0.100	4.000	0.350	6.800
AR-31AG	60	2.06	2.0606	14.49	0.100	8.700	0.400	16.500
AR-37AG			2.0532	15.18	0.100	9.000	0.400	17.000
AR-38AG			2.0513	14.34	0.100	8.700	0.200	15.000
AR-3BA	40	0.01	0.0088	14.83	0.150	0.170	0.500	0.450
AR-4BA			0.0087	14.60	0.150	0.150	0.300	0.320
AR-8BA			0.0093	14.75	0.150	0.170	0.270	0.345
AR-3BB	40	0.05	0.0502	14.83	0.450	0.520	0.500	0.640
AR-4BB			0.0497	14.60	0.430	0.490	0.500	0.600
AR-8BB			0.0495	14.75	0.590	0.520	0.800	0.710
AR-3BC	40	0.10	0.1014	14.83	1.000	1.120	1.250	1.220
AR-4BC			0.1012	14.60	1.000	1.000	1.000	1.000
AR-8BC			0.1009	14.75	1.600	1.350	1.500	1.190
AR-6BD	40	0.51	0.5150	14.17	2.200	2.100	2.000	2.100
AR-11BD			0.5126	15.03	2.000	2.250	2.000	2.200
AR-10BF	40	1.55	1.5415	15.37	0.800	4.000	0.080	2.200
AR-17BF			1.5496	14.21	1.000	5.000	0.200	2.300
AR-24BF			1.5477	14.40	1.500	6.000	0.100	2.000
AR-12CA	20	0.01	0.0091	14.70	500.000	0.480	200.00	0.410
AR-15CA			0.0096	14.62	450.000	0.420	400.000	0.650
AR-28CA			0.0087	14.82	200.000	0.300	200.000	0.510
AR-12CB	20	0.05	0.0485	14.70	450.000	0.760	500.000	1.000
AR-15CB			0.0489	14.62	500.000	0.780	425.000	0.950
AR-28CB			0.0487	14.82	340.000	0.700	350.000	1.040
AR-12CC	20	0.10	0.0981	14.70	350.000	1.000	350.000	1.100
AR-15CC			0.0980	14.62	470.000	1.000	280.000	1.000
AR-28CC			0.0986	14.82	400.000	1.050	350.000	1.350

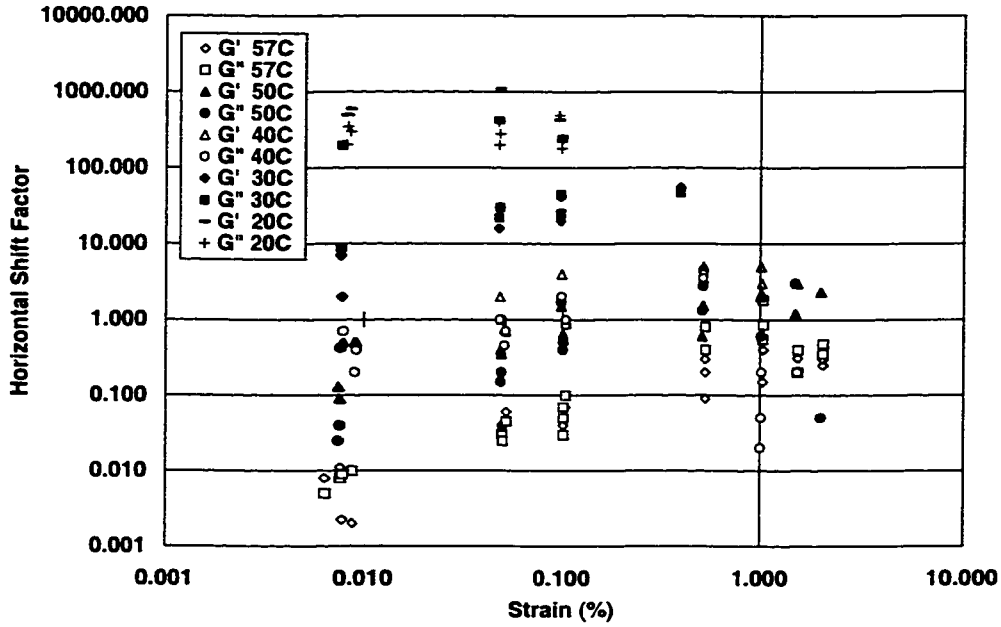

Figure 4.7 Horizontal Shift Factor as a Function of Strain Level, DGAC

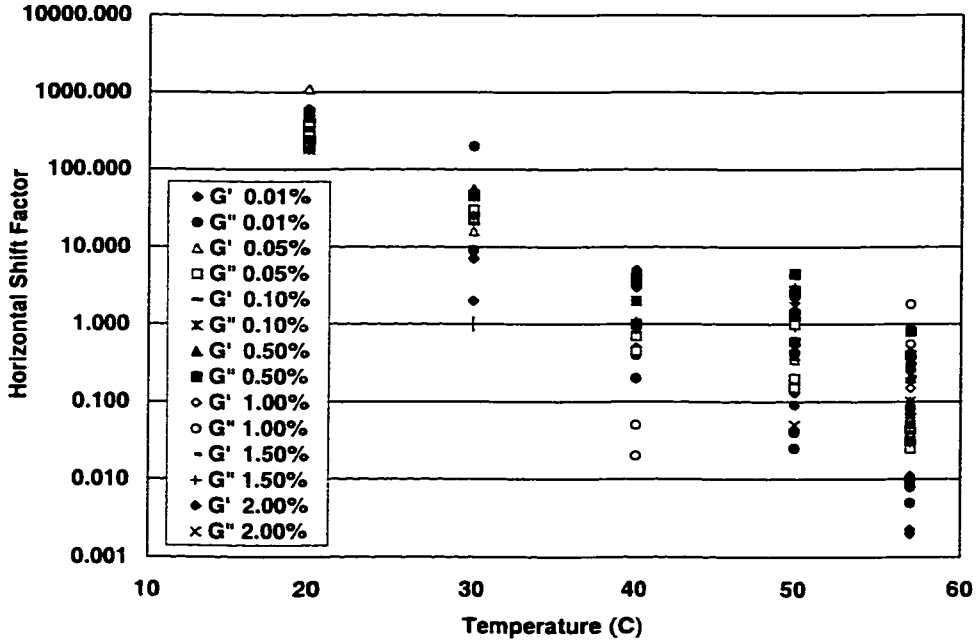

Figure 4.8 Horizontal Shift Factor as a Function of Temperature, DGAC

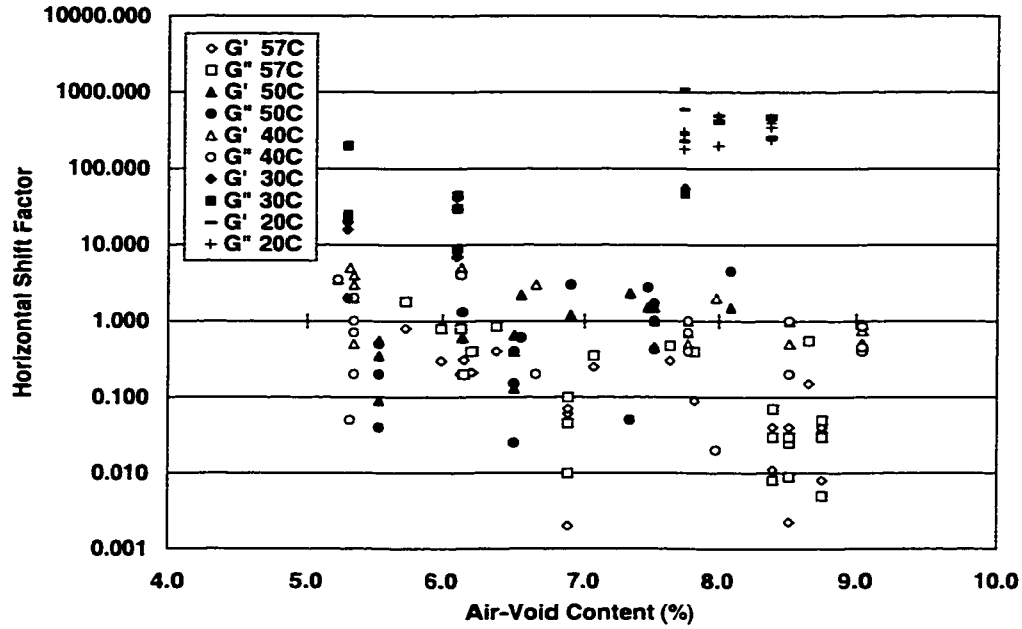

Figure 4.9 **Horizontal Shift Factor as a Function of Air-Void Content and Temperature, DGAC**

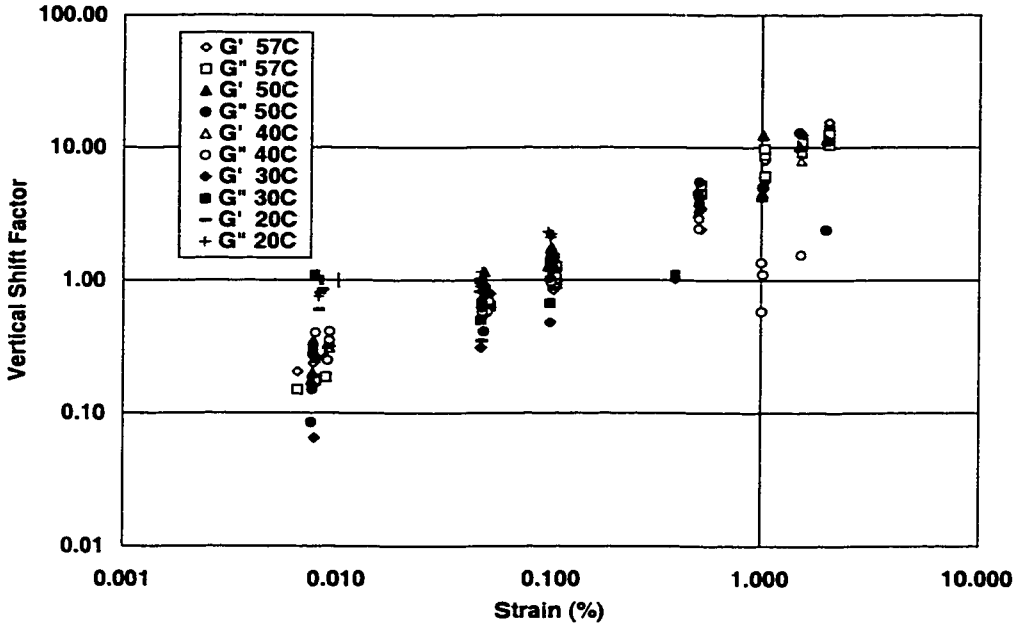

Figure 4.10 **Vertical Shift Factor as a Function of Strain Level, DGAC**

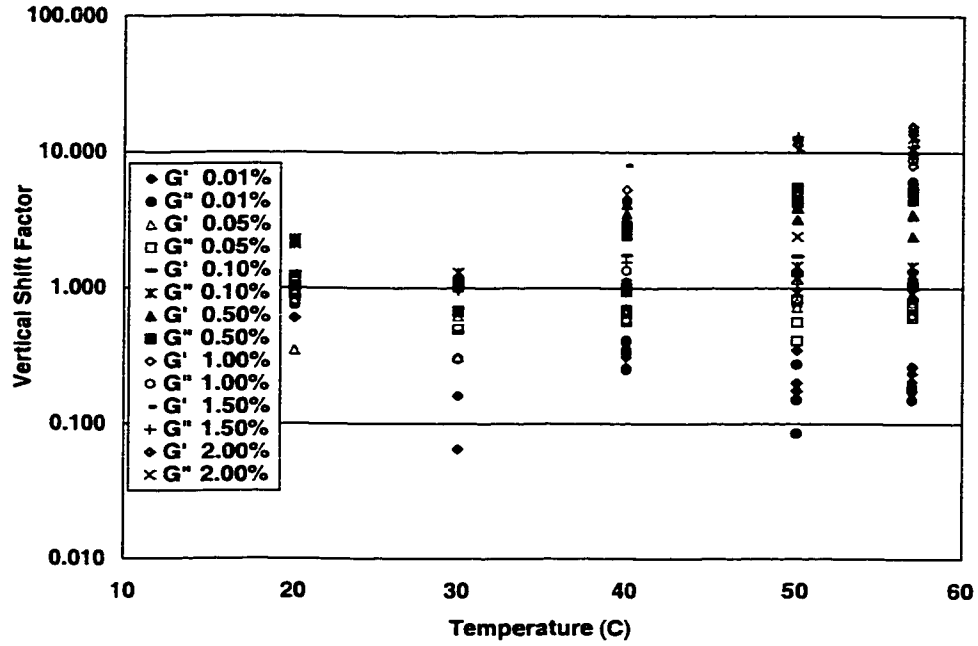

Figure 4.11 Vertical Shift Factor as a Function of Temperature, DGAC

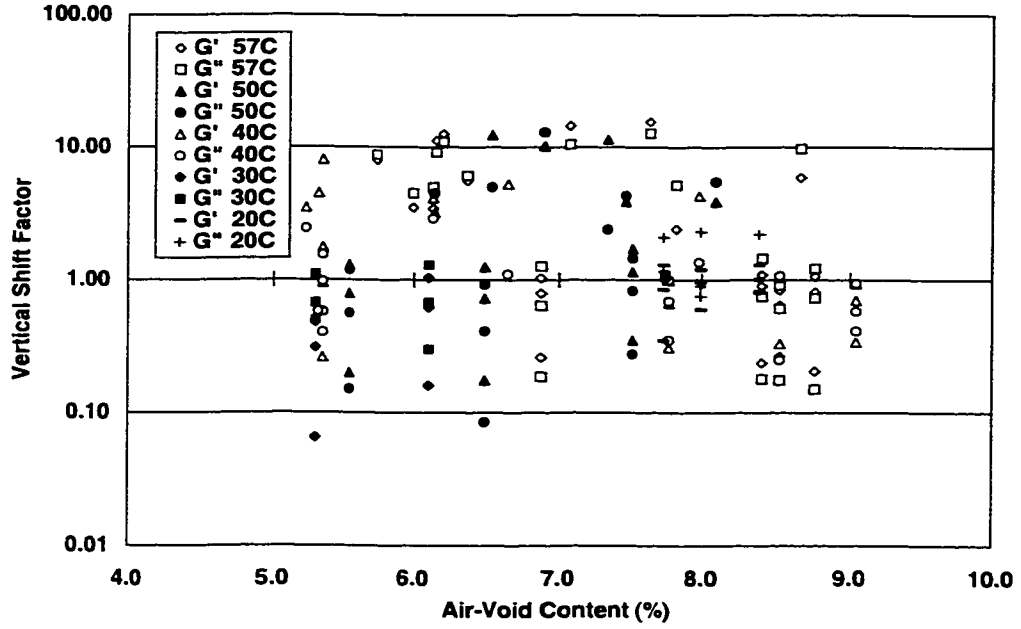

Figure 4.12 Vertical Shift Factor as a Function of Air-Void Content and Temperature, DGAC

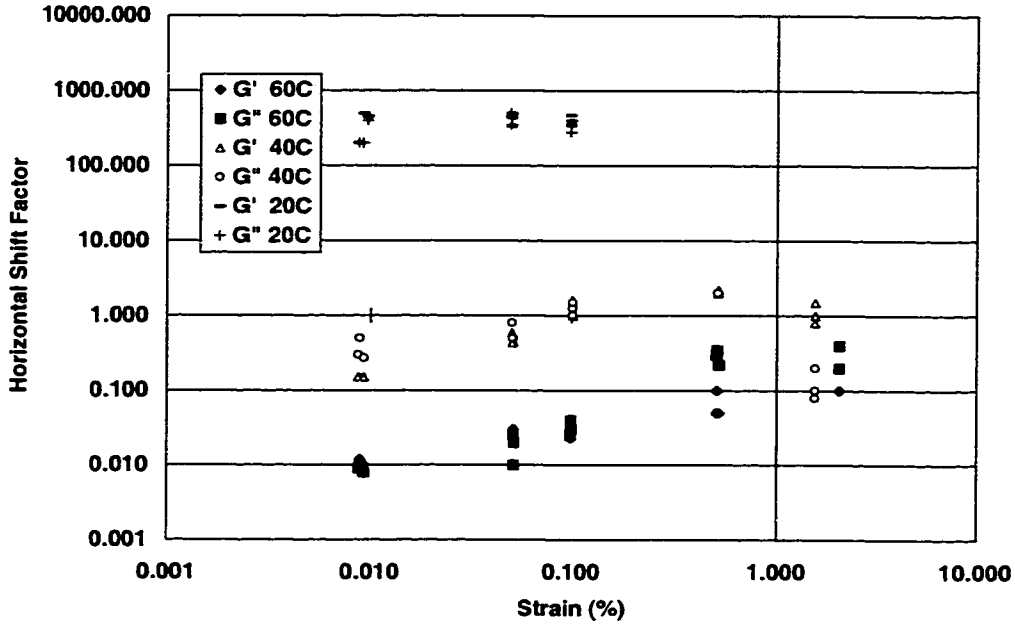

Figure 4.13 Horizontal Shift Factor as a Function of Strain Level, ARHM

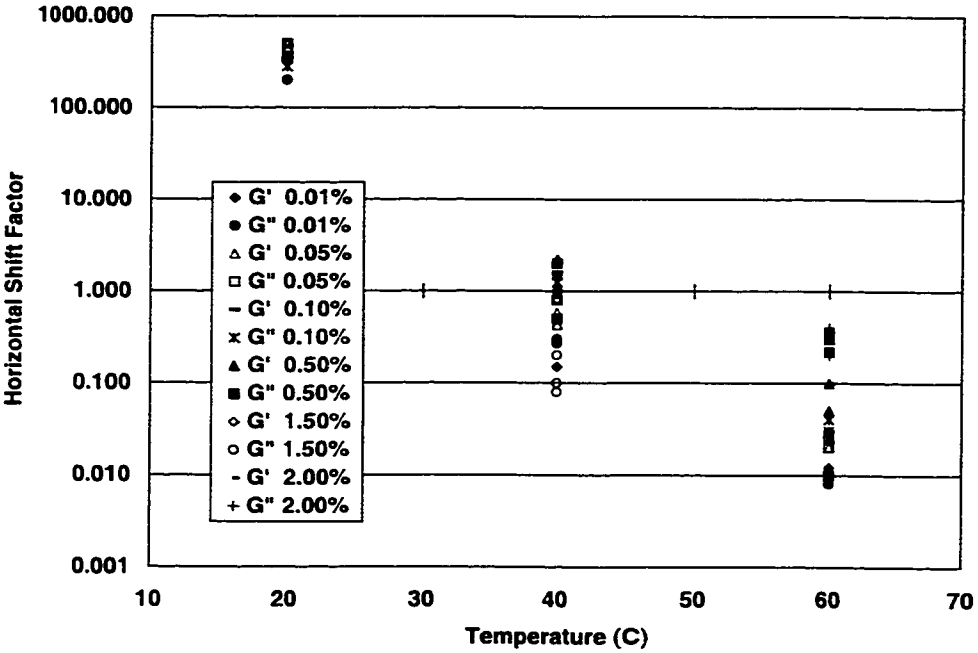

Figure 4.14 Horizontal Shift Factor as a Function of Temperature, ARHM

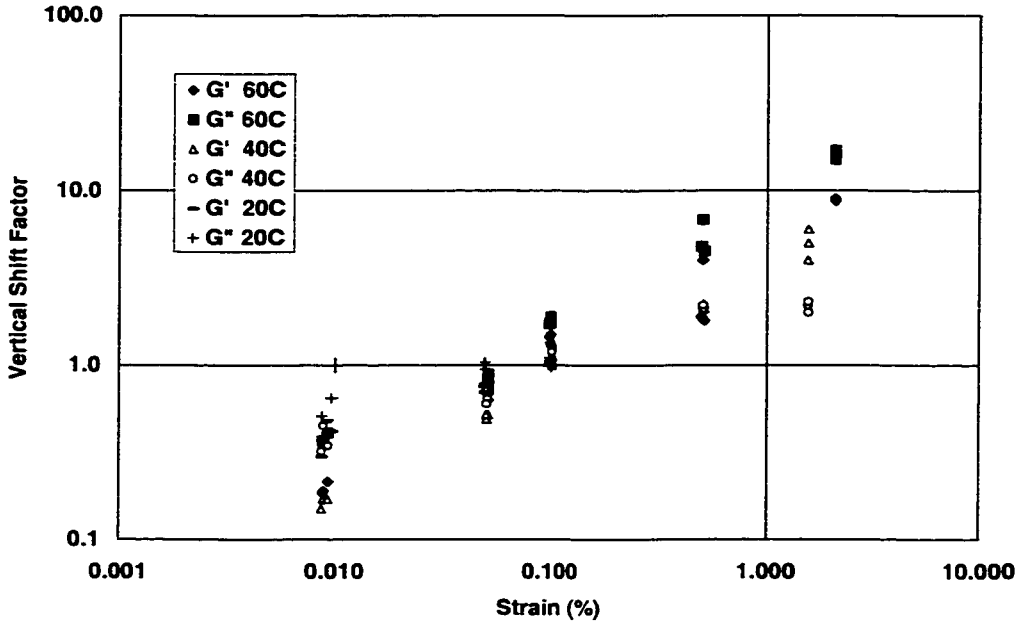

Figure 4.15 Vertical Shift Factor as a Function of Strain Level, ARHM

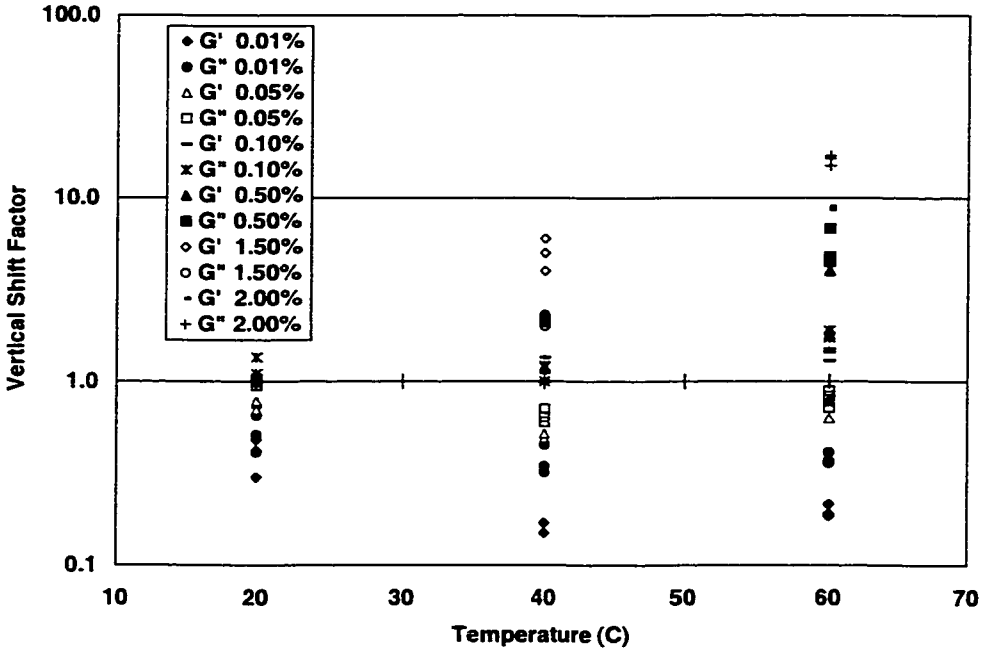

Figure 4.16 Vertical Shift Factor as a Function of Temperature, ARHM

The following discussion is limited to some preliminary observations drawn from the figures. A more detailed discussion and interpretation is contained in the next section, where expressions are fit to the shift factor data and the final master curve is used to fit a viscoelastic material properties.

Even though there is some variability, Figures 4.7 and 4.8, and 4.13 and 4.14 show clear temperature trends that highlight the large influence of temperature on the horizontal shift. This was as expected because the temperature shift is classically only a horizontal shift, and the horizontal shift due to strain is small, as shown in Figures 4.5 and 4.7. Shift factors less than one indicate the curve was shifted to the left, and values greater than one shift the curve to the right. The higher temperatures were shifted to the left and the lower temperatures were shifted to the right of the reference curve creating the lower and upper portions of the master curve, respectively. The result was that when the mix was shifted to a higher temperature, the relaxation times are shortened (relaxation time is the reciprocal of the frequency in radians per second). Shorter relaxation times accelerate the relaxation of the material, which, as discussed in Section 4.1, retards the recovery after removal of the load, causing residual strains. In addition, for a fixed loading time or frequency, the modulus was smaller for the higher temperature, increasing the deformation.

The trends in the horizontal shift factor versus strain (Figures 4.7 and 4.13) showed that the effect of strain on the material was more significant at the high temperatures. For the limited range of 20°C data, the effect of strain on the shift factor appeared to be very small.

In Figures 4.7, 4.8, 4.13 and 4.14, the shift factor increases as the strain level increases. This trend is more apparent in Figures 4.7 and 4.13, because the dominant temperature effect in the horizontal shift is masking the strain effect shown in Figures 4.8 and 4.14.

Figures 4.10, 4.11, 4.12, 4.15 and 4.16 show the vertical shift factor as a function of strain, temperature and air-void content. Shift factors greater than one shift the curve up, increasing the moduli, and shift factors less than one lower the curve, decreasing the moduli. Figures 4.10 and 4.15 show the shift factor is strongly dependant on the strain level, with the shift factor increasing as the strain level increases. When shifting to a higher strain the modulus decreases, indicating the material will deform more under the same load.

The effect of temperature on the vertical shift factor was not as pronounced as the strain. For the smaller strains, especially at the higher temperatures (Figures 4.11 and 4.16), an increase in temperature decreased the shift factor, whereas for the larger strains the shift factor increased with an increase in temperature.

The air-void content of the DGAC, within the 5.2 to 9.0 percent range of the test specimens, did not have a noticeable effect on the shift factors. The dominant effects of strain level and temperature masked possible effects of the air-void content, as shown in Figures 4.9 and 4.12. The extremely narrow range of air-void contents of the ARHM test specimens (14.2 to 15.4 percent) prevented identification of any air-void effects on the ARHM mix behavior.

The final master curves constructed with the laboratory data are shown in Figures 4.17, 4.18, 4.19 and 4.20 for the storage and loss moduli and DGAC and ARHM, respectively. The temperatures from which the data were reduced to 40°C are shown in the different shading. There was a large amount of overlap between the different temperature data, which enabled the good reduction to the master curve.

The master curve is more variable at the upper and lower edges, especially for the loss modulus (Figures 4.18 and 4.20). This is most likely due to less overlap between these data and the reference curve, and therefore it was more difficult to perfectly align the curves. The data at these points may also be more variable, particularly at the higher frequencies because the physical testing was more difficult at lower temperatures and higher frequencies where the increased stiffness of the material made the test harder to control. As discussed in Chapter 3, the loss modulus was more sensitive to the testing

difficulties. The data at the edges of the master curve are less important because loading frequencies are typically in the middle range, where the data fit within a small band.

The good fit of the reduced data to the master curves confirms the applicability and appropriateness of shifting these data horizontally and vertically for both temperature and strain.

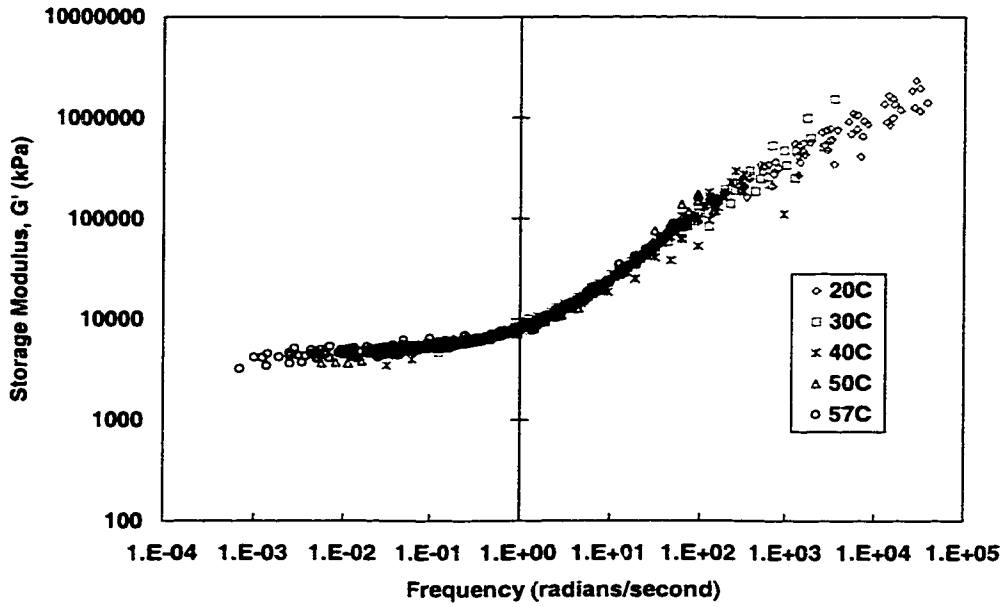

Figure 4.17 Storage Modulus Master Curves from Shifting the Laboratory Data Independantly, DGAC

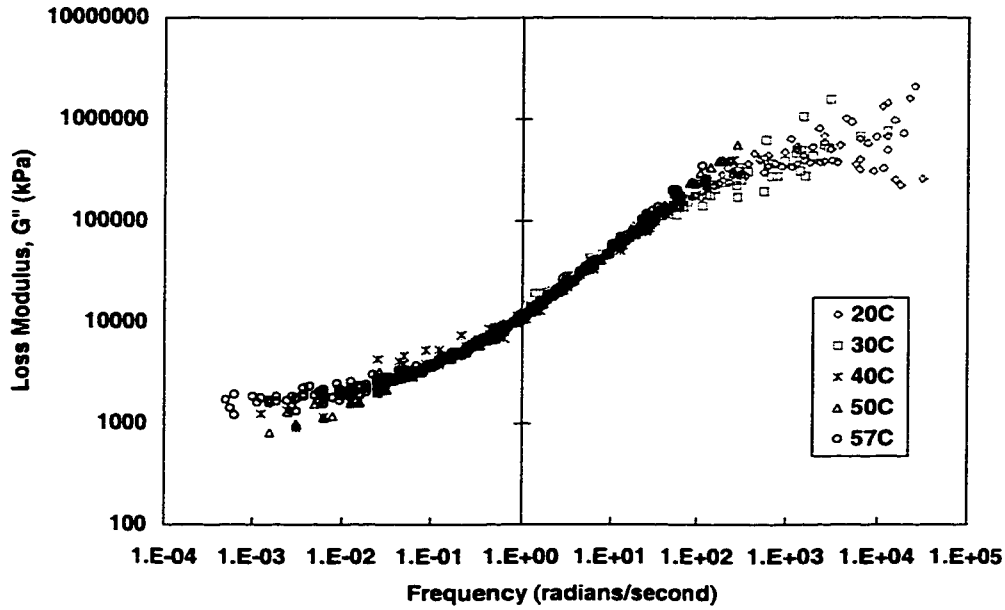

Figure 4.18 Loss Modulus Master Curves from Shifting the Laboratory Data Independantly, DGAC

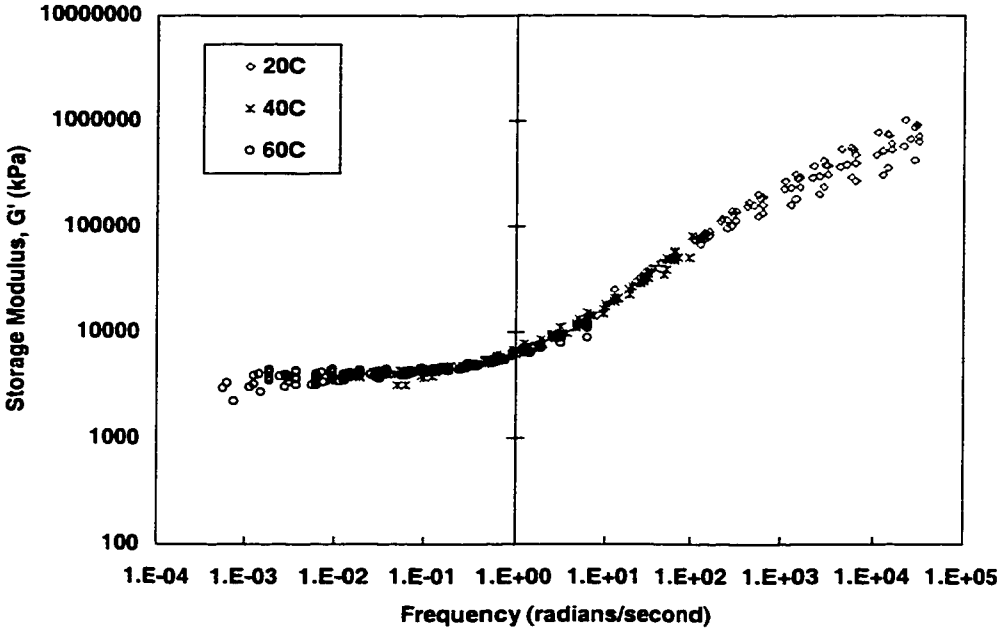

Figure 4.19 Storage Modulus Master Curves from Shifting the Laboratory Data Independantly, ARHM

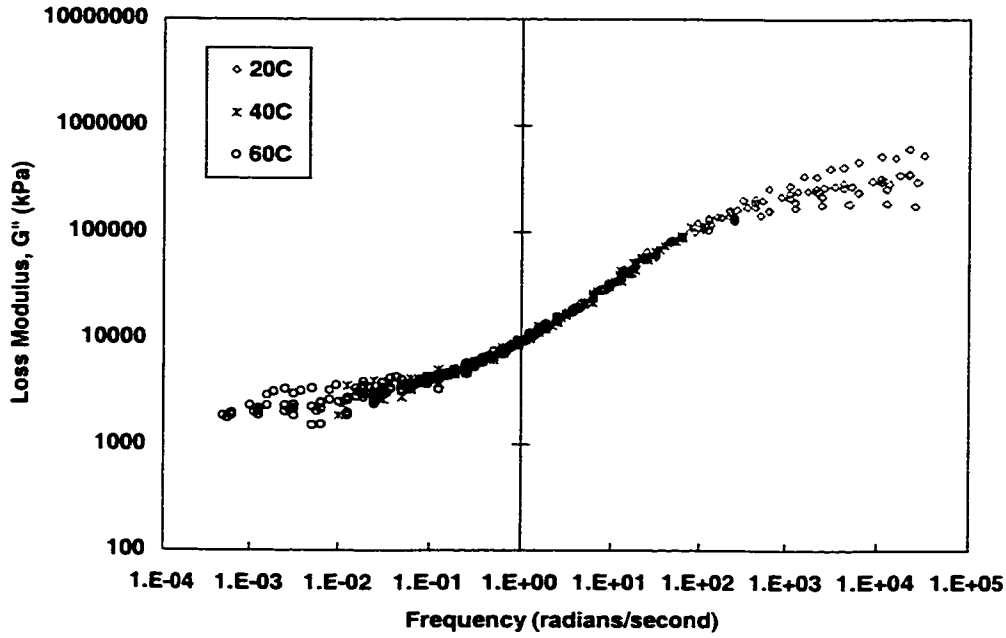

Figure 4.20 Loss Modulus Master Curves from Shifting the Laboratory Data Independantly, ARHM

4.3 Shift Factor Functions for the Shear Response

The shift factors developed in the previous section were used to fit functions for the shift factors used in the finite element implementation.

The first step in developing the shift factor functions was to look for clear trends in the data. Some of these trends were discussed in the preceding section. The trends were used to form an equation relating the test variables to the shift factor. This section discusses the development of the frequency (horizontal) and modulus (vertical) shift

factor functions. In developing the shift factor functions, attention was focused first on the DGAC mix. Then the final functions were fit to the ARHM data.

4.3.1 Strain Measure Used in Shift Functions

The strain measure used in the shift factor functions was the strain deviator norm $\|\mathbf{e}\|$, shown in Equation (4.7). This norm is a measure of the magnitude of the shear strains in the material. The deviatoric strain was calculated from the strain tensor (ε) as shown in Equation (4.8) where ε_0 is defined in Equation (4.9) and δ_{ij} is the Kronecker delta.

$$\|\mathbf{e}\| = \sqrt{e_{11}^2 + e_{12}^2 + e_{13}^2 + e_{21}^2 + e_{22}^2 + e_{23}^2 + e_{13}^2 + e_{23}^2 + e_{33}^2} \tag{4.7}$$

$$e_{ij} = \varepsilon_{ij} - \varepsilon_0 \delta_{ij} \tag{4.8}$$

$$\varepsilon_0 = \frac{1}{3}(\varepsilon_{11} + \varepsilon_{22} + \varepsilon_{33}) \tag{4.9}$$

In the shear frequency sweep test, the strain level reported was the strain measured between the positive and negative peaks of the sinusoidal load, i.e., the total strain as the specimen was displaced from one side to the other. This strain is referred to as γ_{test} or as the strain level for the values of 0.0001, 0.0005, 0.001, 0.005, 0.01, 0.015, 0.02 used in the laboratory testing. For this test setup, the engineering shear strain, γ_{12}, is the value

from zero to the peak displacement, i.e., $\gamma_{test} = 2\gamma_{12}$. The strain and strain deviator tensors were equal for these testing conditions, and are shown in Equation (4.10)

$$\boldsymbol{\varepsilon} = \mathbf{e} = \begin{bmatrix} 0 & \varepsilon_{12} & 0 \\ \varepsilon_{21} & 0 & 0 \\ 0 & 0 & 0 \end{bmatrix} \tag{4.10}$$

where ε_{12} is the tensorial shear strain equal to half the engineering shear strain. The strain norm for the shear frequency sweep tests is shown in Equation (4.11).

$$\|\mathbf{e}\| = \sqrt{2}\varepsilon_{12} = \frac{\gamma_{12}}{\sqrt{2}} = \frac{\gamma_{test}}{2\sqrt{2}} \tag{4.11}$$

4.3.2 Dense-Graded Asphalt Concrete Shift Factor Functions

4.3.2.1 Frequency (Horizontal) Shift Factor Function

The data discussed in the preceding section, Figures 4.7 and 4.8, show that the logarithm of the frequency (horizontal) shift factor is a linear function of the temperature and a linear function of the logarithm of the strain. In addition, the slope of the trend between the logarithm of the shift factor and the logarithm of the strain decreases as the temperature decreases, i.e., the slope of this linear trend is a function of temperature. Similarly, although less apparent, the linear trend between the logarithm of the shift factor and temperature is a function of the strain.

The shift factor functions typically include the difference between the actual and reference condition, as shown in the WLF Equation (Equation (4.3)) for temperature. In the shift factor functions, the temperature term is the difference between the actual (T) and the reference (T_{ref}) temperatures, ($T-T_{ref}$).

Because strain is related to the shift factors on the logarithmic scale, the actual deviatoric strain norm ($\|\mathbf{e}\|$) is related to the deviatoric strain norm of the reference strain ($\|\mathbf{e}_{ref}\|$) using the strain term $\left(\log \frac{10^{-6} + \|\mathbf{e}\|}{10^{-6} + \|\mathbf{e}_{ref}\|} \right)$, where the logarithm to the base 10 is used. The 10^{-6} value in the numerator and denominator is necessary to ensure the strain term is never undefined. The small value was assumed because it has very little effect on the shift factor. Both the strain and temperature terms reduce to zero when the actual temperature or strain equals the reference.

With these observations, the basic form of the frequency (horizontal) shift factor function can be formed. The function needs the strain and temperature term and some form of interaction term to account for the effects of temperature and strain on the slope. The form of the function is shown in Equation (4.12). The individual temperature and strain terms are necessary to ensure that if the reference temperature is used and the temperature term reduces to zero, there is still a shift for strain. If both the reference temperature and strain are used, all the terms reduce to zero, resulting in no shift.

$$\log a_H = C_1(T\text{-}T_{ref}) + C_2\left(\log\frac{10^{-6}+\|\mathbf{e}\|}{10^{-6}+\|\mathbf{e}_{ref}\|}\right) + C_3(T\text{-}T_{ref})\left(\log\frac{10^{-6}+\|\mathbf{e}\|}{10^{-6}+\|\mathbf{e}_{ref}\|}\right) \quad (4.12)$$

In this equation, $\log a_H$ is the logarithm to the base 10 of the horizontal shift factor, T and $\|\mathbf{e}\|$ are the temperature (°C) and strain respectively from which the data are shifted, T_{ref} and $\|\mathbf{e}_{ref}\|$ are the reference temperature (°C) and strain to which the data are reduced, and C_i are constants determined by the data fit.

Various forms and extensions of Equation (4.12) were attempted. The temperature and strain terms were squared and the equation was extended to include the squares and all the interaction terms between the squares. This did not enhance the model fit.

Inclusion of possible air-void content effects was also attempted. One example of how the air-void content term was included in Equation (4.12) is shown in Equation (4.13), where the symbols are the same as those used earlier with the addition of the actual (AV) and reference (AV_{ref}) air-void contents. Because it is difficult to visualize the effect of the air-void content on the shift factors (Figures 4.9 and 4.12) a logarithmic term was also attempted; where ($AV\text{-}AV_{ref}$) in Equation (4.13) was replaced by $\left(\log\frac{AV}{AV_{ref}}\right)$, as shown below.

$$\log a_H = C_1(T\text{-}T_{ref}) + C_2\left(\log\frac{\|e\|}{\|e_{ref}\|}\right) + C_3(T\text{-}T_{ref})\left(\log\frac{\|e\|}{\|e_{ref}\|}\right) + C_4(T\text{-}T_{ref})(AV\text{-}AV_{ref}) + C_5\left(\log\frac{\|e\|}{\|e_{ref}\|}\right)(AV\text{-}AV_{ref}) \quad (4.13)$$

The WLF equation (Equation (4.3)) was also investigated as a basis for developing shift factor functions. The form of this type of function is given in Equation (4.14) where all the constants are the same as defined previously. This type of equation required a nonlinear fit.

$$\log a_H = \frac{C_1(T\text{-}T_{ref})}{C_2 + T\text{-}T_{ref}} + \frac{C_3(\|e\| - \|e_{ref}\|)}{C_4 + \|e\| - \|e_{ref}\|} + \left(\frac{C_5(T\text{-}T_{ref})}{C_6 + T\text{-}T_{ref}}\right)\left(\frac{C_7(\|e\| - \|e_{ref}\|)}{C_8 + \|e\| - \|e_{ref}\|}\right) \quad (4.14)$$

The best shift factor function was determined by visually checking the fit to the data for reasonableness and to ensure that the trends followed the expected trends.

In all the functions that included a term for the air-void content, the term was statistically insignificant. It was therefore concluded that, for these data and the range of air-void contents in the specimens tested, it is not possible to determine the effect of the air-void content on the mix behavior. The air-void content term was therefore omitted from the functions.

The extension of the WLF equation, shown as Equation (4.14), did not provide a good fit to the data, and therefore this approach was not used.

The best fit for the shift factor function is in the form of Equation (4.12). Fits to the other functions did not produce reasonable results. To fit the coefficients for this function, some of the data that were clearly outliers were eliminated. The specimens finally used to fit the equation are those in Table 4.3, which is the updated version of Table 3.4. The data set was skewed by the lack of laboratory test results at the low temperatures and high strains. These data could not be obtained due to testing difficulties, as discussed in Chapter 3, therefore the available data for the low temperature and high strains were extrapolated to obtain estimates of the data at the higher strains. These additional data were used to fit the shift factor functions and therefore these equations do not represent the best statistical fit, but rather a physically reasonable fit. Because rutting typically occurs at temperatures greater than 40°C the data fits at 20°C are not critical. The function for the frequency (horizontal) shift factor is shown in Equation (4.15) with the same variables as defined before.

$$\log a_H = C_{H1} + C_{H2}(T - T_{ref}) + C_{H3}\left(\log\frac{10^{-6}+\|\mathbf{e}\|}{10^{-6}+\|\mathbf{e}_{ref}\|}\right) + C_{H4}(T - T_{ref})\left(\frac{10^{-6}+\|\mathbf{e}\|}{10^{-6}+\|\mathbf{e}_{ref}\|}\right) \quad (4.15)$$

DGAC:

$C_{H1} = 0.460195$

$C_{H2} = -0.098896$

$C_{H3} = 0.473146$

$C_{H4} = 0.018655$

Table 4.3 Laboratory Test Data Used in Shift Factor Functions, DGAC

Strain Level (%)	Temperature (°C)				
	20	30	40	50	57
0.01	31 CA (7.73)[1] 33 CA (7.99) 35 CA (8.38)	112DA[2] (5.29) 112DA (6.10)	25 BA (9.04) 40 BA (7.77) 43 BA (8.52) 129 BA (5.35)	105 EA (7.51) 111 EA (5.53) 113 EA (6.49)	29 AA (8.40) 39 AA (7.76) 42 AA (8.52) 86 AA (6.88)
0.05	31 CB (7.73) 33 CB (7.99) 35 CB (8.38)	112DB (5.29) 112DB (6.10)	25 BB (9.04) 40 BB (7.77) 43 BB (8.52)	105 EB (7.51) 111 EB (5.53) 113 EB (6.49)	29 AB (8.40) 39 AB (7.76) 42 AB (8.52) 86 AB (6.88)
0.10	31 CC (7.73) 33 CC (7.99) 35 CC (8.38)	112DC (5.29) 112DC (6.10)	25 BC (9.04) 40 BC (7.77) 43 BC (8.52) 129 BC (5.35)	105 EC (7.51) 111 EC (5.53) 113 EC (6.49)	29 AC (8.40) 39 AC (7.76) 42 AC (8.52) 86 AC (6.88)
0.50		104DD (7.74)	126 BD (6.13) 132 BD (5.22)	92 ED (7.46) 98 ED (8.09) 120 ED (6.14)	53 AD (6.13) 55 AD (5.99) 81 AD (7.82)
1.00			118 BE (5.31) 125 BE[2] (6.65)	107 EE (6.54)	56 AE (6.37) 59 AE (5.73) 83 AE (8.66)
1.50			128 BF[2] (5.34)	94 EF (6.90)	85 AF (6.20) 87 AF (6.15)
2.00				89 EG[2] (7.33)	80 AG (7.07) 84 AG (7.63)

1 Air-void content
2 Only the storage modulus data was used

Equation (4.15) has a constant term, C_{H1}. Ideally, if the temperature and strain are the same as the reference, then log a_H should equal zero and hence a_H equal one, resulting in no shift. It is preferable not to have this constant term, which results in a small shift factor when the reference temperature and strain are used. However, the DGAC specimen selected as the reference (40BC) is not the only specimen that was tested at 40°C and 0.1 percent strain. The curves from the other DGAC specimens (25BC, 43BC and 129BC) are not exactly the same as the reference curve, as shown in Figures 3.22 and

3.23, but are well within a reasonable level of variability. This results in the introduction of an intercept in the expression. Attempts to force the function to equal zero when the reference temperature and strains were used did not provide an adequate fit. It was therefore decided to leave the constant term in the equation.

The fit given by the horizontal shift factor function, Equation (4.15), is shown in Figures 4.21 and 4.22 as functions of strain and temperature, respectively. The figures show the temperature dependency of the slope in the shift factor versus strain chart (Figure 4.21) and the strain dependency of the slope in the shift factor versus temperature chart (Figure 4.22).

The fit follows the observed trends, in that the slope of the log shift factor versus log strain decreases with decreasing temperature and the log of the shift factor decreases with increasing temperature. Figure 4.21 shows that if the strain range is expanded the curves for the different temperatures will meet. This was not a concern because the strains at that point are extremely high, and will not be reached in the material.

In Figure 4.22, the trend lines meet at about 15°C. The temperature of asphalt concrete pavements when rutting occurs is typically between 30 and 70°C.*(61)* Hence, the temperatures outside of this range are not relevant, and the extrapolation of the shift

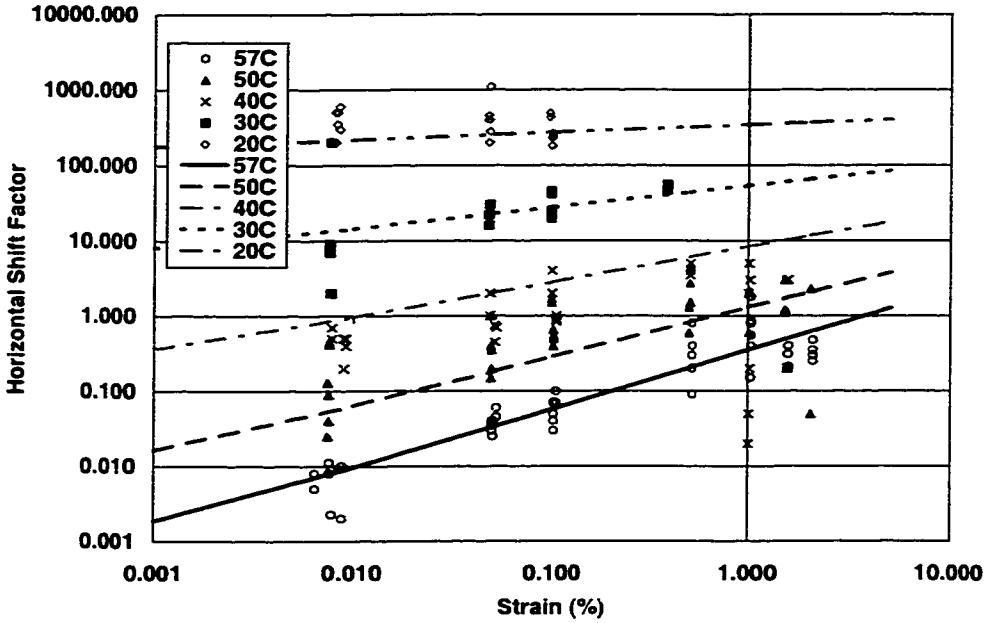

Figure 4.21 Horizontal Shift Factor Function versus Strain Level, DGAC

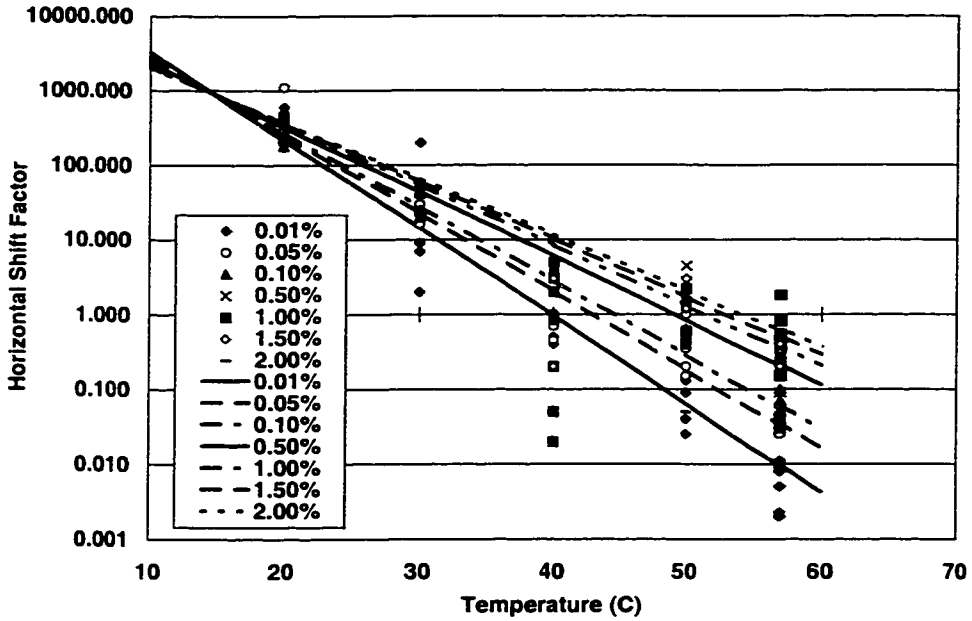

Figure 4.22 Horizontal Shift Factor Function versus Temperature, DGAC

factor functions beyond this range is not of interest. Within the relevant temperature and strain ranges, the shift factor function provides a reasonable fit.

4.3.2.2 Modulus (Vertical) Shift Factor Function

The modulus (vertical) shift factor function was determined in much the same manner as the frequency (horizontal) shift factor function. The vertical shift factor showed a stronger dependence on strain level than on temperature, as discussed earlier. In the strain versus vertical shift factor plot (Figure 4.10), the trend between the logarithms of the shift factor and strains appeared to be linear and the effects of temperature were indistinguishable. For the vertical shift factor versus temperature plot (Figure 4.11), the trend between the logarithm of the shift factor and the temperature also appeared to be linear, but showed some temperature dependence. For the lower strains, the shift factor decreased as the temperature increased, whereas for the higher strains, the shift factor increased as the temperature increased. This temperature dependency needs to be accounted for in the vertical shift factor function.

From these observations, it was reasonable to use the same basic form of the modulus (vertical) shift factor function as was used for the frequency (horizontal) shift factor function, given in Equation (4.12), with $\log a_V$ replacing $\log a_H$ to represent the vertical shift. A possible dependence on air-void content was not included in the vertical shift factor due to the lack of an apparent trend.

The best fit for the modulus (vertical) shift factor function is shown in Equation (4.16) with same the variables as defined earlier.

$$\log a_V = C_{V1} + C_{V2}\left(\log\frac{10^{-6}+\|\mathbf{e}\|}{10^{-6}+\|\mathbf{e}_{ref}\|}\right) + C_{V3}(T-T_{ref})\left(\log\frac{10^{-6}+\|\mathbf{e}\|}{10^{-6}+\|\mathbf{e}_{ref}\|}\right)$$

DGAC:

$C_{V1} = 0.085866$

$C_{V1} = 0.584795$

$C_{V1} = 0.009665$ (4.16)

The same specimens were used to develop Equation (4.16) as for the horizontal shift factor function. These are shown in Table 4.3. Again, the lack of data at the low temperatures and high frequencies was accounted for in the final fit. The best fit was obtained by omitting the temperature term ($T-T_{ref}$) and including a constant. The constant value is very small, therefore the shift is very small when the reference temperature and strains were used.

Equation (4.16) gives a reasonable fit to the vertical shift factor data, as shown for strain level and temperature in Figures 4.23 and 4.24. In Figure 4.23, the different temperature lines cross at approximately 0.1 percent strain. This behavior was not evident from the data, but because the vertical range of shift factor values is small for the applicable strain range this behavior is not significant. Extrapolation of the lines back to 0.0001 percent strain ($1x10^{-6}$ strain) gave a range in shift factors from about 0.04 for 57°C to 0.2 for 20°C, approximately an order of magnitude, which is reasonable. The relatively

insignificant differences in the slopes of the shift factor and strain curves indicated that the temperature does not have a large influence on the vertical shift factor. This explains the insignificance of the individual temperature term in the vertical shift factor expression. This may indicate that the strain dependence is primarily due to the temperature independent aggregate and could explain why adopting the linear viscoelastic properties of the binder to describe the mix had been relatively unsuccessful.*(3, 35)*

The trends shown in Figure 4.24 show the strain dependency of the slope of the log vertical shift factor and temperature, as are apparent in the data. The fit is therefore very reasonable, especially in the temperature range of interest, 30 to 70°C.

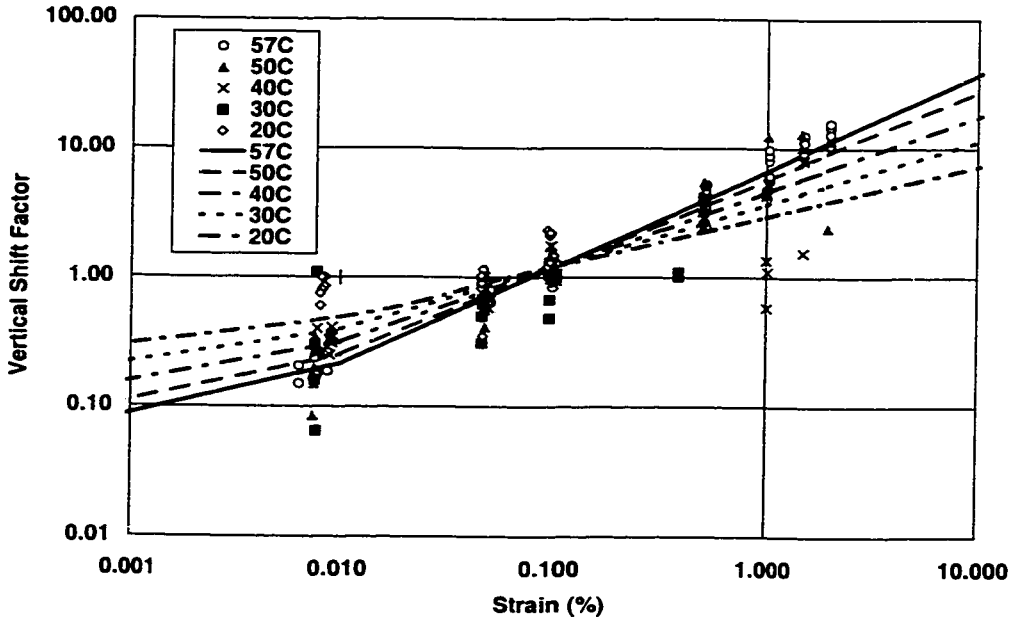

Figure 4.23 Vertical Shift Factor Function versus Strain Level, DGAC

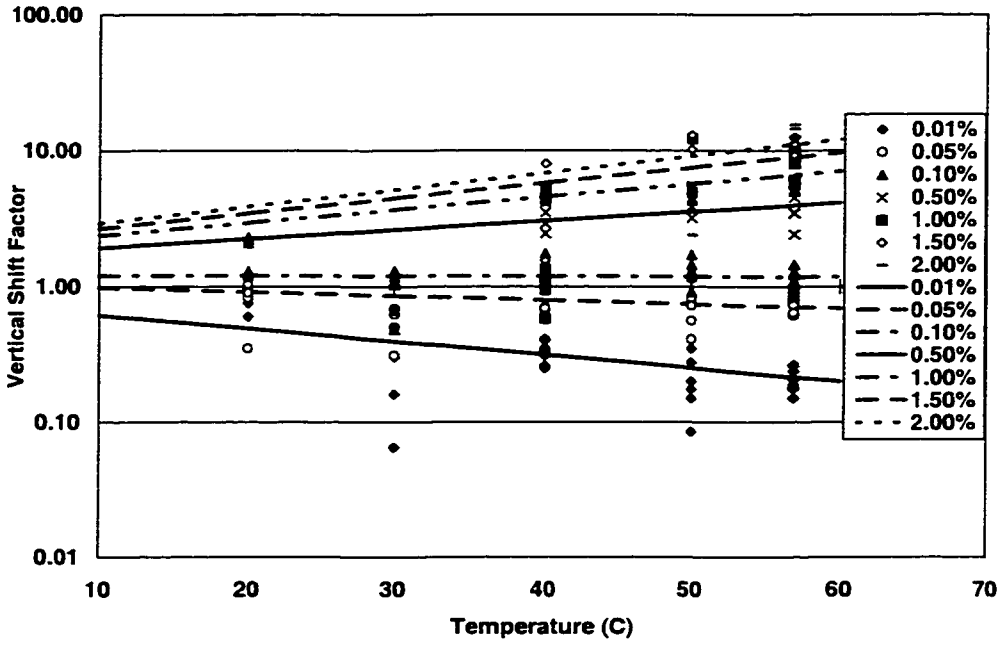

Figure 4.24 Vertical Shift Factor Function versus Temperature, DGAC

It is important to note that these shift factor functions, Equations (4.15) and (4.16), are only applicable when the reference temperature is 40°C and the reference strain level is 0.1 percent. These reference values should not be replaced with other values without recalculating the shift factors and recalibrating the coefficients.

4.3.2.3 Creation of Master Curves Using Shift Factor Functions

The modulus (vertical) and frequency (horizontal) shift factors were used with the original laboratory test data to create master curves for the storage and loss moduli. These master curves are shown in Figures 4.25 and 4.26 for the two moduli respectively. The data points marked with a solid symbol represent the master curves that were created

by manually shifting the specimens individually. They represent the same data that are shown in Figures 4.17 and 4.18.

As expected, the master curves were considerably more scattered than the master curve from the individually shifted data. Given the amount of variability inherent to asphalt concrete mixes discussed in Chapter 3, and the variability experienced in the laboratory tests used to develop these results, these master curves are reasonable. This shows that the method of shifting the data horizontally and vertically for strain and temperature is appropriate for asphalt concrete mixes. These master curves can be used to fit a shear viscoelastic model.

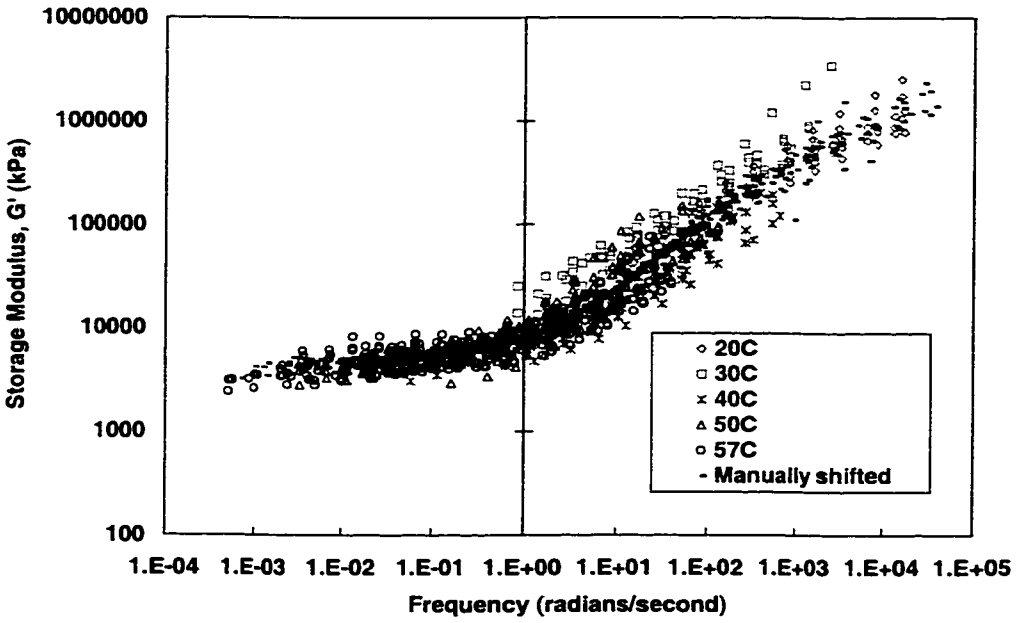

Figure 4.25 Storage Modulus Master Curve Created Using Shift Factor Functions, DGAC

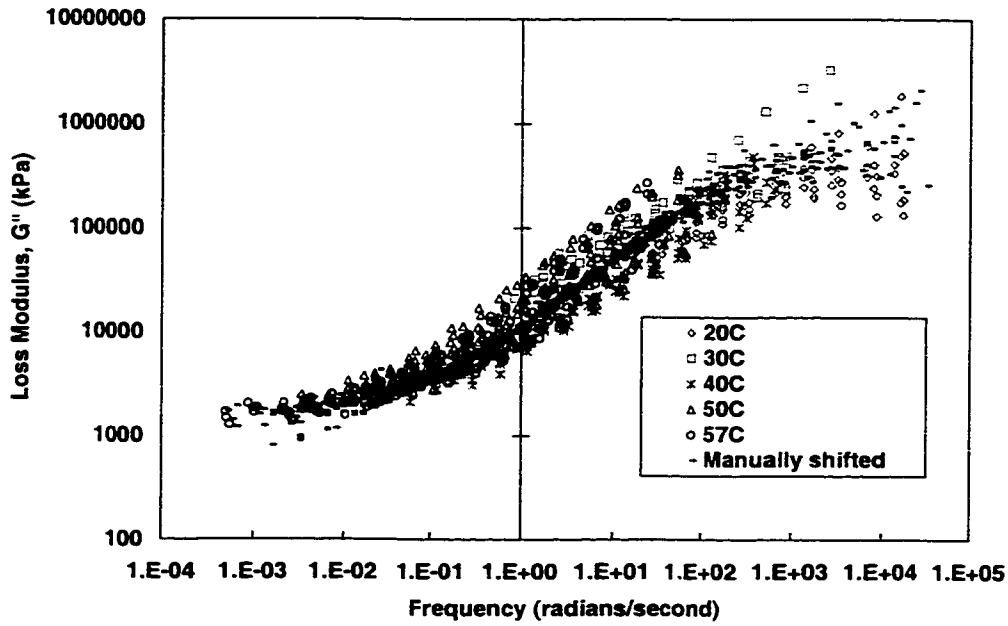

Figure 4.26 Loss Modulus Master Curve Created Using Shift Factor Functions, DGAC

4.3.3 Asphalt-Rubber Hot Mix Shift Factor Functions

The ARHM shift factor data presented in Section 4.2.3.2 show that the trends in the horizontal and vertical shift factors are the same for both mixes. The same basic forms of the shift factor functions are therefore used to fit the ARHM data, using the specimens shown in Table 4.4. The data for 40°C and 1.5 percent strain do not shift reasonably, and therefore these data were eliminated. The horizontal and vertical shift factor functions for the ARHM are given in Equations (4.17) and (4.18), respectively, and are plotted in Figures 4.27, 4.28, 4.29 and 4.30.

Table 4.4 Laboratory Test Data Used in Shift Factor Functions, ARHM

Strain level (%)	Temperature (°C)		
	20	40	60
0.01	12 CA (14.70)[1] 15 CA (14.62) 28 CA (14.82)	3 BA (14.83) 4 BA (14.60) 8 BA (14.75)	35 AA (14.82) 45 AA (14.84) 93 AA (14.78)
0.05	12 CB (14.70) 15 CB (14.62) 28 CB (14.82)	3 BB (14.83) 4 BB (14.60) 8 BB (14.75)	35 AB (14.82) 45 AB (14.84) 93 AB (14.78)
0.10	12 CC (14.70) 15 CC (14.62) 28 CC (14.82)	3 BC (14.83) 4 BC (14.60) 8 BC (14.75)	35 AC (14.82) 45 AA (14.84) 93 AC (14.78)
0.50		6 BD (14.17) 11 BD (15.03)	1 AD (14.40) 7 AD (14.18) 14 AD (15.11)
2.00			31 AG (14.49) 37 AG (15.18) 38 AG (14.34)

1 Air-void content

$$\log a_H = C_{H1} + C_{H2}(T - T_{ref}) + C_{H3}\left(\log\frac{10^{-6}+\|\mathbf{e}\|}{10^{-6}+\|\mathbf{e}_{ref}\|}\right) + C_{H4}(T - T_{ref})\left(\log\frac{10^{-6}+\|\mathbf{e}\|}{10^{-6}+\|\mathbf{e}_{ref}\|}\right)$$

ARHM:

$C_{H1} = 0.324886$

$C_{H2} = -0.099539$

$C_{H3} = 0.329099$

$C_{H4} = 0.014692$

(4.17)

$$\log a_V = C_{V1} + C_{V2}\left(\log\frac{10^{-6}+\|\mathbf{e}\|}{10^{-6}+\|\mathbf{e}_{ref}\|}\right) + C_{V3}(T - Tref)\left(\log\frac{10^{-6}+\|\mathbf{e}\|}{10^{-6}+\|\mathbf{e}_{ref}\|}\right)$$

ARHM:

$C_{V1} = 0.049158$

$C_{V2} = 0.530642$

$C_{V3} = 0.008332$

(4.18)

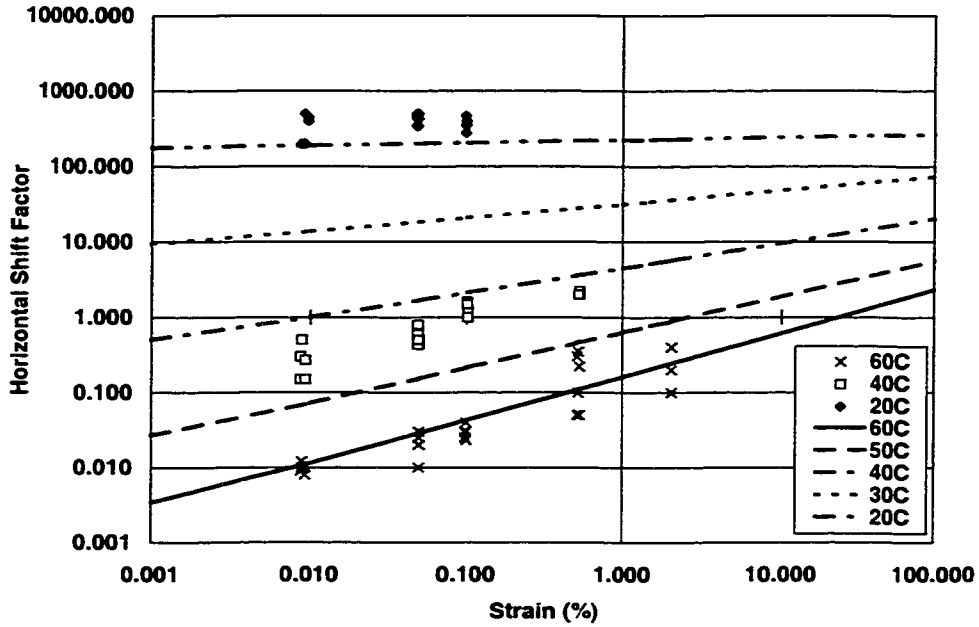

Figure 4.27 Horizontal Shift Factor Function versus Strain Level, ARHM

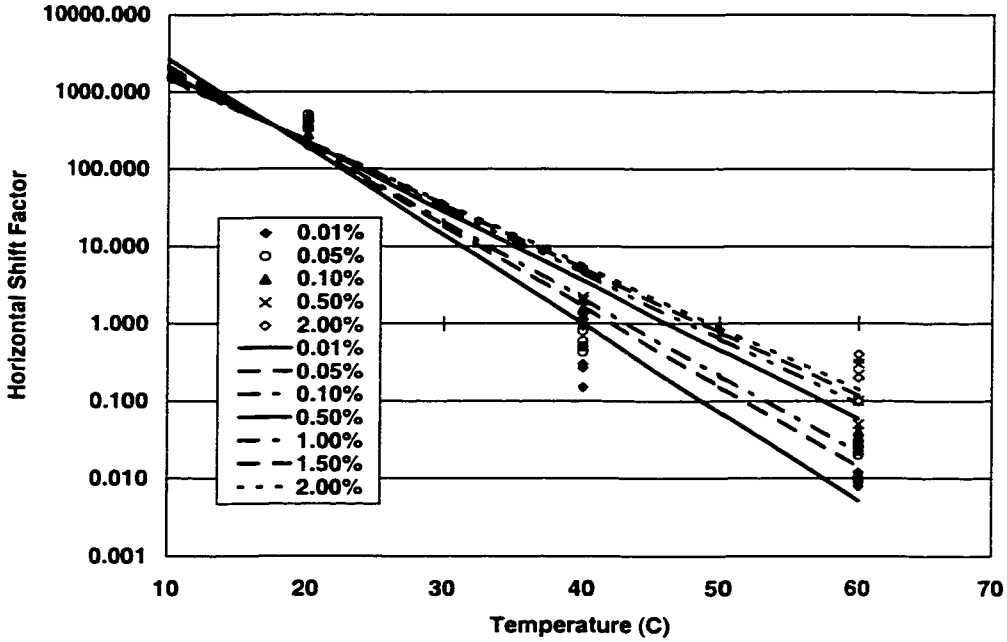

Figure 4.28 Horizontal Shift Factor Function versus Temperature, ARHM

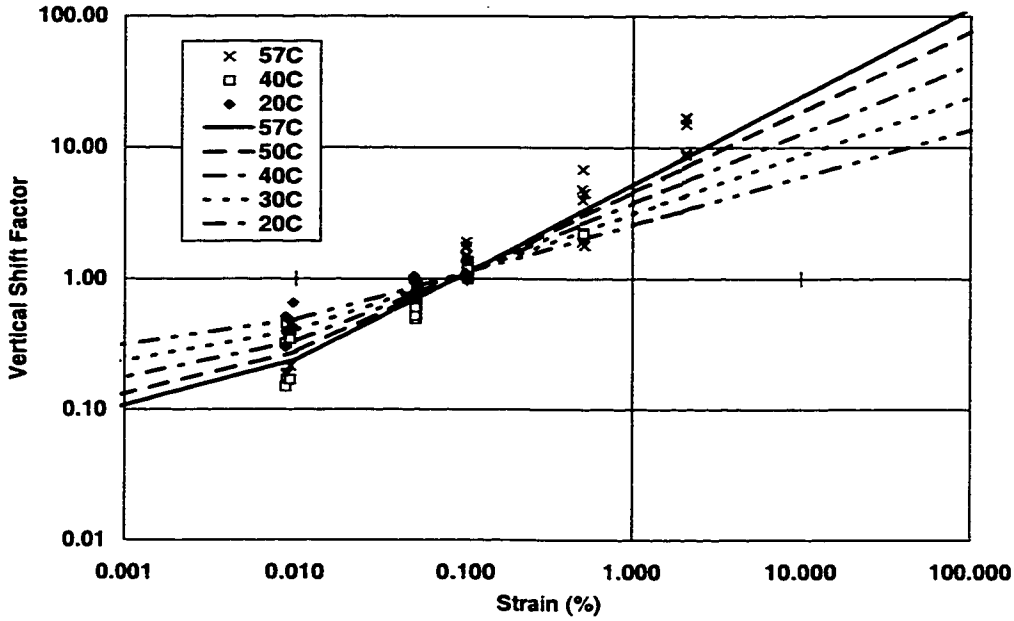

Figure 4.29 Vertical Shift Factor Function versus Strain Level, ARHM

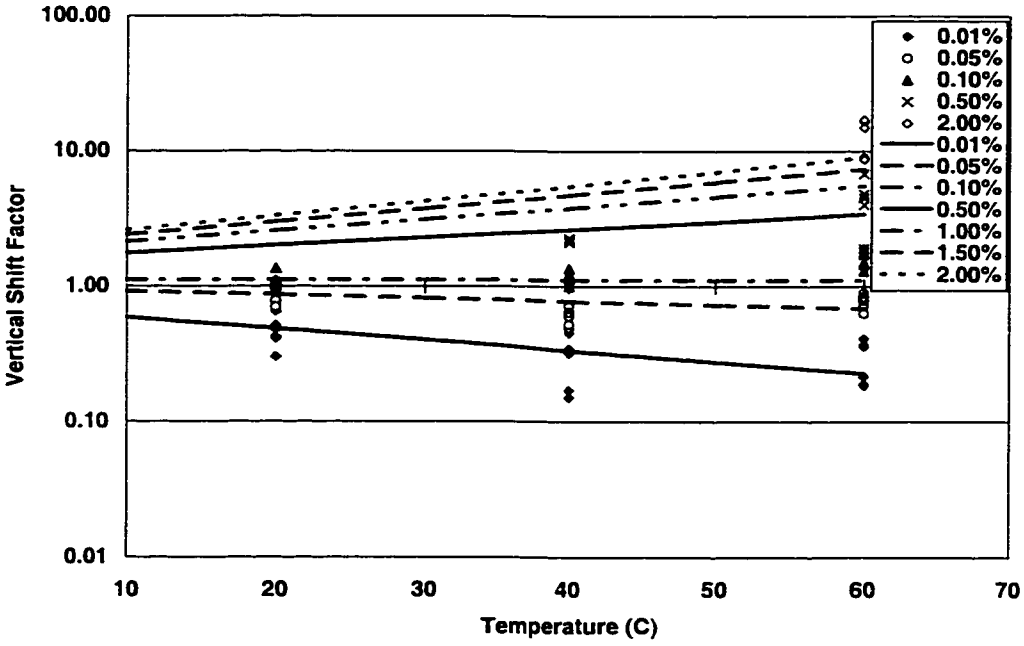

Figure 4.30 Vertical Shift Factor Function versus Temperature, ARHM

The data fit is good for the 57°C data, but not as good for 40°C and 20°C. The worst fit is for 20°C, but this temperature is the least important for permanent deformation of asphalt concrete pavements and is therefore not a significant problem. Fewer data were available for the ARHM, which reduced the ability to obtain as good a fit as for the DGAC.

The master curves created with the shift factor functions and the original laboratory test data are given in Figures 4.31 and 4.32. The relatively bad fit for 20°C causes most of these data to lie above the manually shifted master curve for the storage modulus. The 40°C data also deviate from the manually shifted master curves for both the storage and loss modulus. The small data set exacerbated the bad fit.

Figures 4.33 and 4.34 show comparisons of the DGAC and ARHM shift factor functions for the horizontal shift factor versus temperature and the vertical shift factor versus strain level. Figures 4.35 and 4.36 compare the manually shifted master curves. These figures show that the two mixes have very similar responses. The field performance of the DGAC and ARHM, for the air-void contents obtained in the test sections, are very similar. It is therefore not surprising that the master curves and the shift factor functions of the two mixes are so similar.

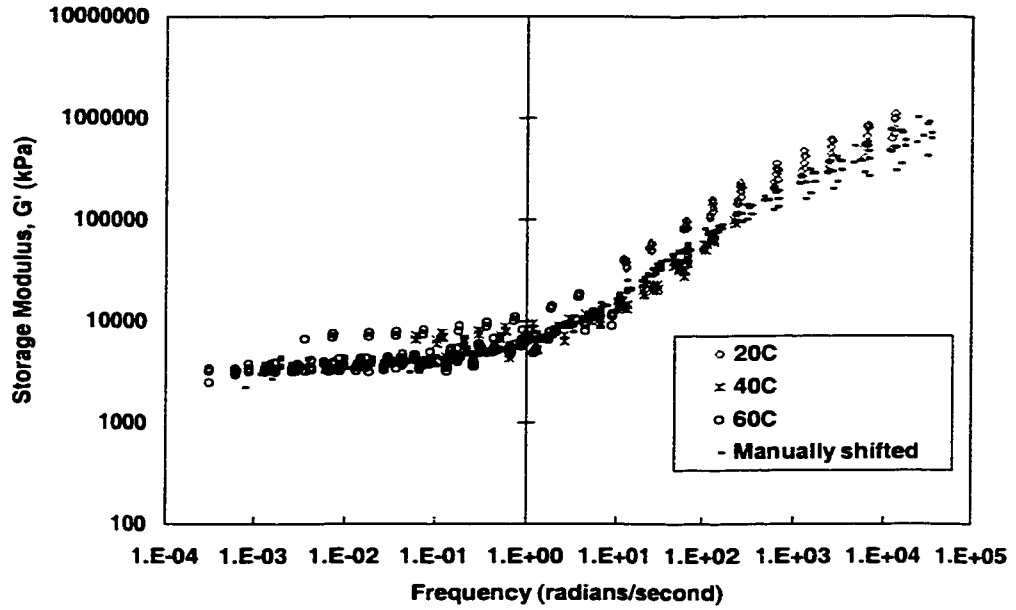

Figure 4.31 **Storage Modulus Master Curve Created Using Shift Factor Functions, ARHM**

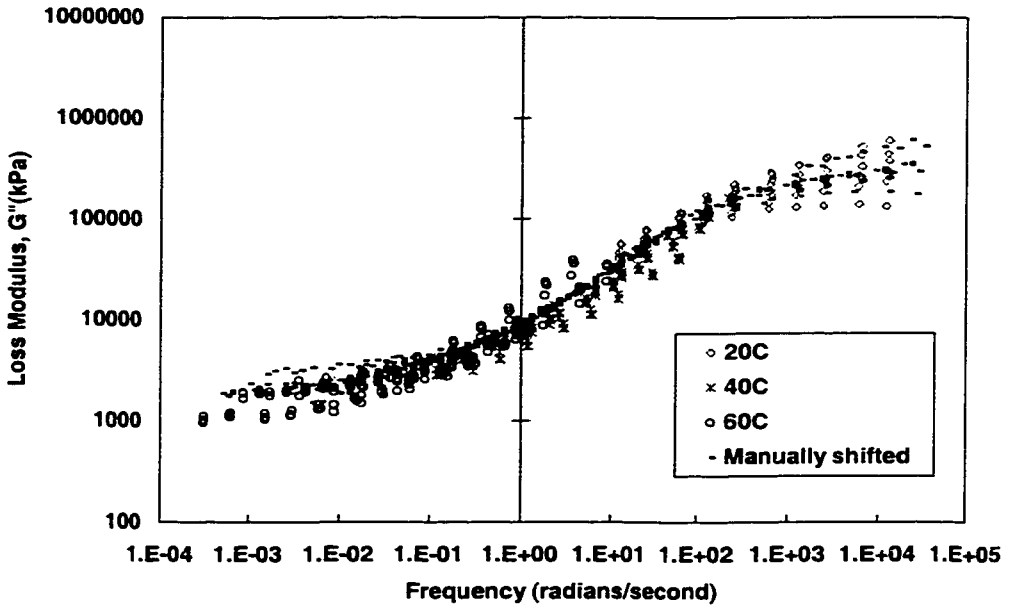

Figure 4.32 **Loss Modulus Master Curve Created Using Shift Factor Functions, ARHM**

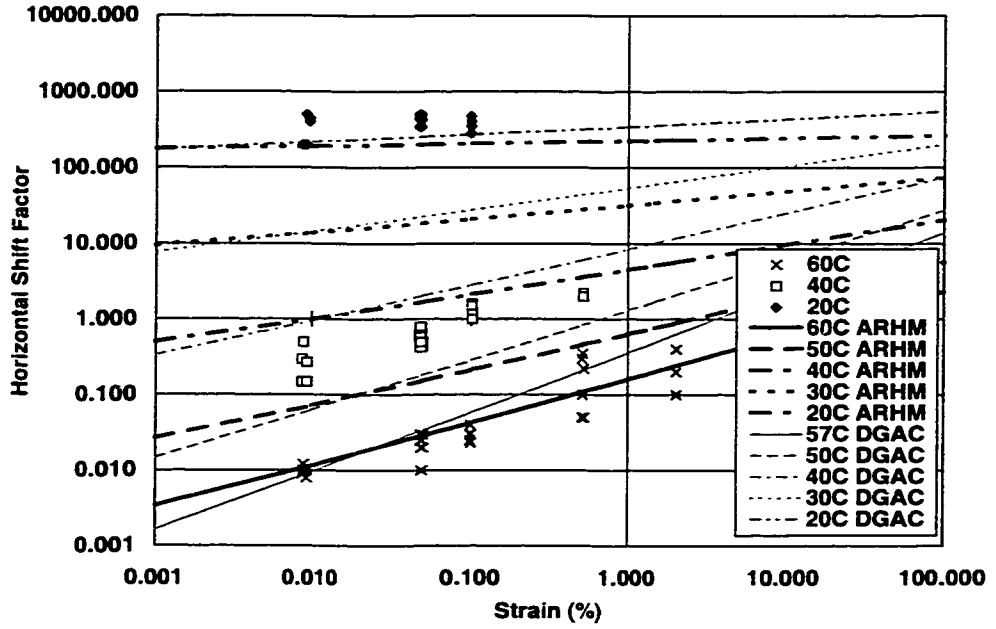

Figure 4.33 Comparison of Horizontal Shift Factor Function versus Strain Level for DGAC and ARHM

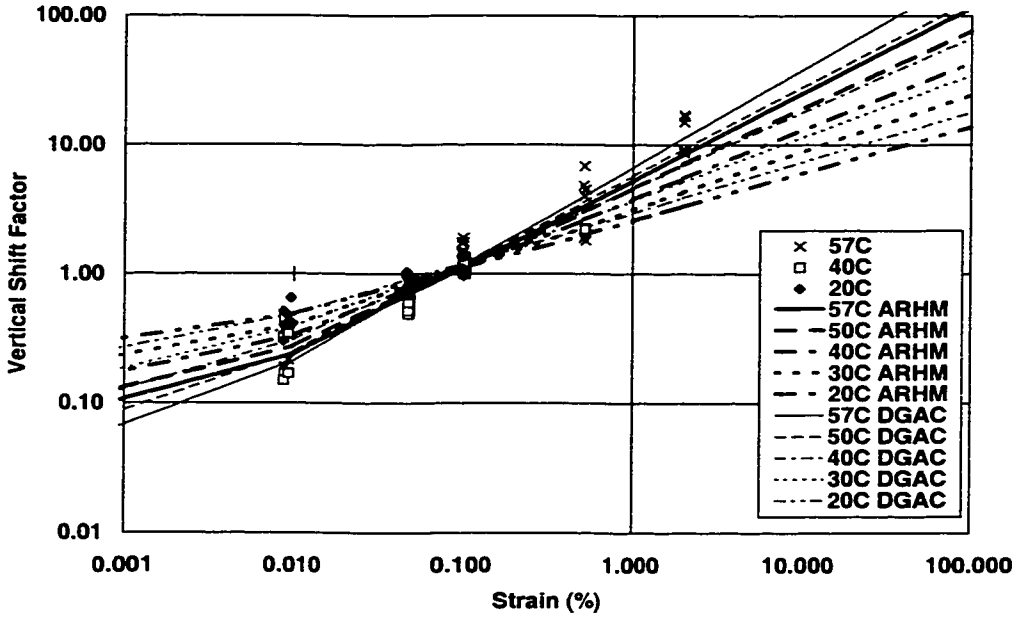

Figure 4.34 Comparison of Vertical Shift Factor Function versus Strain Level for DGAC and ARHM

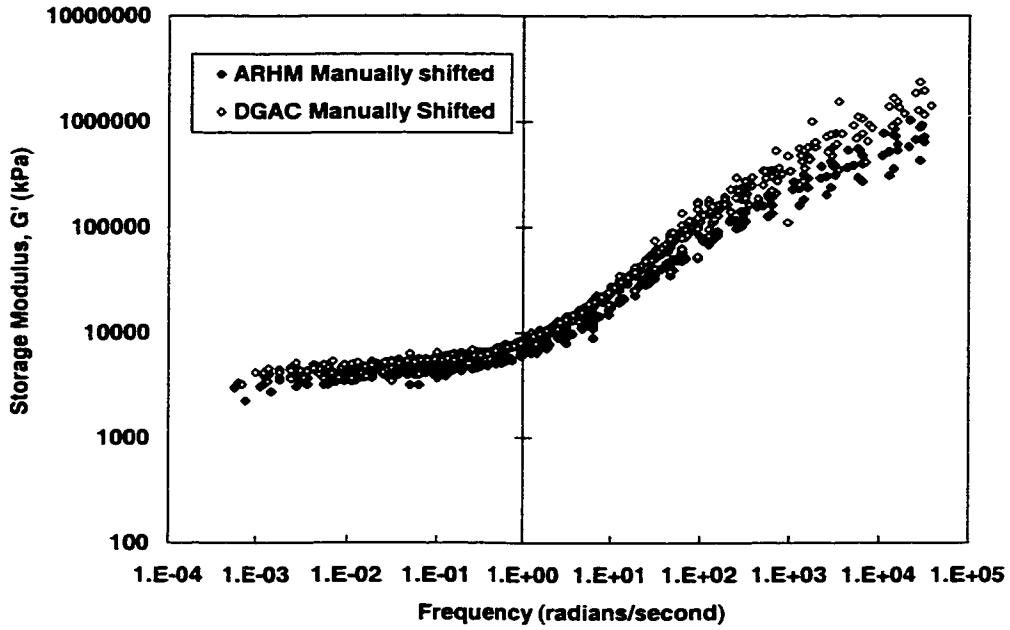

Figure 4.35 Comparison of Manually Shifted Storage Modulus Master Curves for DGAC and ARHM

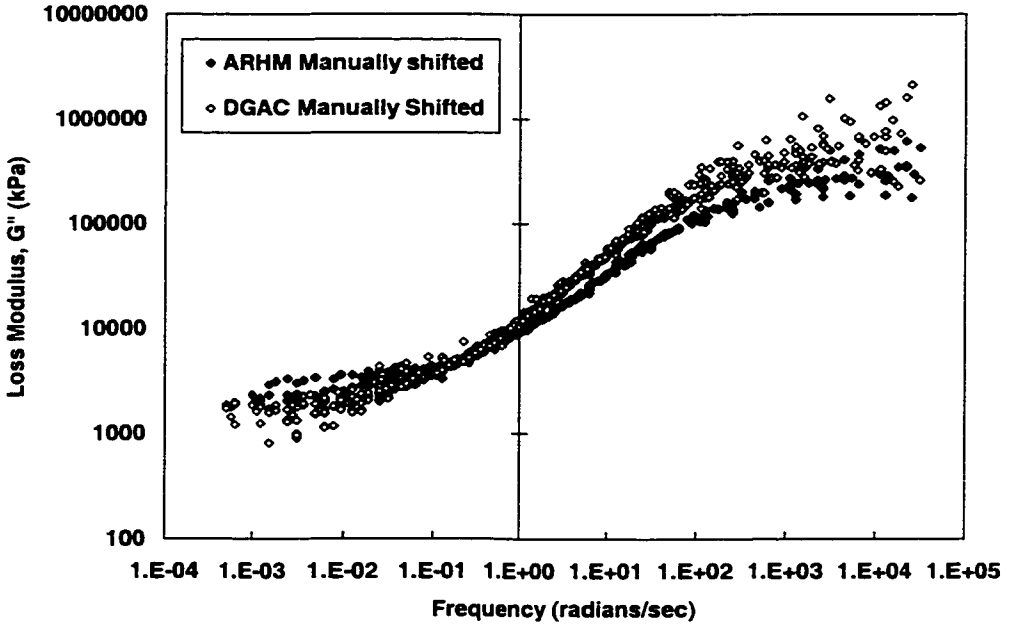

Figure 4.36 Comparison of Manually Shifted Loss Modulus Master Curves for DGAC and ARHM

The ease with which this approach to obtain the shift factor functions is used with the ARHM data demonstrates the applicability of the approach for modified binders. Investigation of another modified binder, which gives different field performance than the ARHM and DGAC, would be interesting. Unfortunately no data were available for such a modified mix.

4.4 Volumetric Component

As discussed in Chapter 2, there are many reasons why the shear behavior is more important than the volumetric behavior for understanding modeling permanent deformation of asphalt concrete. Thus, the development of the constitutive model predominantly focused on the shear behavior. However, it is necessary to define a volumetric (bulk) component.

4.4.1 Justification for Volumetric Model

The model chosen to describe the volumetric behavior was a linear viscoelastic model. The bulk response of asphalt concrete is temperature dependent and, as will be shown, time dependant. It was therefore appropriate to use a viscoelastic model. The volumetric behavior is limited to a linear model; it would take considerably more laboratory testing to also develop a nonlinear volumetric viscoelastic model.

A disadvantage of the model selected for the bulk response is that the behavior of the material is the same in tension and compression, which is not valid for asphalt concrete. *(9)* However, it is beyond the scope of this project to develop a model that could account for the differences in tension and compression.

4.4.2 Materials

In previous research by Alavi, extensive laboratory testing was performed on asphalt concrete using hollow cylinder specimens.*(19, 20)* From these data it was possible to extract a linear viscoelastic model for the volumetric response of asphalt concrete. This section describes the materials used in the tests.

The mixes used in the hollow cylinder tests were very similar to the mix used in the shear laboratory testing. The binders were of similar origin and the gradations followed the same specification, as shown in Figure 4.37. The primary differences were the aggregate source and manufacture, with the hollow cylinders having a rougher, more bulky aggregate. Watsonville aggregate was used in the hollow cylinder specimens. The binder was an AR-4000 California Valley asphalt, a conventional, unmodified binder. The asphalt content of the hollow cylinder mixes was either 4.9 percent AC or 5.5 percent AC. The lower asphalt content specimens are denoted V0W1 and the higher asphalt content specimens V1W1. The asphalt content of the DGAC mix used in the shear testing was 5.0 to 5.3 percent, which is within the range of the hollow cylinder

specimens. The air-void content of all the specimens was 8 percent, which is within the range of the air-void contents of the DGAC specimens.

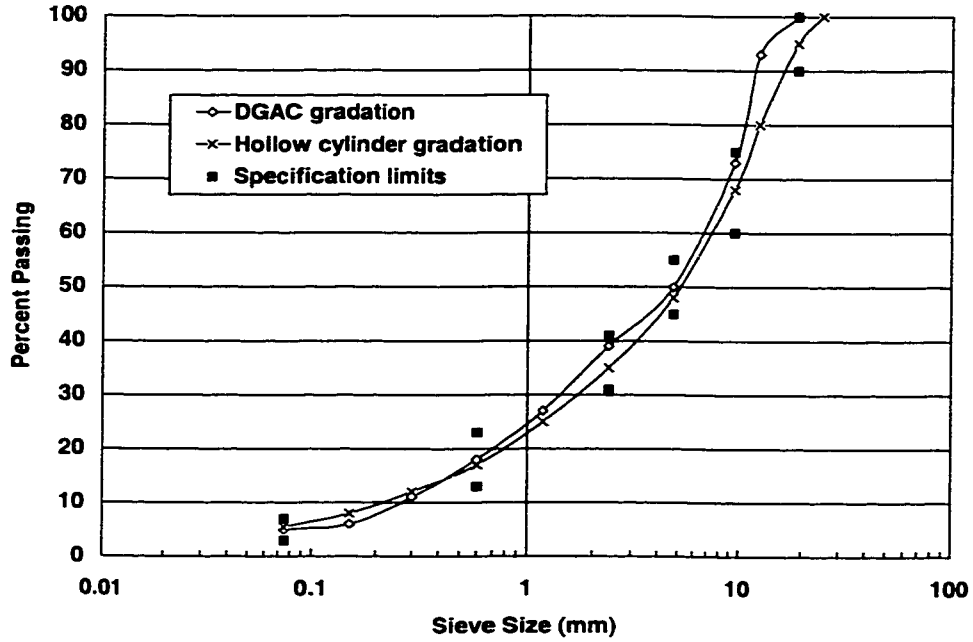

Figure 4.37 Gradation of Mixes Used in Hollow Cylinder Test and DGAC Shear Frequency Sweep Tests

4.4.3 Hollow Cylinder Laboratory Test Results

Both axial and shear frequency sweep tests were conducted with hollow cylinder specimens. The specimens were 203 mm tall, with 89 mm inner and 114 mm outer radii. The frequency range was the same as for the shear frequency sweep tests reported in Chapter 3, viz., 0.01, 0.02, 0.05, 0.1, 0.2, 0.5, 1, 2, 5, 10 Hertz. The tests were performed by first applying an axial sinusoidal compressive stress pulse with zero shear stress over

the frequency range, and then applying a shear cyclic stress pulse, with zero axial stress over the frequency range. The stress levels used were 414, 207 and 103 kPa for the axial stress and 138, 69 and 34 kPa for the shear stress. Three test temperatures were used, 4.4°C, 25°C, and 40°C. Each specimen was tested at all three temperatures. Within these stress levels and temperature ranges the material was essentially in the linear range. Therefore, it was not possible to determine the strain dependency of the mix.*(20)*

The data obtained from these tests included the magnitude of the dynamic Young's modulus (|E*|), the dynamic shear modulus (|G*|), and the dynamic Poisson's ratio (ν). Figure 4.38 shows a comparison between the shear complex modulus (|G*|) master curves from the hollow cylinder tests and the simple shear tests at constant height at 40°C. The complex modulus (G*) is related to the storage (G') and loss (G") moduli as shown in Equation (4.19) where i is $\sqrt{-1}$. The magnitude of the complex modulus can be determined using Equation (4.20). The hollow cylinder mixes had higher moduli than the DGAC mix. This may be due to the small differences in the mix, or from the different modes of testing. The Young's modulus data are also shown in Figure 4.38.

$$G^* = G' + iG'' \tag{4.19}$$

$$|G^*| = \sqrt{G'^2 + G''^2} \tag{4.20}$$

From data presented in reference *(20)*, the parameters for the Williams, Landel, and Ferry (WLF) equation were determined, and are shown in Equation (4.21). This equation

predicts values that agree with the shift factor ranges for asphalt concrete given in reference *(62)*.

$$\log a_T = \frac{-37.037(T - T_{ref})}{349.7851 + T - T_{ref}} \tag{4.21}$$

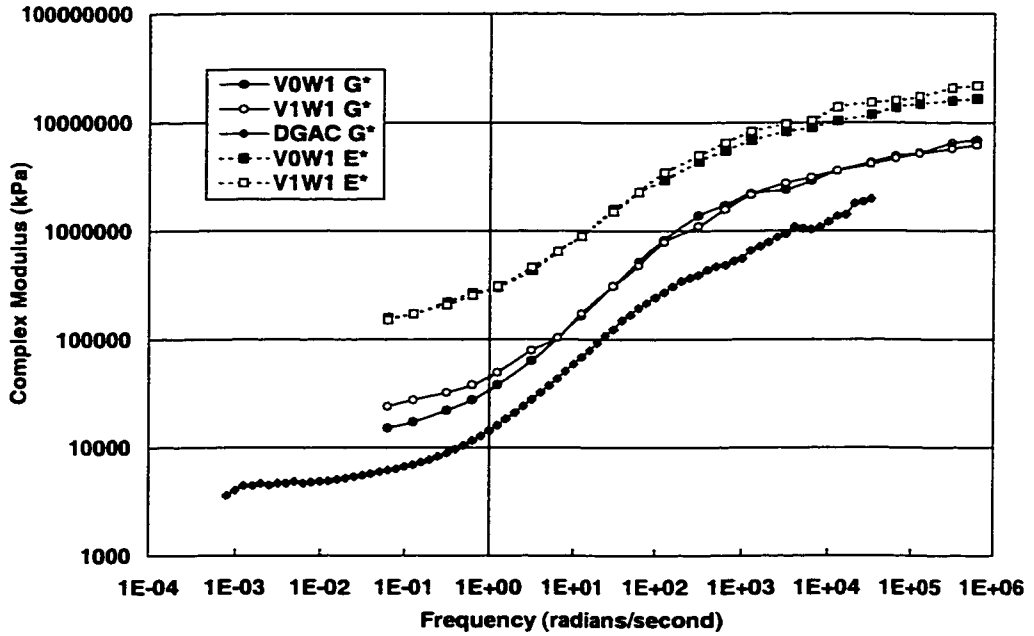

Figure 4.38 Complex Shear Moduli from Volumetric and Shear Tests

4.4.4 Conversion to Bulk Moduli

The bulk modulus (K*) was calculated from the dynamic axial modulus (E*), dynamic shear modulus (G*), and Poisson's ratio (υ) data from the hollow cylinder test using the following three expressions from classical mechanics.*(63, 64)*

$$K^* = \frac{G^* \cdot E^*}{3(3G^* - E^*)} \tag{4.22}$$

$$K^* = \frac{2G^*(1+\upsilon)}{3(1-2\upsilon)} \tag{4.23}$$

$$K^* = \frac{E^*}{3(1-2\upsilon)} \tag{4.24}$$

For the data available, Equation (4.22) predicts negative values, which are not reasonable. This may be due to the different behavior of asphalt concrete in tension and compression, which makes these conversions inapplicable. However, these conversions are the only method of obtaining a bulk modulus master curve without embarking on a laboratory testing program.

Poisson's ratio data were only available for a small frequency range. It was not possible to reduce the data to 40°C from the other temperatures. Therefore, using Equations (4.23) and (4.24) the bulk storage and loss moduli were calculated for each temperature. These results are shown in Figures 4.39 and 4.40, where the "G' and nu" curves were calculated with Equation (4.23) and the "E' and nu" curves with Equation (4.24). The same equations are used to calculate the loss moduli using G", K", and the Poisson's ratio, "nu". The largest difference between the two curves is for the 40°C data. This demonstrates that as the temperature increases, the asphalt concrete becomes more nonlinear and these types of conversions become less valid.

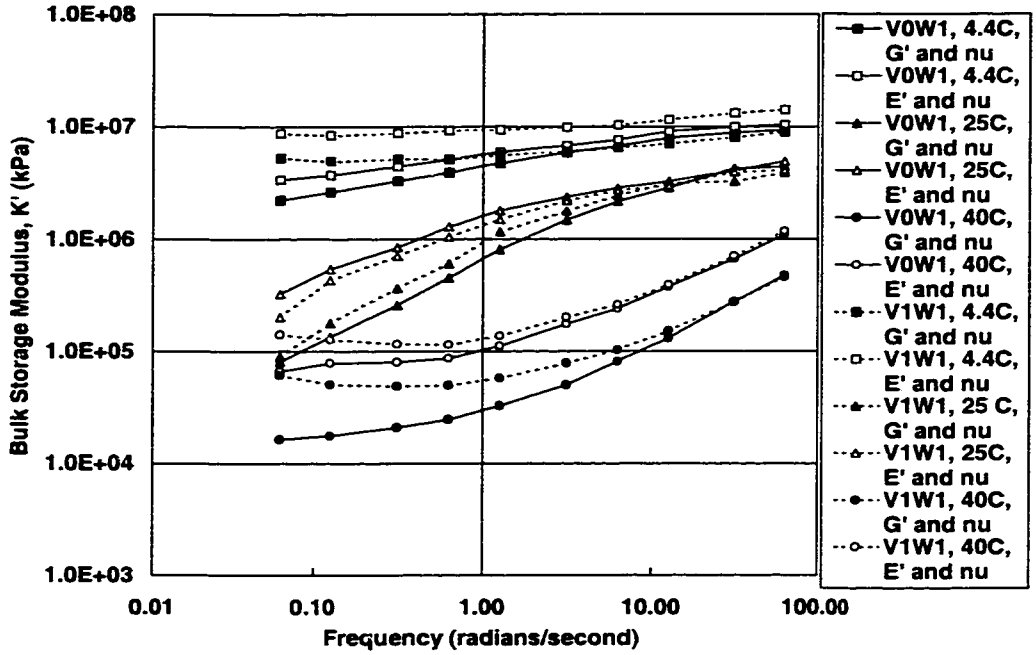

Figure 4.39 Bulk Storage Modulus Data for V0W1 (4.0% asphalt content) and V1W1 (5.5% asphalt content)

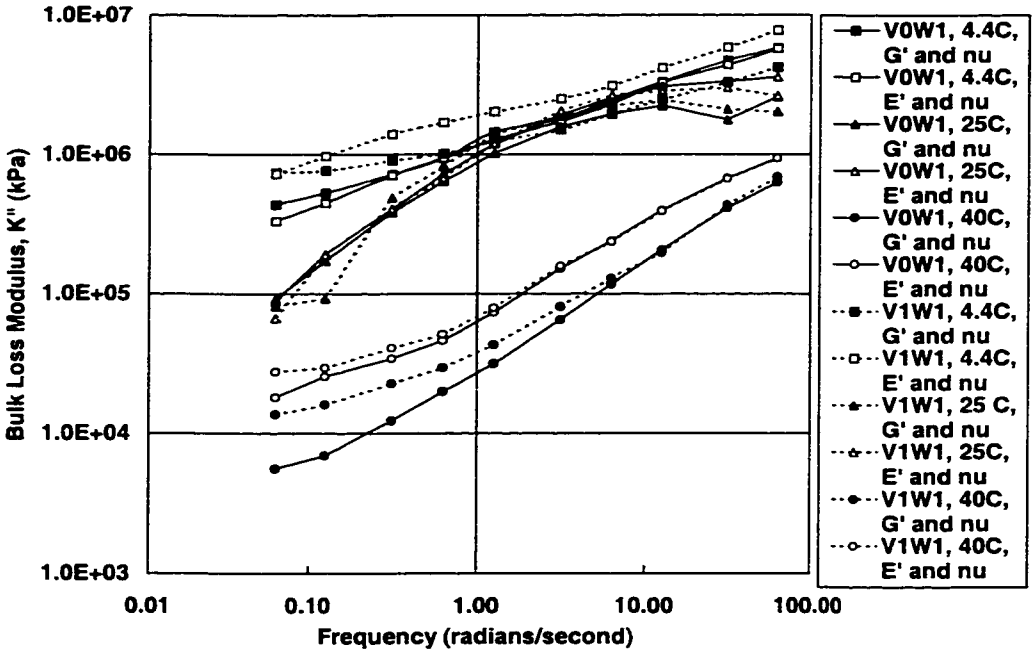

Figure 4.40 Bulk Loss Modulus for V0W1 (4.0% asphalt content) and V1W1 (5.5% asphalt content)

4.4.5 Volumetric Master Curves

The data from the two different equations were averaged, and then reduced to 40°C by shifting the data horizontally along the frequency scale. Using the WLF equation gave reasonable reduced master curves, but improved, smoother curves were obtained by manually shifting the data. The results from the shifting are shown in Figures 4.41 and 4.42 for the bulk storage and loss moduli, respectively. There was little difference between the two hollow cylinder mixes. As was found for the shear data, different shift factors were necessary for the storage and loss modulus data, and the storage modulus shifted better than the loss modulus. The shifted loss modulus master curve was not very good. The storage modulus master curve spans a wider range of frequencies. Although these data show much variability, they give a reasonable estimate of the volumetric properties of the DGAC mix.

No volumetric data, nor data from which to extract the volumetric properties, were available for asphalt-rubber mixes. Because the DGAC and ARHM showed such similar behavior, the volumetric master curve developed in this section was also used for the ARHM.

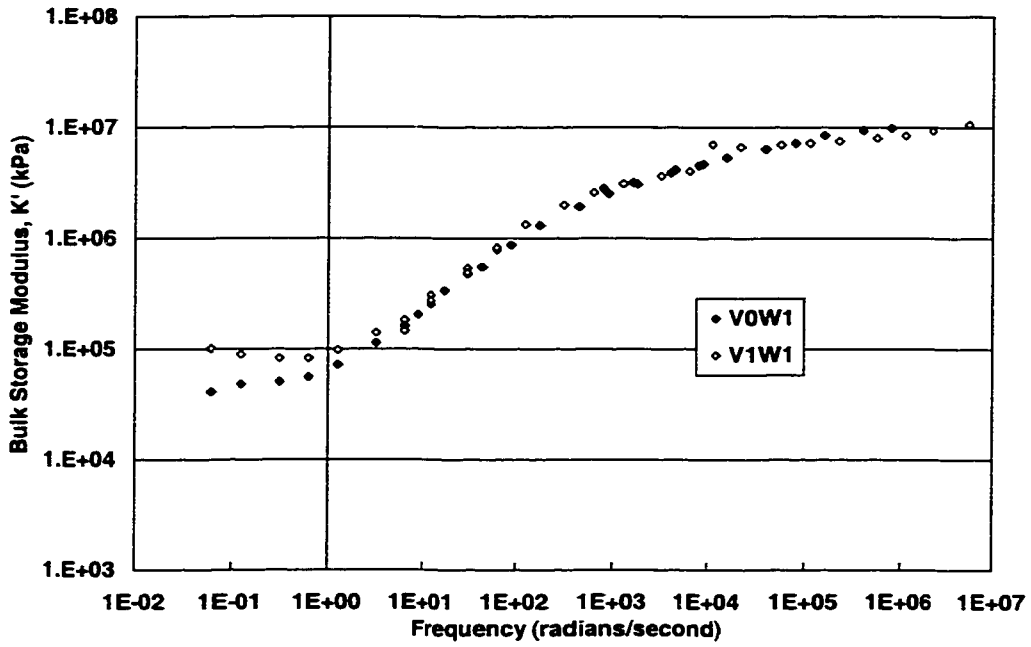

Figure 4.41 Bulk Storage Modulus Master Curves at 40°C

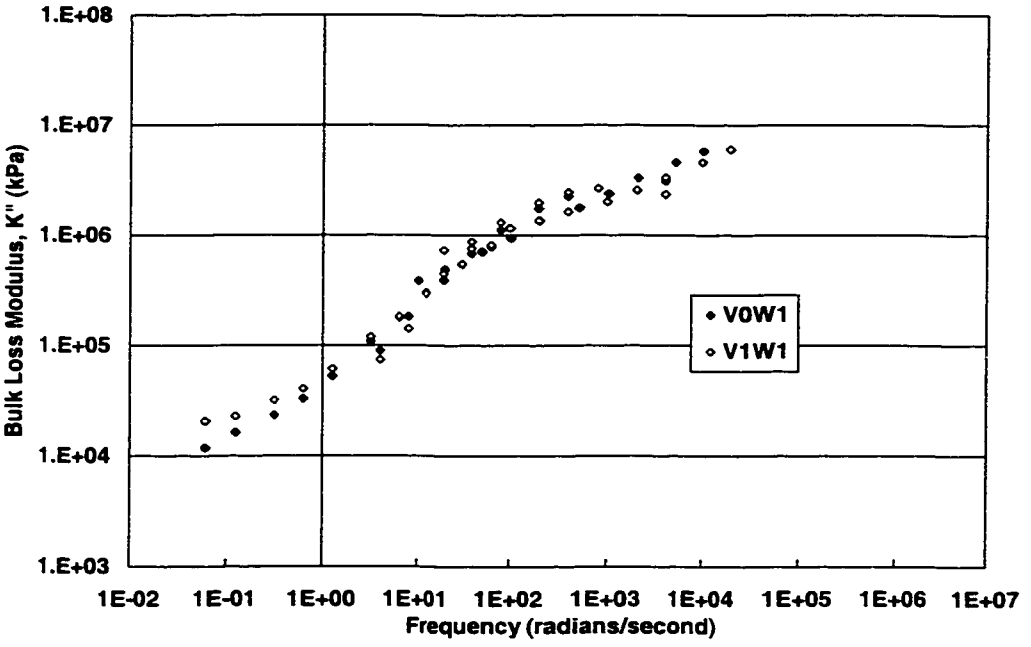

Figure 4.42 Bulk Loss Modulus Master Curves at 40°C

4.5 Summary

This chapter discusses master curves for the shear and volumetric response of the DGAC and ARHM, and shift factor functions to account for the temperature and strain dependence of the shear response are determined. The ARHM and DGAC show very similar behavior, which was expected because the field performance was very similar. In Chapter 5, these master curves are used to fit viscoelastic properties.

CHAPTER 5

CONSTITUTIVE MODEL FORMULATION

Chapter 4 discussed the appropriateness of using a nonlinear viscoelastic material model to describe the permanent deformation behavior of asphalt concrete mixes. Also in that chapter, horizontal and vertical shift factor functions for the shear response were developed. The next step is to formulate and implement the constitutive model and fit the material properties.

This chapter describes the shear (deviatoric) and volumetric (bulk) components of the complete nonlinear viscoelastic constitutive model. An algorithm for the model is derived and implemented in a finite element code. The material properties are fit to the master curve data obtained in Chapter 4, and, finally, the limitations of the model are discussed.

5.1 Linear Viscoelasticity

Linear viscoelasticity was used as the basis for formulating the nonlinear viscoelastic model. Material response is often decomposed into the shear and volumetric response using additive decomposition, as shown in Equation (5.1)

$$\boldsymbol{\sigma} = p\mathbf{1} + \mathbf{s} \tag{5.1}$$

where $\boldsymbol{\sigma}$ is the stress, p the hydrostatic pressure, $\mathbf{1}$ the second rank identity, and $\mathbf{s}$ the deviatoric stress. Viscoelastic materials typically have very different volumetric and deviatoric responses, with the deviatoric response dominating. For asphalt concrete the bulk stiffness is significantly larger than the shear stiffness. The shear response to loading is therefore larger than the volumetric and it has less recovery than the volumetric, as discussed in Chapter 2. Because of these differences additive decomposition of the volumetric and deviatoric response was appropriate.*(10, 65)*

The one-dimensional rheological model shown in Figure 5.1 represents a viscoelastic material. The spring and dashpot in series form a Maxwell element. Any number of Maxwell elements can be combined in parallel, with the free spring, to form the viscoelastic model. For the shear component, the modulus of the free spring and the i^{th} Maxwell element spring are denoted G_∞ and G_i, respectively, and the relaxation time of the i^{th} Maxwell element is τ_i. For the volumetric component, G_∞, G_i and τ_i are replaced

by K_∞, K_i and λ_i. This model is known as a generalized standard linear solid. When the free spring is not present, G_∞ or K_∞ equal zero, the model represents a viscous liquid.

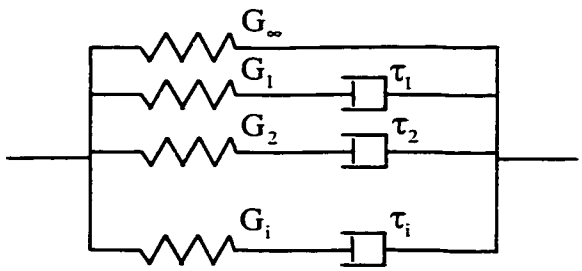

Figure 5.1 One-dimensional Representation of Linear Viscoelastic Material

Although some of the concepts discussed in this section have already been defined in previous sections, for clarity they will be repeated here. Within the assumption of additive decomposition of the shear and volumetric behavior, the constitutive relationships for a standard linear solid are presented in this section. The constitutions for the bulk and shear components are shown in Equations (5.2) and (5.3)

$$p(t) = \int_{-\infty}^{t} K(t-s)\frac{d}{ds}[\theta(s)]ds \tag{5.2}$$

$$\mathbf{s}(t) = \int_{-\infty}^{t} 2G(t-s)\frac{d}{ds}[\mathbf{e}(s)]ds, \tag{5.3}$$

where p is the hydrostatic pressure, t is the time, s is the integration variable, $K(t-s)$ and $G(t-s)$ are the bulk and shear relaxation functions, θ is the trace of the strain, $\mathrm{tr}(\boldsymbol{\varepsilon})$, and $\mathbf{e}$ is the deviatoric strain. The relaxation functions are approximated with a Prony series, shown in Equations (5.4) and (5.5) for the bulk and shear response.*(48)*

$$K(t) = K_\infty + \sum_{i=1}^{N} K_i e^{-\frac{t}{\lambda_i}} \tag{5.4}$$

$$G(t) = G_\infty + \sum_{i=1}^{M} G_i e^{-\frac{t}{\tau_i}} \tag{5.5}$$

In these equations K_∞ and G_∞ are the moduli of the free springs, K_i and G_i are the moduli of the springs in the i^{th} Maxwell elements, λ_i and τ_i are the relaxation times of the dashpots in the i^{th} Maxwell elements, N is the number of bulk Maxwell elements, and M is the number of shear elements. The bulk and shear responses are calculated independently. Hence, it is not necessary to have the same number of shear and bulk Maxwell elements.

The effect of temperature is included in the constitutive relationships using the reduced or intrinsic time concept.*(48, 65, 66)* The time-temperature superpositioning of linear viscoelastic materials results in a horizontal shift with frequency (time), thereby changing the relaxation times, as shown for the bulk component in Equation (5.6)

$$\lambda(T_{ref}) = \frac{\lambda(T(t))}{a_T(T(t))} \tag{5.6}$$

where $\lambda(T_{ref})$ and $\lambda(T)$ are the bulk relaxation times at the reference temperature (T_{ref}) and current temperature (T(t)), respectively, and a_T is the shift factor. The shifted shear relaxation times are calculated in the same manner. This shifted time is called the reduced or intrinsic time, is denoted $\chi(t)$ for the bulk component, and is defined in Equation (5.7). The shear reduced time is denoted $\xi(t)$. The reduced time is

incorporated into the constitutive relationships by replacing the time, t, with the reduced time, $\chi(t)$ or $\xi(t)$, as show in Equations (5.8) and (5.9), which replace Equations (5.2) and (5.4) for the bulk component.

$$\chi(t) = \int_{-\infty}^{t} \frac{1}{a_0(T(s))} ds \tag{5.7}$$

$$p(t) = \int_{-\infty}^{t} K(\chi(t) - \chi(s)) \frac{d}{ds}[\theta(s)] ds \tag{5.8}$$

$$K(t) = K_\infty + \sum_{i=1}^{n} K_i e^{\frac{\chi(t)}{\lambda_i}} \tag{5.9}$$

5.2 Constitutive Model for Asphalt Concrete

The linear viscoelastic framework discussed in the previous section was used to formulate the nonlinear viscoelastic constitutive model, which describes the permanent deformation behavior of asphalt concrete. The bulk component is described first.

5.2.1 Bulk Component

The volumetric data presented in Chapter 5 indicate that, for the strain ranges available, a linear viscoelastic model is appropriate for the bulk response. The volumetric algorithm was therefore derived from Equations (5.8) and (5.9). The bulk response was assumed to be thermorheologically simple, and the temperature effects were included using the

Williams, Landel, and Ferry equation (WLF, Equation (4.21)) to calculate the shift factor, denoted a_T.

5.2.2 Shear Component

Linear viscoelasticity can account for the time and temperature dependence of a thermorheologically simple viscoelastic material, but not for the strain dependence that is observed in the shear data in Chapters 3 and 4. The material is thermorheologically complex due to the strain effects. This complex behavior was incorporated into the constitutive relationships for asphalt concrete using linear viscoelasticity as the basis.

Analyses of the laboratory test data in Chapter 4 showed that the strain and temperature dependency of the material response could be accommodated by including both vertical and horizontal shift factors. Functions to determine these shift factors for particular reference conditions were developed in Chapter 4 from the data, and are given in Equations (4.15) and (4.16).

The horizontal shift factor was incorporated into the linear viscoelastic framework through the reduced time. For the shear component of this model, the horizontal shift factor, a_H (Equation (4.15)), was used to calculate the reduced time. It is important to note that in addition to the temperature term, a strain term was included in this horizontal shift factor.

The vertical shift factor, a_V, shifts the modulus of the material as a function of the strain level and the temperature. In this context, the constitutive relationship for linear viscoelasticity, Equation (5.3), can be adapted to include the vertical shift factor, a_V, (Equation (4.16)). Although some literature discusses vertical shifting, little is available on how such shifting is actually implemented in a finite element model. Most of the available literature includes a factor in the constitutive relationship, either a damping function or a ratio of the reference and current states, that effectively reduces the modulus with increased strain, resulting in a strain softening response.*(54, 57, 58, 59)* The most detailed discussion is by Simo *(60),* in which a damage factor is included, that is a function of the past maximum strain. An increase in strain results in a degradation of the modulus, which is known as Mullins' effect. Simo's model is formulated in finite deformation.

5.2.2.1 Strain Value for Evaluating Shift Factor Functions

The horizontal and vertical shift factors developed in Chapter 4 are functions of temperature and the deviatoric strain norm. The question arose as to which deviatoric strain norm should be used to calculate the shift factors. The reference value used to develop the shift factor functions was the norm of the peak strain in the steady state oscillatory laboratory tests, and the measured moduli were a function of this peak strain. Use of the current deviatoric strain norm was therefore not appropriate. When a load is removed and the material is relaxing, it will not "remember" that it has experienced a high strain and will respond in approximately the same manner with further loading. If

two loads of very different magnitudes are applied, and the material is allowed to relax to the same residual strain, when a subsequent load is applied the two pavements will have the same response. The higher, more damaging load will have had no residual or damaging effect.

In addition to the laboratory testing discussed in Chapter 3, additional testing was performed to investigate how the material responds to the application of a strain level smaller than the maximum strain previously applied. ARHM specimens tested at the 0.5 percent strain level were subjected to additional frequency sweep tests first at 1.0 percent and then again at 0.5 percent. Similarly, the specimens tested at the 1.5 percent strain level were subjected to further testing at the 2.0 percent and then again at 1.5 percent.

Representative selections of these data are shown in Figures 5.2 and 5.3 for ARHM specimens 6 and 17, respectively. The results indicate that when a specimen has already experienced a higher strain level and is then tested at the original strain level, the measured modulus is smaller than before, i.e., the specimen has weakened as a result of the damage. The specimens at the higher strain levels showed more damage than those at the lower levels, i.e., the response at the original strain level was closer to the higher strain level, as shown in Figure 5.3. The data show that if the material has experienced a higher strain than it is currently experiencing, then it will remember this and respond to

additional loading with a reduced modulus. This is essentially damage and is included as the vertical modulus shift.

Based on the observations made from the data, the deviatoric strain norm selected to calculate the shift factors was the maximum strain that had occurred in the time history. As a load is applied, for example the first load, the response of the material will keep changing while the maximum strain increases. When the load is removed, the maximum strain that was achieved is used. The material properties will stay constant at the adjusted values until a new maximum strain was reached from further loading. This is similar to Simo's viscoelastic model with damage.*(60)*

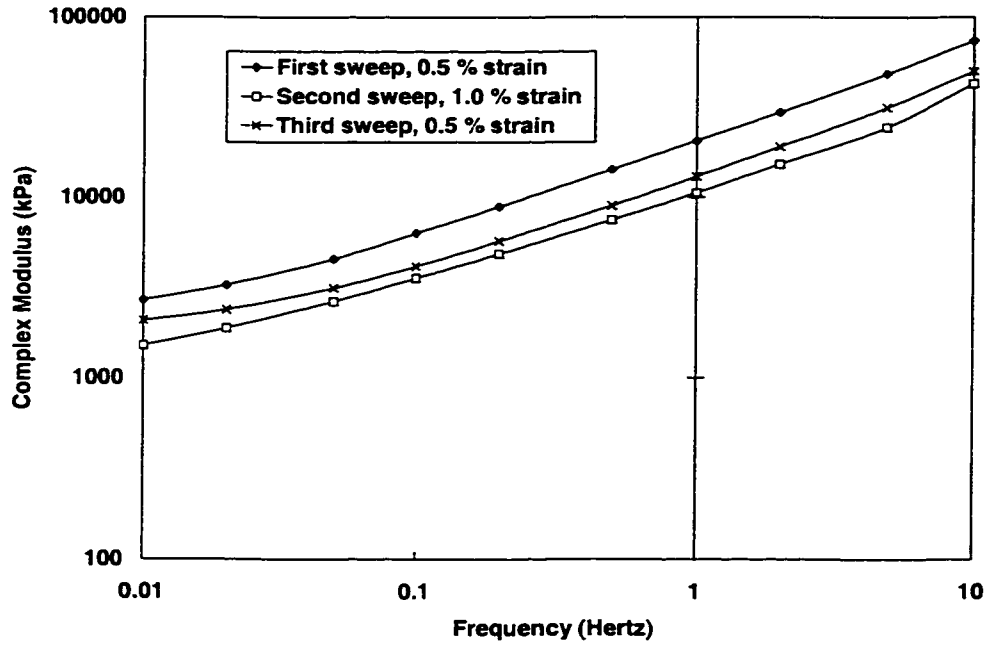

Figure 5.2 Complex Modulus Master Curves from Sequential Frequency Sweep Tests with Strain Levels of 0.5%, 1.0% and 0.5%

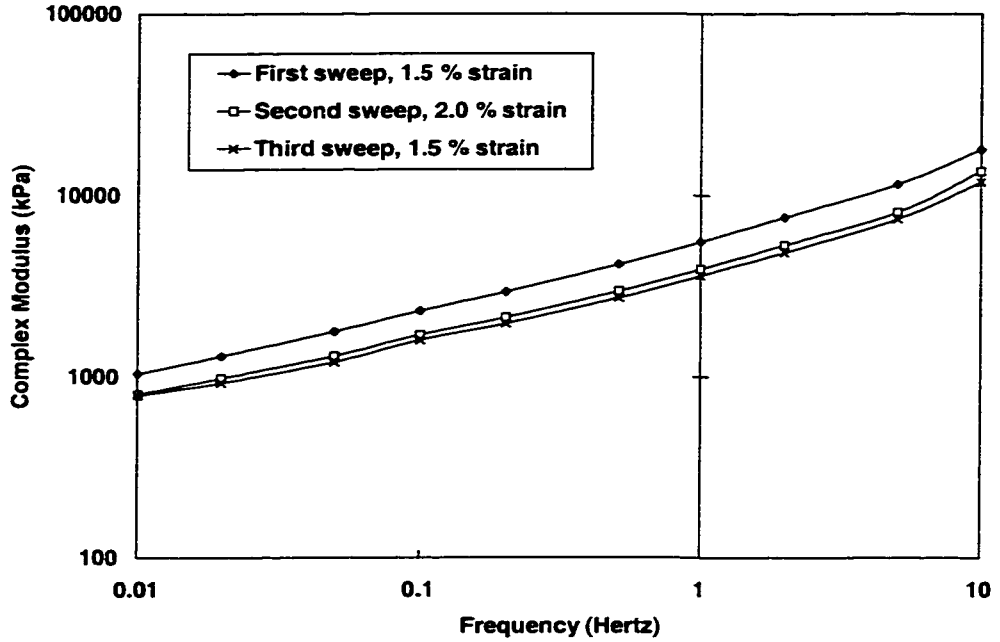

Figure 5.3 Complex Modulus Master Curves from Sequential Frequency Sweep Tests with Strain Levels of 1.5%, 2.0% and 1.5%

It is important to note that the maximum strain, not the maximum load, was used. If a heavy load is applied which increases the maximum strain, a subsequent application of this heavy load will again increase the maximum strain. A pavement that has carried many heavy loads should have more damage, and hence deform more than a pavement that has carried only a few of these heavy loads. For example, if two loads are applied to a pavement at different intervals, the material response, and, thus, the permanent deformation, will differ. This is illustrated in Figures 5.4 and 5.5 where the same load was applied twice, but at different intervals. Figure 5.4 shows the shear stress during loading and recovery. For both loading sequences the shear stress was the same. Figure 5.5 shows the displacement during loading and recovery. The shorter rest period resulted

in higher peak displacements and larger residual deformation. If the material relaxed considerably between loads, then the response of the pavement would be approximately the same for both cases. However, if the loads were applied within short time intervals, more permanent deformation would accumulate in the pavement that carried more of the heavy loads. This behavior is what is expected in asphalt concrete. Therefore, the use of the maximum strain in the time history for calculation of the vertical and horizontal shift factors appears to be a reasonable approach.

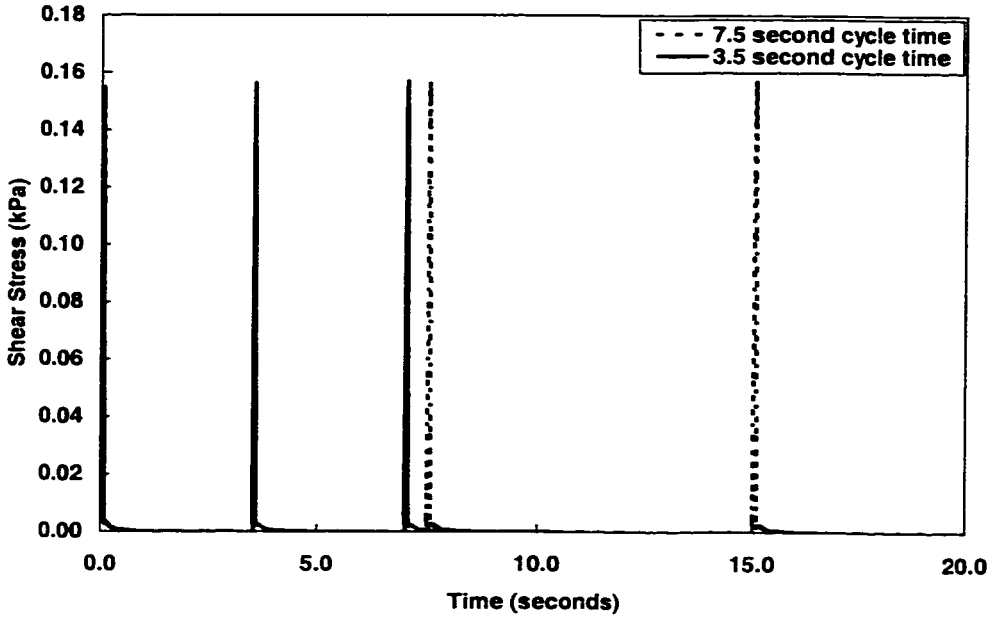

Figure 5.4 Shear Stress versus Time for Loading with Different Rest Periods

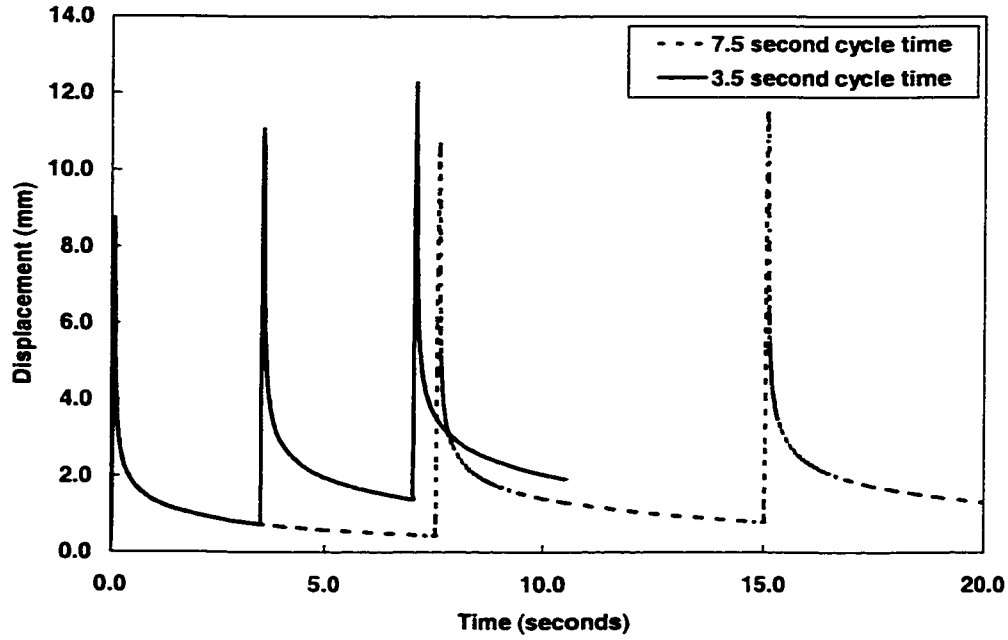

Figure 5.5 Displacement versus Time for Loading with Different Rest Periods

5.2.2.2 Constitutive Relationships for Nonlinear Viscoelastic Model

The horizontal and vertical shift factors, a_H and a_V, were incorporated into the linear viscoelastic shear constitution, as shown in Equations (5.10) to (5.16). Equation (5.10) is the nonlinear equivalent of Equation (5.3). The deviatoric stress, s_i, is defined in Equation (5.11). Using the relaxation function Equation (5.10) reduced to Equation (5.12). The variables used in the equations are defined in Section 5.1. The complete derivation is given in Appendix 2.

$$s(t) = \sum_{i=0}^{M} \left(\int_{-\infty}^{t} e^{\frac{\xi(t,a_H)-\xi(s,a_H)}{\tau_i}} \frac{d}{ds}[s_i(s)]ds \right) \tag{5.10}$$

$$\mathbf{s}_i = \frac{2G_i}{a_V(s)}\mathbf{e}(s) \tag{5.11}$$

$$\mathbf{s}(t) = \int_{-\infty}^{t}\left(2G_\infty + \sum_{i=1}^{M} 2G_i e^{\frac{\xi(t,a_H)-\xi(s,a_H)}{\tau_i}}\right)\frac{d}{ds}\left[\frac{\mathbf{e}(s)}{a_V(s)}\right]ds \tag{5.12}$$

The reduced time, $\xi(t)$, is defined in Equation (5.13), and the horizontal and vertical shift factors, a_H and a_V, are defined in Equations (5.14) and (5.15). All three equations are functions of α, which is defined as the maximum deviatoric strain norm in the time history from $-\infty$ to the current time, t, Equation (5.16).

$$\xi(t) = \int_{-\infty}^{t} \frac{1}{a_H(\alpha(s), T(s))}ds \tag{5.13}$$

$$a_H = 10^{C_{H1}+C_{H2}(T-T_{ref})+C_{H3}\left(\log\frac{10^{-6}+\alpha}{10^{-6}+\|\mathbf{e}_{ref}\|}\right)+C_{H4}(T-T_{ref})\left(\log\frac{10^{-6}+\alpha}{10^{-6}+\|\mathbf{e}_{ref}\|}\right)} \tag{5.14}$$

$$a_V = 10^{C_{V1}+C_{V2}\left(\log\frac{10^{-6}+\alpha}{10^{-6}+\|\mathbf{e}_{ref}\|}\right)+C_{V3}(T-T_{ref})\left(\log\frac{10^{-6}+\alpha}{10^{-6}+\|\mathbf{e}_{ref}\|}\right)} \tag{5.15}$$

$$\alpha = \max_{s\in(-\infty,t]} \|\mathbf{e}(t)\| \tag{5.16}$$

Including the vertical shift factor causes the relaxation function to be dependent on the strain level. In this model, when the material is damaged from loading, the material properties will not return to their original state because the peak strain in the time history determines the material properties. This is reasonable because a pavement that has experienced heavy loads will not deform in the same manner as a new, unloaded or

lightly loaded pavement. This model will also generate more residual strain than a linear viscoelastic model.

5.3 Algorithm Formulation

The time continuous expressions for the nonlinear viscoelastic model derived in the preceding section need to be adapted to an algorithm for implementation in a finite element code. The expressions must be reduced to allow the integrals, and therefore the constitutive relationship, to be evaluated in discrete time steps.

The finite element procedure calculates the stress at the end of a time step, $\boldsymbol{\sigma}(t_{n+1})$, for a given strain, $\boldsymbol{\varepsilon}(t_{n+1})$. The stress is calculated with Equation (5.17)

$$\boldsymbol{\sigma}(t_{n+1}) = p(t_{n+1})\mathbf{1} + \mathbf{s}(t_{n+1}) \tag{5.17}$$

where $p(t_{n+1})$ is the hydrostatic pressure, $\mathbf{s}(t_{n+1})$ the deviatoric stress at t_{n+1}, and $\mathbf{1}$ the second rank identity. This is the discrete equivalent of the time continuous expression in Equation (5.1). The response of viscoelastic materials, because of the viscous effects, depends on the time and loading history of the material. At the end of each time step, the current state of the material is stored in history variables, for use in the next time step. This allows the complete history to be included without recalculating all the previous solutions at each time step.

This section presents the expressions for calculating the terms in Equation (5.17) and discusses the assumptions used in the derivation. The volumetric component is discussed first, followed by the deviatoric component, and, finally, the consistent tangent. The complete derivation is given in Appendix 2.

5.3.1 Algorithm for Volumetric (Bulk) Component

The algorithm for the bulk component of the model was determined from the time continuous constitution, Equations (5.7), (5.8) and (5.9). The bulk stress, $p(t_{n+1})$, is shown in Equation (5.18)

$$p(t_{n+1}) = K_\infty \theta(t_{n+1}) + \sum_{i=1}^{n} K_i q(t_{n+1})_i \tag{5.18}$$

where K_∞ and K_i are the bulk moduli of the free spring and the i^{th} Maxwell element spring, θ_{n+1} is the trace of the strain, $\mathrm{tr}(\varepsilon(t_{n+1}))$, n is the number of Maxwell elements, and $q(t_{n+1})_i$ is the history term for the i^{th} Maxwell element evaluated at time t_{n+1}. This history variable was calculated with Equation (5.19)

$$q(t_{n+1})_i = e^{-\frac{\Delta\chi}{\lambda_i}} q(t_n)_i + \Delta\theta \left(\frac{\lambda_i}{\Delta\chi}\right)\left(1 - e^{-\frac{\Delta\chi}{\lambda_i}}\right) \tag{5.19}$$

where $q(t_n)_i$ is the history evaluated at the beginning of the time step for the i^{th} Maxwell element, λ_i is the corresponding relaxation time, $\Delta\theta$ is the change in bulk stress in the time step, and $\Delta\chi$ is the change in the reduced time. At the beginning of a simulation, t_0,

it was assumed that the material is stress and strain free, and therefore $q(t_0)_i$ equals zero. The history term was derived using the Taylor, Pister and Goudreau recursion where the rate of change of strain in a time step is assumed constant.*(66)* This allowed the integral from Equation (5.8) to be evaluated. The derivation is contained in Appendix 2. The change in reduced time, $\Delta\chi$, is shown in Equation (5.20)

$$\Delta\chi = \frac{\Delta t}{2}\left[\frac{1}{a_T(T(t_{n+1}))} + \frac{1}{a_T(T(t_n))}\right] \tag{5.20}$$

where a_T is the shift factor calculated for the temperatures at the beginning and end of the time step. Equation (5.20) approximates the integral in Equation (5.7) using the trapezoidal rule. For the bulk response, the shift factor was calculated using the WLF equation, Equation (5.21)

$$a_T = 10^{\left[\frac{-C_{T1}(T-T_{ref})}{C_{T2}+T-T_{ref}}\right]} \tag{5.21}$$

where C_{T1} and C_{T2} are constants, and T and T_{ref} are the temperatures at the applicable time and the reference temperature, respectively. Using Equations (5.18) to (5.21), the pressure, $p(t_{n+1})$, is calculated.

5.3.2 Algorithm for Deviatoric (Shear) Component

The algorithm for the deviatoric component was developed in the same manner as the bulk component, with the additional inclusion of the vertical shift factor and the modified horizontal shift factor. The complete derivation is included in Appendix 2.

As discussed earlier, the deviatoric strain norm used to calculate the vertical and horizontal shift factors in the shear component was the maximum strain that has occurred in the time history. When a load is increasing, resulting in a strain that exceeds the previous maximum, the new maximum strain will constantly increase as the load is applied and therefore equals the current strain. In the discrete constitutive relationships the strain used to calculate the shift factors is the maximum of the deviatoric strain norm that has occurred up until the beginning of the time step, i.e., $\|\mathbf{e}(t_n)\|$. During the time step, Δt, the maximum strain may be increasing, but the model still uses the maximum at time t_n, the beginning of the time step. This choice is justified below. It is important to note that this is only an issue when the maximum strain is increasing. When a load is removed, or a load resulting in a smaller strain than previously experienced is applied, the maximum strain remains constant and therefore the material properties remain constant.

The justification for using $\|\mathbf{e}(t_n)\|$ not $\|\mathbf{e}(t_{n+1})\|$ is that during a time step of a reasonable size for accuracy considerations, the difference will be small. The driving reason for this

assumption is that it considerably simplifies the implementation of the model if variables are not dependent on the current time, t_{n+1}. This assumption is not conservative: $\|\mathbf{e}(t_n)\|$ is smaller than $\|\mathbf{e}(t_{n+1})\|$ when the load is increasing, and therefore the moduli at t_n are larger than at t_{n+1}, resulting in less deformation. However, because the time steps used in any simulation are relatively small, the difference in results between using $\|\mathbf{e}(t_n)\|$ or $\|\mathbf{e}(t_{n+1})\|$ are small. In addition, the algorithmically simpler approach will still allow observations to be drawn about permanent deformation prediction using this nonlinear viscoelastic model. Modifications, such as using $\|\mathbf{e}_{n+1}\|$ rather than $\|\mathbf{e}_n\|$ or some combination of both, can be made in future work. It is not anticipated that such changes would result in observations different from those discussed in this work.

The derivation in Appendix 2 arrives at Equation (5.22) for the deviatoric stress at the end of the time step, $\mathbf{s}(t_{n+1})$, from the time continuous expressions, Equations (5.10) to (5.16).

$$\mathbf{s}(t_{n+1}) = \mathbf{h}(t_{n+1})_\infty + \sum_{i=1}^{m} \mathbf{h}(t_{n+1})_i \tag{5.22}$$

In this equation $\mathbf{h}(t_{n+1})_\infty$ and $\mathbf{h}(t_{n+1})_i$ are the tensorial history terms for the free spring and the i^{th} Maxwell element, respectively, calculated at the end of the time step. These history terms are calculated with Equations (5.23) and (5.24) using the history terms at the beginning of the time step, $\mathbf{h}(t_n)_\infty$ and $\mathbf{h}(t_n)_i$, the relaxation times, τ_i, the deviatoric

strain at the beginning and end of the time step, $\mathbf{e}_n$ and $\mathbf{e}_{n+1}$, and, the change in the reduced time, $\Delta\xi$.

$$\mathbf{h}(t_{n+1})_\infty = e^{-\frac{\Delta\xi}{\tau_1}}\mathbf{h}(t_n)_\infty + 2G_\infty\left(\frac{\mathbf{e}(t_{n+1})}{a_V(t_n)} - \frac{\mathbf{e}_n(t_n)}{a_V(t_{n-1})}\right) \tag{5.23}$$

$$\mathbf{h}(t_{n+1})_i = e^{-\frac{\Delta\xi}{\tau_1}}\mathbf{h}(t_n)_i + 2G_i\left(\frac{\mathbf{e}(t_{n+1})}{a_V(t_n)} - \frac{\mathbf{e}_n(t_n)}{a_V(t_{n-1})}\right)\left(\frac{\tau_i}{\Delta\xi}\right)\left(1-e^{-\frac{\Delta\xi}{\tau_1}}\right) \tag{5.24}$$

In these equations $a_V(t_n)$ and $a_V(t_{n-1})$ are the vertical shift factors evaluated at time t_n and t_{n-1}, respectively, G_∞ and G_i are the shear relaxation moduli of the free and the i^{th} shear Maxwell element springs. The history term, $\mathbf{h}(t_n)_i$, was again assumed to equal zero in the first time step.

The change in reduced time, $\Delta\xi$, is defined in Equation (5.25)

$$\Delta\xi = \Delta t\left(\frac{1}{a_H(t_n)} + \frac{1}{a_H(t_{n-1})}\right) \tag{5.25}$$

where the time step, Δt, equals $t_{n+1} - t_n$, $a_H(t_n)$ and is the horizontal shift factor at the beginning of the time step, and $a_H(t_{n-1})$ is the horizontal shift factor at the beginning of the previous time step. The horizontal, a_H, and vertical, a_V, shift factors are shown in Equations (5.26) and (5.27), respectively

$$a_H = 10^{\left[C_{H1}+C_{H2}(T-Tref)+C_{H3}\left(\log\frac{10^{-6}+\alpha}{10^{-6}+\|e_{ref}\|}\right)+C_{H4}(T-Tref)\left(\log\frac{10^{-6}+\alpha}{10^{-6}+\|e_{ref}\|}\right)\right]} \tag{5.26}$$

$$a_V = 10^{\left[C_{V1}+C_{V2}\left(\log\frac{10^{-6}+\alpha}{10^{-6}+\|e_{ref}\|}\right)+C_{V3}(T-T_{ref})\left(\log\frac{10^{-6}+\alpha}{10^{-6}+\|e_{ref}\|}\right)\right]} \tag{5.27}$$

where C_{H1} to C_{H4} and C_{V1} to C_{V3} are constants, T is the temperature at time t_n, T_{ref} the reference temperature, $\|\mathbf{e}_{ref}\|$ the reference deviatoric strain norm, and α the maximum strain at the beginning of the step, as shown in (5.28).

$$\alpha = \max_{s\in(-\infty,t_n]} \|\mathbf{e}(s_n)\| \tag{5.28}$$

The temperature is typically maintained constant during simulations of a pavement, thus the use of the temperature at the beginning of the time step rather than the current temperature has no effect on the solution.

Using the equations presented in this section, the deviatoric stress at t_{n+1}, $\mathbf{s}(t_{n+1})$, can be calculated. With the deviatoric stress and the volumetric stress, $p(t_{n+1})$, the stress, $\boldsymbol{\sigma}(t_{n+1})$ is calculated using Equation (5.17), completing the constitutive model.

5.3.3 Consistent Tangent

The consistent tangent is the linearized moduli and is necessary to ensure a quadratic rate of convergence in Newton's method, which is used in the finite element method to converge to the solution.*(60)* The consistent tangent, **C**, is the partial derivative of the

stress with respect to the strain, as shown in Equation (5.29), where the variables are the same as defined earlier. $\mathbf{C}$ is a rank four tensor.

$$\mathbf{C} = \frac{\partial \boldsymbol{\sigma}(t_{n+1})}{\partial \boldsymbol{\varepsilon}(t_{n+1})} = \frac{\partial \mathbf{s}(t_{n+1})}{\partial \boldsymbol{\varepsilon}(t_{n+1})} + \frac{\partial p(t_{n+1})}{\partial \boldsymbol{\varepsilon}(t_{n+1})}\mathbf{1} \tag{5.29}$$

Equations (5.30) and (5.31) give the volumetric and deviatoric terms used to evaluate Equation (5.29). The derivation of these terms is given in Appendix 2.

$$\frac{\partial p(t_{n+1})}{\partial \boldsymbol{\varepsilon}(t_{n+1})}\mathbf{1} = \left[K_\infty + \sum_{i=1}^{n} K_i \left(1 - e^{-\frac{\Delta\chi}{\lambda_i}} \right) \left(\frac{\lambda_i}{\Delta\chi} \right) \right] \mathbf{1} \otimes \mathbf{1} \tag{5.30}$$

$$\frac{\partial \mathbf{s}(t_{n+1})}{\partial \boldsymbol{\varepsilon}(t_{n+1})} = \frac{1}{a_V(t_n)} \left[2G_\infty + \sum_{i=1}^{m} 2G_i \left(1 - e^{-\frac{\Delta\xi}{\tau_i}} \right) \left(\frac{\tau_i}{\Delta\xi} \right) \right] \mathbf{I}_{dev} \tag{5.31}$$

In these equations $\mathbf{1} \otimes \mathbf{1}$ is the rank four tensor product of the rank two identity, $\mathbf{1}$, and $\mathbf{I}_{dev}$ is the rank four deviatoric identity. For this nonlinear viscoelastic model the consistent tangent is symmetric.

5.3.4 Implementation

The algorithm is implemented in a finite element code, FEAP.*(67)* Up to 15 Maxwell elements each can be used for the shear and volumetric response. The smaller the number of Maxwell elements, the faster the solution time. Only the number of Maxwell elements actually specified in the input were included in the computations. A fairly large number of elements were sometimes necessary to completely characterize the material, and

because small time steps were necessary to precisely apply a load wave form and accurately calculate the solution, the simulations were often very time consuming. In addition, for each Maxwell element a history term was stored. This history term is a scalar for the bulk and a tensor for the shear elements. For a large number of Maxwell elements this was a substantial amount of stored history terms, which further slowed the solution time.

The model passed all forms of the patch test, and converged in two iterations, as expected for a closed form solution.*(68)*

In application of the intrinsic time, a temperature or strain change instantaneously changes the reduced time. It is necessary to ensure that within a time step, changes in the strain rate are not large. Therefore, the time steps should be small to maintain the accuracy of the results.*(65)* Temperature changes in pavement simulations are very slow compared to loading changes and are therefore constant, or approximately constant, during a time step. The strains however, do change fairly rapidly. Thus, it is still important to use small time steps. This is especially important in the first load cycle because the strains and, therefore, the shift factors and material properties are changing rapidly during each time step and an error will accumulate. This has the potential to greatly effect the accuracy of the final solution. In later load cycles, the history terms do

not change as significantly as in the first load cycle and, hence, the solution is not as sensitive to the time step duration.

5.4 Material Properties

The final step before finite element simulations could be run with the nonlinear viscoelastic model was to obtain the material properties. A classical approach was used to obtain the viscoelastic properties for the relaxation function from the master curves developed in Chapter 4 using the laboratory test data.*(48, 52, 53)*

Direct determination of the relaxation function from relaxation tests on asphalt concrete is difficult. However, the relaxation function can also be evaluated from frequency sweep data using the storage and loss moduli master curves. The shear storage (G') and loss (G") moduli can be represented as functions of the shear relaxation moduli (G_i), relaxation times (τ_i) and frequency (ω in radians/second) for each Maxwell element, as shown in Equations (5.32) and (5.33).*(48)* The bulk storage (K') and loss (K") are described with similar expressions.

$$G' = G_\infty + \sum_{i=1}^{m} G_i \frac{(\omega\tau_i)^2}{1+(\omega\tau_i)^2} \tag{5.32}$$

$$G'' = \sum_{i=1}^{m} G_i \frac{\omega\tau_i}{1+(\omega\tau_i)^2} \tag{5.33}$$

The master curve data were fit to these equations, and the fitted number of Maxwell elements, relaxation times and moduli were used in the relaxation function, Equation (5.5). Various methods of fitting the data are discussed in the literature. Some of them do not result in the best mathematical fit, but give a good physical fit, and therefore the fitted parameters are more likely to approach the intrinsic material properties.*(48, 52, 53, 69, 70)*

The simplest method of determining the relaxation times and moduli is to select a number of Maxwell elements, fix the relaxation times, typically using one or two times per decade, and solve for the relaxation moduli using either Equation (5.32) or (5.33) with linear regression. Unfortunately, this problem is ill posed and can give negative values for some relaxation moduli, which are not physically possible. The solution is dependent on the assumed relaxation times and number of Maxwell elements. In addition, typically either Equation (5.32) or Equation (5.33) is used, ignoring the other data. When the storage and loss moduli are fit independently, the fitted parameters often differ.

As a consequence of the simple linear fit not providing a good fit for the relaxation function, other methods of fitting the data have been developed, for example, Baumgaertel and Winter *(69)*, Emri and Tshoegl *(70)*, and Simhambhatla and Leonov *(71)*. These methods typically use a non-linear fit to obtain both the relaxation times and

moduli and ensure the values are physically feasible. Some of these methods also calculate the optimum number of Maxwell elements.

The method selected to determine the relaxation function was that of Baumgaertel and Winter.*(69)* In this method the number of Maxwell elements is assumed, and the shear relaxation moduli and relaxation times are determined by minimizing the sum of the squares of the ratio of the calculated and measured storage and loss moduli, as shown in Equation (5.34)

$$\min \sum_{j=1}^{k} \left(\left[\frac{G'(\omega_j)_{calculated}}{G'(\omega_j)_{measured}} - 1 \right]^2 + \left[\frac{G''(\omega_j)_{calculated}}{G''(\omega_j)_{measured}} - 1 \right]^2 \right) \tag{5.34}$$

where k is the number of data points, ω_j the frequency, $G'(\omega_j)_{calculated}$ and $G''(\omega_j)_{calculated}$ the storage and loss moduli calculated using Equations (5.32) and (5.33), and $G'(\omega_j)_{measured}$ and $G''(\omega_j)_{measured}$ the laboratory test data. The advantage of this method is that it is relatively simple and simultaneously uses both the storage and loss moduli data.

The Matlab optimization toolkit software *(72)* was used to perform the curve fitting. The optimum fits for the master curves were obtained in an iterative process. The first step fixed the relaxation times and fitted the relaxation moduli; this is termed the "linear fit". The second step used the solution to the linear fit as the input for the "nonlinear fit", in which both the relaxation times and moduli are fit. The relaxation moduli, G_i or K_i were constrained to be non-negative. The solution procedure found an optimal solution in the

linear problem, but the nonlinear solution is frequently at a local minimum. The nonlinear solution is also dependent on the initial conditions; hence, the linear fit was used for the initial conditions in the nonlinear fit. The nonlinear fit was repeated using the previous solution as the initial conditions until the solution converges.

In the first iteration, a large number of Maxwell elements were assumed, typically 15. For the linear fit, at least one relaxation time per decade was selected. The range of relaxation times spans the frequency range of the master curve. Once the nonlinear solution has ran a few times and the solution converged, some of the relaxation moduli were very small, which indicated that the particular Maxwell element was not significantly contributing to the solution, and could be eliminated. In addition, some relaxation times were close in value and could be combined into one element. In the finite element implementation of the viscoelastic model, the smaller the number of Maxwell elements, the faster, and therefore more efficient, the computations. It was therefore optimal to use the minimum number of Maxwell elements, while still providing a sufficiently good fit. The process of determining the relaxation times and moduli for the assumed number of Maxwell elements was repeated iteratively, reducing the number of elements until each Maxwell element had a distinct relaxation time and a significant relaxation modulus. By beginning the process with a large number of Maxwell elements, it was assured that enough elements were used in the final solution and the initial values covered the range of possible relaxation times.

5.4.1 Shear Master Curves and Relaxation Function Parameters

The procedure described above was used to fit the shear relaxation function using the manually shifted master curve data shown in Figures 4.17 and 4.18 for the DGAC and Figures 4.19 and 4.20 for the ARHM. The manually shifted curves lie within the range of the curves shifted with the shift factor functions (Figures 4.25, 4.26, 4.31 and 4.32).

5.4.1.1 Dense Graded Asphalt Concrete, DGAC

The first attempt to fit the shear relaxation times and moduli of the DGAC resulted in a zero value for the free spring, G_∞, i.e., the asphalt concrete was a viscous liquid. A second fit was done in which the modulus of the free spring was fixed to ensure the material was modeled as a solid. The fixed value for G_∞ was determined by extrapolating the storage modulus data to estimate the asymptotic value of these data at the lower frequencies. From the data, shown in Figure 4.25, a value of $G_\infty = 3200$ kPa was chosen. The justification for using a solid, rather than a viscous liquid is discussed after the results are presented.

Figures 5.6 and 5.7 show the original master curves and the master curves created with the fitted shear relaxation times and moduli. When $G_\infty = 0$, ten Maxwell elements were used, whereas when G_∞ was fixed, eleven were used. The values for the shear relaxation

times and moduli are provided in Table 5.1 and are plotted in Figure 5.8, which shows the range of relaxation times.

The storage modulus master curves have better fits than the loss modulus master curves, especially at the higher frequencies. The fit to both the storage and the loss master curves is not as good when below approximately 5 radians per second. However, at all frequencies the fit is adequate, given the inherent variability in the data, as discussed in Chapter 3 and Appendix 1. Figures 5.9 and 5.10 show the same fitted master curves and the laboratory test data shifted using the shift factor functions. The curves are within the range of the laboratory data, except at the extremes, indicating the reasonableness of the fitted relaxation times and moduli.

Table 5.1 Shear Relaxation Times and Relaxation Moduli, DGAC and ARHM

	DGAC Liquid		DGAC Solid		ARHM Solid	
Element Number	Relaxation Time, τ (seconds)	Shear Modulus, G (kPa)	Relaxation Time, τ (seconds)	Shear Modulus, G (kPa)	Relaxation Time, τ (seconds)	Shear Modulus, G (kPa)
Free spring		0		3200		3400
1	1.274×10^{-5}	3627709	9.710×10^{-6}	4551036	1.793×10^{-5}	2126725
2	2.322×10^{-4}	574413	2.291×10^{-4}	624692	4.352×10^{-4}	290999
3	8.069×10^{-4}	317880	8.332×10^{-4}	295963	3.010×10^{-3}	135043
4	4.053×10^{-3}	184469	4.049×10^{-3}	194985	1.208×10^{-2}	49295
5	1.56×10^{-2}	97085	1.691×10^{-2}	90452	6.160×10^{-2}	30308
6	8.966×10^{-2}	31358	7.346×10^{-2}	26656	7.664×10^{-1}	5301
7	8.960×10^{-1}	5733	3.048×10^{-1}	8016	1.594×10^{1}	954
8	1.322×10^{1}	2654	1.661	2366	7.480×10^{1}	969
9	1.234×10^{2}	1744	7.664	1307	4.261×10^{2}	868
10	1.690×10^{3}	3159	3.368×10^{1}	1567		
11			3.441×10^{2}	1900		

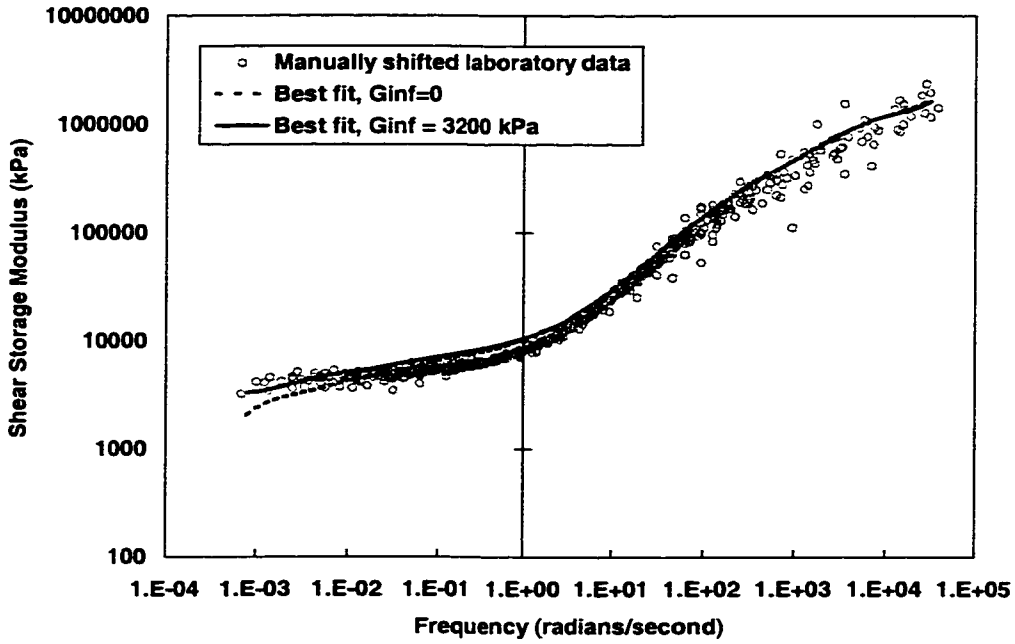

Figure 5.6 **Shear Storage Modulus Master Curve, Input Data and Best Fit, DGAC**

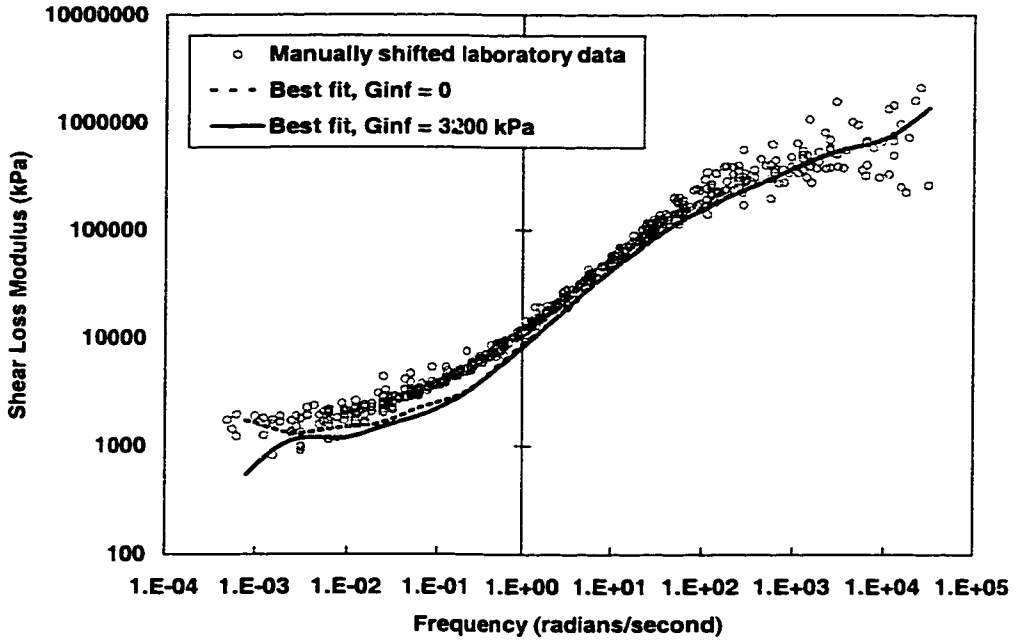

Figure 5.7 **Shear Loss Modulus Master Curve, Input Data and Best Fit, DGAC**

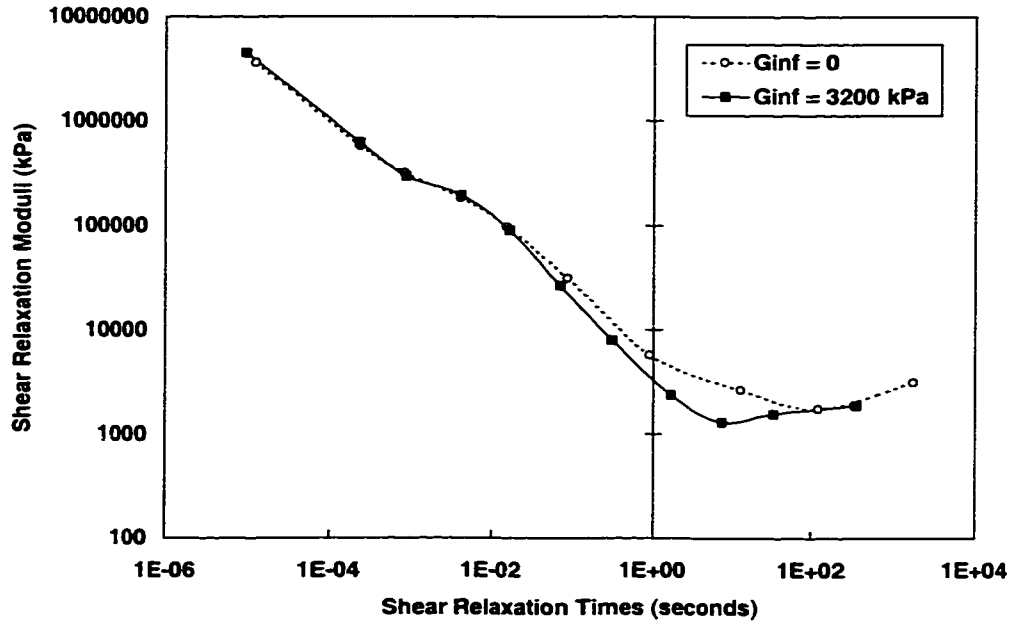

Figure 5.8 Shear Relaxation Times and Relaxation Moduli, DGAC

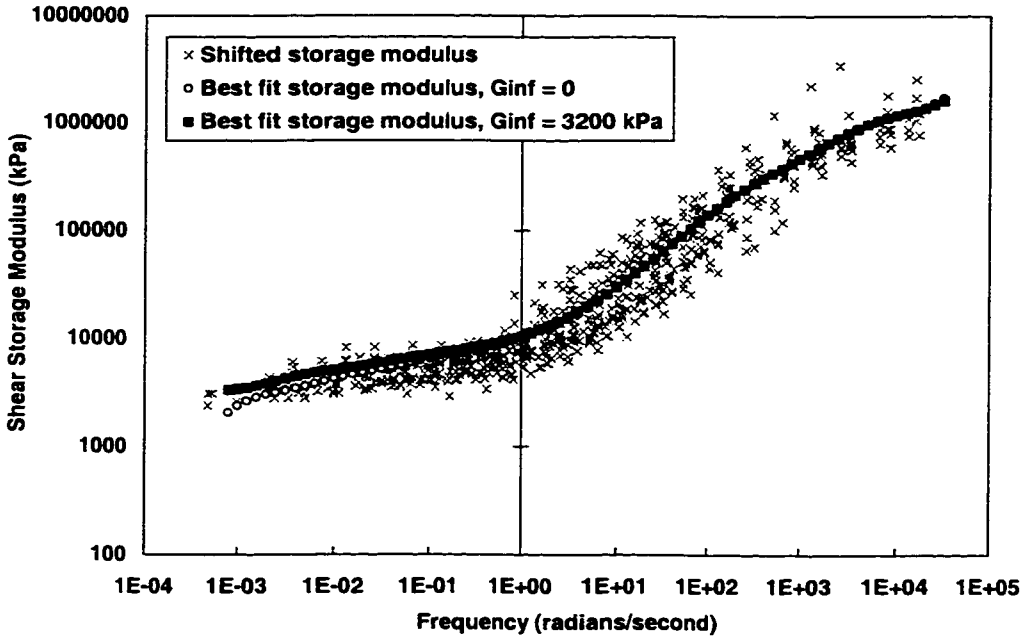

Figure 5.9 Shear Storage Modulus Master Curves, Best Fit and Data Shifted with Shift Factor Functions, DGAC

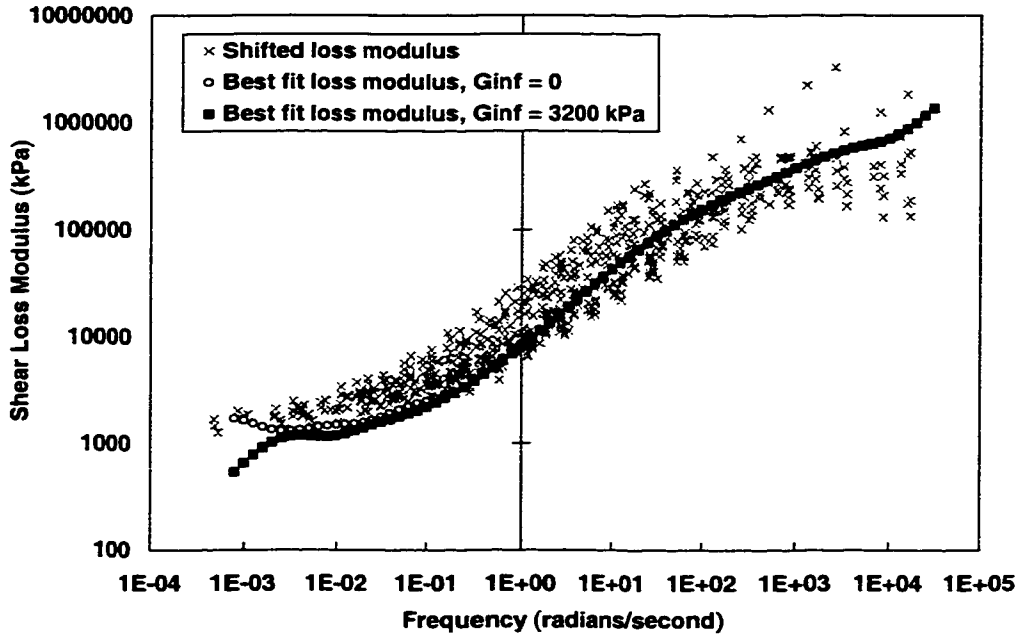

Figure 5.10 Shear Loss Modulus Master Curves, Best Fit and Data Shifted with Shift Factor Functions, DGAC

The difference between the liquid ($G_\infty = 0$) and solid ($G_\infty = 3200$ kPa) fits is apparent at the lower frequencies. Figure 5.11 shows the same storage and loss moduli fits and the complex modulus (defined in Equation (4.20)) master curve for a wide frequency range. When $G_\infty = 0$, the storage and complex modulus curves drop off dramatically below a frequency of approximately $1x10^{-3}$ radians per second. Although there is no laboratory data at or below this frequency, the dramatic drop in the moduli values is not reasonable. The drop off was not anticipated because the laboratory data appear to be flattening off at the lower frequencies. The master curves for the G_∞=3200 kPa were therefore more reasonable, because the master curves are asymptotic to the G_∞ value at the lower

frequencies. The shear relaxation times and moduli from the 11 element, G_∞=3200 kPa case are therefore used in the model implementation. This is another example of the need to interpret the mathematical fit, and ensure the solution is physically reasonable.

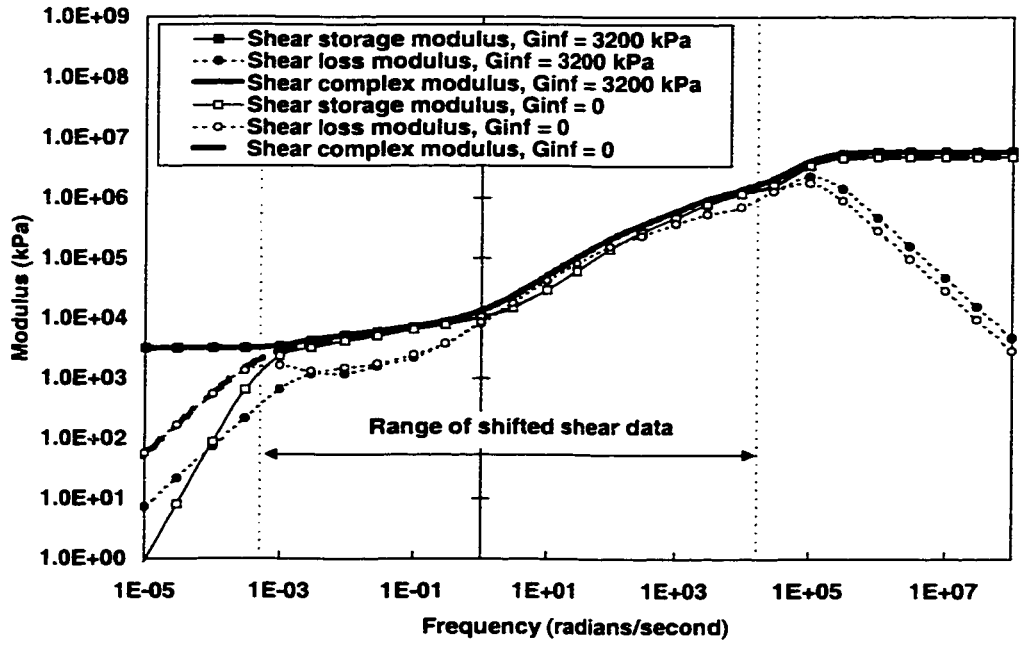

Figure 5.11 Comparison of Shear Master Curves for $G_\infty = 0$ and $G_\infty = 3200$ kPa, DGAC

Figures 5.12 and 5.13, for G_∞=3200 kPa, show how the Maxwell elements sum up to produce the storage, loss, and complex modulus master curves. Each curve shows the master curve for the particular Maxwell element. The sum of all the elements gives the combined master curve, Equations (5.32), (5.33) and (4.20). These figures demonstrate why a sufficient number of Maxwell elements are necessary, and that the range of relaxation times should span the data range. The figures also show the sudden drop off of

the loss modulus master curve below a frequency of 2.906 x 10^{-3} radians per second, which corresponds to the longest relaxation time, 3.441 x 10^{2} seconds. Without the inclusion of a value for G_∞ the storage modulus would also drop off below the longest relaxation time.

5.4.1.2 Asphalt-Rubber Hot Mix, ARHM

The fitted ARHM master curves have 9 Maxwell elements and assume a free spring shear modulus of G_∞=3400 kPa. The fitted shear relaxation times and shear moduli are given in Table 5.1 and Figure 5.14. The manually shifted and fitted master curves for the ARHM are shown in Figures 5.15 and 5.16 for the storage and loss moduli, respectively, and in Figure 5.17 for the complex modulus.

While the storage modulus fit was good, the loss modulus fit below 1 radian per second (1 second relaxation time) showed considerable deviation from the input data. This was the best fit that could be obtained with the method described in Section 5.1, despite using many iterations and different initial conditions. Given the relatively good fit of the complex modulus, Figure 5.17, the fitted relaxation times and shear moduli were adequate for use in implementation.

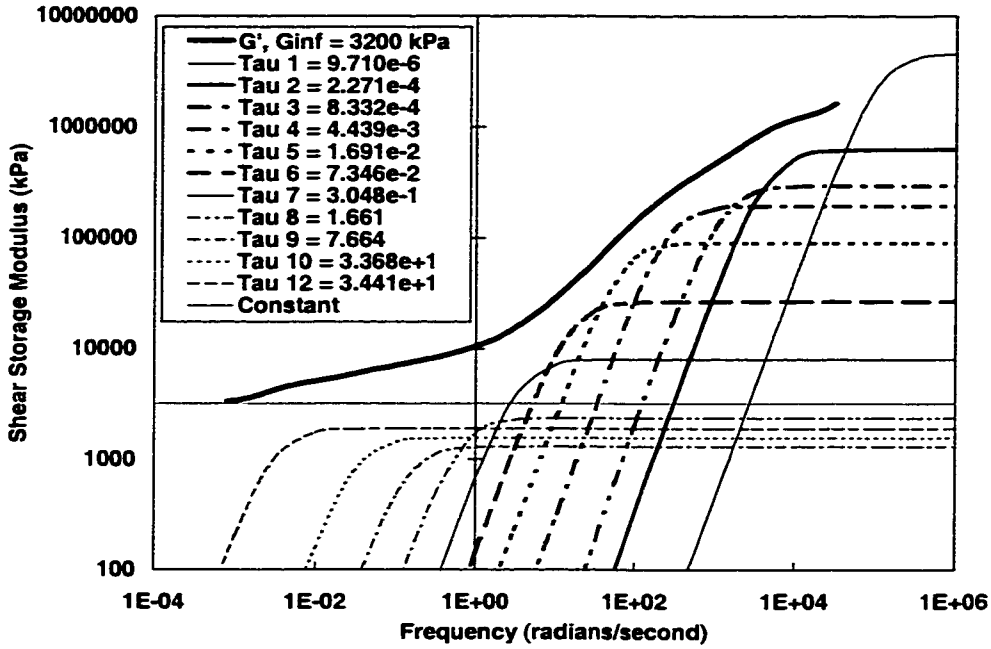

Figure 5.12 Contribution of Each Maxwell Element to the Shear Storage Modulus Master Curve

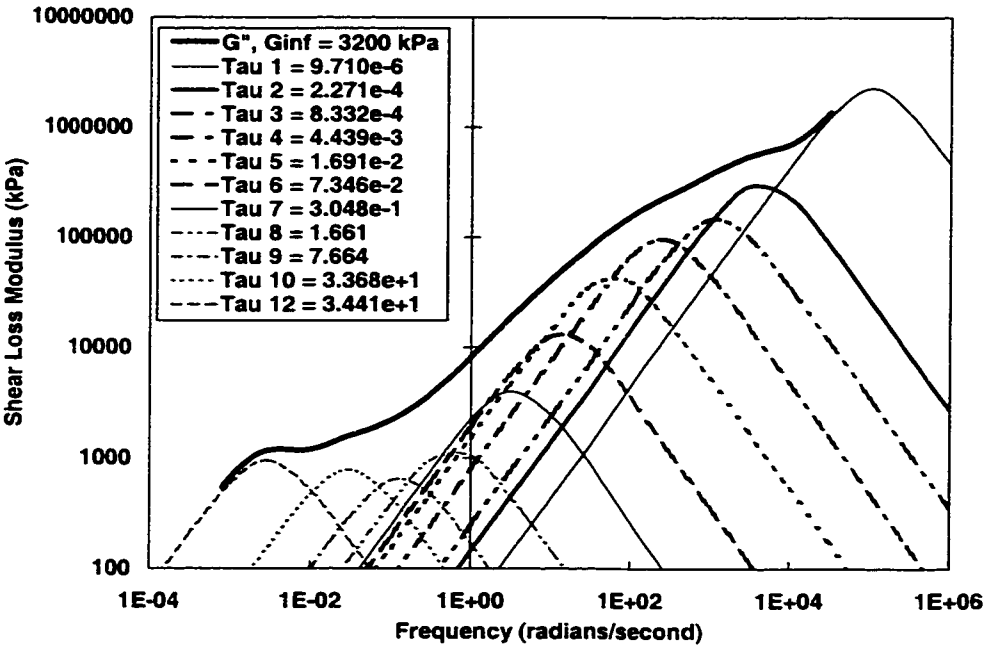

Figure 5.13 Contribution of Each Maxwell Element to the Shear Loss Modulus Master Curve

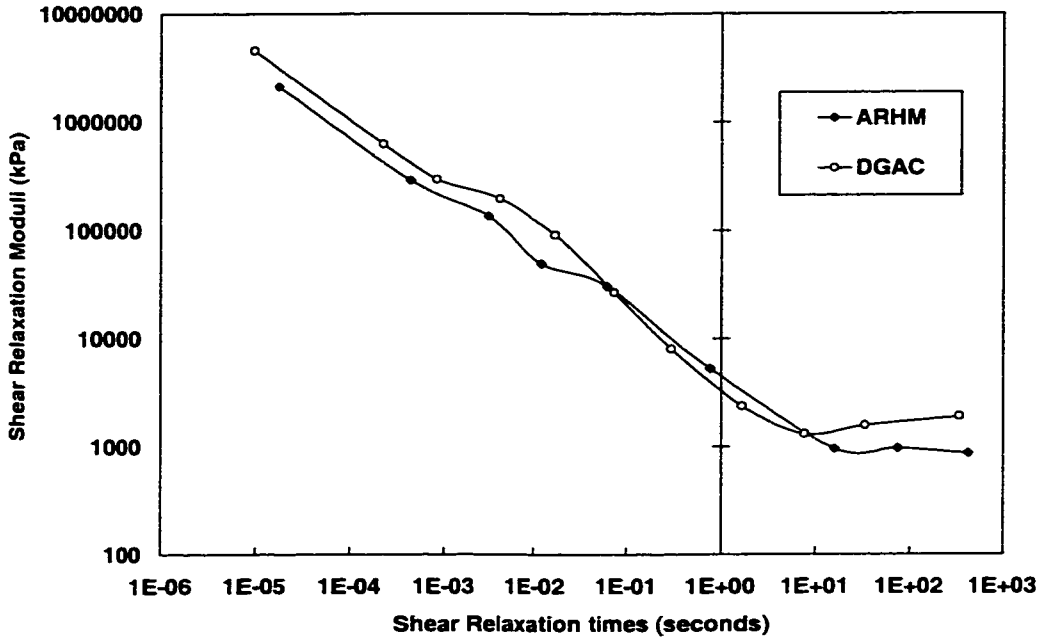

Figure 5.14 Shear Relaxation Times and Relaxation Moduli, ARHM

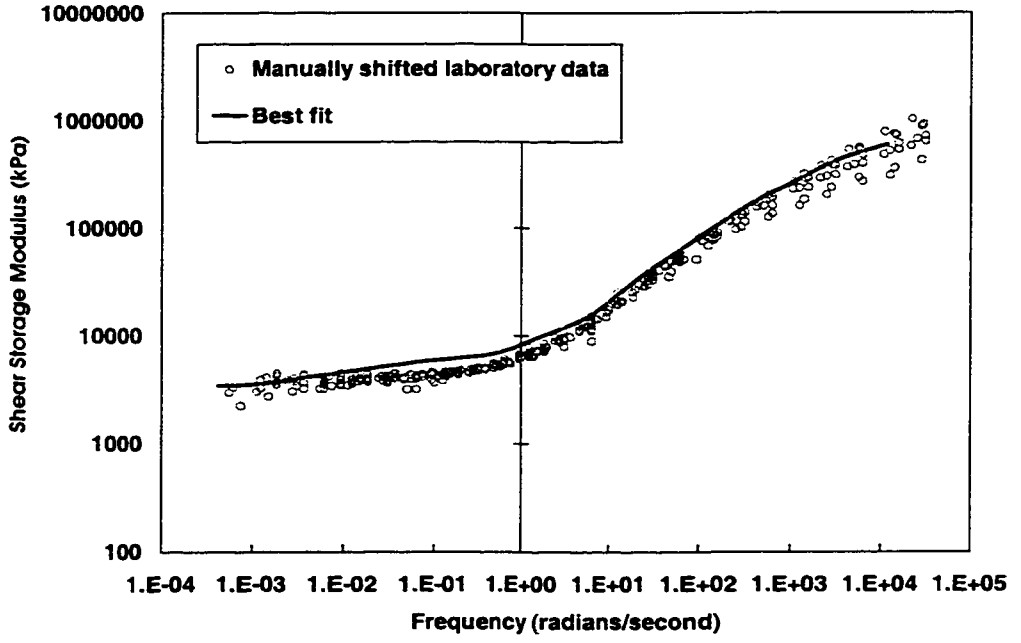

Figure 5.15 Shear Storage Modulus Master Curve, Input Data and Best Fit, ARHM

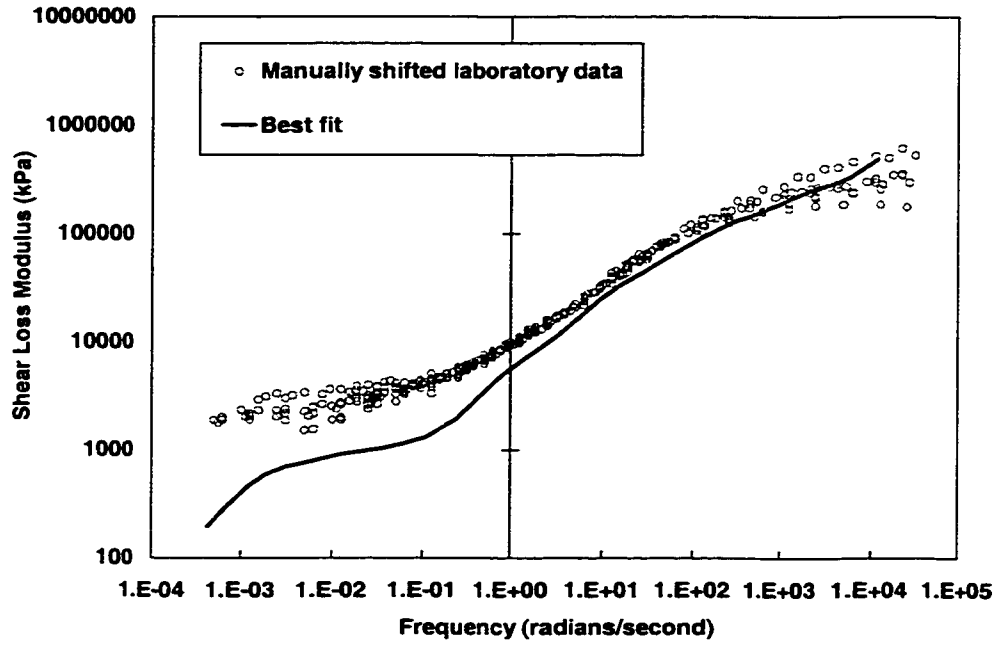

Figure 5.16 Shear Loss Modulus Master Curve, Input Data and Best Fit, ARHM

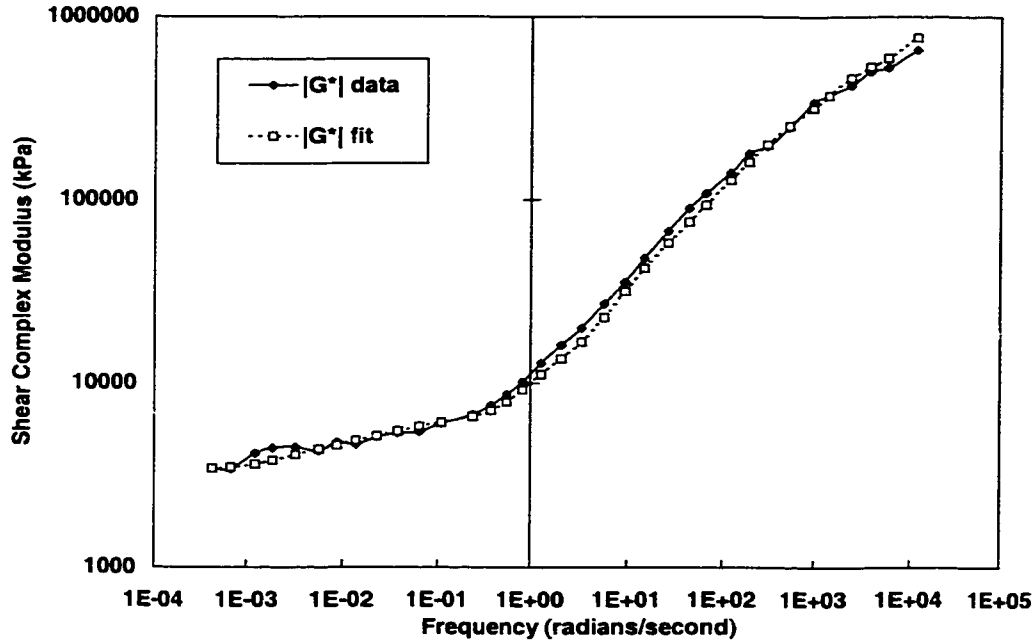

Figure 5.17 Shear Complex Modulus Master Curve, Input Data and Best Fit, ARHM

5.4.2 Volumetric Master Curves and Relaxation Function Parameters

The volumetric (bulk) modulus master curves created in Chapter 4 were used to fit the material properties for the linear viscoelastic volumetric model. The loss modulus data have a maximum frequency of approximately 2 x 10^4 radians per second, whereas the maximum frequency for the storage modulus data is 10^7 radians per second. To take advantage of the higher frequency data for the storage modulus, the loss modulus data were extrapolated above 10^4 radians per second. The original data and the input data used are shown in Figures 5.18 and 5.19 for the storage and loss moduli, respectively. The fitted master curves are also shown in the Figures. The volumetric relaxation times and moduli are given in Table 5.2 and Figure 5.20. Eight Maxwell elements were used to fit the master curves. A value was fit for the K_∞ term during the fitting procedure without being fixed.

Table 5.2 Volumetric Relaxation Times and Relaxation Moduli

	Hollow Cylinder DGAC	
Element	**Relaxation Time, λ (seconds)**	**Volumetric Modulus, K (kPa)**
Free Spring		47616
1	9.000×10^{-8}	130947592
2	9.380×10^{-6}	3997524
3	9.9240×10^{-5}	3478408
4	9.3034×10^{-4}	1950310
5	6.2856×10^{-3}	1371006
6	3.5866×10^{-2}	514958
7	6.1809×10^{-1}	61349
8	1.1986×10^{1}	25551

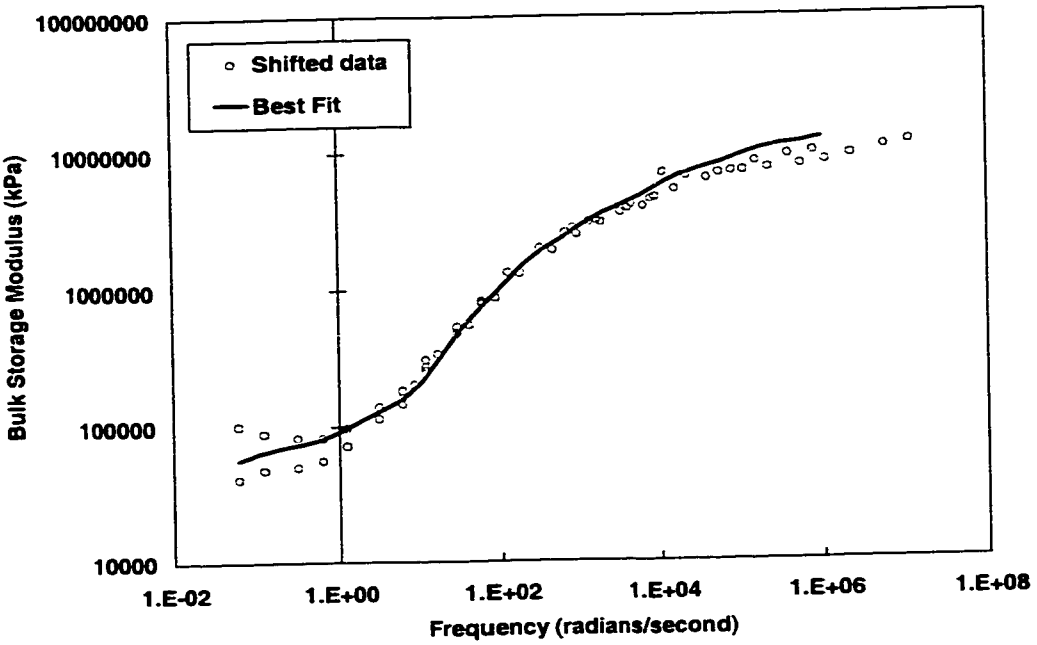

Figure 5.18 Volumetric Storage Modulus Master Curves, Best Fit and Original Data

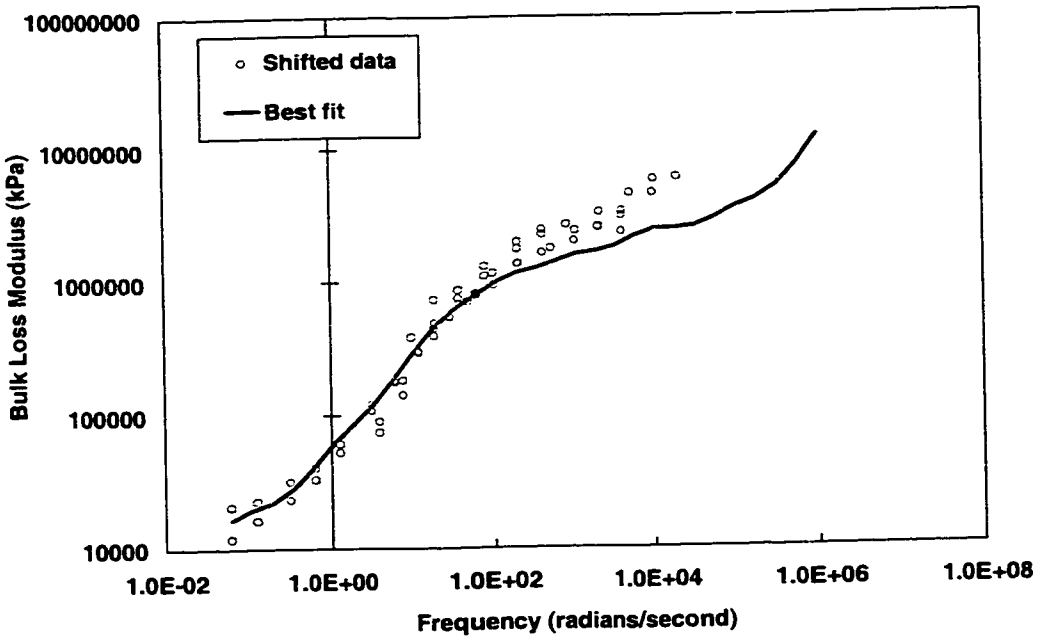

Figure 5.19 Volumetric Loss Modulus Master Curves, Best Fit and Original Data

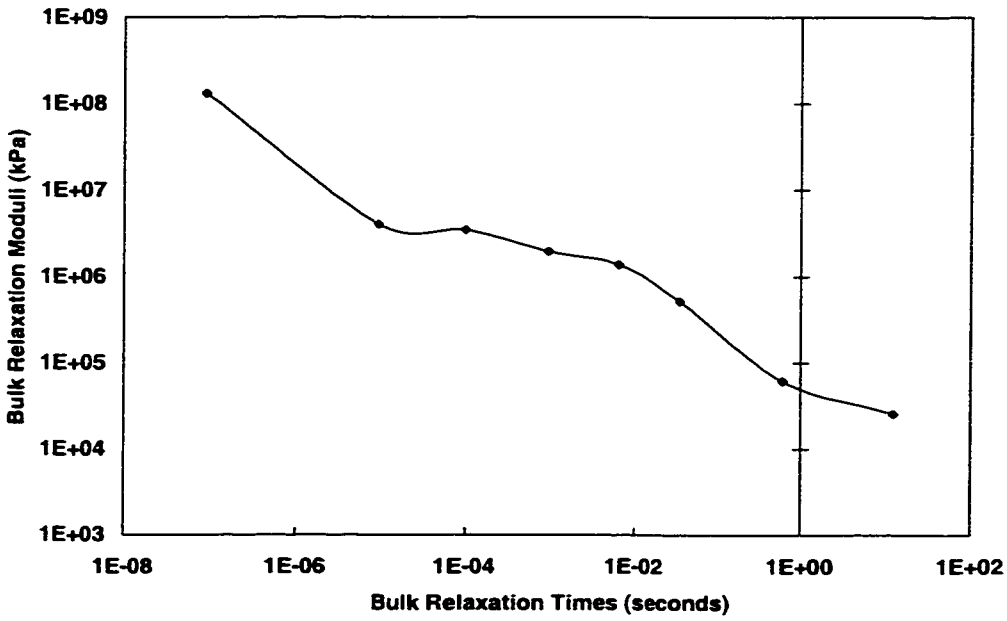

Figure 5.20 Volumetric Relaxation Times and Relaxation Moduli

The fit to the storage modulus master curve is good (Figure 5.18), whereas the fit for the loss modulus master curve is not good above 100 radians per second. This fit could not be improved. Because the data used to fit the master curve were extrapolated beyond approximately 10000 radians per second, and may not have been accurately extrapolated, the lack of fit is not surprising. However, because the fit to the storage modulus is good, and the fit to the bulk modulus is good within the frequency range most commonly used, the material properties are acceptable.

5.4.3 Comparison of Volumetric and Shear Master Curves

The fitted volumetric and shear complex modulus master curves for the reference temperature, 40°C, are shown in Figure 5.21. The master curves are drawn over a wider frequency range than the available data. The volumetric moduli are almost an order of magnitude greater than the shear moduli for the same relaxation times, as expected.*(9)*

Also shown on Figure 5.21 are the frequency ranges of the volumetric and shear data, and the typical frequency range of interest for loading on highways. Although the frequency range of the volumetric data does not fully contain the range of interest, and the master curve has flattened off at the lower frequencies within the range of interest, the fit is still reasonable. The difference between the modulus values from the curve shown and values obtained if the downward trend of the master curve is continued are relatively small and within the same level of variability as the fitted and laboratory data.

5.4.4 Shifted Shear Master Curves

The fitted master curves shown in Figure 5.21 are for the reference conditions of 40°C and 0.1 percent strain from the frequency sweep tests. Using the shear shift factor functions, the DGAC master curve was shifted to demonstrate the effect of strain and temperature on the material properties.

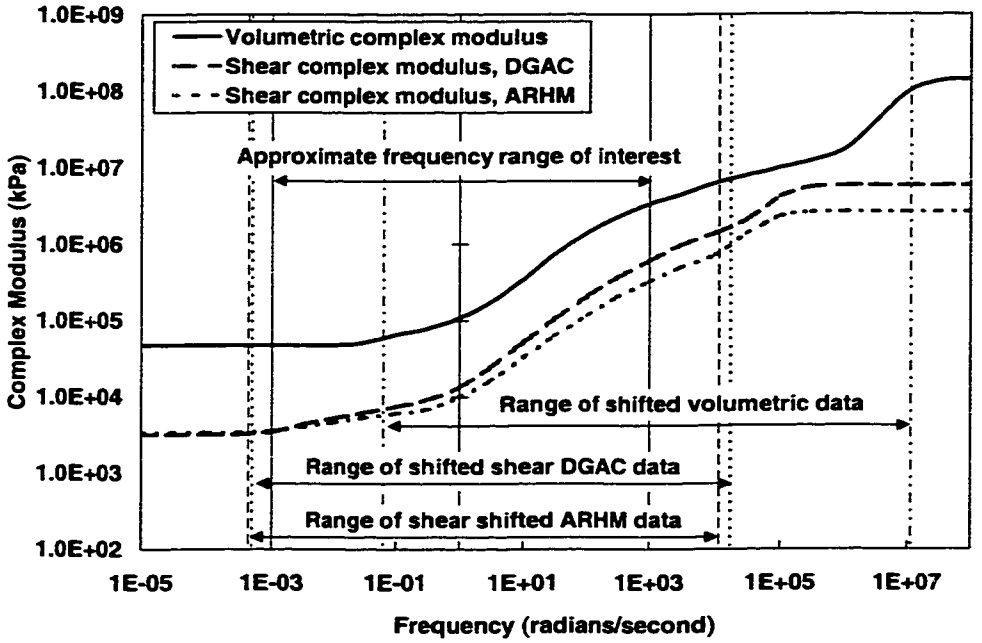

Figure 5.21 Volumetric and Shear Complex Modulus Master Curves

Figure 5.22 shows the reference DGAC complex shear modulus master curves shifted to 20°C, 50°C, and 1.5 percent strain. Increasing the temperature for a constant strain shifts the master curves to the right, decreasing the relaxation times. Increasing the strain for a constant temperature shifts the master curve down and slightly left, decreasing the complex moduli and marginally increasing the relaxation times.

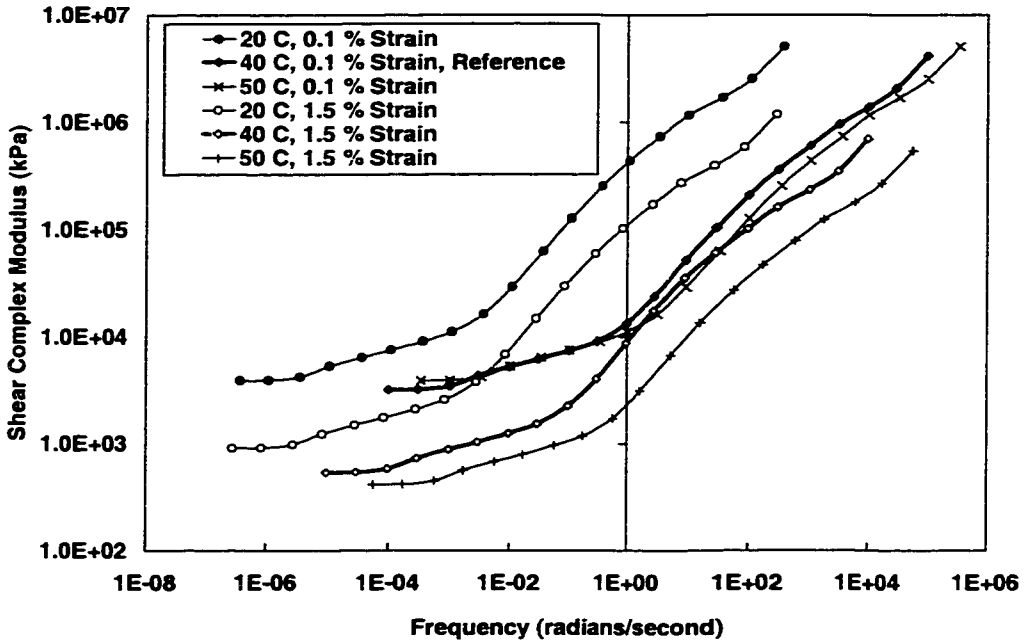

Figure 5.22 Shifted Shear Master Curves

5.5 Model Limitations

A model can seldom fully capture the material behavior. The nonlinear viscoelastic model developed herein has some limitations, in terms of the mechanics involved and in some aspects of asphalt concrete behavior that are not adequately captured. This section presents several of the limitations in the model and discusses the implications thereof. Where applicable, suggestions are made for improving the model.

5.5.1 Mechanics Limitations

The nonlinear viscoelastic model will (even with the nonlinearities) recover, leaving little, if any permanent deformation at infinite time. Rutting in pavements does not rebound when the loading is no longer applied. However, permanent deformation will be present at the conclusion of the simulation, before additional recovery takes place. Therefore, the model can be used for predictive purposes.

The model is formulated using small strain theory. It is observed, and will be shown in Chapters 6 and 7, that large deformations and rotations of material particles are experienced in rutted pavements. This indicates that it may be more appropriate to formulate the model using finite deformation theory.

The use of the peak value of the deviatoric strain norm at the beginning of the time step to evaluate the horizontal and vertical shift factors is discussed and justified in Sections 5.2.2.1 and 5.3.2. The accumulation of residual strains from rapidly applied heavy loads will result in more permanent deformation than the application of a few heavy loads, which is the expected field behavior. If a large load is followed by a series of smaller loads, as long as the maximum strain is not exceeded, the material properties are dependent on the strain resulting from the large load, regardless of the number of smaller loads. The damaging effect of many smaller loads is therefore ignored. It would be worth investigating the use of some kind of moving average of the peak strains to

calculate the shift factors. This might account for the application of the smaller but nevertheless damaging loads, but would, be significantly more difficult to implement computationally.

A limitation in the implementation of the shift factor functions developed in Chapter 4 is the presence of the constant terms C_{H1} in the horizontal expressions and C_{V1} in the vertical expression. These terms result in a small shift when the reference conditions are used, which is theoretically incorrect. However, because the reference master curves are not exactly the same as other master curves from specimens tested in the laboratory at the same temperature and strain level, and the reference curve is subject to some variability, the constant terms are expected. The small shift is therefore acceptable.

The horizontal and vertical shift factor equations developed in Chapter 4, Equations (4.15) and (4.16), are only applicable for the specific reference conditions of 40°C and 0.1 percent strain level (0.1 percent peak strain in the frequency sweep test). Data may be shifted to or from these references, but other reference values cannot be substituted.

5.5.2 Limitations in Capturing the Behavior of Asphalt Concrete

A major limitation in the nonlinear viscoelastic model is the exclusion of the effects of the air-void content. The stiffnesses obtained from the laboratory are dependent on the

air-void content of the specimens but, as described in Chapter 3, attempts to incorporate an air-void term in the shift factor equations were unsuccessful. Although any effect of the air-voids was not clearly visible for the air-void content range of the laboratory test data, it is expected that for a wider range of air-void contents, the effect on stiffness would be more significant. It is widely known that mix stiffness is reduced at high air-void contents, and that stiffer mixes are more rut-resistant. As discussed in Chapter 2, mixes with an air-void content below a threshold of three percent have increased rutting potential, which cannot be observed in this model.

It may be possible to determine a significant air-void term in the shift factor equations if laboratory data is obtained for a much wider range of air-void contents. This would significantly improve the prediction capabilities of the model. Within the same range of air-void contents, the model is a reasonable estimate of the material behavior. However, care should be taken when applying the results or the model to mixes at significantly higher or lower air-void contents.

The bulk properties of the model are obtained indirectly from a limited number of hollow cylinder tests. With the available data, it is not possible to directly obtain the properties, nor to explore aspects of the material behavior with which to modify the linear viscoelastic model. One of the aspects of the bulk response that is omitted in this model is densification. For new pavements, especially at higher air-void contents, some

densification occurs under traffic loading. The densification contributes to the rutting, but also results in a lower air-void content, thereby increasing the stiffness of the mix and retarding further deformation. These effects are not accounted for in the model. To improve the bulk component, a significant laboratory testing program needs to be performed, preferably with a simpler test than the hollow cylinder test.

In Chapter 2, the different behavior of asphalt concrete in tension and compression was discussed. The nonlinear viscoelastic model has the same properties in tension and compression. It is not possible to directly quantify the difference in tension and compression with the available data. Because shear deformation dominates permanent deformation in asphalt concrete pavements, limitations in the bulk component are not as important as limitations in the shear component.

The laboratory tests from which the model was developed were performed on fresh mix. The asphalt in the mix had not aged, and therefore the model captures the behavior of a fresh mix. Aging, which causes the binder to oxidize and harden, increases the rutting resistance of the mix. This is not accounted for in the model. The critical stage for rutting is in the early life of the pavement, and, thus, not including aging effects gives conservative rutting predictions.

5.6 Summary

This chapter formulates the nonlinear viscoelastic model for the permanent deformation behavior of asphalt concrete, using the framework of linear viscoelasticity. The algorithm for the model is derived and implemented in a finite element code and the material properties are fit from the master curves developed in Chapter 4. Finally, some limitations in the model are discussed, both in terms of mechanics issues and in aspects of the behavior of asphalt concrete that are not captured.

CHAPTER 6

SIMULATIONS TO VALIDATE THE CONSTITUTIVE MODEL

To validate the ability of the nonlinear viscoelastic constitutive model to capture the rutting behavior of asphalt concrete, several simulations were performed. The first series simulated the repeated load simple shear test at constant height (RSST-CH). The second series simulated the rutting performance of mixes tested with the Heavy Vehicle Simulator (HVS). The results from these simulations were compared with actual data from physical tests. This chapter presents these results.

6.1 Repeated Load Simple Shear Test at Constant Height Simulations

The repeated load simple shear test at constant height (RSST-CH) was used to measure the rutting resistance of asphalt concrete mixes. The RSST-CH test is similar to the shear frequency sweep test discussed in Chapter 3, in that the same specimen, machine and test setup were used. The RSST-CH test followed the AASHTO TP7-94 test method with a few modifications.*(44, 45)* The tests were performed at a constant temperature. A load

of 69 kPa (10 psi) was used. Although stresses in the pavement are likely greater than 69 kPa, it has been found that using a larger stress in the shear test causes excessive deformation early in the test. The test applied the load in a haversine wave for 0.1 seconds, followed by a 0.6 second rest period. This load cycle was repeated for 5000 repetitions, or until the specimen had a residual shear strain of 5 percent. The number of repetitions to 5 percent shear strain was used as a measure of the rutting resistance of an asphalt concrete mix. This will be discussed further in Chapter 7.

To validate the performance of the nonlinear viscoelastic model developed herein, simulations of the RSST-CH were performed using the finite element code FEAP.*(67)*

6.1.1 Simulation Setup

Three different simulations were run for the DGAC mix, as shown in Table 6.1. The material properties and coefficients for the shift factor functions were obtained from the Goal 3, DGAC mix. The shear properties and coefficients are given in Table 5.1, and Equations (4.15) and (4.16), respectively. The volumetric properties and coefficients are given in Table 5.2 and Equation (4.21). The temperature was held constant during each simulation, as in the laboratory tests. The simulations used mixed elements, rather than displacement elements. Mixed elements are more suitable for highly incompressible materials, such as asphalt concrete.*(67)*

Table 6.1 RSST-CH Simulations

Simulation	Mix	Material Model	Temperature
1	Dense graded (DGAC)	Nonlinear viscoelastic	40°C
2	Dense graded (DGAC)	Nonlinear viscoelastic	50°C
3	Dense graded (DGAC)	Linear viscoelastic	40°C

6.1.1.1 Mesh, Boundary Conditions, and Loading

A three-dimensional mesh was created that replicates the physical specimen, although symmetry was utilized and only half the specimen was modeled, as shown in Figure 6.1. The boundary conditions imposed fix the specimen in all directions on the bottom face, and fix the vertical height along the top face to maintain the specimen at constant height, as in the laboratory test. The specimen glued between the load platens with the measuring devices mounted is shown in Figure 3.3.

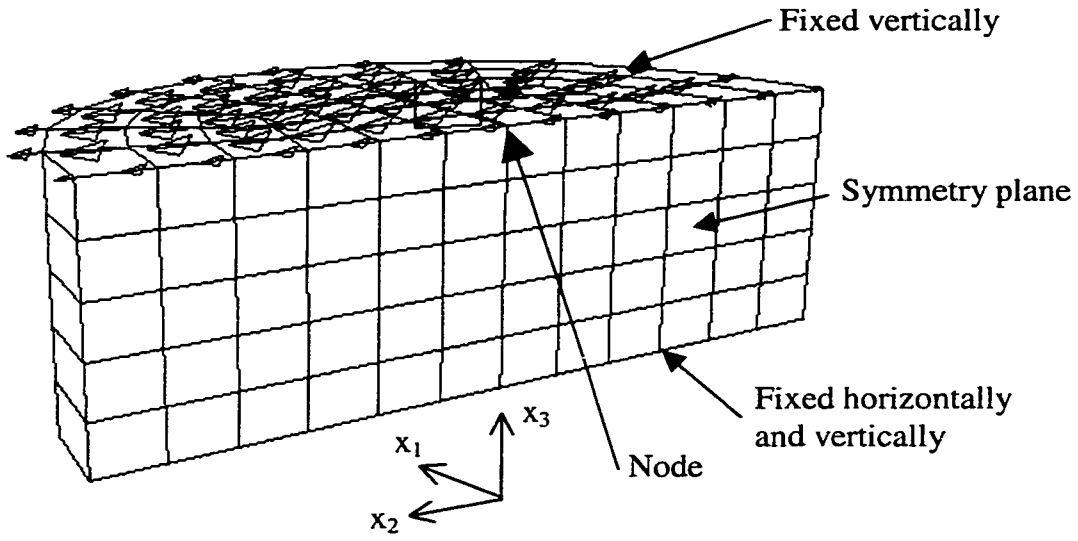

Figure 6.1 Finite Element Mesh of RSST-CH, 150 mm Diameter and 50 mm Height

The total force applied in the laboratory test, for the 70 kPa imposed stress, was 1300 N. In the simulation, half this load was applied to the half specimen modeled. The load was applied in the x_2 direction. The load was distributed amongst the nodes on the top surface of the mesh, as shown by the arrows in Figures 6.1 and 6.2. Figure 6.2 is a plan view of the top surface of the specimen. The exact force applied at each node does not equal the exact nodal force that should be applied for a constant shear stress. However, the resultant force was the same and the differences between the actual and exact forces were small. In the laboratory test the exact distribution of the forces across the loaded face of the specimen is also unknown. Following the principle of St. Venant, away from this boundary, the material response was the same as if the exact forces were used.

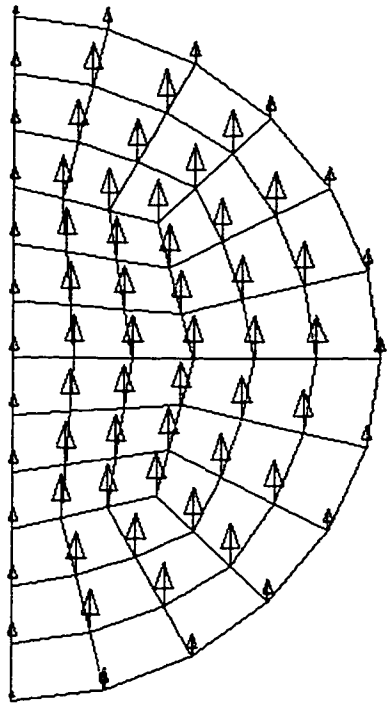

Figure 6.2 Plan View of Loaded Specimen

A haversine load was applied, in keeping with the laboratory test. The load was applied in a sine wave for 0.1 seconds, followed by a 0.6 second rest period. The simulations were run for 5000 load cycles (repetitions) for the nonlinear viscoelastic cases, and for 470 repetitions for the linear viscoelastic case. The laboratory test protocol requires the test to be run for 5000 repetitions or until five percent residual shear strain has accumulated.*(44, 45)*

6.1.1.2 Displacement, Stress and Strain

The node in the middle of the specimen on the top face, as shown in Figure 6.1, was selected as the location to obtain the displacement and stress values during the simulations. The middle of the specimen was chosen to avoid the edge effects on the sides of the specimen. This node is within the St. Venant boundary. The displacement and stresses from all nodes on the vertical face (symmetry plane) were examined and it was found that the loading approximations at this boundary had a negligible effect on the displacement and stress at this node. The edge effects on the sides of the specimen had significantly more influence.

The displacement values, u_2, reported in the analyses are in the x_2 direction, and the stress is the shear stress on the symmetry plane, σ_{23}. The strains were calculated from the displacement values as is done in the laboratory test. The engineering shear strain, γ_{23}, is

the displacement in the x_2 direction divided by the vertical height (x_3), as shown in Equation (6.1).

$$\gamma_{23} = \frac{u_2}{x_3} \tag{6.1}$$

The vertical height is the gage length of the vertical LVDT. This height remained constant during the test, and the gage length was 50 mm in the simulations. Even though the physical gage length was 50 mm in the laboratory test, a value of 38 mm was used to calculate the laboratory results. This was to account for the effect of the stiff glue bonding the specimen and the platens, which prevents the deformation of the specimen in a boundary layer at this interface.

The displacement at the end of the load cycle was used to calculate the residual or permanent shear strain, using Equation (6.1). The elastic strain is the difference between the peak (maximum) strain in the load cycle and the residual strain at the end of the cycle.

6.1.1.3 Time Steps

Results from the simulations depended on the time steps used during the loading cycles. The smaller the time step, the more accurate the solution, but the longer the simulation took to run. It was also important to keep the time steps relatively small to limit the effects of some of the assumptions used to derive the model. For example, using the maximum strain in the time history up to the beginning of the time step rather than up to the current time in the shift factors, and in the implementation of the reduced time.*(66)* A

brief investigation indicated a very small difference in the solutions when the maximum strain at the beginning of the time step rather than the end of the time step is used.

The simulation results were very sensitive to the time step duration used in the first load cycle. This is shown in Figure 6.3 for four time steps, $\Delta t = 0.0002$, 0.0005, 0.001, and 0.002 seconds for the 40°C RSST-CH simulation. The larger the time step, the smaller the displacement. During the first load cycle the history terms are small because the viscous effects have not yet accumulated. The small history terms and the rapid changes in the strain which cause $\Delta\xi$ to also change rapidly resulted in the first load cycle being very sensitive to the time step duration. In all the simulations the time step used in first load cycle was 0.001 seconds. With this value the simulation ran reasonably fast and the error is unconservative in comparison to $\Delta t = 0.0002$. The error was approximately 5 percent in the peak displacement and 7.5 percent in the residual displacement.

After the first load cycle the simulation stabilizes and the subsequent load cycles were less sensitive to the time step duration. For the remaining load cycles, four different time steps were investigated: $\Delta t = 0.001$, 0.002, 0.005, and 0.010 seconds. For each time step, the second load cycle for the 40°C nonlinear viscoelastic simulation is shown in Figure 6.4. Increasing the time step resulted in underestimating the displacement. The difference between the minimum and maximum displacements for the time steps and $\Delta t =$

0.001 seconds was less than 1 percent for $\Delta t = 0.002$ seconds, approximately 2 percent for $\Delta t = 0.005$ seconds, and approximately 4 percent for $\Delta t = 0.010$ seconds.

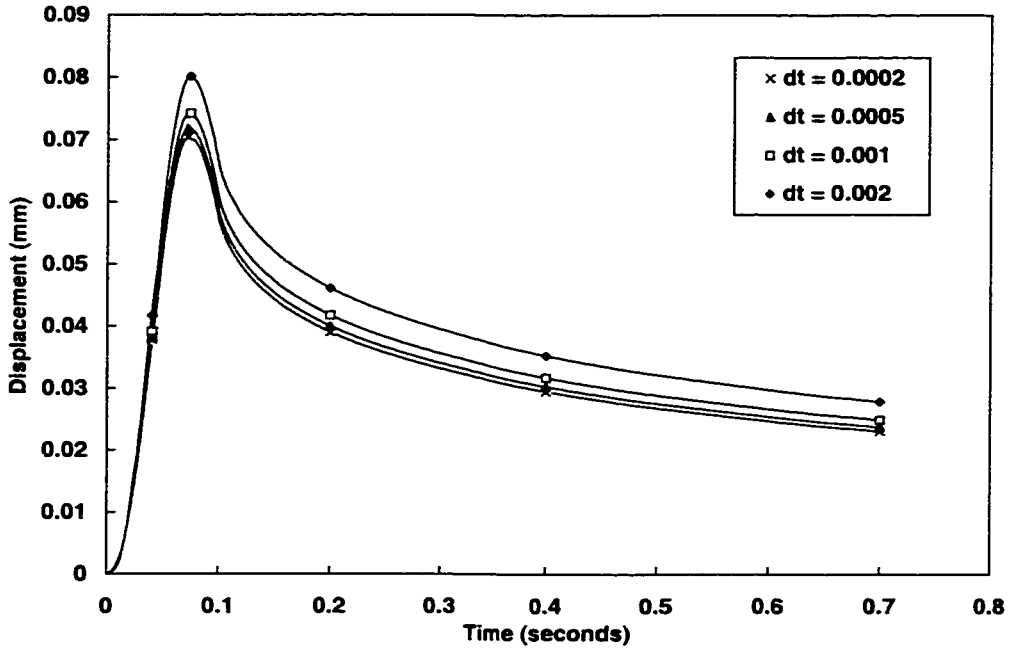

Figure 6.3 Effect of Time Step on Displacement in First Load Cycle During RSST-CH Simulations

After the first load cycle, for the loading and initial unloading portions of the load cycle a time step of 0.005 seconds was used in the simulations. For this time step, the simulation ran approximately 2.5 or 5 times faster than the 0.002 and 0.001 time steps, respectively. This saving in computation time is significant, and the error is relatively small. Furthermore, this small error is almost negligible when compared to the variability in the laboratory test results, as discussed in Chapter 3 and later in this section.

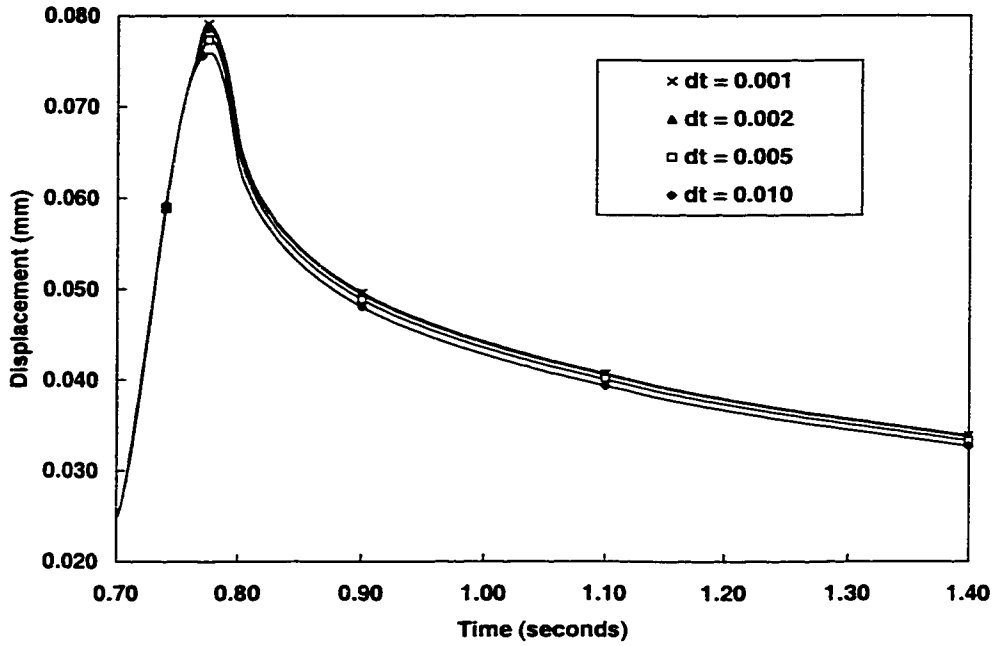

Figure 6.4 Effect of Time Step on Displacement During RSST-CH Simulations

In an effort to further reduce the simulation time, the time step was increased to $\Delta t = 0.01$ seconds during the rest period, 0.1 seconds after the load was removed and to $\Delta t = 0.05$ seconds for the last 0.45 seconds of the rest period. This had no effect on the displacements, as shown in Figure 6.5 for the second load cycle. The solid line is for $\Delta t = 0.005$ seconds, and the markers are the results for the simulation in which the time step was increased during the rest period. The results agree exactly.

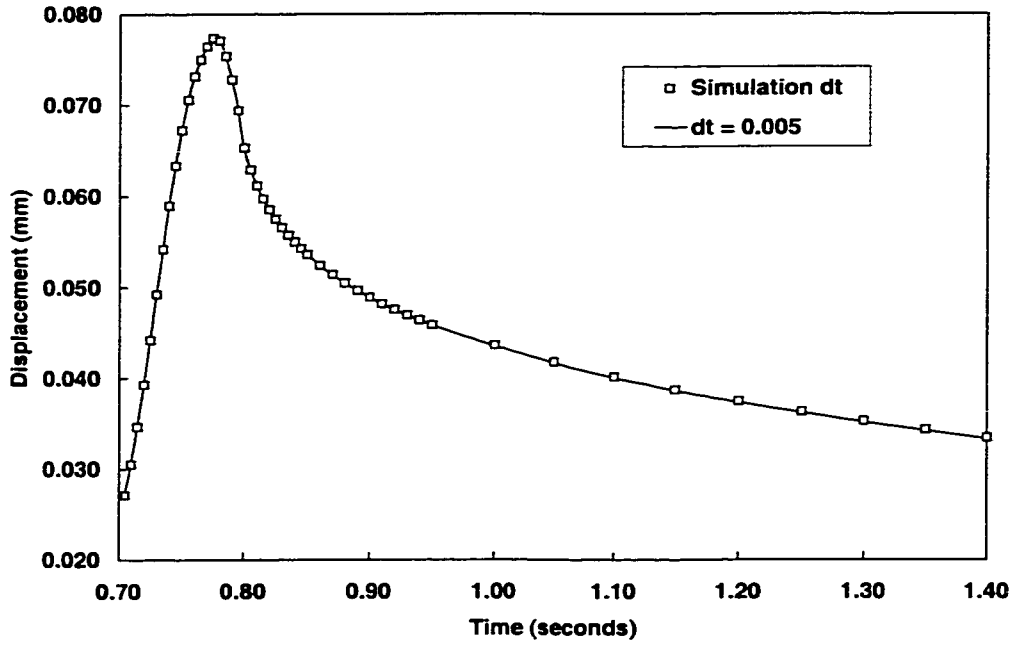

Figure 6.5 Effect of Increasing the Time Step During the Load Cycle Rest Period

6.1.2 RSST-CH Laboratory Test Data

Numerous RSST-CH laboratory tests have been performed on field cores for the Goal 3 DGAC and ARHM mixes. The cores were obtained at the same time as many of the cores used in the frequency sweep tests discussed in Chapter 3 and from the same location. Therefore the air-void contents are in the same range. These tests were run at 40°C, 50°C and 57°C. Results from these tests were compared to the simulation results to validate the nonlinear viscoelastic model. When only one specimen was used in a comparison, it was data from specimen G3DC-03, which was tested at 40°C and had an air-void content of 6.7 percent.

The laboratory test data do not begin at zero strain because the first data point is at the end of the first load cycle and a small amount of residual strain had already accumulated. The data are sometimes adjusted to begin at zero. The procedure used to determine the offset is to fit a fourth order polynomial through the first 10 data points and then to subtract the constant term from all the data.*(34)* This significantly affects the data below 100 repetitions, but has a negligible effect on data above 100 repetitions. All the laboratory test data reported herein have been adjusted with the offset to start at zero.

6.1.3 RSST-CH Simulation Results

A comparison of the peak displacements and the recovery for the 40°C nonlinear viscoelastic simulation and for a laboratory test specimen is shown in Figure 6.6 for the 101, 102, and 103 load repetitions. The dotted and dashed lines are the imposed loads, with the values shown on the right hand side axis.

The laboratory test and simulation results have similar behavior. The peak displacement lags the peak stress, and during the rest period the material continues to recover, which is typical viscoelastic behavior. The simulation deforms and recovers considerably more than the laboratory test.

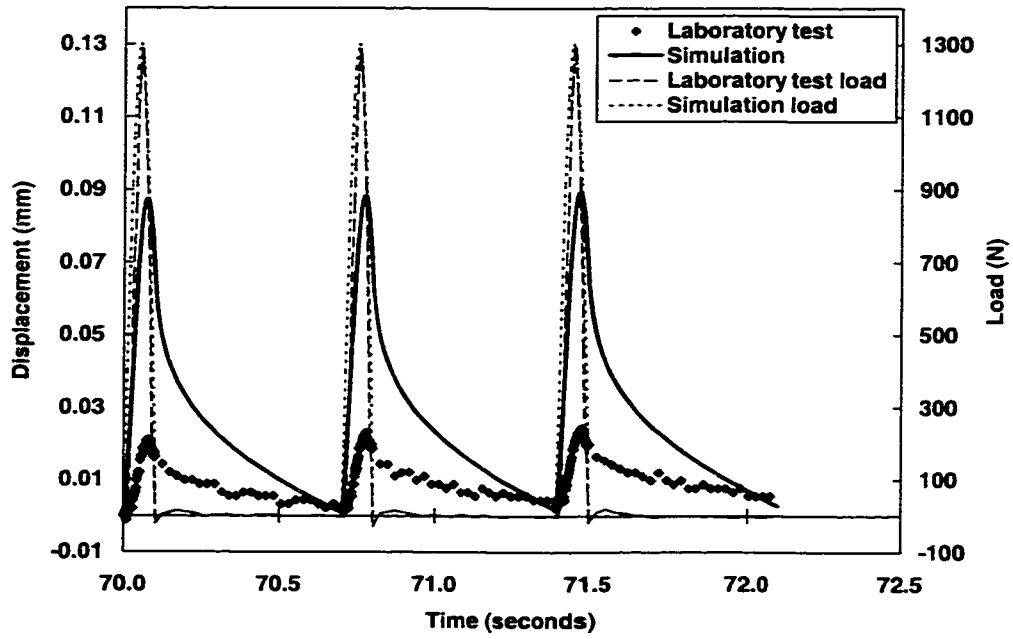

Figure 6.6 Comparison of Load Cycles from 40°C Nonlinear Viscoelastic Simulation and Specimen Tested in the Laboratory

Typical shear strain versus repetition results are shown in Figure 6.7 for the 50°C nonlinear viscoelastic simulation. The peak strain was calculated from the maximum displacement during the load repetition and the residual strain from the displacement at the end of the cycle. The peak and residual strains follow the same trends; the rate of increase in strain decreases as the repetitions increase. The increase in strain is substantial in the first 100 repetitions. This trend is similar to that observed in rutted pavements, with most of the rutting developing early in the trafficking period.

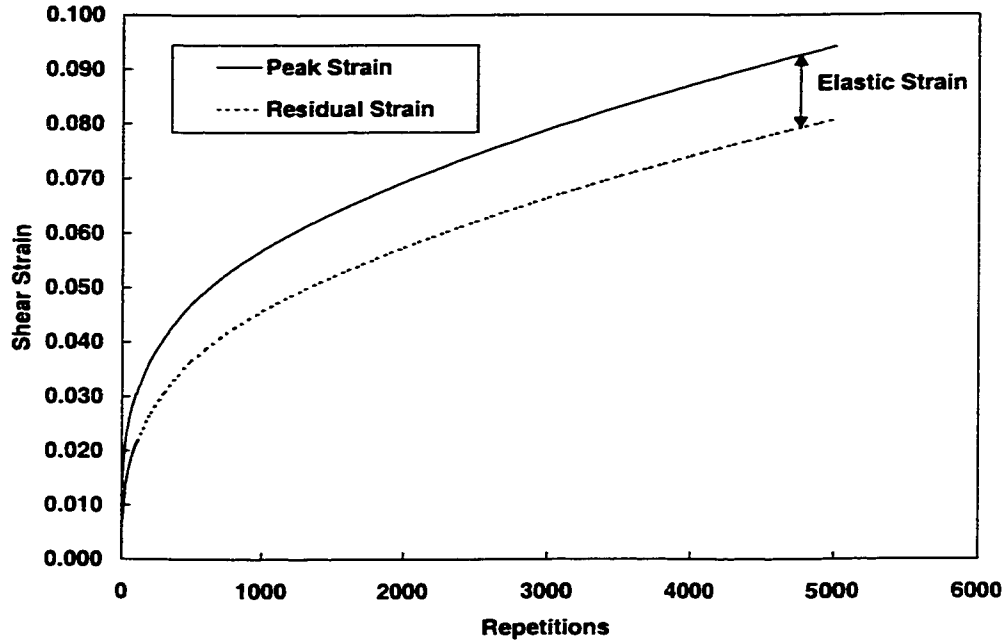

Figure 6.7 Peak and Residual Strains for 50°C Nonlinear Viscoelastic Simulation

6.1.3.1 Elastic strain

The difference between the peak strain and the residual strain at the end of the load cycle is known as the "elastic" strain, as shown in Figure 6.7. This elastic strain is shown in Figure 6.8 for all three simulations and a laboratory test specimen. After the first load cycle, the elastic strain remained constant for the laboratory test data and the linear viscoelastic simulation. In the nonlinear viscoelastic simulations, the elastic strain increased, although the rate of change of the elastic strain decreased with increasing repetitions. The linear viscoelastic model therefore gives an improved representation of the real elastic strain. However the development of the residual strain is a more important factor in rutting prediction.

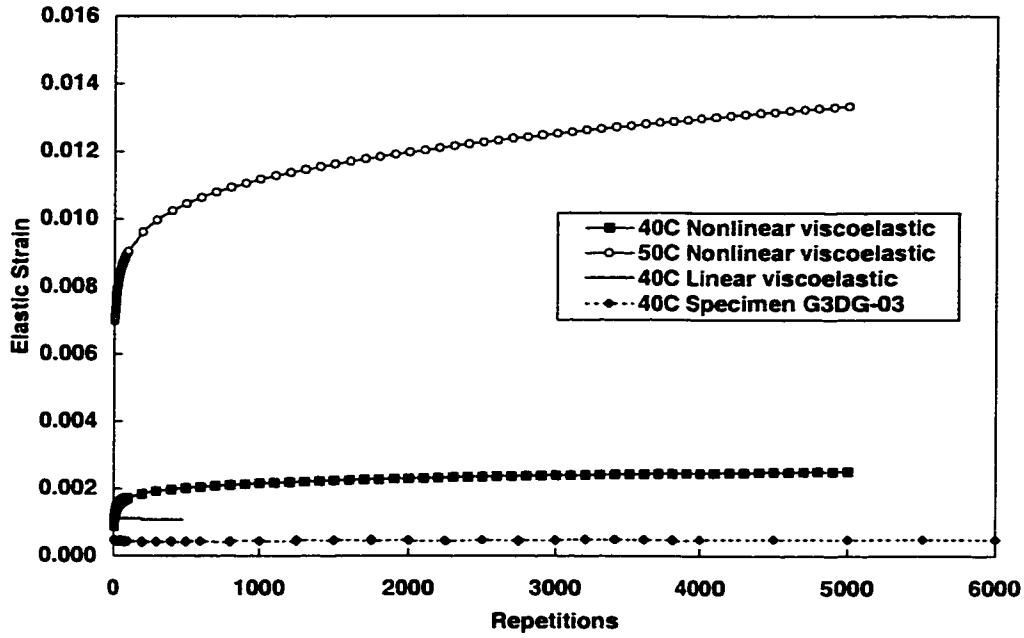

Figure 6.8 Elastic Strain for All Simulations

6.1.3.2 Residual Strain

Figure 6.9 shows the residual strain for each simulation as a function of the load repetitions. The strain in the 50°C simulation was larger than for the 40°C simulation. Asphalt concrete becomes less stiff as the temperature increases, therefore, this behavior in the simulation agrees with that of the physical material. After the first 10 repetitions the shape of the strain versus repetition curves is the same for both temperatures for the nonlinear viscoelastic predictions.

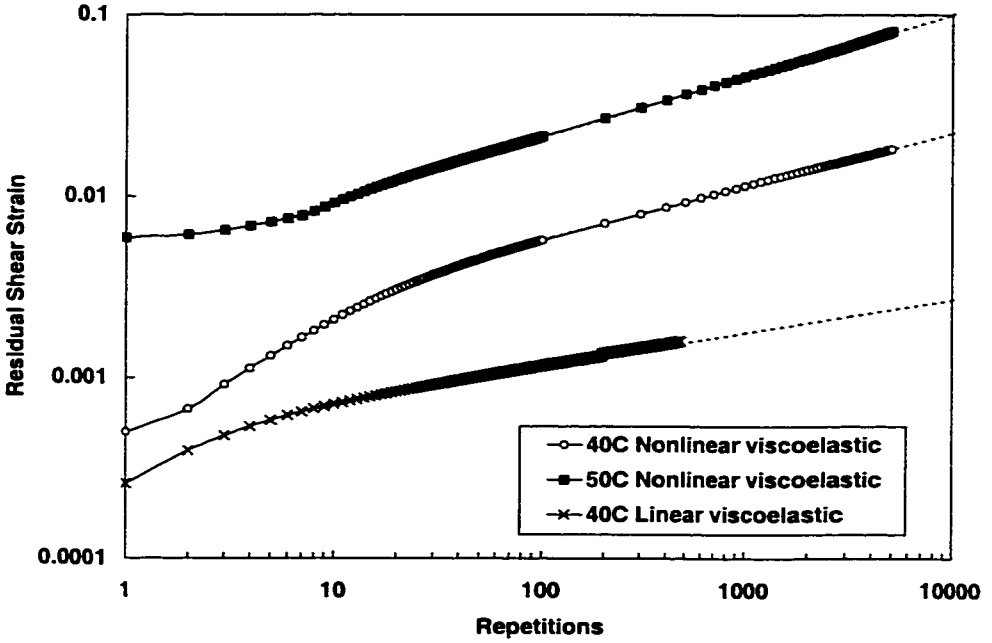

Figure 6.9 Residual Shear Strain for All Simulations

A large displacement is experienced in the first load cycle in the nonlinear viscoelastic simulations. During this load cycle the material properties are changing rapidly within each time step. Rapid changes in the strain during application of the load caused rapid changes in the shift factors and therefore in the change in the reduced time, $\Delta\xi$. The shift factors were initialized to a value of one at the beginning of the simulation but rapidly changed as the strain accumulates. And, in the first load cycle the history terms, which account for the viscous material response, were small. The first load cycle was therefore atypical. After the first few load cycles the solution stabilized. The atypical effects of the first load cycle influenced the subsequent load cycles but after five to ten repetitions the accumulation of residual strains became more reasonable. The effect of the first load

cycle was greater on the 50°C simulation than for the 40°C simulation, as shown in Figure 6.9. It may be possible to reduce this effect by using smaller time steps during the first load cycle of the 50°C simulation.

The linear viscoelastic simulation at 40°C predicts significantly smaller residual strains than the nonlinear viscoelastic simulation. The rate of residual strain accumulation was also less for the linear case, indicated by the flatter slope on the log-log scales in Figure 6.9.

After approximately 100 repetitions, the slopes of the strain versus repetition curves were approximately linear in the log-log scale. This is the kind of behavior that is observed in laboratory tests and in wheel tracking and accelerated pavement tests.*(7, 34)*

6.1.3.3 Stress and Strain State in Simulation of Specimen

Figures 6.10 and 6.11 show the shear stress, σ_{23}, distribution at the end of the 5000 load cycles, after the rest period for the 40°C and 50°C nonlinear viscoelastic simulations. These figures were obtained from the finite element program, FEAP *(67)*. The edge effects along the sides of the specimens are visible. The boundary effect from the imposed load distribution is also apparent, but is limited to the areas immediately surrounding the nodes. In the majority of the specimen, the shear stress is fairly constant. The load distribution in the laboratory test is also not perfect and therefore similar

boundary effects are expected in the specimen. The edge effects from the missing tractions, discussed in Chapter 2, are also present in the laboratory test specimen.

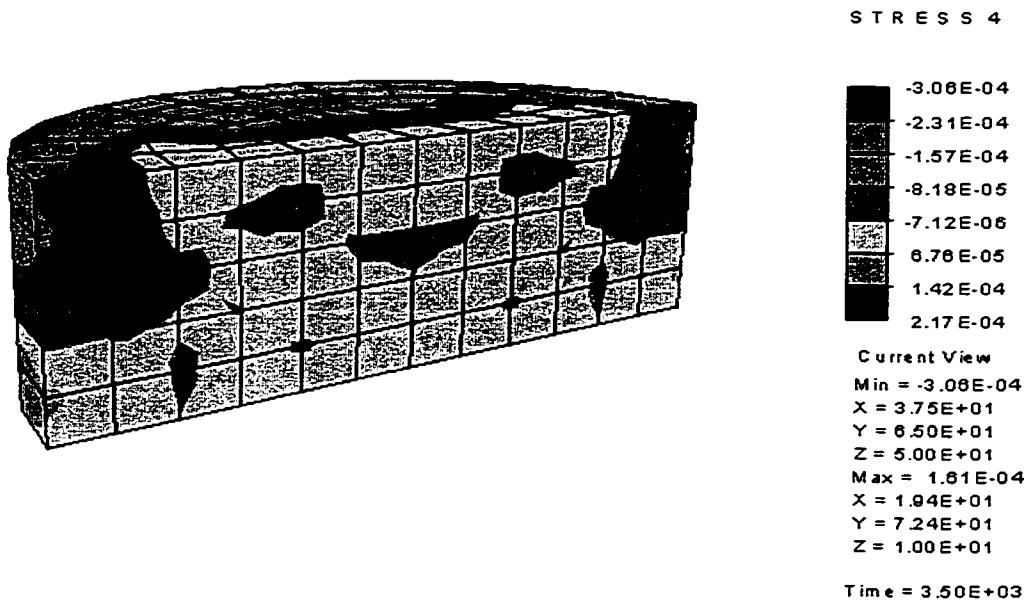

Figure 6.10 Shear Stress (σ_{23}) Distribution after 5000 Repetitions, 40°C

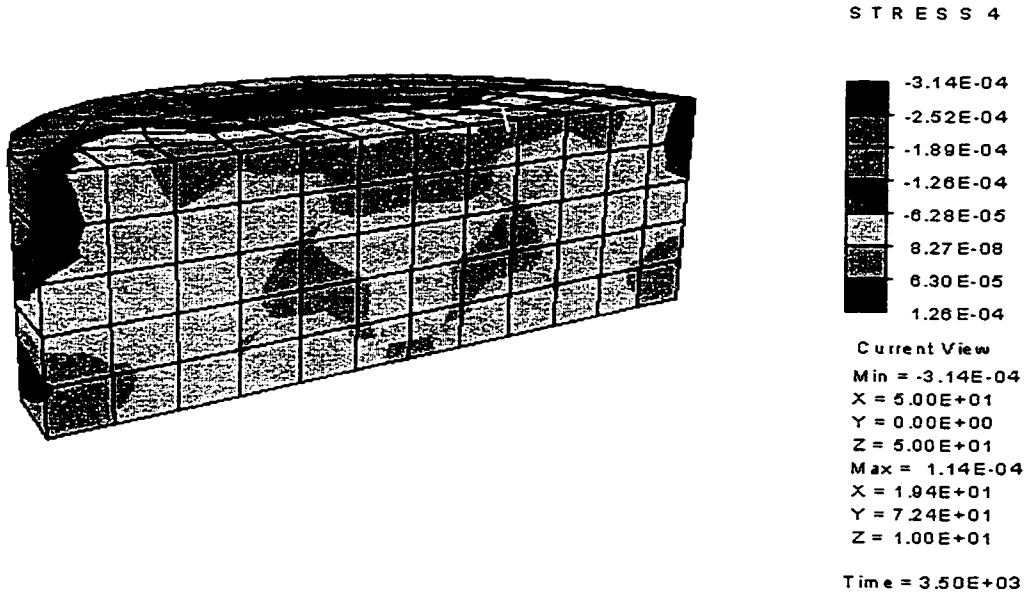

Figure 6.11 Shear Stress (σ_{23}) Distribution after 5000 Repetitions, 50°C

Similarly, Figures 6.12 and 6.13 show the engineering shear strain ($\gamma_{23} = 2\varepsilon_{23}$) distribution on the symmetry plane for the two temperatures. The figures were drawn in MATLAB with data obtained from FEAP. The data were obtained from the Gauss points in each element and therefore the distance between the minimum and maximum Gauss points and the edge of the specimen is excluded. This distance is approximately 7.5 mm on the edge and 5.0 mm on the top and bottom of the specimen. The same boundary effects are visible, and the interior of the specimen shows a constant strain.

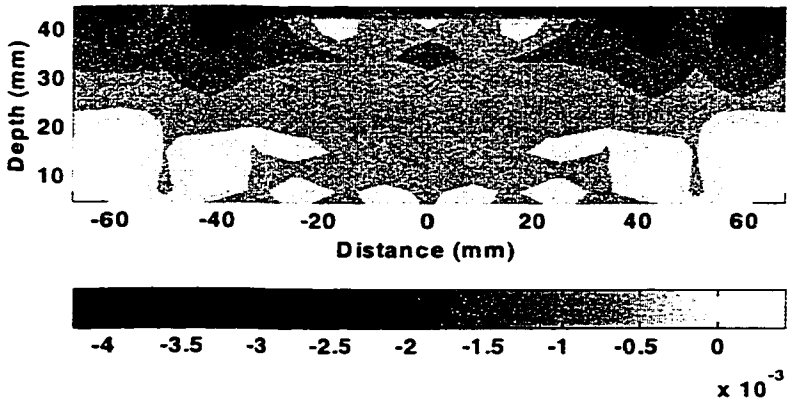

Figure 6.12 Engineering Shear Strain (γ_{23}) Distribution after 5000 Repetitions, 40°C

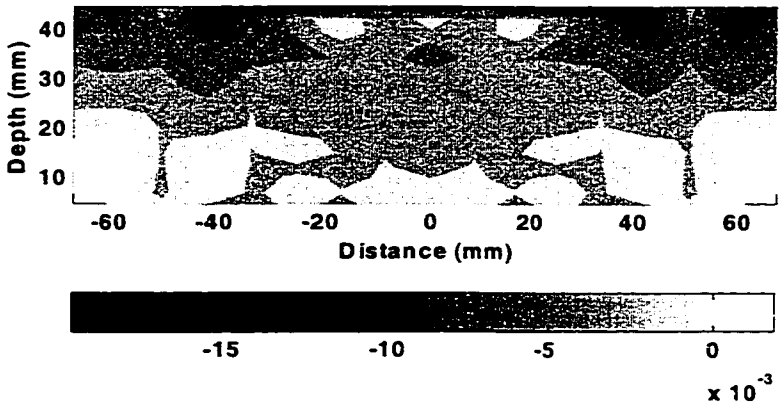

Figure 6.13 Engineering Shear Strain (γ_{23}) Distribution after 5000 Repetitions, 50°C

6.1.4 Comparison of RSST-CH Laboratory Test Data and Simulations

Figures 6.14 and 6.15 compare the nonlinear viscoelastic simulation results and laboratory test data for 40°C and 50°C, respectively. The thinner lines are the laboratory test data. Only the specimens with air-void contents in the same range as the data from which the model was developed are shown. The variability between the laboratory specimens is fairly large; reasons for this are discussed in Chapter 3. It was expected that as the air-void content decreased, the material would become stiffer and therefore more resistant to deformation. This trend was not demonstrated for these data and air-void content range. Attempts to incorporate the air-void content in the shift factor functions in Chapter 4 were unsuccessful.

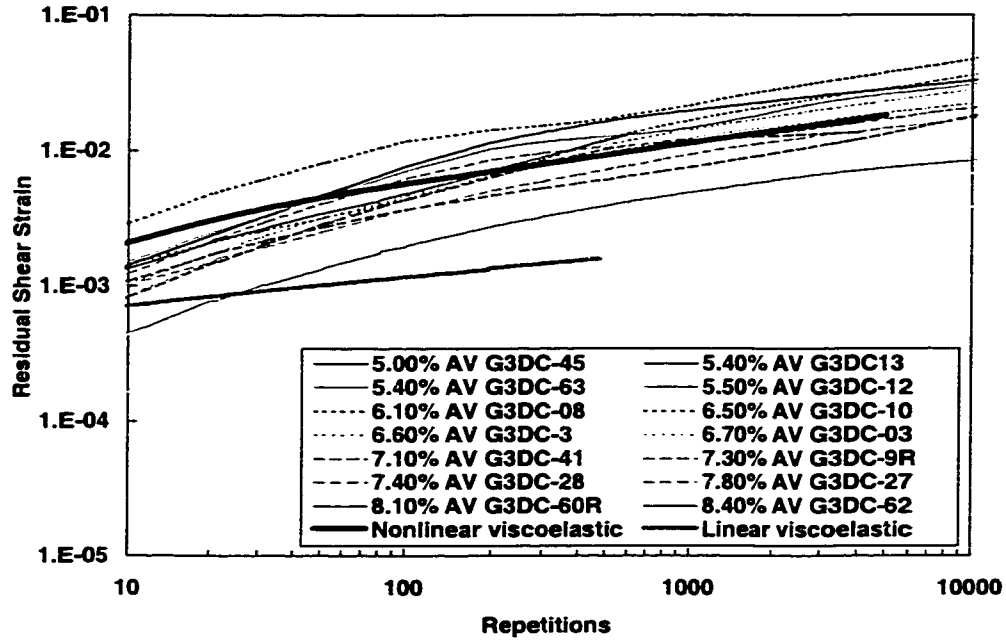

Figure 6.14 Comparison of Model Predictions and Laboratory Test Data at 40°C

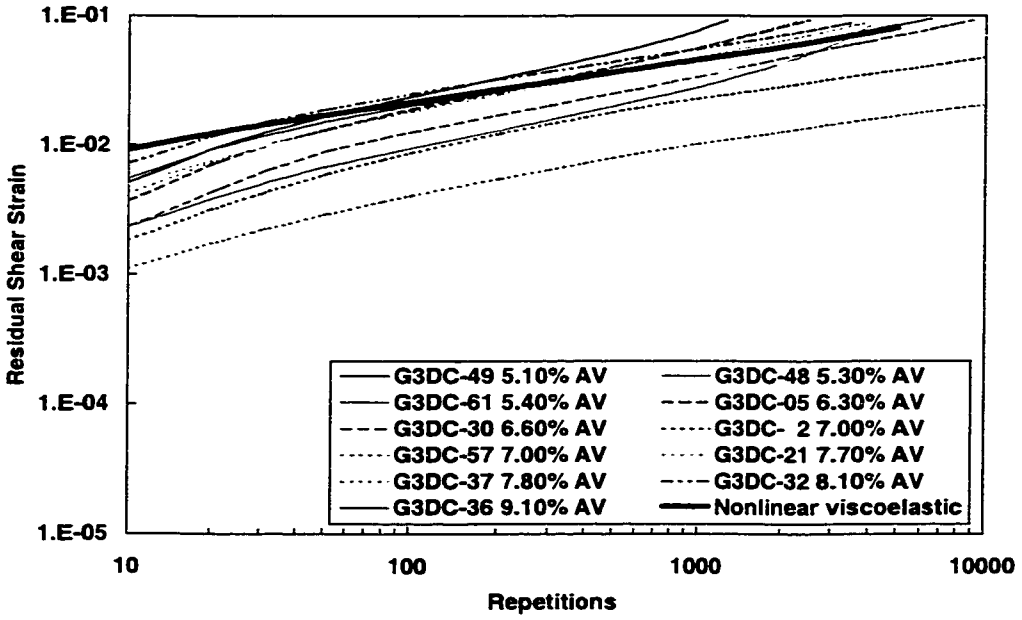

Figure 6.15 Comparison of Model Predictions and Laboratory Test Data at 50°C

After the first 50 repetitions the nonlinear viscoelastic model predicts residual strains that are similar to the laboratory test data, whereas the linear viscoelastic model prediction is not a good fit. At 40°C the residual strain from the simulation is within the ranges of the laboratory test data, even though the slope of the curve appears marginally flatter than some of the data. The slope of the linear viscoelastic simulation at 40°C is consistently flatter than the laboratory data. The 50°C prediction starts with a slightly higher residual strain than most of the laboratory data. After 100 repetitions, the slope and the magnitude of the strain from the 50°C simulation match the laboratory data well.

The residual strain curves were fit with a curve of the form shown in Equation (6.2) to the data after 100 repetitions.*(34)*

$$\gamma_{res} = aN^b \tag{6.2}$$

In this equation γ_{res} is the residual shear strain, a is the intercept, b is the slope from the log-log plot of the data, and N is the number of repetitions. Figure 6.9 shows the residual strain curves from the simulations extrapolated beyond 5000 repetitions using Equation (6.2).

Table 6.2 contains the slopes and intercept values for all the data. The slope values for all three simulations are within one standard deviation of the corresponding laboratory test data. The intercept value is also within one standard deviation of the laboratory data for the 40°C nonlinear viscoelastic prediction, but the intercept for the 50°C nonlinear

viscoelastic prediction is greater than one standard deviation above the mean. This is due to the behavior of the model in the first few load cycles, as discussed earlier. The intercept of the linear viscoelastic prediction is greater than one standard deviation of the mean of the laboratory test data.

Although the predicted elastic strain was closer to the laboratory test data for the linear viscoelastic model, the nonlinear viscoelastic predictions of the residual strain were closer to the laboratory test data. The development of the residual strain is a more important indicator of rutting resistance of an asphalt concrete mix, and, therefore, the nonlinear viscoelastic model gives improved predictions of the rutting behavior of asphalt concrete.

In the physical test an axial stress is necessary to maintain the constant height. In the simulations the nodal reactions on the face of the specimen would give an indication of the axial forces required to maintain the height of the specimen constant. These nodal reactions were not investigated and therefore no comparisons have been made with the axial stress in the physical test.

Because the RSST-CH test is a shear test these simulations relied predominantly on the shear component of the nonlinear viscoelastic model. The next series of validation tests discussed below utilized both the shear and volumetric components of the model.

Table 6.2 Comparison of Slopes and Intercepts

	Specimen Name	Air-void Content	Intercept, a	Slope, b
Laboratory Data, 40°C	G3DC-45	5.0	5.203×10^{-3}	0.199
	G3DC-13	5.4	4.077×10^{-4}	0.546
	G3DC-63	5.4	1.783×10^{-3}	0.165
	G3DC-12	5.5	2.456×10^{-3}	0.275
	G3DC-08	6.1	2.204×10^{-3}	0.336
	G3DC-10	6.5	2.432×10^{-3}	0.290
	G3DF-03	6.6	2.997×10^{-3}	0.216
	G3DC-03	6.7	2.435×10^{-3}	0.265
	G3DC-41	7.1	6.540×10^{-3}	0.092
	G3DC-9R	7.3	4.499×10^{-4}	0.403
	G3DC-28	7.4	2.487×10^{-3}	0.227
	G3DC-27	7.8	1.863×10^{-3}	0.243
	G3DC-60R	8.1	5.031×10^{-4}	0.283
	G3DC-62	8.4	9.487×10^{-4}	0.151
	Average		**2.336×10^{-3}**	**0.264**
	Standard Deviation		**1.743×10^{-3}**	**0.113**
Nonlinear Viscoelastic Prediction, 40°C			**1.499×10^{-3}**	**0.293**
Linear Viscoelastic Prediction, 40°C			**5.042×10^{-4}**	**0.182**
Laboratory Data, 50°C	G3DC-49	5.1	2.756×10^{-3}	0.817
	G3DC-48	5.3	3.162×10^{-3}	0.387
	G3DC-61	5.4	1.239×10^{-3}	0.777
	G3DC-05	6.3	1.249×10^{-3}	0.551
	G3DC-30	6.6	1.658×10^{-3}	0.442
	G3DC-02	7.0	1.946×10^{-3}	0.351
	G3DC-57	7.0	1.433×10^{-3}	0.291
	G3DC-21	7.7	1.081×10^{-3}	0.576
	G3DC-37	7.8	2.282×10^{-3}	0.442
	G3DC-32	8.1	4.494×10^{-3}	0.366
	G3DC-36	9.1	4.595×10^{-3}	0.298
	Average		**2.354×10^{-3}**	**0.482**
			1.265×10^{-3}	**0.181**
Nonlinear Viscoelastic Prediction, 50°C			**4.466×10^{-3}**	**0.337**

6.2 Pavement Simulations

In this section the ability of the nonlinear viscoelastic constitutive model to predict the permanent deformation behavior of asphalt concrete pavements is investigated. A pavement structure is simulated and the results are compared to a rutting study performed with the Heavy Vehicle Simulator.

6.2.1 Heavy Vehicle Simulator Rutting Study

An extensive rutting study was performed with the Heavy Vehicle Simulator (HVS) as part of the Caltrans Accelerated Pavement Testing Program, CAL/APT.*(7)* The HVS, shown in Figure 6.16, is capable of applying a range of loads, from 20 kN to 200 kN. A variety of wheel configurations and tire types are possible. The typical configuration is half a truck axle. The loading is applied to a test section eight meters long and up to one meter wide, and the loading can be applied in either a channelized or wandering pattern. The load is either applied in one direction only (unidirectional) or in both directions (bidirectional) as the wheel moves forward and backwards along the test section modes. On average, the HVS applies approximately 15000 bidirectional (7500 unidirectional) load repetitions a day. The temperature of the tests is controlled with the use of a temperature control chamber containing heaters and air-conditioners.

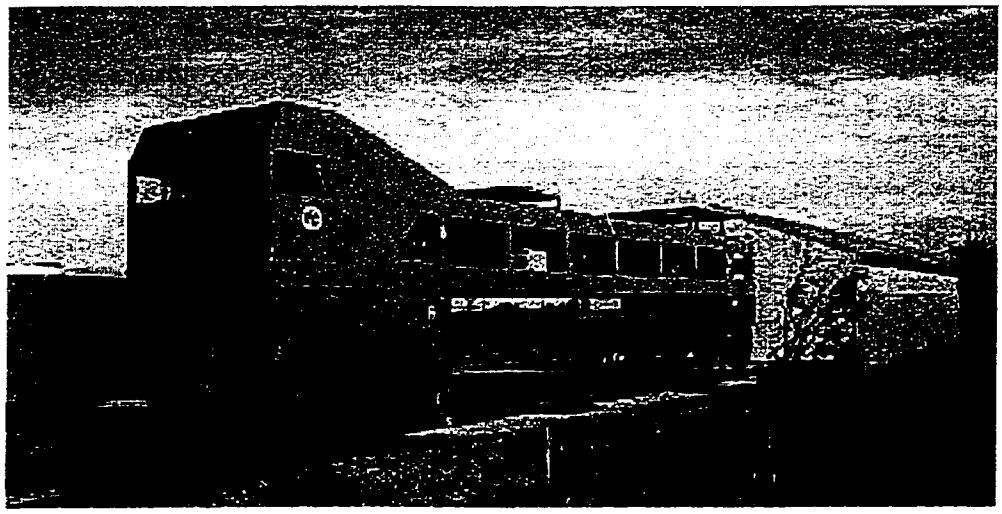

Figure 6.16 Heavy Vehicle Simulator

The rutting study was performed on the overlays constructed for the Goal 3 testing. The overlays were placed on an existing asphalt concrete pavement.*(41)* The mixes in the overlays were the same dense graded asphalt concrete (DGAC) and asphalt-rubber hot mix (ARHM) that were used to develop the constitutive model. The laboratory test results presented in Chapter 3 were performed on specimens obtained from the HVS test sections. Properties of the mixes were discussed in Chapter 3.

Nine sections were tested, as shown in Table 6.3. Most of the tests were run with either dual radial tires or a wide-base single tire. The load on the half axle is 40 kN, a standard axle load. The loading was applied in a unidirectional and channelized mode. One test, 513 RF, used an aircraft tire at 100 kN. The tire pressure depended on the type of tire. In each test the temperature at a depth of 50 mm was maintained at the target temperature of ± 2°C.

Table 6.3 HVS Rutting Study Test Program

Test section	Tire			Temperature at 50 mm depth (°C)	Overlay	
	Type	Pressure (kPa)	Load (kN)		Material	Thickness (mm)
505 RF	Dual bias	690	40	50	DGAC drained[1]	54
506 RF	Dual radial	720	40	50	DGAC undrained	78
507 RF	Wide-base single	760	40	50	ARHM undrained	76
508 RF	Wide-base single	760	40	50	ARHM undrained	73
509 RF	Dual radial	720	40	50	ARHM undrained	75
510 RF	Dual radial	720	40	50	ARHM undrained	35
511 RF	Wide-base single	760	40	50	ARHM undrained	35
512 RF	Wide-base single	760	40	40	DGAC drained	49
513 RF	Aircraft	1070	100	50	DGAC undrained	80

1 "Drained" indicates the original asphalt concrete pavement contained a drainage layer beneath the asphalt concrete

The rut depth used in the analyses was the vertical displacement from the original position. This is termed the "maximum rut depth below original surface." The "maximum rut depth" is the maximum difference between the bottom of rut and the height of the highest adjacent hump.*(73)* The rut depth is determined from the maximum displacement along a transverse profile. The transverse profiles were measured at 0.5 m intervals throughout the tests. Figure 2.2 illustrates some results from Section 508RF.

The test sections selected for the simulations were 506RF, which has the DGAC overlay, and 509RF, which has the ARHM overlay. Both tests used dual radial tires. The results from these test sections are presented with the simulation results in Sections 6.2.4 and 6.2.5 for the DGAC and ARHM, respectively.

6.2.2 Pavement Simulations

The simulations replicate the pavements as closely as possible. The simulations were time consuming, therefore it was preferable to reduce the three-dimensional (3D) representation of the pavement to a two-dimensional (2D) plane strain representation with the infinite third dimension being the direction of travel. As a check of the plane strain simulation, results from the 3D and plane strain simulations were compared. Most of the results presented are for the 2D, plane strain simulations.

6.2.2.1 Mesh and Boundary Conditions

The thicknesses of the overlays in the HVS test sections were 78 mm and 75 mm for the DGAC and ARHM, respectively. The original asphalt concrete layer over which the overlays were placed was approximately 160 mm at the DGAC section and 146 mm at the ARHM section. The underlying granular layers consisted of approximately 274 mm of base and 177 mm of aggregate subbase. In the simulations, the thicknesses of the layers were the same in both sections, to facilitate easy comparison between the DGAC and ARHM. The thickness of the overlay was 78 mm and that of the original asphalt concrete was 157 mm thick. The granular layers are combined into one 391 mm thick layer. The mesh used in the plane strain simulation is shown in Figure 6.17, and in Figure 6.18 for the 3D simulation.

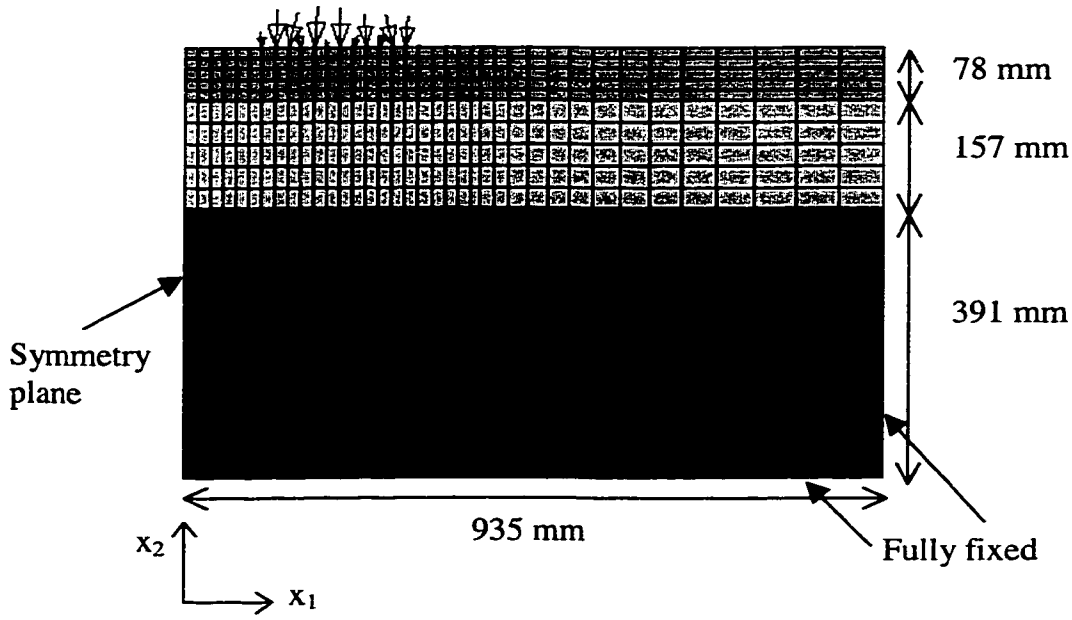

Figure 6.17 Mesh for Plane Strain Pavement Simulations

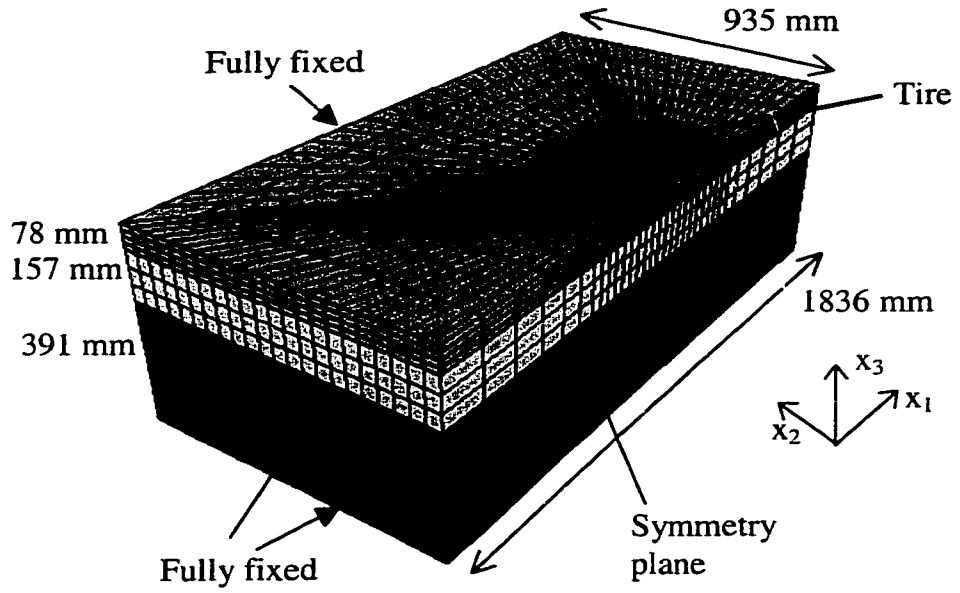

Figure 6.18 Mesh for Three Dimension Pavement Simulations

The boundary conditions imposed in the simulations are also shown in Figures 6.17 and 6.18. In addition to the boundary conditions shown, the 3D mesh was also modeled with the boundary conditions in the x_1 planes being fixed in the x_1 direction only, to replicate the plane strain boundary conditions of the 2D simulation. Differences in the solutions were negligible.

6.2.2.2 Material Properties

The nonlinear viscoelastic model was used for all the asphalt concrete layers in the simulations. The material properties are given in Tables 5.1 and 5.2. The shift factor functions and coefficients are given in Equations (4.15), (4.16) and (4.21) for the DGAC and in Equations (4.17), (4.18) and (4.21) for the ARHM. The temperature of the overlays was 50°C, which was the temperature at a depth of 50 mm in the HVS tests.

The original asphalt concrete layer contained a conventional asphalt concrete mix. The DGAC material properties were used to model this layer. The temperature of this was 44°C, which is a reasonable average of the temperature during the HVS tests.*(7)*

Linear elasticity was assumed for the granular layer. The Young's modulus was 250 MPa and the Poisson's ratio was 0.35. This modulus was estimated from the moduli of the aggregate base and subbase, determined with available laboratory and falling weight deflectometer data.*(7)*

A mixed element formulation is used for the overlays and asphalt concrete layers and displacement elements are used for the granular, linear elastic layer.*(67)*

6.2.2.3 Loading

The two sections selected for comparison with the simulations were both loaded with dual radial tires, with a tire pressure of 720 kPa and a half-axle load of 40 kN with 20 kN on each tire. To simplify the simulation, only one tire was modeled and the effect of both tires was captured through symmetry.

The specific tire used in the dual radial configuration was a Goodyear G159A, 11R22.5. The contact stress distribution of this tire was measured using the VRSPTA, described in Chapter 2, and this distribution was used in the simulations.*(11, 12)* The full load pattern is shown in Figure 6.19. For the plane strain simulation, the loading, shown in Figure 6.19, was averaged along the x_1 axis to obtain the load pattern shown in Figure 6.17. Figure 6.20 shows this load pattern in more detail, and it is clear that the load was not uniform across the width of the tire. The loads were measured on pins on the VRSPTA, which were spaced at discrete 17 mm intervals. Sometimes a pin was located in the grooves between the tire treads, and therefore measured no load. The loading actually applied to a pavement is more continuous than these data represent.

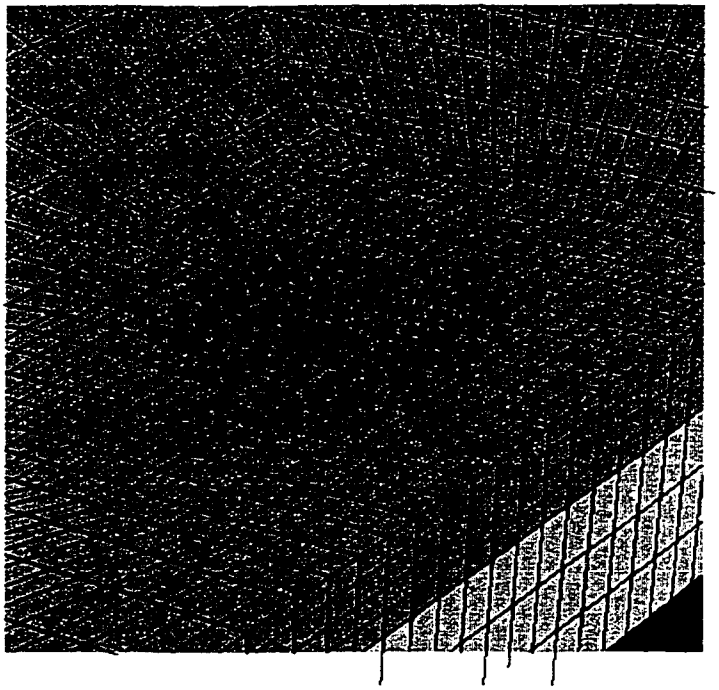

Figure 6.19 Load Distribution of Radial Tire on 3D Mesh

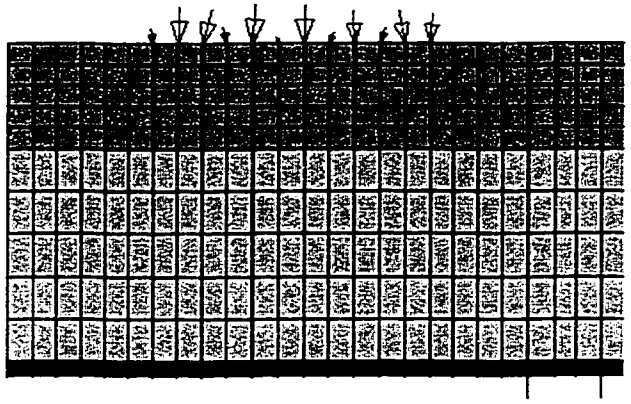

Figure 6.20 Load Distribution of Radial Tire, Reduced to 2D

The wheel speed of the HVS was approximately 8 km per hour, or 2.22 meters per second. The time between load applications on a point in the pavement was approximately 7.5 seconds. In the simulations, the time of loading on a material point

was assumed to be 0.1 seconds. The load was applied in a waveform shown in Equation (6.3)

$$q = \sin^2(\pi t) \tag{6.3}$$

where q is the proportion of the load, π is pi, and t is the time during the 0.1 seconds that the load was applied.*(12)* It was discussed earlier that the selection of the time steps for application of the load and calculation of the solution is an important issue for obtaining accurate results. The time steps used in these simulations were carefully selected to ensure that the speed of the solution did not compromise the solution accuracy.

6.2.3 Comparison of Plane Strain and Three Dimensional Simulations

A comparison of the rutting profiles after a few repetitions in the plane strain and 3D simulations indicated large discrepancies in the recoverable displacement and the amount of permanent deformation accumulated. The rut depth from the plane strain simulation was significantly larger. Figure 6.21 shows the 3D profile, which had a maximum rut depth of approximately 0.012 mm. Figure 6.22 shows both the 2D and 3D profiles, but because of the magnitude of the rutting in the 2D simulation, in the figure the 3D pavement appears to have hardly rutted at all. The maximum rut depth in the 2D pavement was approximately 2.5 mm.

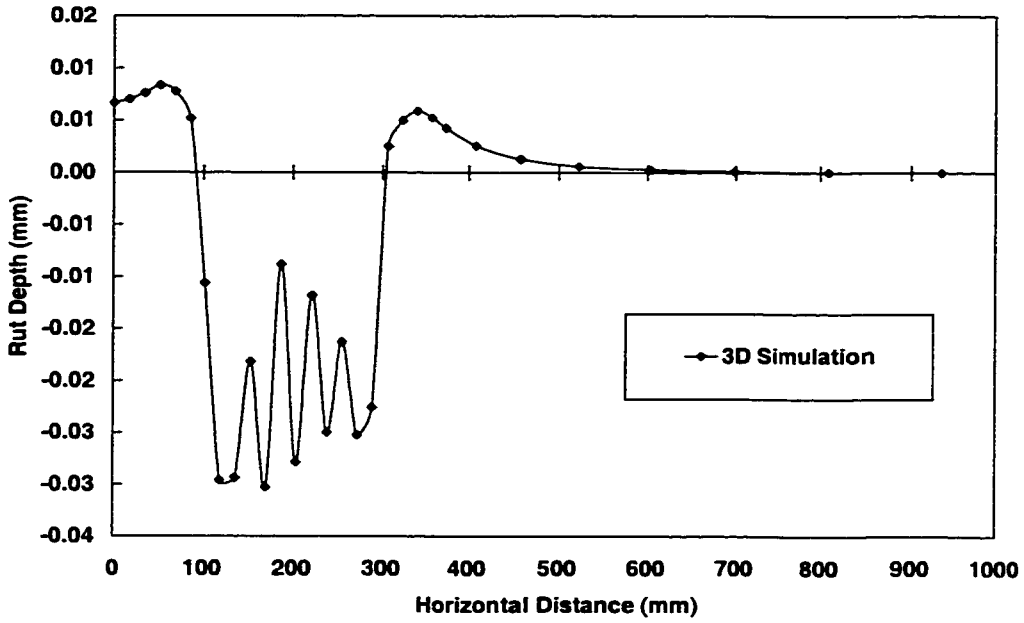

Figure 6.21 Rutting Profile in 3D Pavement Simulation

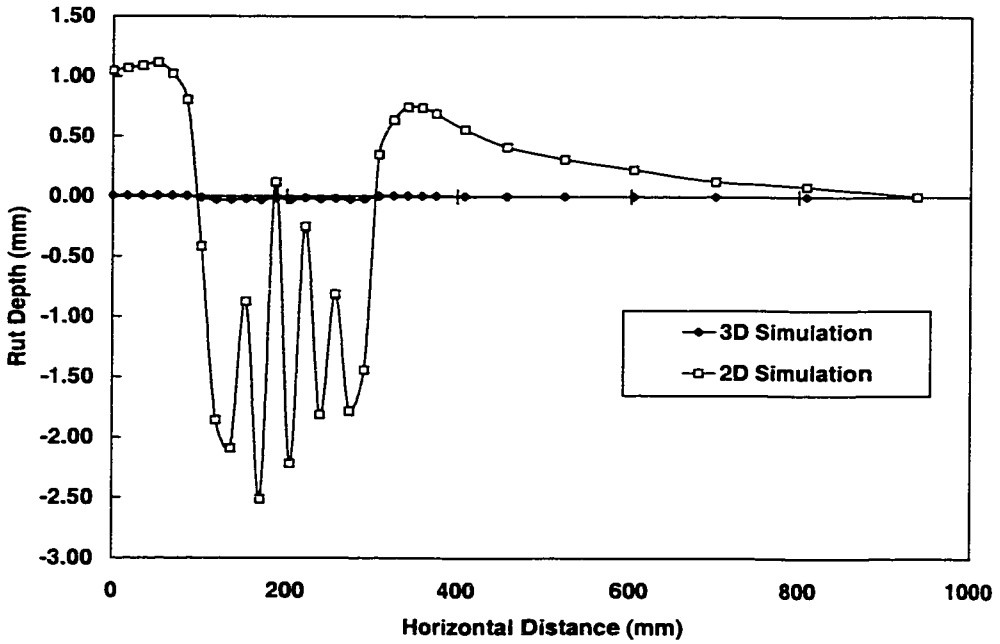

Figure 6.22 Rutting Profile in 2D and 3D Pavement Simulations

The plane strain conditions assume the pavement is infinitely long in the third dimension, and the load and boundary conditions are the same along this infinite dimension. The tire load, shown in Figure 6.20, was therefore effectively a strip load. It was expected that the application of this load would result in more deformation, because the total load is higher.

In an effort to determine if these results were in error, linear elastic simulations were run with one material and the same mesh dimensions in 2D and 3D were run. A point load was applied and the results were compared with the theoretical solutions for a point load applied on a semi-infinite half space. These analyses are presented in Appendix 3. The theoretical solutions confirmed the simulation results. For the same material properties used in the simulations, the 3D displacements were significantly smaller than those of the 2D approximation were. It was therefore concluded that the finite element code and the constitutive model were calculating the correct solution. Although the large difference between the 2D and 3D simulations seems unreasonable, it is a modeling issue rather than an error.

A plausible explanation for the differences is that the load is only applied for the time in which the tire is in contact with a point on the pavement. In a pavement, when the tire travels to an adjacent point, but is not actually in contact with it, some load is still being imparted to the point. In the 3D simulations this is not accounted for, and the smaller

amount of deformation is therefore expected. The equivalent strip load in the 2D plane strain simulations effectively applies the adjacent loads continuously, which is more aggressive than the real moving tire load, and therefore results in more deformation.

A comparison of the deformation in the 2D and 3D simulations and the HVS test confirms that the 3D predicts too little deformation, and the 2D too much (Figure 6.4). Therefore, simply scaling down the 2D load to match the 3D deformations would not provide a reasonable estimate of the rutting. Extensive analyses of the loading and deformations in the 2D and 3D simulations may give more insight how best to modify the simulations to obtain more reasonable results.

To reduce the 2D deformations to match those of the HVS test the 2D load was reduced to one-third of the actual load measured with the VRSPTA. Reducing the load reduced all the deformations proportionately. The one-third load was used for the remainder of the analyses in this Chapter and in Chapter 7.

6.2.4 Simulations of DGAC Pavement

The 2D plane strain simulation of the pavement with the DGAC overlay was run for 7209 repetitions. The data collected included the displacements and stresses at the end of the load repetition, for a selected number of repetitions. There was no elastic displacement data available for the HVS test sections. Therefore, the analyses presented focus on the

accumulation of the residual deformations and stresses present at the end of the load repetition.

6.2.4.1 Effect of VRSPTA Loading

The upper section of the rutted pavement after 3509 repetitions in the simulation is shown in Figure 6.23. The rut profile is not smooth because the irregular tire loading results in large localized effects. The nodes with the larger loads deformed considerably more than the adjacent nodes, which had much smaller loads. Although small distinct ridges from the tire tread pattern are observed in the HVS test section, the magnitudes of the local effects in the simulation are not reasonable and are largely due to the coarseness of the VRSPTA load data. The loading actually applied to a pavement is more continuous than the VRSPTA data, and so the localized effects immediately under the load were not reasonable. The VRSPTA data do, however, provide a good representation of the distribution of the tire contact stresses away from the immediate location where the load was applied. Therefore, the pavement response was more reasonable at these points. On average the rut profile is reasonable.

It appears that at 50°C, the temperature at which these simulations were performed, the material was too soft, which allowed the large difference in the deformations at adjacent nodes. The shear stiffness of the material is dependent on both the temperature and the maximum strain in the time history. As one point in the material deforms more than a

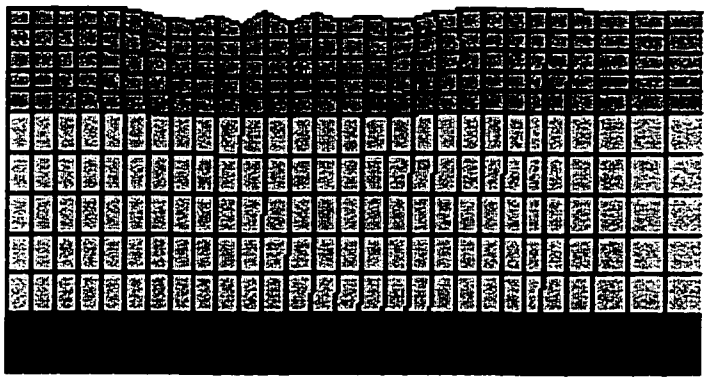

Figure 6.23 Pavement Rutting after 3509 Repetitions (26317 seconds), DGAC

nearby point, the stiffness of that material point decreased more, enabling an even greater differential in the deformation with further loading. If the loads were applied continuously along the nodes, this problem would be reduced.

To alleviate the localized effects and the increased deformation under the large loads, the extremes in the rut profile were averaged. The maximum rut depth reported for each repetition is the average of the four largest rut depth values. This value gives a reasonable estimate of the rut depth, and smoother rut profiles. Figure 6.24 shows the original and averaged rutting profiles at 11 and 3509 repetitions.

6.2.4.2 Location of Rutting in Pavement Depth

It was also observed, as shown in Figure 6.23, that the deformation occurred in the upper section of the pavement, immediately beneath the load. Little deformation occurred in

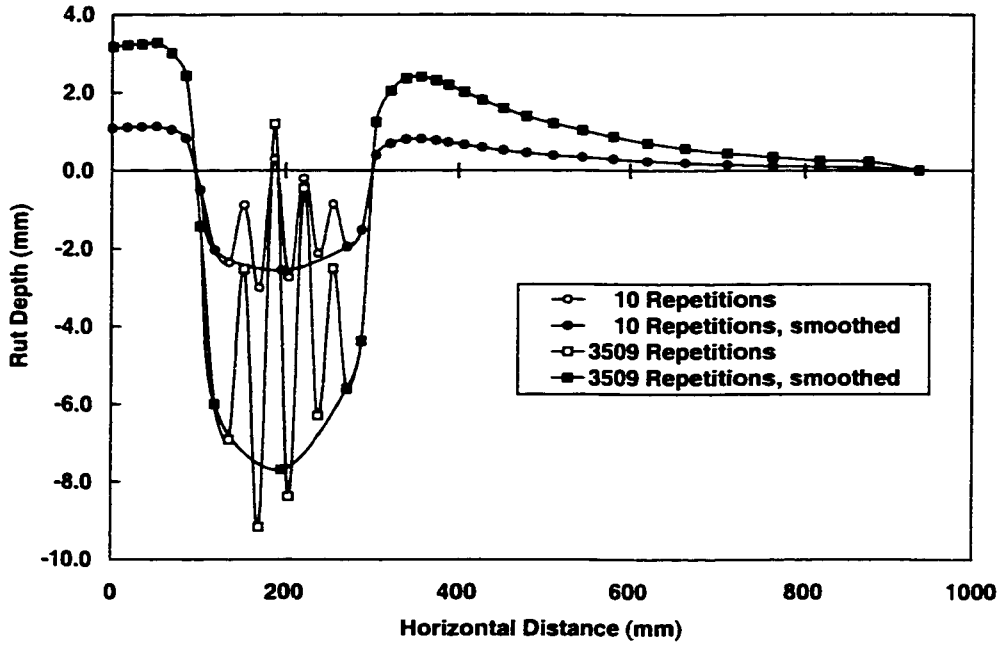

Figure 6.24 Rutting Profile in DGAC Pavement, 10 and 3509 Repetitions

the upper part of the second layer (original asphalt concrete) and no deformation occurred in the lower part of the second layer. The same behavior was apparent at the end of the simulation, 7209 repetitions shown in Figure 6.25, and agrees with the behavior in the HVS test section.*(7)*

The distribution of shear stresses and strains in the pavement also showed that the rutting occurred in the upper part of the pavement, underneath and at the edge of the tire. Figures 6.26 and 6.27 show the shear strain and shear stress distribution after 98 repetitions, and Figures 6.28 and 6.29 show the same after 5509 repetitions. The shear strains were concentrated at the edge of the tires, below the surface of the pavement. The shear strains on the surface of the pavement in the middle of the tire were ignored

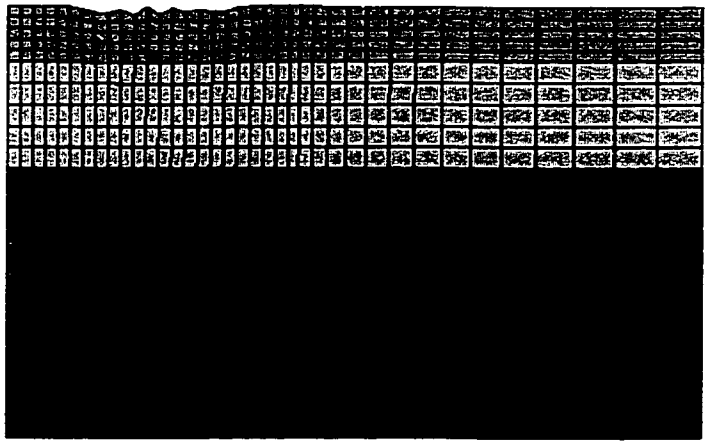

Figure 6.25 Pavement Rutting after 7209 Repetitions (54067.5 seconds), DGAC

because they were likely due to the discrete loading distribution from the VRSPTA data. The shear strain distribution was the same for both repetitions, but the magnitude increased at the higher repetitions. Figures 6.26 and 6.28 are not plotted on the same scale, if the same scale is used the higher magnitudes in Figure 6.28 mask the distribution in Figure 6.26.

The stress distributions in Figures 6.27 and 6.29 are plotted on the same scale and the patterns are again similar. The peak shear stresses also occurred under and at the edge of the tire. At the higher repetitions the magnitude of the shear stress underneath the tires is larger and penetrated deeper into the pavement. The shear stresses were also relatively high at the interface between the overlay and the existing asphalt concrete layer.

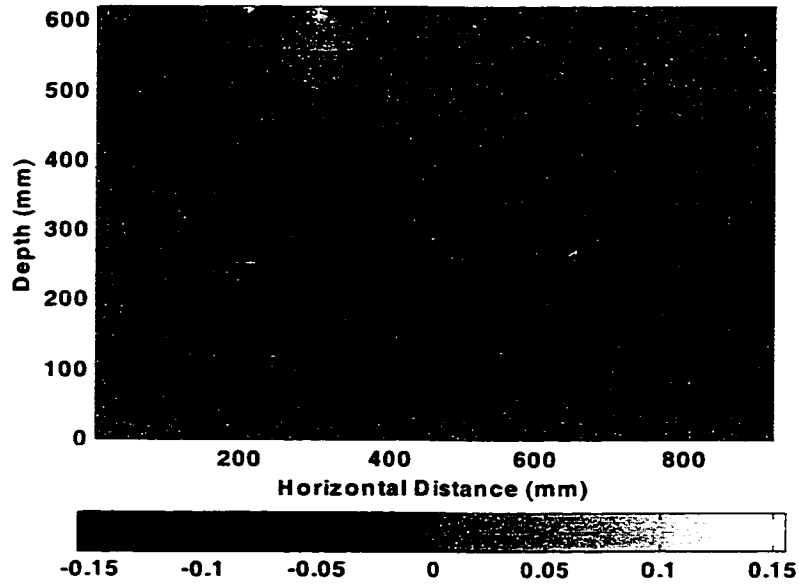

Figure 6.26 Shear Strain in DGAC Pavement, 98 Repetitions

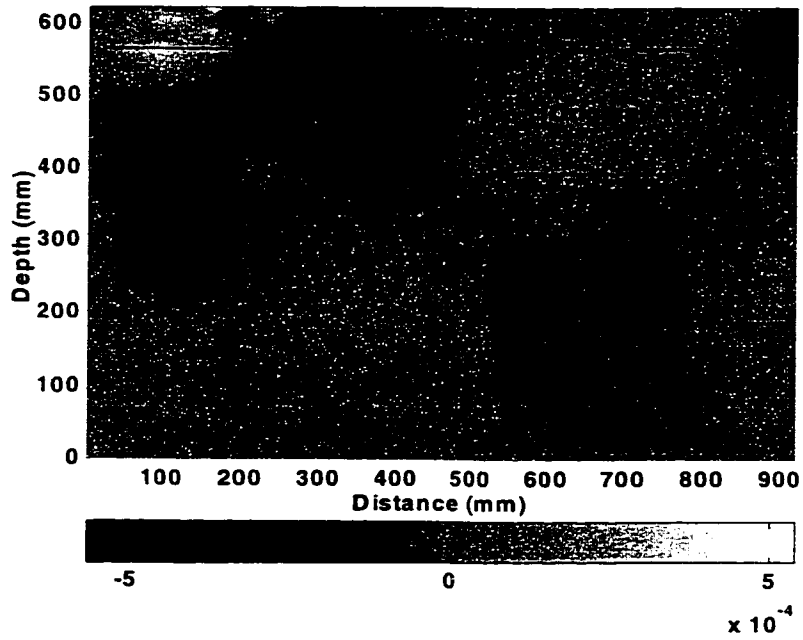

Figure 6.27 Shear Stress (MPa) in DGAC Pavement, 98 Repetitions

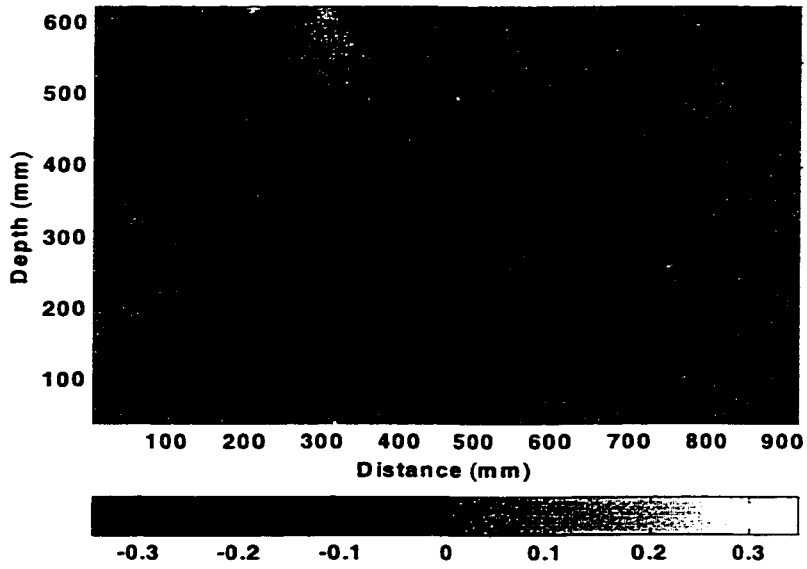

Figure 6.28 Shear Strain in DGAC Pavement, 5509 Repetitions

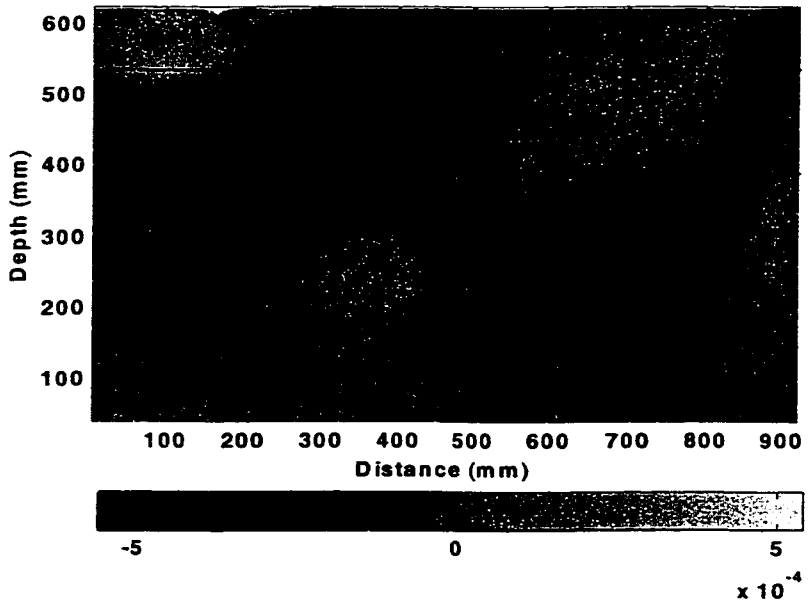

Figure 6.29 Shear Stress (MPa) in DGAC Pavement, 5509 Repetitions

6.2.4.3 Shape of the Rutting Profile

In Figures 6.30, 6.31, 6.32, and 6.33 the smoothed rut profiles are superimposed on the DGAC HVS test section (506RF) profiles at 125, 500, 1000 and 2500 repetitions. The rut profile from the simulation is the thicker line, and the mirror image is plotted to represent the dual tires. The thinner, dashed lines are the data from thirteen locations of the HVS rutting study. It is important to note that the proportion with which the load was reduced in the 2D simulations was selected to match the permanent deformation in the HVS test sections. Therefore the good agreement in the magnitude of the rut depths observed in the figures was expected and observations can still be made regarding the shape of the rut profile and the rate of permanent deformation accumulation.

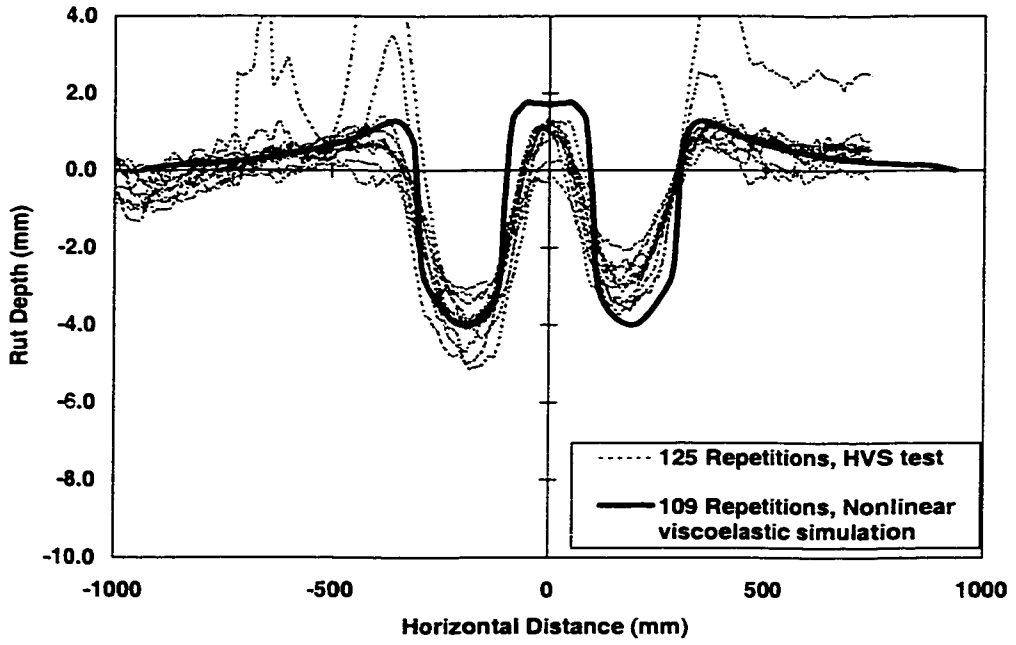

Figure 6.30 Comparison of Rutting Profiles in DGAC Pavement Simulation and Section 506 RF, 125 Repetitions

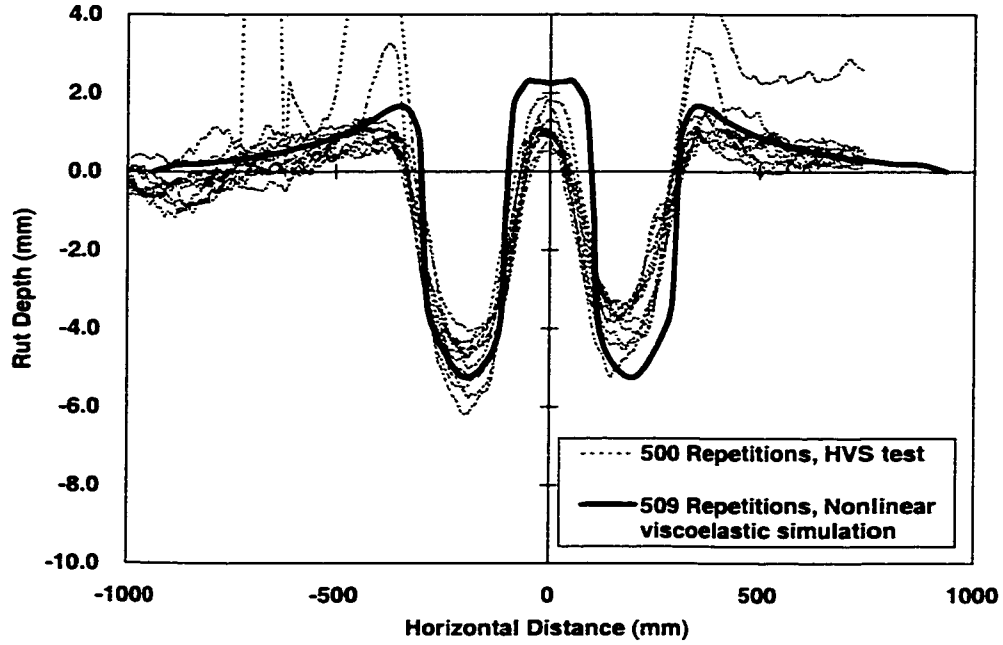

Figure 6.31 Comparison of Rutting Profiles in DGAC Pavement Simulation and Section 506 RF, 500 Repetitions

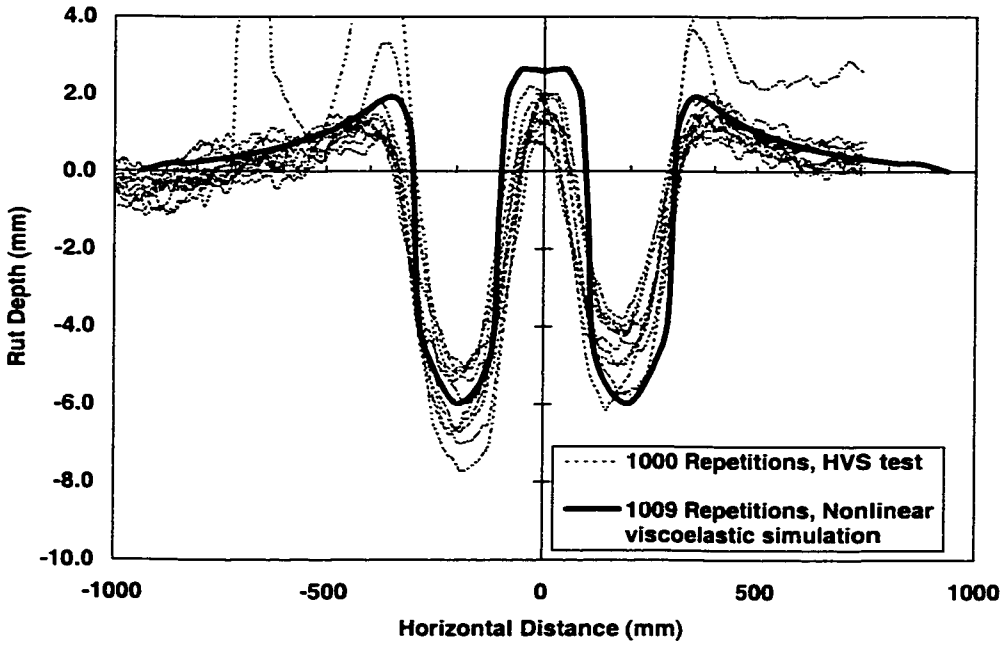

Figure 6.32 Comparison of Rutting Profiles in DGAC Pavement Simulation and Section 506 RF, 1000 Repetitions

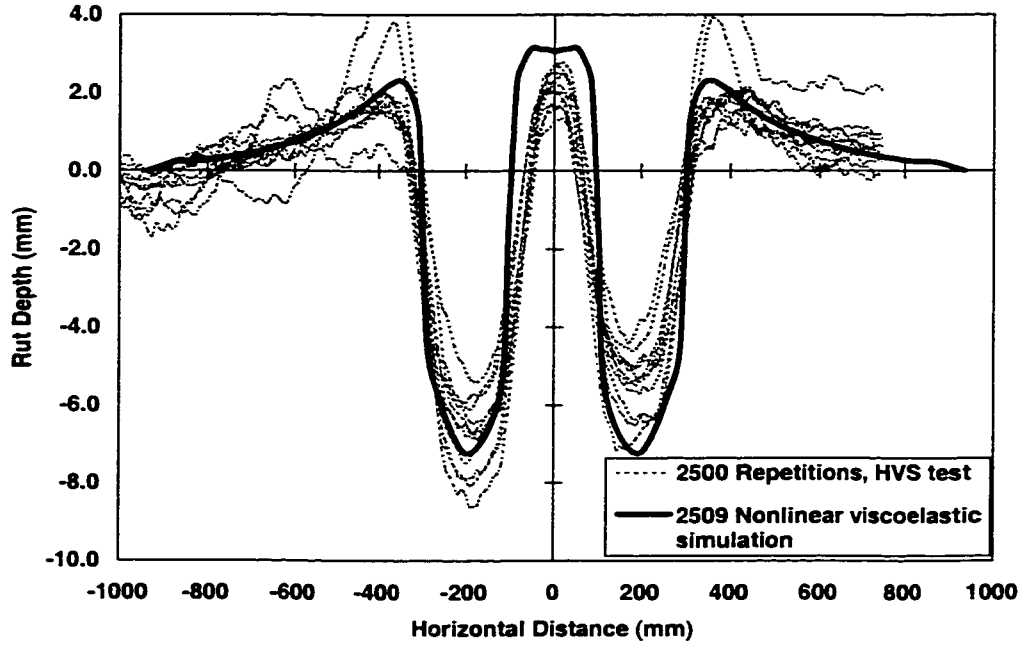

Figure 6.33 Comparison of Rutting Profiles in DGAC Pavement Simulation and Section 506 RF, 2500 Repetitions

The "humps" present on the sides of the rut matched those of the HVS test section. The humps from the simulation had sharper edges, which was not unexpected considering the loading issues discussed earlier. It has also been observed in the HVS test sections that the humps were more severe than the profiles obtained from the laser profilometer data. Many of the methods used to predict rutting in asphalt concrete pavements, discussed in Chapter 2, do not predict these humps.

6.2.4.4 Permanent Deformation Accumulation

The accumulation of rutting in the HVS test section is shown in Figure 6.34. The maximum rut depth below the original surface for each transverse profile and the average

are drawn and the 12.5 mm terminal rut depth is shown as the dashed line. The rutting accumulated rapidly in the early part of the test, and then the rate of accumulation slowed. Some of the average values appear unreasonable. In an accelerated test, like the HVS test, rutting in a pavement does not recover during the test, which some data indicate. These data are likely due to placement of the laser profilometer measuring device. In Figures 6.30 to 6.33, some of the inaccurate data is visible. These outliers were excluded from the average maximum rut depth, as shown in Figure 6.34.

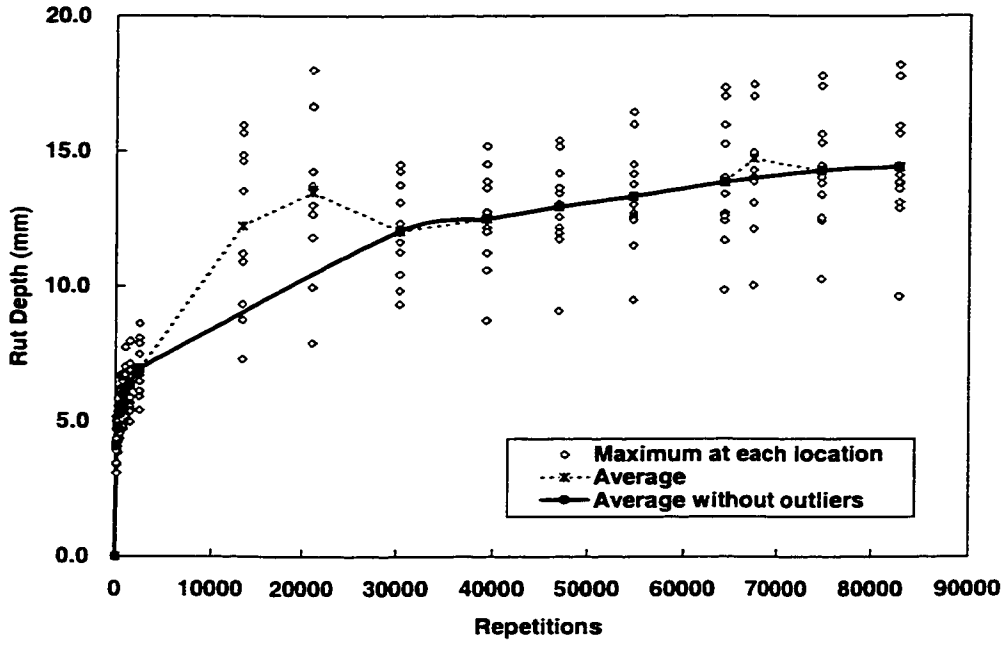

Figure 6.34 Permanent Deformation Accumulation in HVS Test Section, DGAC Section 506 RF

In Figure 6.35 the first 10000 repetitions of the HVS test are compared to the permanent deformation from the 7209 repetitions run in the simulation. The shapes of the curves are

very similar, with the simulation data showing the same rapid accumulation of rutting in the early stages of the test, after which the rate of rutting slowed. In Figure 6.35 it seems as if after approximately 1000 repetitions the simulation results predicts more rutting than the HVS test. However, Figure 6.34 shows that for the HVS test the average data curve has no data between approximately 2500 and 30000 repetitions. From the shape of the curve in Figure 6.34 it is reasonable to assume that if more data were available for the range the HVS data would follow a similar trend to the simulation data. This observation is substantiated in Figure 6.36, which shows a logarithmic plot of the same data as in Figure 6.35. Both curves are approximately linear although at the end of the simulation the curve appears to be deviating from the linear trend. This may indicate that the rate of rutting accumulation is decreasing. In the range of repetitions simulated, the DGAC mix matches the HVS test section results reasonably well.

6.2.5 Simulations of ARHM Pavement

A 2D plane strain simulation was performed on the same pavement structure as in the previous section with the ARHM material properties. The same large differences in the nodal displacements were present, due to the application of the radial tire load data. Therefore the rut profiles were again smoothed.

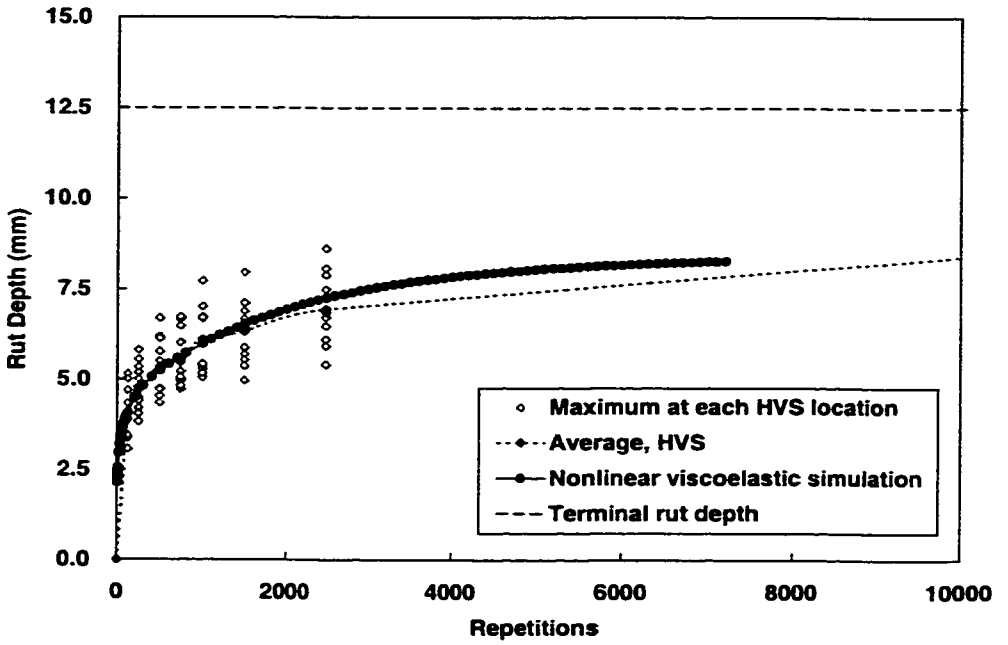

Figure 6.35 Comparison of Permanent Deformation in HVS Test Section and Simulation, DGAC

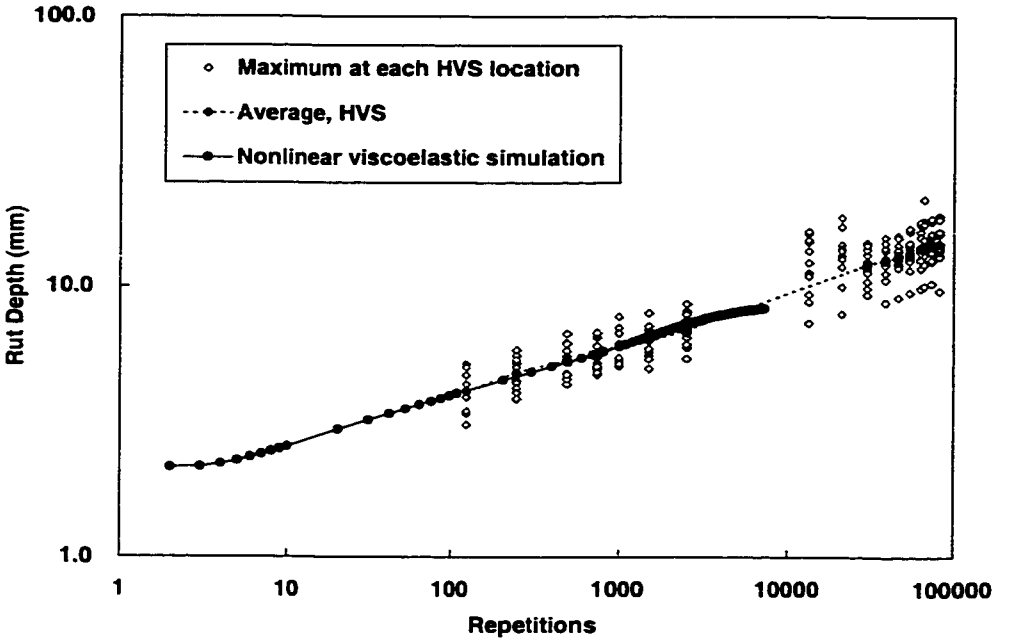

Figure 6.36 Comparison of Permanent Deformation in HVS Test Section and Simulation, DGAC, Logarithmic Scale

6.2.5.1 Shape of the Rutting Profile

The rut profiles for 500, 1000, and 2500 repetitions for the HVS Test Section, 509 RF, and the ARHM simulation are shown in Figures 6.37 to 6.39. The same "humps" are apparent and are similar in shape to those of the HVS tests. At 500 repetitions, the simulation profile matched the HVS test data. As the repetitions increased, the fit to the shape of the profiles was still good, but the magnitude of the simulation rut depths was becoming slightly smaller than the majority of the HVS test data (Figure 6.39).

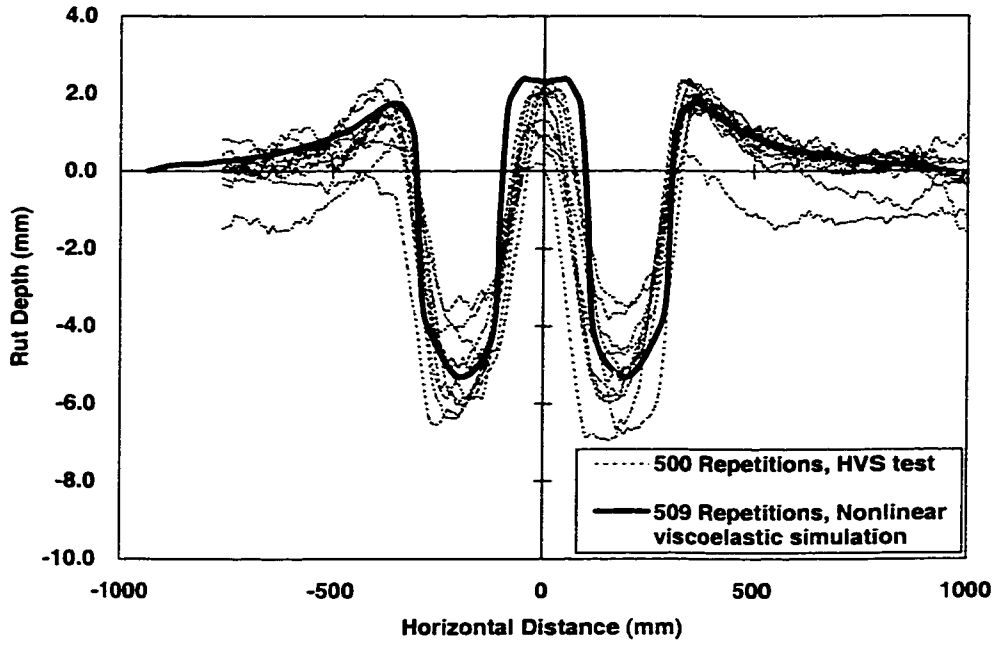

Figure 6.37 Comparison of Rutting Profiles in ARHM Pavement Simulation and Section 506 RF, 500 Repetitions

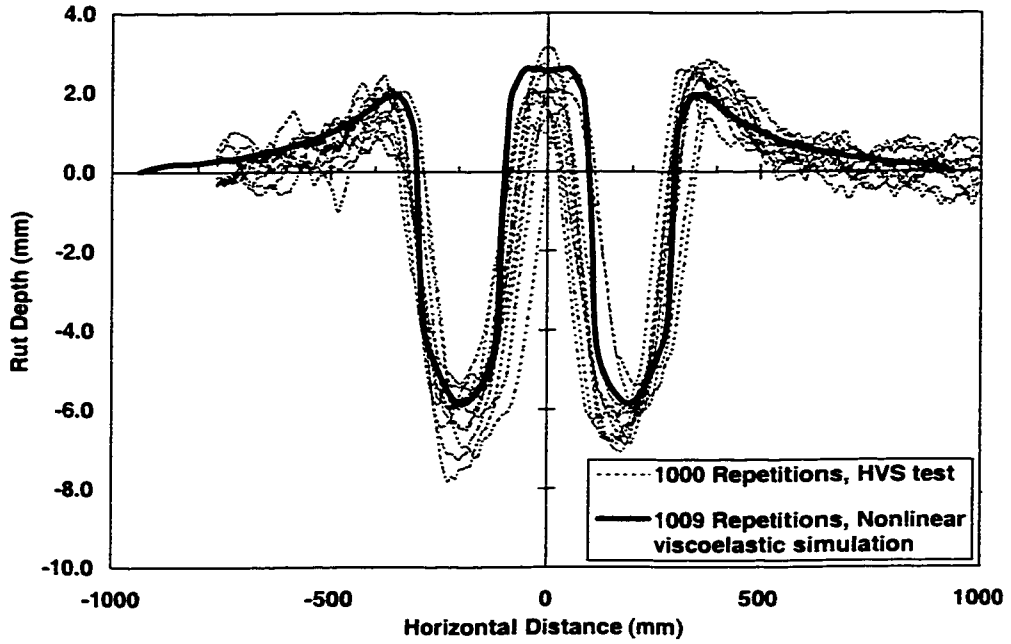

Figure 6.38 Comparison of Rutting Profiles in ARHM Pavement Simulation and Section 506 RF, 1000 Repetitions

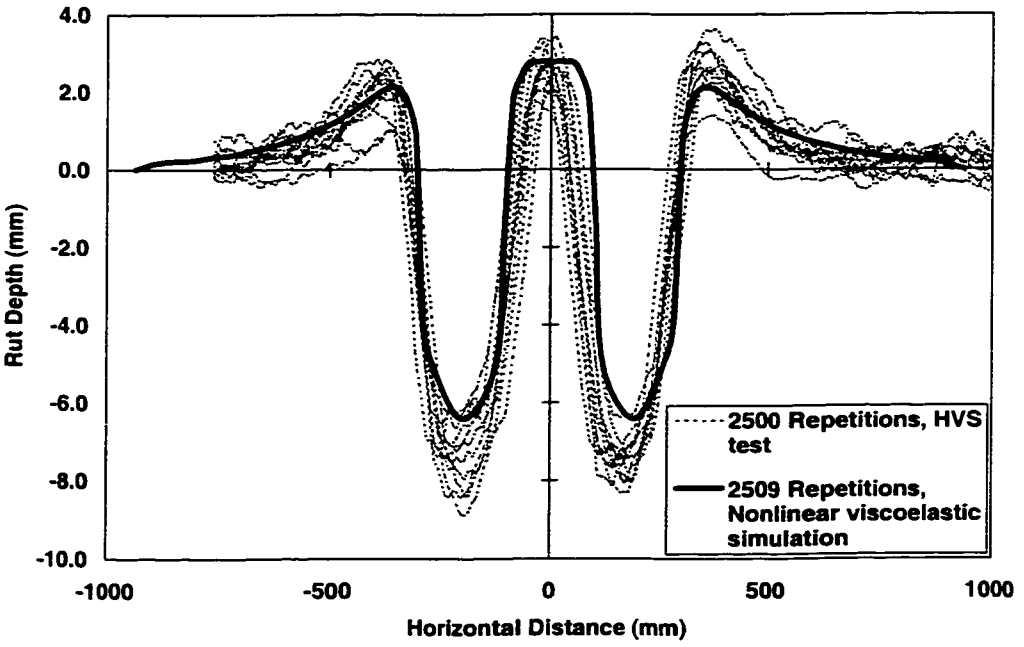

Figure 6.39 Comparison of Rutting Profiles in ARHM Pavement Simulation and Section 506 RF, 2500 Repetitions

6.2.5.2 *Permanent Deformation Accumulation*

The rutting accumulation data shown in Figures 6.40 and 6.41 also show the ARHM pavement simulation predicts less, and, in the early stages of the simulation, a slightly slower rate of rutting than the HVS test section. After approximately 1000 repetitions the rate of rutting accumulation in the simulation is fairly small and is decreasing. The rut depth appears to asymptoting to some value. This behavior does not match the HVS test data.

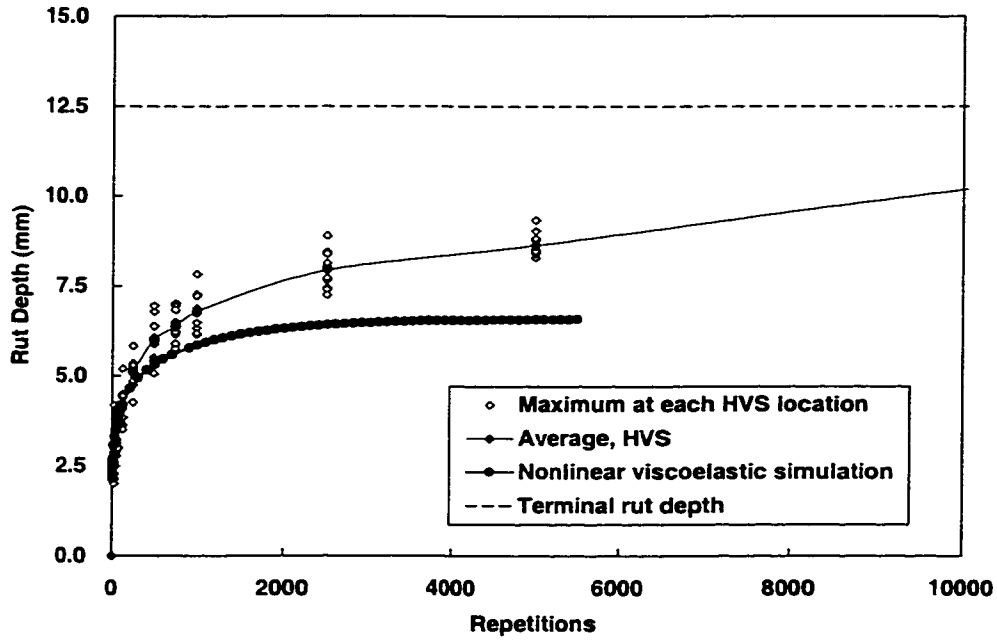

Figure 6.40 Comparison of Permanent Deformation in HVS Test Section and Simulation, ARHM

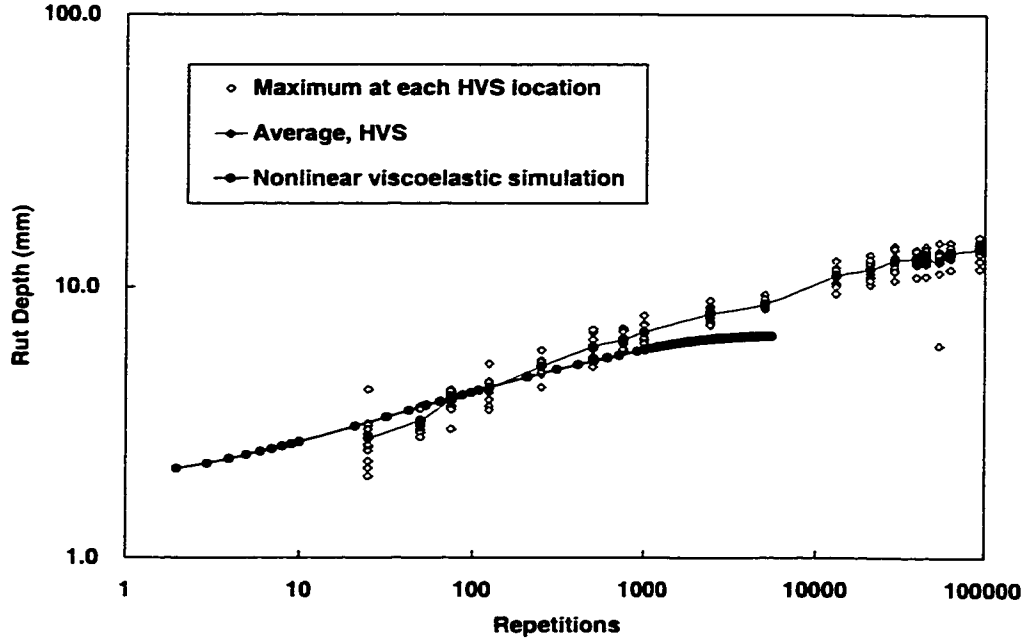

Figure 6.41 Comparison of Permanent Deformation in HVS Test Section and Simulation, ARHM, Logarithmic Scale

The ARHM in the HVS test section had a higher air-void content than the DGAC. During the test the ARHM air-void content decreased from a starting value of 10 percent to 7.5 percent at the end of the test.*(7)* This densification accounted for approximately 2 mm of vertical deformation, which is not accounted for in the nonlinear viscoelastic model. This is a reason for the rut accumulating in the simulation at a slower rate than the HVS test. The air-void content in the DGAC reduced from 4.7 percent to 4 percent. This small decrease did not significantly contribute to the rut accumulation in the HVS test. This may account for the improved fit of the DGAC simulation to the HVS test section.

The shape of the simulation rut depth versus repetition curve is similar in shape to the linear viscoelastic RSST simulation (Figure 6.9). The similarity between the shapes of the curves indicates that in the later stage of the ARHM pavement simulation, the linear viscoelastic bulk component of the constitutive model may be dominating the material response. If more repetitions were run in the DGAC pavement simulation, the same behavior might be apparent after 7000 repetitions. The slight decrease in the accumulation of rutting may indicate the early stage of this behavior (Figures 6.35 and 6.36).

No data for the volumetric properties of the ARHM mix are available. Therefore, the same bulk properties, obtained from a mix very similar to the DGAC mix, were used for both mixes. These properties may not be reasonable for the ARHM mix, particularly because the air-void contents of the mixes were significantly different and therefore the amount of densification that occurs in the mixes was different. A brief investigation of the effect of the bulk properties was performed. The results revealed that reducing the bulk material properties by 25 percent had no effect on the rutting accumulation for the relatively small number of repetitions run in the simulation. This demonstrates that the deformation is controlled by the shear component of the model, especially in the early stages of a test.

The load on the 2D plane strain simulation was reduced to obtain permanent deformation in the DGAC simulation matching the HVS test sections. The ARHM data may have shown an improved fit if the load was adjusted to match the ARHM field performance. However, the rate of rutting accumulation would still be different from the HVS test section.

6.2.5.3 Location of Rutting in Pavement Depth

In the ARHM pavement simulation, the rutting again occurred in the upper part of the pavement, with little rutting evident at the bottom of the existing asphalt concrete layer, as shown in Figure 6.42. The shear strain distribution was similar to that of the DGAC and is shown in Figure 6.43 for 5509 repetitions, the end of the simulation.

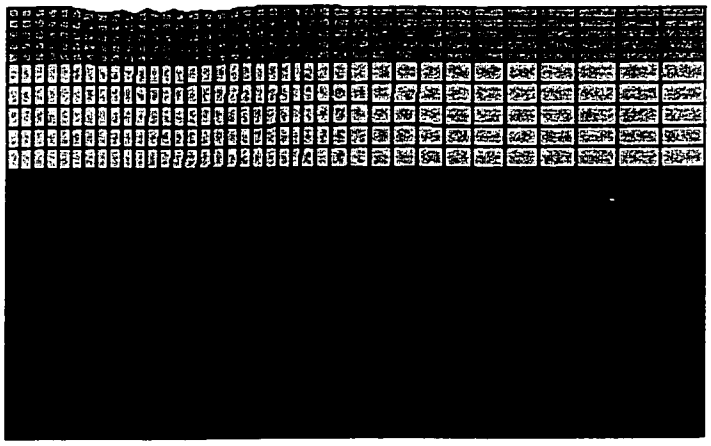

Figure 6.42 Pavement Rutting after 5509 Repetitions (41317.5 seconds), ARHM

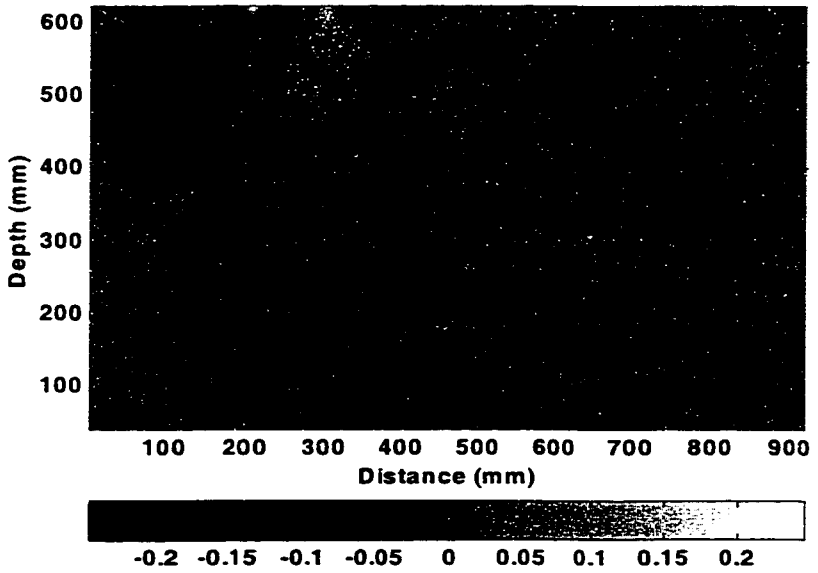

Figure 6.43 Shear Strain in ARHM Pavement, 5509 Repetitions

The maximum shear strains were located underneath the tire, close to the surface of the pavement and under the edge of the tires. The magnitude of the shear strains throughout the simulations was in the same range for both the DGAC and ARHM simulations. Observations from trenches cut in the HVS test sections also showed most of the deformation occurred underneath and at the edge of the tire.

6.2.6 Comparison of DGAC and ARHM Simulation Results

A comparison between the rut profiles of the DGAC and ARHM simulations after 3509 load repetitions is shown in Figure 6.44 for the single radial tire modeled in the simulation. The shapes of the profiles are the same, which, as noted earlier, match the

behavior in the HVS test sections. The magnitudes of the maximum rut depths are different. The rutting accumulation for both simulations and the average of the HVS test sections is shown in Figure 6.45.

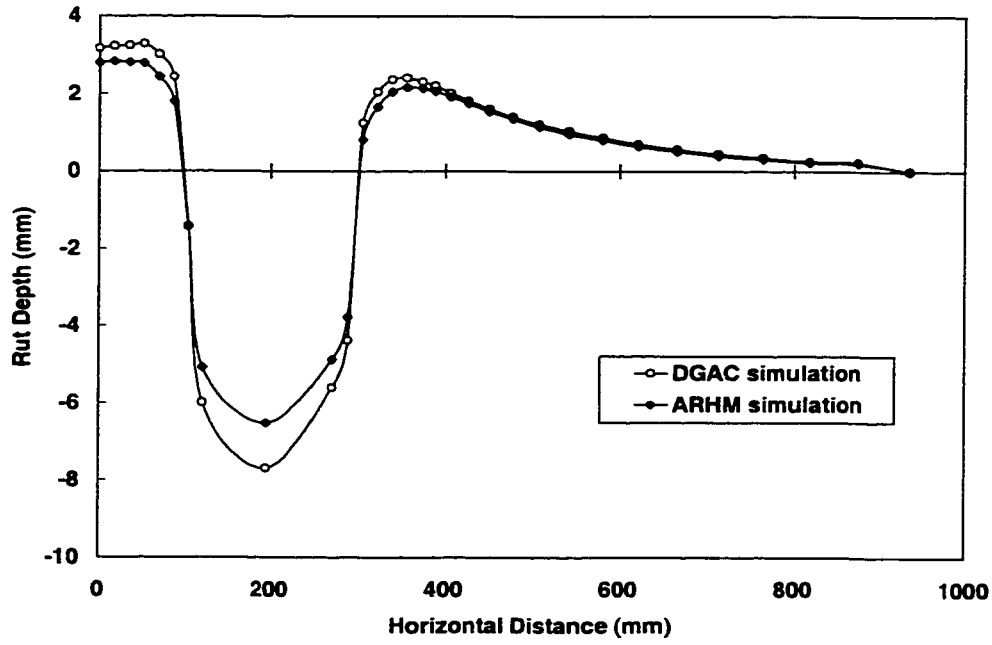

Figure 6.44 Comparison of Rut Profiles in DGAC and ARHM Simulations, 3509 Repetitions

The ARHM HVS test section rutted more than the DGAC section, whereas the opposite result was obtained in the simulations. The ARHM rut depth approaches an asymptotic value earlier than the DGAC simulation. The amount of rutting accumulated in the ARHM pavement was smaller than the ARHM HVS test section, although if the densification due to the reduction in the air-void content were accounted for in the model the differences would be less. In addition, if the load magnitudes were increased for the

ARHM simulation the differences would be reduced. It would be unreasonable to reduce the load by different factors for each mix.

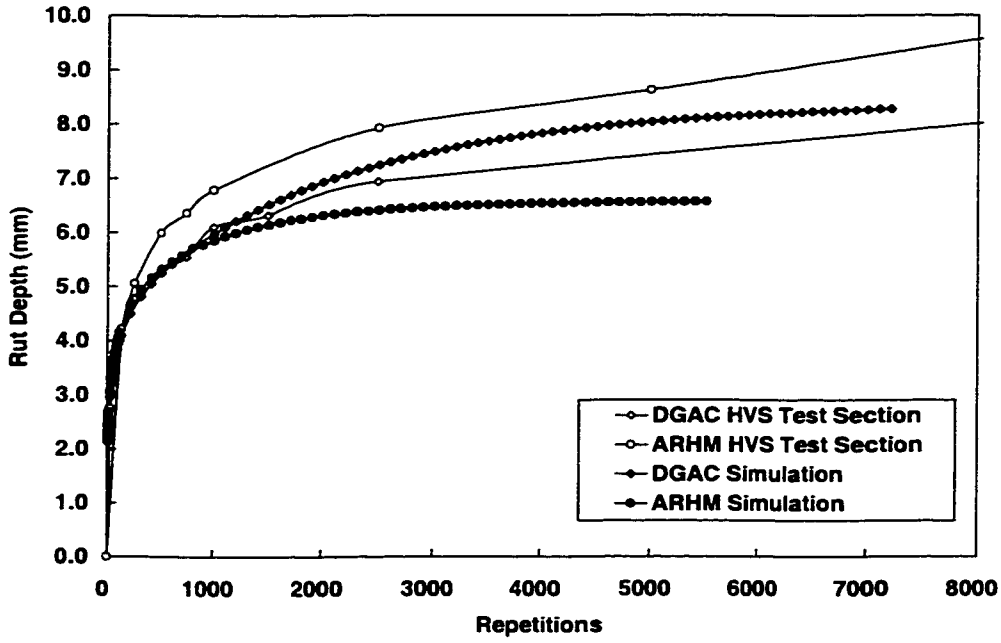

Figure 6.45 Comparison of Rutting Accumulation for DGAC and ARHM Simulations and HVS Test

The shear material properties of the DGAC and ARHM appeared very similar in Chapters 4 and 5, and the bulk properties were assumed to be the same. The fits to the shear master curves were not as good for the ARHM as for the DGAC. The different behavior observed in the DGAC and ARHM simulations may be a result of these differences in material properties.

Although the ARHM simulation results did not match the HVS test data as well as the DGAC simulation, the results were still reasonable. The behavior of the ARHM mix in the pavement simulation needs to be investigated further to determine the ability of the nonlinear constitutive model to capture the behavior of modified binders. The model appears to have the potential to capture the behavior of modified binders, although definite conclusions cannot be drawn with the data presented in this section.

6.2.7 Recovery After Removal of Loading

All the analyses presented for the pavement simulations used the residual deformation present at the end of the 7.5 second load cycle. If a load is not reapplied at the end of the load cycle, the material will continue to recover. To investigate how much recovery occurs, the DGAC pavement was allowed to relax for an additional 5000 seconds (equivalent to 666 load repetitions) after removal of the load at 22567 seconds (3009 repetitions). The displacement was recorded during the recovery, and is shown in Figure 6.46. Immediately after the last load is removed, the deformation recovered considerably, but the rate of recovery diminished rapidly, and a return to zero deformation would only occur at infinite time, if at all.

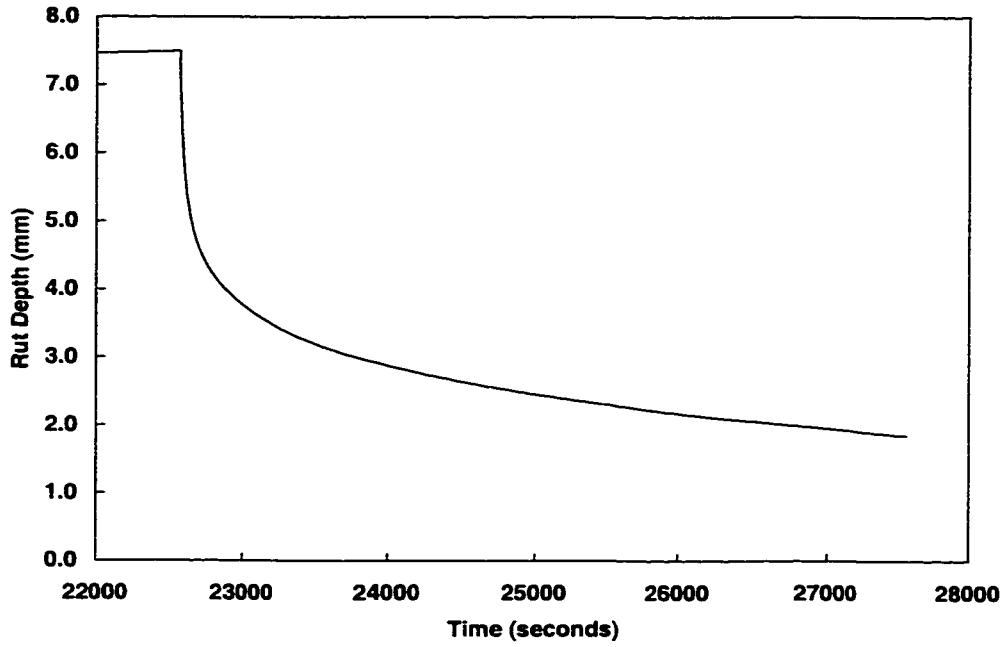

Figure 6.46 Relaxation After Removal of the Load

The large amount of recovery that occurs after the removal of the load in the simulation does not match the field performance. Rutted pavements show little, if any, recovery although more recovery may occur if the mix remains at the high temperatures at which the rutting occurs. The mix also ages and stiffens over time which retards any recovery. The large amount of recovery experienced after the load in removed in the simulation is a limitation of the constitutive model.

6.3 Summary

The nonlinear viscoelastic model successfully predicts the behavior of asphalt concrete in the RSST-CH laboratory tests, and shows improved predictions when compared to a

linear viscoelastic model. In the simulations of the HVS pavements, the model also shows reasonable, albeit not as good, predictions of the rutting behavior of asphalt concrete pavements. The ability of the model to fully capture the behavior of the modified mix, the ARHM, is inconclusive.

While it is likely that no "reasonable" model will give a perfect prediction of the highly variable asphalt concrete, it does appear that the nonlinear viscoelastic constitutive model captures sufficient material response to provide reasonable predictions of the behavior of asphalt concrete. It can therefore be used with some confidence, for example, for mix design purposes.

CHAPTER 7

MIX ANALYSES AND DESIGN

Wheel loads, tire inflation pressures, and load repetitions applied to highway and airfield pavements are increasing. This requires increasingly rut-resistant asphalt concrete mixes. However, many current mix design procedures are not able to provide such rut-resistant mixes. Furthermore, these procedures were not developed to evaluate the performance of modified binders. It has been observed that the field performance of modified binders is not matched by their performance in these mix design procedures.

The nonlinear viscoelastic constitutive model developed in this dissertation has limited value unless it can be used in mix design and analyses to facilitate the design of pavements resistant to permanent deformation. A procedure which aims to design mixes that adequately resist increased traffic demands without premature rutting failure and is applicable to conventional and modified binders was developed as part of the Strategic Highway Research Program (SHRP), Project A003A.*(4)*

The SHRP procedure was developed with a viscoelastoplastic constitutive model, finite element analyses, and, laboratory and field data. These finite element analyses resulted in a relationship that relates the permanent shear strain in a laboratory test to the rut depth in the field. In this Chapter the nonlinear viscoelastic constitutive model is used to evaluate this relationship, and to evaluate possible effects of different tire types on the relationship. As an overview, the SHRP mix design procedure is briefly discussed.

7.1 SHRP Performance Based Mix Design Procedure

The mix design procedure developed in the SHRP A003A project relies on laboratory testing that directly measures the shear properties of the mix, which primarily cause rutting in asphalt concrete pavements.*(4, 74)* Specimens prepared with a trial mix are tested with the RSST-CH and the results are empirically related to the rutting behavior in the field. The approach is termed a performance based, mechanistic-empirical design procedure. The advantage of testing the trial mix in the laboratory is that new materials can be evaluated with some level of confidence, even if they were not originally included in the empirical calibration.

Many current mix design procedures evaluate mixes by comparing a parameter obtained from a laboratory test to some fixed value. This is known as a "go, no go" specification, and has limited use in comparing the expected relative field performance of mixes. In the SHRP procedure, the relationship between the performance of the mix in the laboratory

test and the estimated rut depth in the field enables comparisons of the relative field performance of different mixes. In addition, the effects of the environment at the pavement location are incorporated and statistical reliability is included to account for the variability in estimating the input variables.

A flowchart of the mix design procedure is shown in Figure 7.1. The inputs for the analyses are the structural section, estimated design traffic, environment, trial mix, level of reliability and the allowable rut depth. Each of the elements in the flowchart is discussed below.

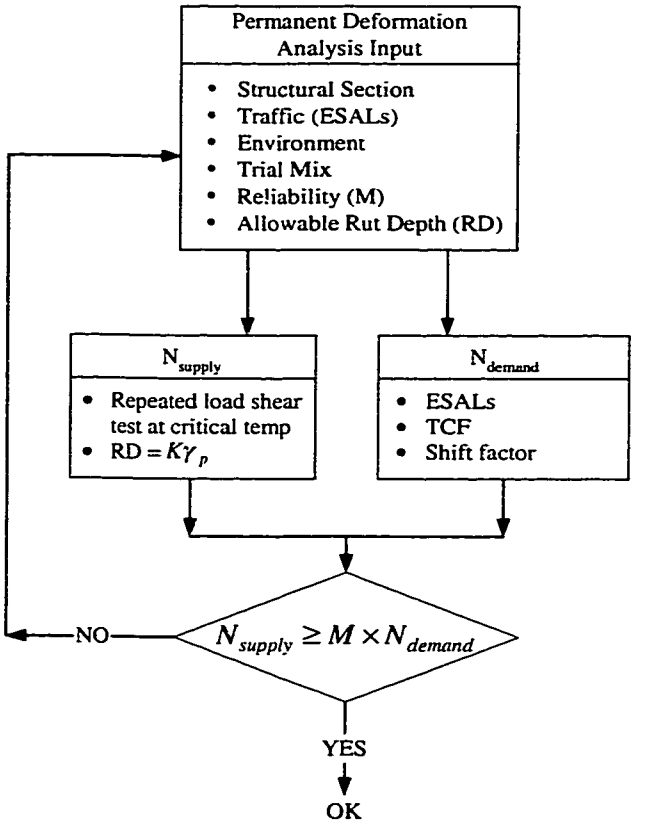

Figure 7.1 Flow Chart for Permanent Deformation Mix Design Procedure

7.1.1 Trial Mix

The purpose of a mix design procedure is to determine the proportions of aggregate and asphalt that will optimize the performance of the mix. Because the binder is resistant to the tensile and bending strains that cause cracking, the resistance to fatigue (cracking) distress increases as the binder content increases. On the other hand, the permanent deformation resistance of the mix decreases as the asphalt content increases. The optimum binder content is, therefore, typically the largest asphalt content that will not result in excessive rutting of the mix within the design period.

In the SHRP mix design procedure, specimens are fabricated from trial mixes and compacted to approximately a three percent air-void content over a range of asphalt contents. Below a three percent air-void content mixes have the potential to become unstable, as discussed in Chapter 2, and mixes with an air-void content larger than three percent may densify under traffic. The maximum resistance to rutting is, therefore, obtained at an air-void content of approximately three percent. For this reason, the trial mixes are tested at this air-void content, based on the observation that mixes above this level would likely densify towards the more stable state at a three percent air-void content. This is somewhat unconservative for poorly compacted mixes, that is mixes with an air-void content greater than seven percent. These mixes have less shear resistance until they compact and further densify. The additional densification also contributes to the rutting. Testing at a three percent air-void content does, however,

allow comparison of the performance of mixes at their maximum rutting resistance, thereby ensuring a consistent comparison.

7.1.2 Laboratory Test and Analyses

The trial mix is tested in the laboratory with the repeated load simple shear test at constant height (RSST-CH). It was reported in Chapter 2 that permanent deformation in asphalt concrete pavements is predominantly due to shear deformation. Therefore the RSST-CH is appropriate because it directly tests the shear resistance of mixes. The RSST-CH test procedure was described in Chapter 6.

Using finite element analyses with the viscoelastoplastic constitutive model described in Chapter 2, the SHRP A003A project developed a relationship between the maximum permanent shear strain determined in the RSST-CH test and the rut depth in the field.*(4)* This relationship is represented by Equation (7.1) and in Figure 7.1.

$$\text{Rut depth (mm)} = K \bullet \left(\gamma_p\right)_{max} \tag{7.1}$$

In this equation, K is a constant ranging between 254 and 280 for rut depths measured in millimeters and ranging between 10 to 11 for rut depths in inches, and $(\gamma_p)_{max}$ is the maximum permanent engineering shear strain determined from the RSST-CH. The factor, K, was determined first with simulations of one pavement structure and 16 mixes, and later with simulations of pavements with varying thickness. The parameter K was

found to depend on the thickness of the pavement. The K values given above were identified as being reasonable for thick pavements, which are the most critical for rutting, and conservative for thinner pavements.*(4)*

Using Equation (7.1), the maximum permanent shear strain in the RSST-CH results in the determination of a terminal rut depth. Typically, a maximum permanent shear strain of 5 percent is used, which corresponds to a terminal rut depth between 12 and 14 mm for pavements with thicknesses larger than 300 mm. The number of repetitions to 5 percent permanent shear strain is determined from the RSST-CH, and is called N_{supply}.

7.1.3 Environment

The environment, particularly the temperature, at a pavement location has an important influence on the rutting potential of the mix. The laboratory tests are performed at one selected temperature, termed the critical temperature. This is the temperature at which most of the rutting will theoretically occur at a specific location because it results in the largest product of the load repetitions and the maximum permanent shear strain accumulated per load repetition.

The temperature conversion factor (TCF) relates the critical temperature and the mixed temperature environment experienced in the field and permits conversion of traffic applied year round to equivalent traffic (in terms of rutting) at the critical temperature.*(4)*

7.1.4 Shift Factor

At this time, no laboratory test is able to completely replicate field behavior. Therefore, a shift factor (SF) is necessary to relate the laboratory test results to rutting in the field. During the SHRP project, a relationship between the number of repetitions in the RSST-CH and the number of load applications in the field was developed. Rut depth, traffic, and temperature environment data were available for about 35 test sections. The traffic was converted to equivalent single axle loads (ESALs) at the critical temperature. This conversion to ESALs is based on the damage per load relative to the damage of a standard load. The conversion factors were developed for other distresses which are more sensitive to the load magnitude than rutting is, but are not particularly sensitive to other factors that influence rutting, such as tire-contact stresses.

From Equation (7.1) the maximum shear strain, $(\gamma_p)_{max}$, was determined for the rut depths measured in the field. RSST-CH tests were performed on specimens from these test sections, and the number of repetitions to the particular maximum shear strain was measured. A regression relationship determined that each repetition of the RSST-CH was equal to 25 applications of an equivalent single axle load (ESAL), which gave a shift factor of 0.04.*(4)*

7.1.5 Reliability

The mix performance and the design traffic cannot be determined with absolute certainty. Accordingly, the inclusion of reliability allowed the variance in these estimates to be included in the design procedure and an acceptable level of risk assigned to a project. More important projects are designed to a higher level of reliability, thereby reducing the risk of premature failure.

Reliability is included in the mix design procedure with the reliability factor (M). Values have been developed for various levels of reliability as a function of the number of replicates used in the laboratory testing to determine N_{supply} and the variance in the estimated traffic.*(4, 74)*

7.1.6 Selection of Mix

In Equation (7.2), the estimated design traffic (ESALs), temperature conversion factor (TCF), and the shift factor (SF) are multiplied to obtain N_{demand}. As shown in Figure 7.1, if the relationship in Equation (7.3) is satisfied, the trial mix should withstand the estimated design traffic before reaching the terminal rut depth with the chosen level of reliability.

$$N_{demand} = ESALs \cdot TCF \cdot SF \qquad (7.2)$$

$$N_{supply} \geq M \bullet N_{demand} \tag{7.3}$$

The optimum binder content selected for the mix design is the largest binder content at which Equation (7.3) is satisfied.

7.1.7 Observations

The K values that relate the rut depth and the maximum shear strain in Equation (7.1) are dependent on the viscoelastoplastic constitutive relationship used in the finite element analyses performed during the SHRP program. The viscoelastoplastic model was an early attempt at formulating a constitutive model for asphalt concrete, and was not well verified prior to its use in calculating the K values. The nonlinear viscoelastic model developed in this dissertation captures more of the mix behavior and is therefore used to evaluate and possibly validate the mix design procedure, in particular Equation (7.1).

It is important to note that Equation (7.1) was used to develop the shift factor, and any changes may require the shift factor to be recalibrated.

7.2 Pavement Simulations

Analyses to validate the relationship between the maximum shear strain, K, and the rut depth, Equation (7.1), and the effect of tire type on this relationship were performed

using the nonlinear viscoelastic model for asphalt concrete. Several finite element simulations of pavement structures were performed with the same configuration as used in the SHRP project. The variables in the simulations included the asphalt concrete layer thickness, temperature of this layer, tire type, and the loading time. The specific set of variables used in each simulation is shown in Table 7.1.

Table 7.1 Simulation Variables

Thickness (mm)	Temperature (°C)	Tire Type	Load Speed (kmph)	Simulation Number
100	50	Dual radial	65	1
	60	Dual radial	65	2
150	50	Dual radial	65	3
	60	Dual radial	65	4
200	40	Dual radial	65	5
	50	Dual radial	65	6
			8	7
		Wide-base single	65	8
	60	Dual radial	65	9
		Wide-base single	65	10

7.2.1 Layer Thicknesses and Material Properties

The pavement section consisted of an asphalt concrete layer placed on a granular base. Three thicknesses were assumed for the asphalt concrete layer, 100, 150, and 200 mm. The constitutive relationship of this layer was the nonlinear viscoelastic model developed in this dissertation, and the material properties for the DGAC mix were used. The

specific values are presented in Chapters 4 and 5. This mix is representative of mixes placed on in-service pavements in California. To study the effects of environment, the temperature of the asphalt concrete layer ranged from 40 to 60°C.

The underlying granular base was 1000 mm thick and was assumed to be linear elastic, with a Young's modulus of 103 MPa and Poisson's ratio of 0.3.

Plane strain conditions were assumed, with the infinite dimension as the direction of travel. The mesh for a simulation with a 200 mm asphalt concrete layer is shown in Figure 7.2. Boundary conditions are also shown. Symmetry was utilized to reduce the mesh size and, therefore, the solution time.

7.2.2 Loading

The loading in the simulations performed in the SHRP A003A project assumed a uniform tire-contact pressure. The VRSPTA data has since become available, and, because they give a more accurate description of the tire-contact stresses they are used for these analyses.*(11)* Both dual radial and wide-base single tires were used in the simulations. The loading pattern for the dual radial tires was the same as used in the pavement simulations in Chapter 6. The wide-base single loading pattern was obtained from a Goodyear G286, 425.65R22.5 tire and is shown in Figures 7.2 and 7.3.*(11)* Due to

symmetry, only half the tire was modeled. Again, the distribution of the loads was not continuous across the nodes, due to the physical configuration of the VRSPTA. The total load on the dual radial tires was the same as on the wide-base single. Because of the issues with the aggressive loading in the plane strain simulations already discussed in Chapter 6, the loads were again reduced by one-third. This provided a more reasonable estimate of the permanent deformation and still allowed comparisons to be made between the tires.

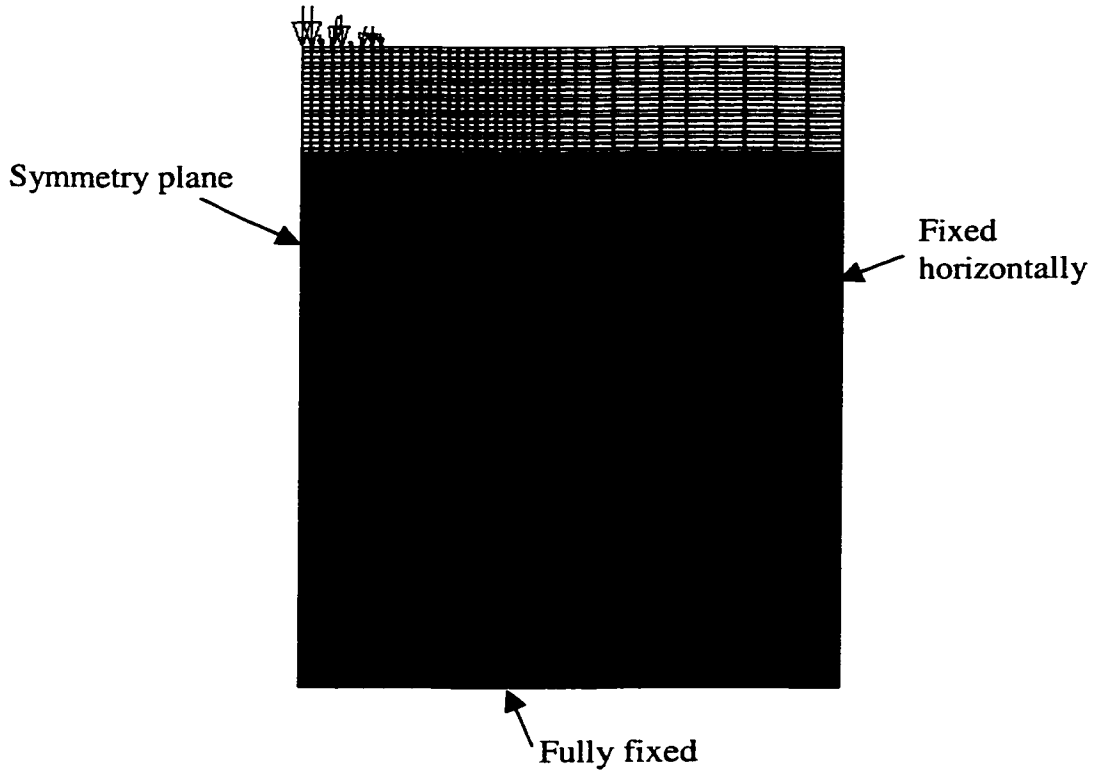

Figure 7.2 Finite Element Mesh for Pavement Simulation

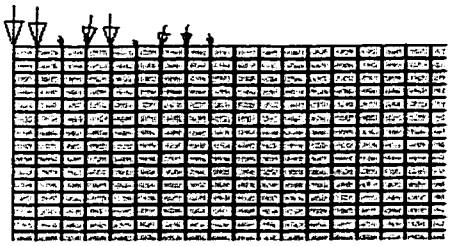

Figure 7.3 Wide-Base Single Tire Loading

The locations of the loads remained constant during each simulation, effectively modeling channelized traffic. This traffic distribution produces more rutting than the wandering traffic patterns experienced on in-service pavements.

Two different loading times were used in the simulations. The load cycles were applied in the waveform used in the pavement simulations given in Equation (6.3) in Chapter 6. The faster load speed, 65 kilometers per hour (60 kmph), is representative of highway truck traffic traveling at speeds critical to rutting. For this speed the load is applied for 0.015 seconds, with a rest period of 0.335 seconds, giving a total cycle time of 0.35 seconds. The slower loading speed, 8 kilometers per hour (8 kmph), is representative of the kinds of speeds that occur in congested traffic. This load speed is the same as the speed of the HVS. For this speed the load was applied for 0.1 seconds with a rest period of 2.65 seconds. The total cycle time for both loading speeds was determined from the estimated distance between truck axles. Between two trucks the rest period is longer, which will result in less deformation. This was not accounted for in the simulations.

Thus the loading in the simulations was more aggressive than is experienced on in-service pavements.

The length of the wide-base single tire contact area is 75 percent that of the dual radial tire; thus, the loading time is shorter with the same cycle time. In these simulations, this difference is ignored, and the same loading time is assumed for the dual radial and the wide-base single tires.

7.3 Results

Simulations were run until the rut depth exceeded a terminal rut depth of 12.5 mm, except for the 40°C case. At a selected number of repetitions, the displacements at the surface of the pavement were used to calculate the rut depth and the engineering shear strains were obtained.

7.3.1 Rut Depth and Accumulation

The application of the tire loading from the VRSPTA again resulted in non-uniform displacements along the surface of the pavement for both tires. The rut profiles from the radial tires were smoothed in the same manner as in Chapter 6. The profiles from the wide-base tire were also smoothed. For the wide-base tire the maximum rut depth was the average of the three largest vertical displacements, as shown in Figure 7.4.

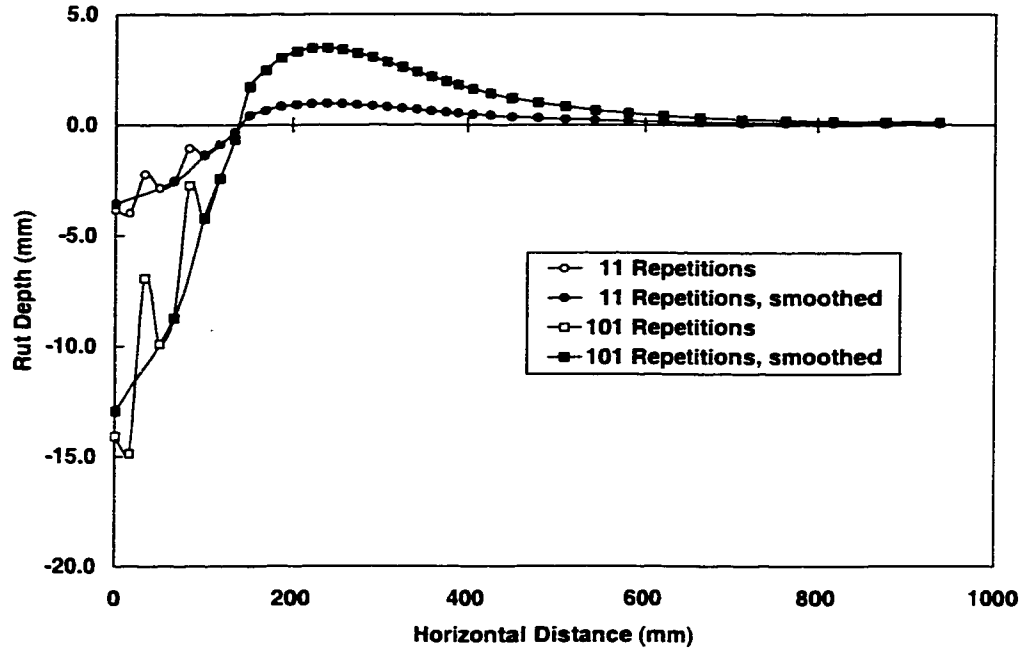

Figure 7.4 Smoothed Rutting Profile for Wide-Base Tire

Accumulation of rutting in each of the simulations is shown in Figure 7.5. The shape of each of the curves is similar. Temperature had a significant effect on the magnitude of the rutting, as expected. The simulations at 60°C showed a large amount of rutting, whereas the 40°C simulation did not reach the 12.5 mm terminal rut depth. The 60°C simulations showed a large amount of rutting in the first few load repetitions. This was largely because of the sensitivity of the model to the first load cycle. It was demonstrated in Chapter 6 that the accumulation of rutting stabilized after the first few load repetitions and predicted reasonable results after 10 repetitions. The large rut depth values obtained are also a result of the aggressive loading applied in the simulations.

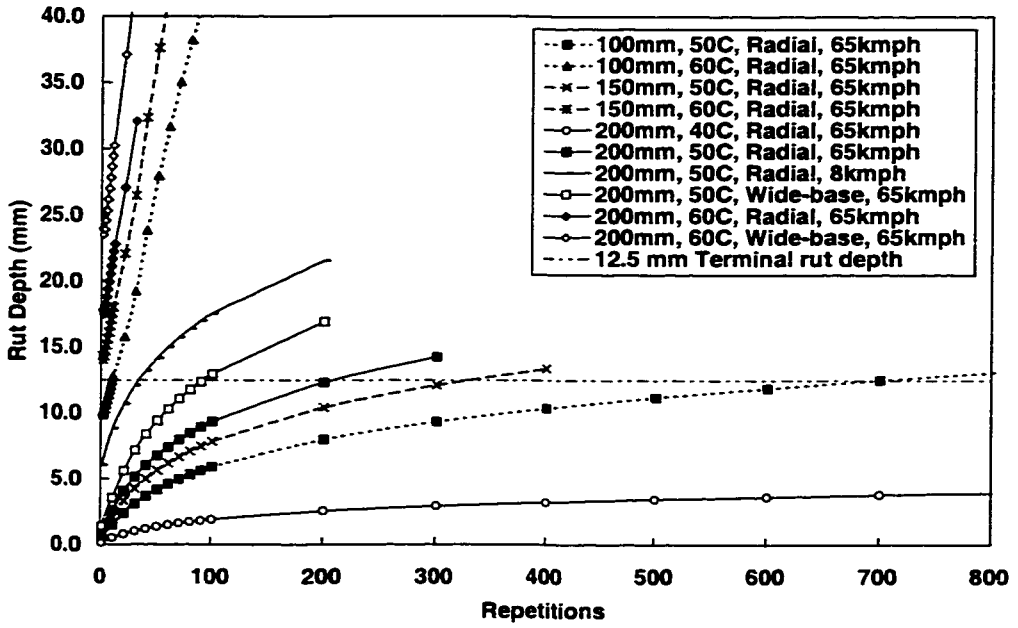

Figure 7.5 Accumulation of Rutting

The wide-base single tire resulted in more rutting than the dual radial tires. In the HVS Rutting Study reported in Chapter 6, similar results were obtained. For the DGAC overlay, the terminal average maximum rut depth of 12.5 mm was reached in 14051 repetitions with the dual radial tires. With the wide-base single tire only 1817 repetitions were needed to reach the maximum rut depth. Similar results were obtained for tests with both tires on two different ARHM overlay thicknesses.*(7)*

The data show that, for the range of thicknesses used, increasing the thickness of the asphalt concrete layer increases the amount of rutting accumulated. These results again agree with the HVS Rutting Study in which the dual radial tires produced 12.5 mm of rutting in approximately 13000 repetitions on the 62 mm thick ARHM overlay, but took

almost 40000 repetitions on the 38 mm ARHM overlay. This pattern was repeated for the wide-base single tire.*(7)*

For the repetitions shown, the slower HVS loading speeds resulted in more rutting, which was expected. Slower rates of loading in viscoelastic materials result in more deformation. This is observed in pavements, where at intersections there is often more rutting than at sections of roadway where vehicles travel at higher speeds.

7.3.2 Maximum Residual Engineering Shear Strain

In the performance based mix design procedure, the maximum residual (permanent) engineering shear strain in the pavement simulations was used to fit the relationship to the rut depth shown in Equation (7.1)).

7.3.2.1 Maximum Engineering Shear Strain Location

The engineering shear strain distribution after 11 repetitions in the 50°C, 200 mm simulations are shown in Figures 7.6 and 7.7 for the radial and wide-base tires, respectively. The same data, plotted differently, are shown in Figures 7.8 to 7.11. In Figures 7.8 and 7.10 the shear strains with depth are plotted for the radial and wide-base tires, respectively. Similarly, the shear strains are plotted with the surface (horizontal) locations in Figures 7.9 and 7.10.

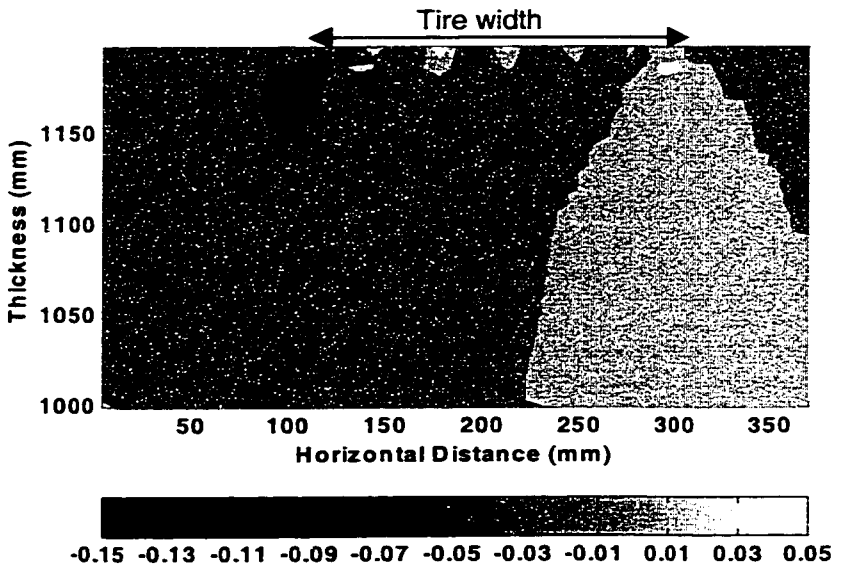

Figure 7.6 **Shear Strain Distribution in 50°C, 200 mm Thick, Radial Tire Simulation, 11 Repetitions**

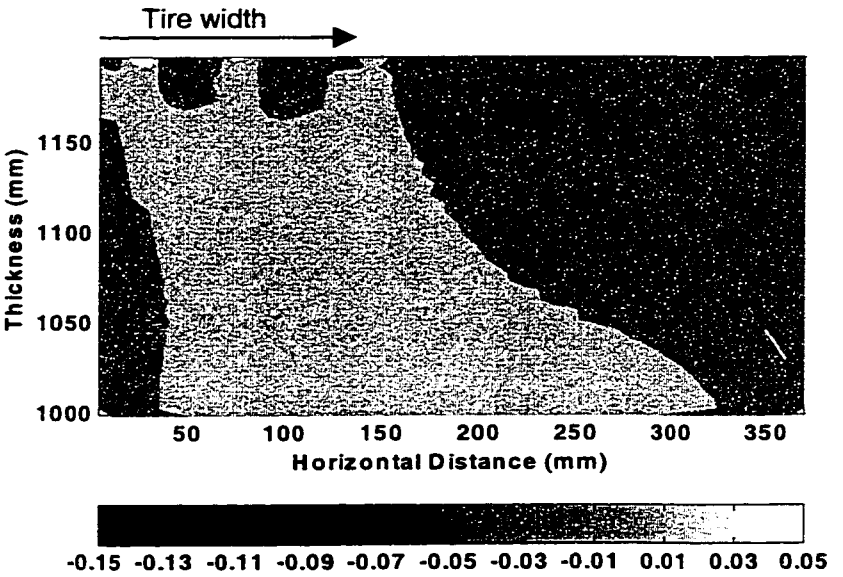

Figure 7.7 **Shear Strain Distribution in 50°C, 200 mm Thick, Wide-Base Tire Simulation, 11 Repetitions**

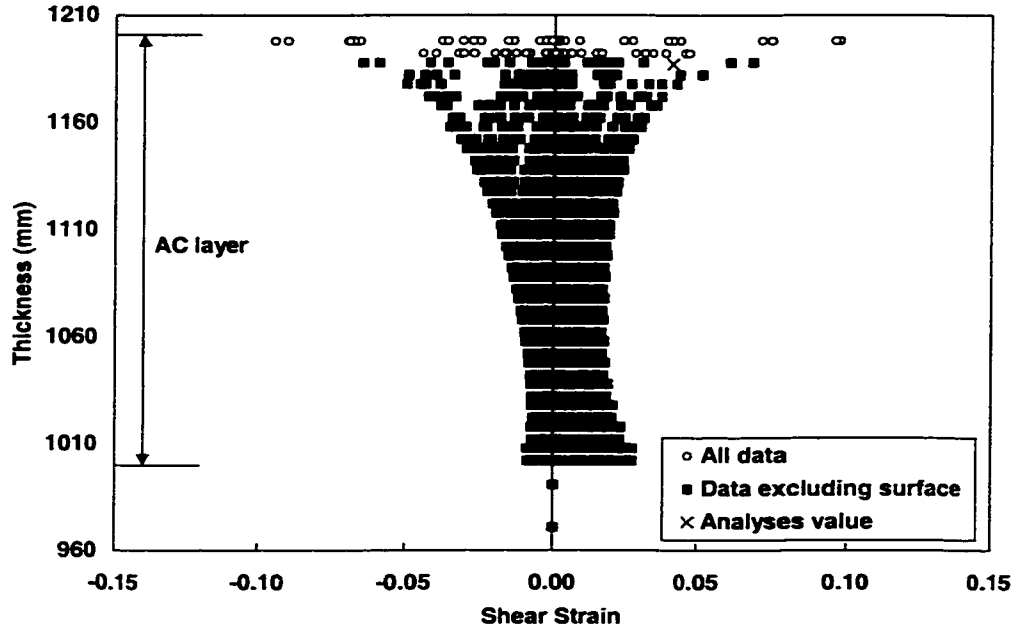

Figure 7.8 **Shear Strain Distribution with Thickness in 50°C, 100 mm Thick, Radial Tire Simulation, 11 Repetitions**

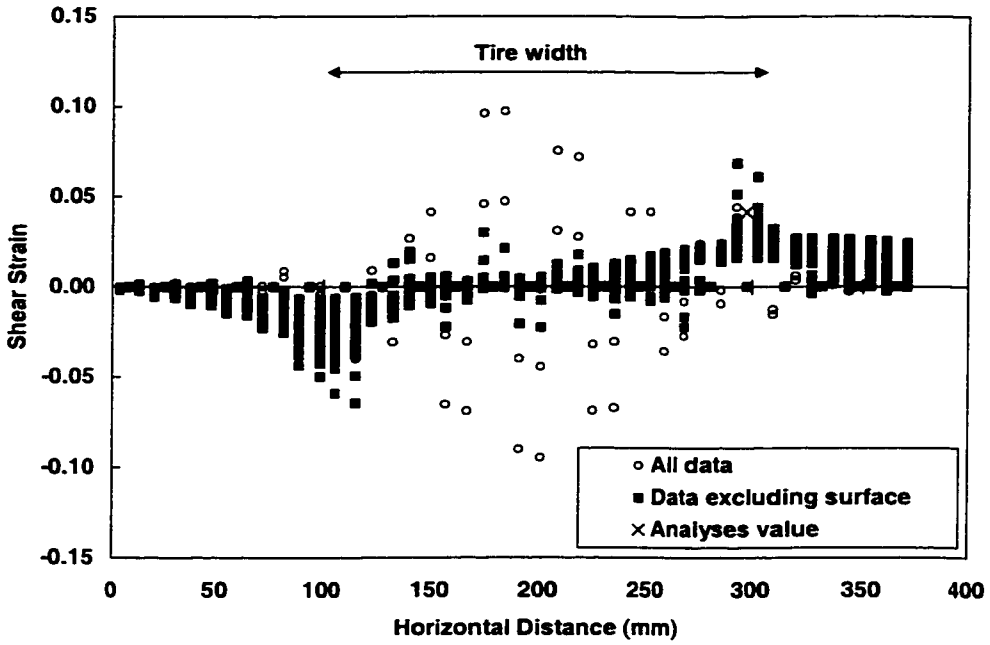

Figure 7.9 **Shear Strain Distribution with Horizontal Distance in 50°C, 100 mm Thick, Radial Tire Simulation, 11 Repetitions**

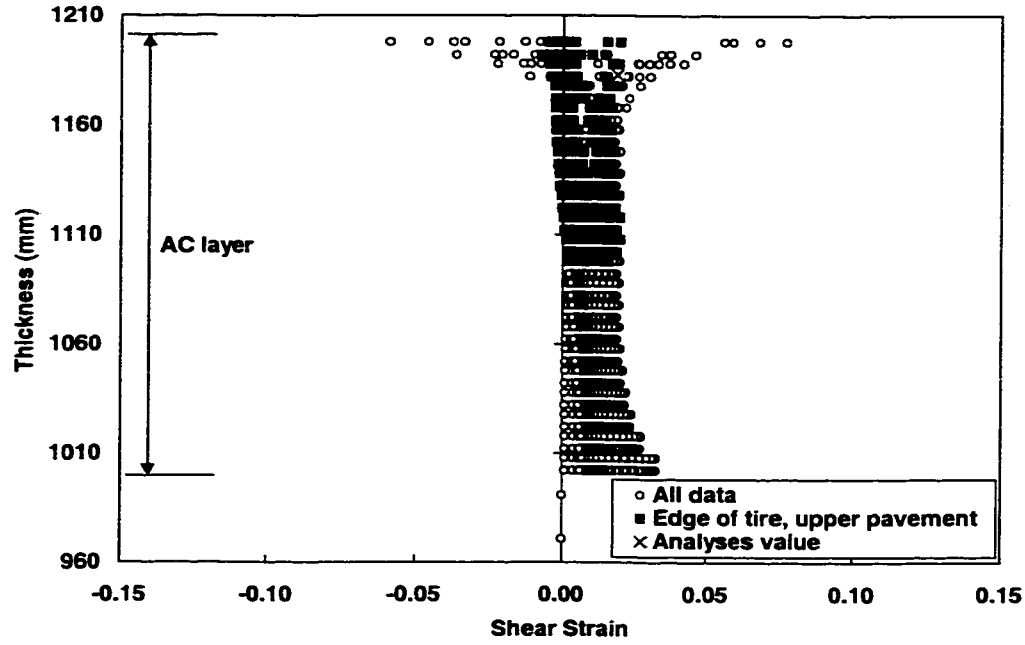

Figure 7.10 Shear Strain Distribution with Thickness in 50°C, 200 mm Thick, Wide-Base Tire Simulation, 11 Repetitions

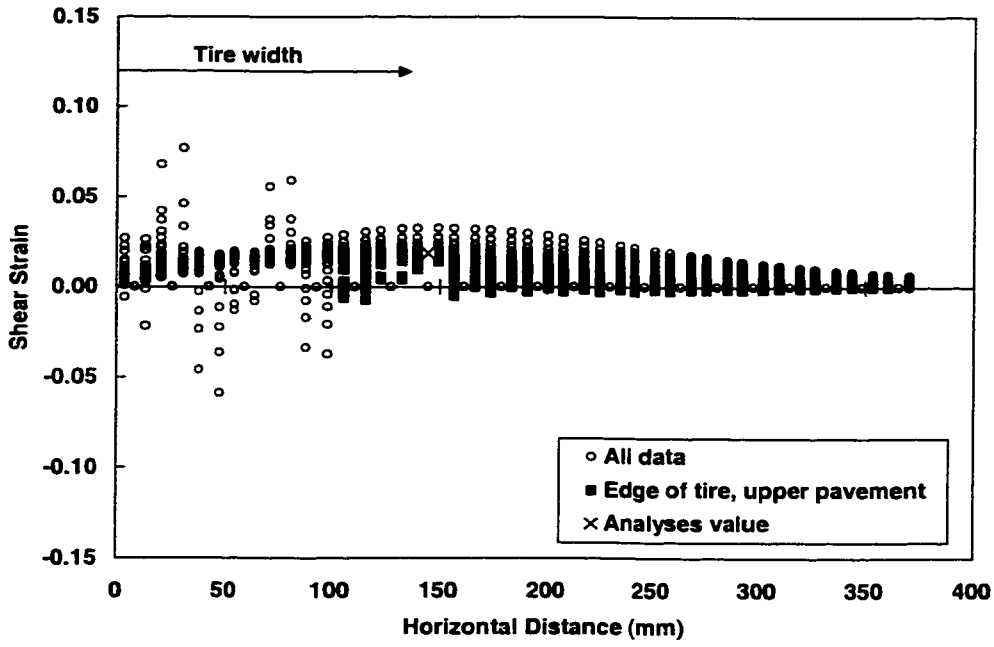

Figure 7.11 Shear Strain Distribution with Horizontal Distance in 50°C, 200 mm Thick, Wide-Base Tire Simulation, 11 Repetitions

As evident in the figures, the shear strain distributions for the tires are different. Away from the immediate areas where the load was applied, the shear stress distribution with the wide-base tire is fairly constant with depth. On the other hand, with the radial tire, as the depth increases the shear strain decreases, and then increases again at the bottom of the asphalt concrete layer. The wide-base tire seems to have a wider influence on the pavement response at depth. The same patterns were evident for the different layer thicknesses and showed the same trends as the repetitions increased. This illustrates the large effect the tire type and the contact stresses have on the rutting behavior of asphalt concrete pavements.

To determine the maximum shear strain, an average value was obtained from the location at which the shear strains appear to be at a reasonable maximum. Simply searching for the maximum value from the data set found the extreme values shown in the plots. These values are most likely due to the differences in load magnitudes at adjacent nodes and are, therefore, not reasonable for typical pavement response. The specific locations from which the maximum shear strains were obtained are shown with the "X" in Figures 7.8 to 7.11. The value is an average of two data points from this area. For the radial tire the specific location was 13 mm below the surface underneath the inside edge of the tire, and for the wide-base tire the location was 17 mm below the surface, underneath the outside edge of the tire.

7.3.2.2 *Comparison of Engineering Shear Strain Accumulation*

The accumulation of the maximum engineering shear strains with repetitions at the locations described above is shown in Figure 7.12. In this figure, it is clear that the temperature again had a significant influence. The thickness of the asphalt concrete layer had little effect on the shear strains; the data for the different thicknesses and same temperatures are very close in value.

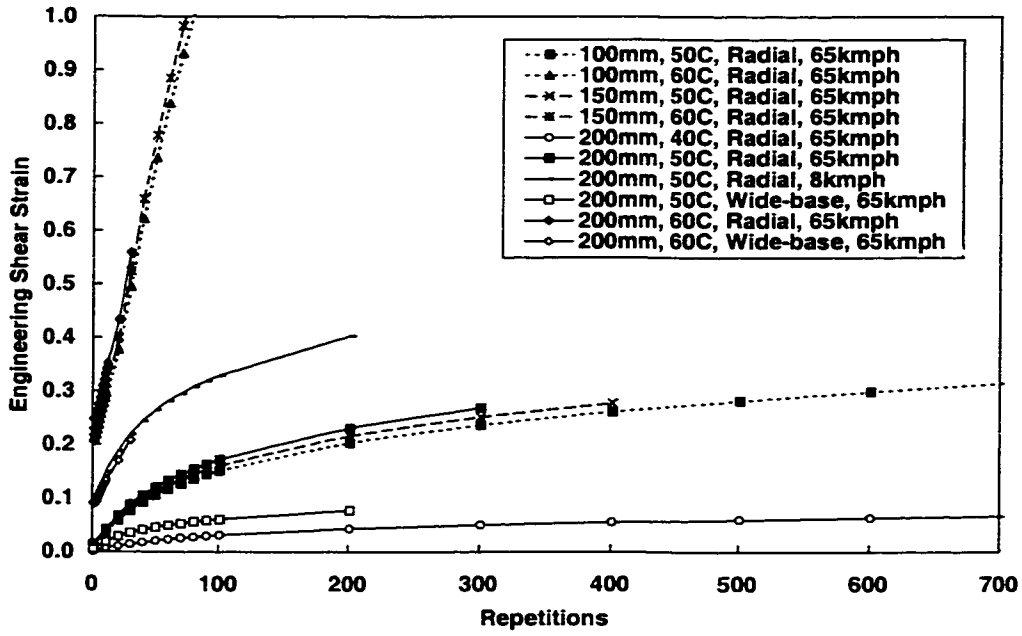

Figure 7.12 Accumulation of Maximum Engineering Shear Strains

The slower loading speed resulted in larger shear strains than for the faster moving loads, as expected.

The wide-base tire had smaller maximum shear strains than the radial tire, although the rut depths were larger. The wide-base tire influenced a larger area of the pavement and, therefore, when the strains were integrated to obtain the displacements, the resulting rut depths were larger. Again, this demonstrates the significant effect that the tire type has on the rutting performance and why contact stresses should be considered in mix and pavement analyses.

7.3.3 Rut Depth and Engineering Shear Strain

The rut depth and engineering shear strain data are plotted in Figure 7.13. For all the simulations, the curves are approximately linear, indicating that a constant value relates the two parameters. This constant value is K in Equation (7.1). A K value was fit to each curve, and is shown in Figure 7.14 as a function of the asphalt concrete layer thickness. The solid lines in the figure are the K values suggested by the results of the SHRP project. These values are within the range of the new K values. The dotted line shown on the chart is for K=254, which is the value currently suggested for use in mix design and analyses of thick pavements. Figure 7.14 shows that temperature and loading time have almost no effect on the K value for the radial tire. The temperature has a small effect on the K value for the wide-base tire. This may be due to the rapid rutting accumulation in the first few repetitions of the 60°C simulation.

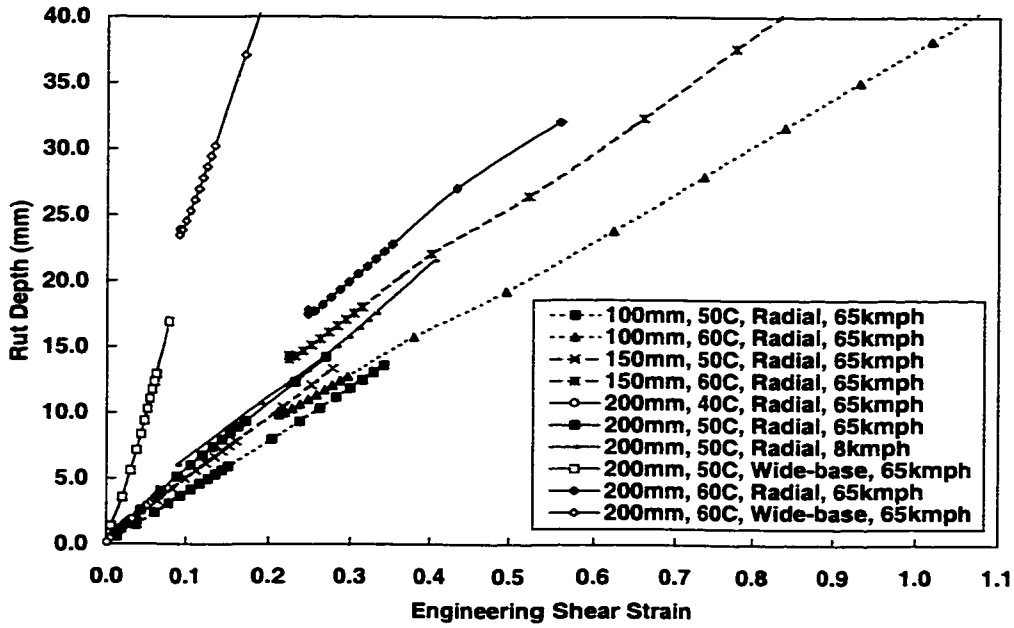

Figure 7.13 Rut Depth and Maximum Engineering Shear Strain

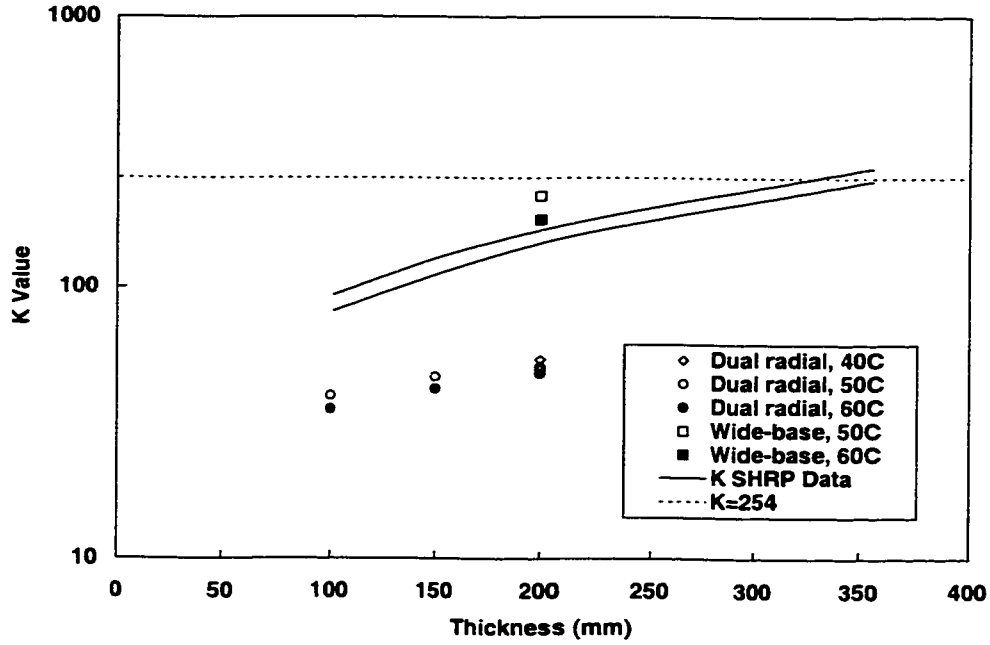

Figure 7.14 K Value versus Asphalt Concrete Layer Thickness

The thickness of the asphalt concrete layer had a small effect on the K value, with higher K values for increasing thickness. This agrees with the results of the simulations performed in the SHRP project. Because the change in K was relatively small for the range of thicknesses, it seems reasonable to use one value, regardless of the actual pavement layer thickness, for less important projects as is currently suggested. This is not recommended, however, for thinner pavements.

The K value is very dependent on the tire type, and is almost an order of magnitude higher for the wide-base tire than the radial tire. This is significant and indicates that different K values are necessary to account for the large effect the different tires and their contact stresses have on the rutting performance of mixes. This effect is very difficult to capture in the laboratory, illustrating the benefit of these modeling simulations. Because the traffic on in-service pavements is a combination of various tire types, the different tires are also difficult to account for in a mix design procedure,

7.4 Observations and Conclusions

The purpose of the analyses presented in this chapter is to use the nonlinear viscoelastic constitutive model to validate the relationship between the maximum shear strain, the factor K, and, the rut depth (Equation (7.1)) used in the SHRP A003A performance based mix design procedure.

The mix design procedure is based on performing RSST-CH laboratory tests on trial mixes to a maximum permanent shear strain and then relating the repetitions to this shear strain to the rut depth in the field through the shift factor. Although different K values were obtained for the simulations with the constitutive model developed in this dissertation, adopting a new set of K values requires the shift factor to be recalibrated. And, if the shift factor were recalibrated, it is likely that similar results would be obtained in the mix design and analyses.

The parameter from the laboratory test data, the repetitions to five percent shear strain, is related to the rut depth in the field. Test results from RSST-CH tests and the test simulations performed in Chapter 6 showed that after approximately 100 repetitions the rutting accumulates linearly on a logarithmic scale. Therefore, regardless of the actual strain value selected for comparison, mixes should be ranked according to their rut resistance. For example, if ten percent shear strain were used, the reported repetitions would be higher, but should be proportionately higher in all mixes. The five percent shear strain should ensure that the deformation is accumulating linearly on a logarithmic scale. In addition, should the deformation in one mix accumulate faster than in another mix, the repetitions to the five percent shear strain should be significantly different, enabling a more statistically reliable ranking of the rutting resistance of the mixes. Five percent shear strain is a convenient terminal strain level at which to run the laboratory test, and is therefore recommended for continued use. A further benefit of the method is

that asphalt concrete mixes can be ranked according to their shear resistance, and how the rutting accumulates rather than using a single parameter from an indirect test as a "go, no go" specification.

Based on these observations, the relationship between the maximum shear strain, the factor K, and the rut depth in the field, Equation (7.1), used in the SHRP performance based mix design procedure is an appropriate relationship for use in evaluating the rutting potential of asphalt concrete mixes. In the current procedure, where recommended K values are within a small range, care should be taken when different tire types are used because of the significant influence they have on the mix rutting performance. It is recommended that the effects of tire type be quantified with further simulations of different tires using contact stresses measured with devices like the VRSPTA. Such simulations may provide data that give relative indications of the damaging effects of different tire types and new tires, which could be useful in legislative considerations.

CHAPTER 8

CONCLUSIONS AND RECOMMENDATIONS

This dissertation presents the development of a nonlinear viscoelastic constitutive model that describes the permanent deformation behavior of asphalt concrete pavements. Because in-service pavements are required to be increasingly rut resistant due to increasing traffic demands, mix design procedures must be able to provide mixes that are sufficiently rut resistant. Constitutive models that capture this type of pavement behavior are useful for developing and validating mix design procedures.

This final chapter summarizes and draws conclusions from the results presented in the earlier chapters, and provides suggestions for future work.

8.1 Summary and Conclusions

There are many factors that influence the permanent deformation behavior of asphalt concrete. In Chapter 2, a literature review identified the critical properties of the aggregate, the asphalt, and the combined mixes. Asphalt concrete is highly dependent on

temperature and the time of loading, typical characteristics of a viscoelastic material. The shear deformation of mixes is a significantly larger contributor to rutting than volume change deformation, which was demonstrated with laboratory test data. A summary of laboratory test methods available for mix testing was presented, and it was concluded that, at this time, the simple shear test at constant height is an appropriate test for characterizing mix behavior. Various methods of predicting permanent deformation in pavements were discussed, and the advantages and disadvantages of each were summarized.

Chapter 3 reviewed results from simple shear at constant height frequency sweep laboratory tests conducted with a conventional dense graded asphalt concrete (DGAC) and a modified mix, asphalt-rubber hot mix (ARHM), over a range of temperatures and strain levels. The data for both mixes showed the large effect that temperature has on the mix, i.e., the mix became less stiff as the temperature increased. The data also showed that the strain level in the test had a significant effect on the material response, i.e., the mix decreased in stiffness as the strain level increased. There was a fair amount of variability in the data, which is typical for asphalt concrete mixes, and reasons for this variability were discussed.

The type of constitutive model selected to describe this type of asphalt concrete behavior was a nonlinear, strain dependent viscoelastic model. Justifications for this choice were

discussed in Chapter 4 using a range of laboratory test data. Briefly, all test data showed typical viscoelastic behavior, but the recovery of the mix was limited, resulting in permanent deformation. This kind of permanent deformation is usually modeled with plasticity. However, defining a constitutive model for plasticity is difficult, even if an extensive laboratory testing program is performed. The introduction of nonlinear effects in a viscoelastic model can result in the material response being similar to that of a plasticity model. As compared to a plasticity model, the nonlinear viscoelastic model was less difficult to define from the available laboratory test data.

Chapter 4 describes how laboratory test data reported in Chapter 3 were used to develop the components of the constitutive model. The development focused on the shear behavior. Superimposing data for time and temperature effects to create a single master curve was not adequate. Therefore, a shift to account for the strain dependence is also necessary. To create a single master curve the master curves were shifted both horizontally and vertically on the modulus and frequency axes to a reference curve. The horizontal and vertical shifts accounted for the strain and temperature dependence of the mix. The horizontal shift is typical for thermorheologically simple materials, but the need for the vertical shift showed that asphalt concrete, for the high strain levels and temperatures tested, is thermorheologically complex. All the data were shifted, and functions were fit to the shift factors. The resulting shift factor functions contained terms for the temperature, the reference temperature, the strain, and the reference strain. The

volumetric component of the model assumed thermorheologically simple linear viscoelasticity. Viscoelastic material properties were obtained from the shifted master curves in Chapter 5 for both the shear and volumetric data.

As explained in Chapter 5, the constitutive model was formulated from the basis of linear viscoelasticity and extended to include the observed dependence of the shear behavior on the strain level by incorporating the horizontal and vertical shift factors in the shear component of the model. The horizontal shift factor was included in the reduced time. The shear moduli in the constitutive relationship were divided by the vertical shift, which is equivalent to including a damage factor. The strain used to calculate the shift factors with the shift factor functions was the maximum deviatoric strain norm experienced in the time history, i.e., when the material had experienced a high strain it showed permanent damage. Temperature effects were also included in the bulk component of the model.

From the formulation of the constitutive model, an algorithm was derived and implemented in a finite element code. In the algorithm, the maximum deviatoric strain norm was determined at the beginning of the time step, which was reasonable because the time steps were small. Small time steps were necessary to accurately impose the load and to ensure the reduced time and material properties did not rapidly change due to large

changes in the strain during a time step. The model is particularly sensitive to the time step duration used in the first load cycle.

Chapter 5 also discussed some limitations in the model, such as the model's inability to account for densification of the mix. From the data available, it was not possible to directly include the effects of air-void content that are observed in laboratory tests and rutted pavements.

To validate the nonlinear viscoelastic model, finite element simulations of the RSST-CH and the HVS pavement structures were performed in Chapter 6. The simulations matched the RSST-CH laboratory test data well. The average shapes of the profiles of the rutted pavements from the simulations compared favorably with those observed in the HVS Rutting Study. The "humps" apparent on the edge of the wheel tracks in rutted pavements were predicted. In the simulations, tire loading from measured tire contact stresses was used. These load data were measured at discrete points, and the application of the discontinuous loads across the nodes did not result in a smooth rutting profile. In addition, in comparison to the HVS tests, the magnitudes of the total load produced more permanent deformation in the plane strain simulation and less in the three-dimensional simulation of the pavement. In the HVS test the load travels across the pavement, whereas in the simulation it was statically applied with the load form discussed in Chapter 6. In the 3D simulation this resulted in a less aggressive load because the

additional loading as the tire moves across the pavement was not accounted for. In the 2D simulation the plane strain conditions essentially applied the load across the full length of the pavement. The reduction in loading as the wheel moves further away from a particular point was not considered, which resulted in more aggressive loading and hence more deformation than is experienced in the actual pavement. To circumvent these effects, the load was arbitrarily reduced in the plane strain simulations to obtain deformations that matched the magnitude of the deformations in the HVS test sections. These load issues should be further investigated in future work.

Simulations using the modified ARHM did not produce results consistent with field behavior, although the shear material properties of both the DGAC and ARHM were similar and the bulk properties were assumed to be the same. The shapes of the rutting profiles were reasonable, but the simulations predicted that the ARHM produces less rutting, which is not consistent with observed field behavior. In the HVS test the ARHM mix densified considerably which contributed to the total rut depth. This densification is not accounted for in the nonlinear viscoelastic model. The model showed potential for reasonably predicting the performance of a modified binder. However, more simulations with the ARHM should be performed, and additional modified binders should be investigated.

Despite these issues, and the limitations of the model discussed in Chapter 5, the conclusion is drawn that the nonlinear viscoelastic model captures the permanent deformation behavior of asphalt concrete, especially the conventional DGAC mix, fairly well.

The final analyses in this dissertation used the constitutive model to validate a relationship used in the performance based mix design procedure developed as part of the SHRP A003A project. This relationship relates the repetitions to a particular shear strain in the RSST-CH laboratory test to the rut depth in the field with a factor, denoted K. Simulations of pavement structures with varying thicknesses, temperatures, tire types and loading speeds are performed in Chapter 7 to validate this relationship. It is found that the same trends observed in the SHRP A003A project are obtained for the effect of thickness on the rutting.

The tire type is shown to have a large effect on the rutting development, which is in agreement with HVS test data, and these effects should be considered in mix design. The K value for the wide-base single tire is significantly larger than for the dual radial tires. This shows that for a pavement with the same mix, i.e., the same repetitions to a given shear strain in the RSST-CH test, the wide-base tire will produce more rutting. These effects are difficult to quantify in the laboratory and, therefore demonstrate an important use of constitutive modeling.

Application of the nonlinear viscoelastic constitutive model developed in this dissertation, validates part of the mix design procedure developed during the SHRP A003A project. Although some issues which should be investigated further are identified, for example the effect of the tire type.

The modeling performed in this dissertation demonstrates an approach that can be used to quantify the damaging effects of different tire types and new tires, which could be useful in legislative considerations.

8.2 Recommendations for Future Work

Although the constitutive model captures the permanent deformation behavior of asphalt concrete fairly well, there are some limitations in the model which should be addressed in future work.

An important limitation is the exclusion of a term that accounts for the dependence of the material response on the air-void content. It is possible that the air-void effects could be captured if simple shear at constant height frequency sweep test data are obtained for a wider range of air-void contents.

The volumetric properties of the mix were obtained indirectly from hollow cylinder tests, and no data were available for the ARHM. The constitutive model may be significantly

enhanced by a more detailed investigation of the volumetric properties. Although the densification of mixes under traffic loading is small, it does occur and this effect is not captured. A more detailed investigation of the bulk material properties could enable the inclusion of this densification effect. It is also recommended that the bulk properties for several different mixes are studied to determine a range of applicable values. Evaluation of these data could ascertain whether a standard set of bulk properties could be used for all similar mixes.

It is described in detail in Chapter 5 how the maximum strain value is used to calculate the shift factors and therefore determine the material properties. The effect of a series of heavy loads could, for some loading situations, result in similar permanent deformation as a series of lighter loads. Consequently, it may be more accurate to use a moving average of the maximum strains to alleviate this effect. This should be investigated in further work.

The impact of the tire load data on the simulations and the unreasonable results obtained need to be resolved to allow a more reasonable prediction of the pavement response immediately under the tire. And, the reduction of the three dimensional pavement to an equivalent plane strain simulation needs to be quantified to ensure that predictions from the plane strain simulations are accurate, and representative of real pavement behavior.

The results presented in this dissertation are a small selection of the kinds of analyses that could be performed with the nonlinear viscoelastic model. In future work it will be necessary to determine the applicability of the constitutive model to mixes with modified binders. Further analyses with the ARHM and other modified binder mixes, such as a polymer modified binder that has been shown to be more rut resistant than mixes with conventional binders should be performed.

An application of the model could be to evaluate temperature conversion factors for use in the mix design procedure. Mixes could be tested over a range of temperatures and the applicable shift factor functions developed and incorporated into the model. Simulations using the actual mixed temperature environment and using the critical temperature could then be compared to determine an appropriate temperature conversion factor to relate the two conditions.

An extensive study of the effect of tire type and contact stresses on the rutting of asphalt concrete pavements of varying thickness would be a valuable extension to the results presented in Chapter 7. It is difficult in mix and pavement design and analyses to directly account for the load spectra experienced on in-service pavements. For this reason the traffic is usually reduced to an equivalent load, typically an equivalent single axle load (ESAL). The relationship used to convert a load to an ESAL is not particularly appropriate for rutting and does not account for different tires, tire pressures and load

speeds. The nonlinear viscoelastic model could be used to evaluate the damage caused by different loads and by an ESAL. This data could be used to develop a more applicable conversion to an ESAL or an improved method of aggregating the damage caused by different loads.

Quantification of the effects of increased legal axle loads, and under or over inflated tires on the rutting performance of mixes could have significant implications for the asphalt concrete pavement industry enabling the design of rut resistant mixes that withstand the increasing traffic demands. These results could be valuable for discussions with the trucking industry and for establishing policy and legislation.

REFERENCES

1. Sousa, J.B., Craus, J., C.L. Monismith, Summary Report on Permanent Deformation in Asphalt Concrete, Strategic Highway Research Program, National Research Council, Washington, D.C., Report No. SHRP-A / IR-91-104, 1991.

2. Bahia, H. U., H. Zhai, K. Bonnetti, S. Kosi, Non-linear Viscoelastic and Fatigue Properties of Asphalt Binders, *Journal of the Association of Asphalt Paving Technologists*, Vol. 68, 1999.

3. Collop, A.C., D.Cebon and M.S.A. Hardy, Viscoelastic Approach to Rutting in Flexible Pavements, *Journal of Transportation Engineering*, Vol. 121, No.1, Jan/Feb 1995.

4. Sousa, J.B., J.A. Deacon, S.L. Weissman, R.B. Leahy, J.T. Harvey, G. Paulsen, J.S. Coplantz, and C.L. Monismith, Permanent Deformation Response of Asphalt Aggregate Mixes, Strategic Highway Research Program, National Research Council, Washington, D.C., Report No. SHRP-A-415. 1994

5. Monismith, C.L. and B.A. Vallerga, Relationship between Density and Stability of Asphaltic Paving Mixtures, *Journal of the Association of Asphalt Paving Technologists*, Vol. 25, 1956.

6. Weissman, S.L., The Mechanics of Permanent Deformation in Asphalt-aggregate Mixtures: a Guide to Laboratory Test Selection, Symplectic Engineering Corporation, December 1997.

7. Harvey, J.T. and L. Popescu, Rutting of Caltrans Asphalt Concrete and Asphalt-Rubber Hot Mix Under Different Wheels, Tires and Temperatures – Accelerated Pavement Testing Evaluation, Pavement Research Center, Institute of Transportation Studies, University of California, Berkeley, January 2000.

8. Kallas, B.F., Dynamic Modulus of Asphalt Concrete in Tension and Tension-Compression, *Journal of the Association of Asphalt Paving Technologists*, Vol. 39, 1970.

9. Weissman, S. L., J. Sackman, J. T. Harvey and F. Long, "Selection of Laboratory Test Specimen Dimension for Permanent Deformation of Asphalt Concrete Pavements", *Transportation Research Record 1681*, pp. 113-120, 1999.

10. C.L. Monismith, J.T. Harvey, F. Long and S. Weissman, Tests to Evaluate the Stiffness and Permanent Deformation Characteristics of Asphalt/Binder-Aggregate Mixes, A Critical Discussion, Pavement Research Center, University of California, Berkeley, TM-UCB-PRC-2000-1, June 2000.

11. de Beer, M. and C. Fisher, Contact Stresses of Pneumatic Tires Measured with the Vehicle-Road Surface Pressure Transducer Array (VRSPTA) System for the University of California at Berkeley (UCB) and the Nevada Automotive Test Center (NATC), CSIR report No. CR-97-97/053, 1997.

12. Blab, R., Introducing Improved Loading Assumptions into Analytical Pavements Models Based on Measured Contact Stresses, *Proceedings*, International Conference on Accelerated Pavement Testing, Reno, Nevada, October 1999.

13. *Shell Pavement Design Manual*, Shell International Petroleum Company, Limited, London, 1978.

14. SUPERPAVE™ Support and Performance Models Management, *Preliminary Recommendations for the Simple Performance Test*, Interim Task C Report, FHWA No. DTFH 61-94-R-00045, Department of Civil Engineering, University of Maryland, College Park, Maryland, May 1998.

15. Lijzenga, J., "On the Prediction of Pavement Rutting in the Shell Pavement Design Manual", *2nd European Symposium on Performance and Durability of Bituminous Materials*, Leeds, April 1997.

16. Monismith, C.L., Permanent Deformation Prediction in Asphalt Concrete Pavements: Use of Creep Test Data, *Proceedings*, 5th International Conference on the Structural Design of Asphalt Pavements, The Netherlands, 1982.

17. Erkens, S.M.J.G., A.A.A. Molenaar, A. Scarpas, Relating Performance Tests to Fundamental Material Behavior, *7th Conference on Asphalt Pavements for Southern Africa*, Victoria Falls, Zimbabwe, August 1999.

18. SUPERPAVE™ Support and Performance Models Management, *Advanced AC Mixture Material Characterization Models Framework and Laboratory Test Plan*, Final Subtask F.2 Report, NCHRP 9-19 and FHWA No. DTFH 61-95-C-00100, College of Engineering and Applied Sciences, Arizona State University, Tempe, Arizona, September 1999.

19. Alavi, S. H. and C. L. Monismith, "Time and Temperature Dependant Properties of Asphalt Concrete Mixes Tested as Hollow Cylinders and Subjected to Dynamic Axial and Shear Loads", *Journal of the Association of Asphalt Paving Technologists*, Vol. 63, 1994.

20. Alavi, S.H., Viscoelastic and Permanent Deformation Characteristics of Asphalt-Aggregate Mixes Tested as Hollow Cylinders and Subjected to Dynamic Axial and Shear Loads, Ph.D. dissertation, University of California at Berkeley, 1992.

21. Harvey, J.T., I. Guada, F. Long, *Analysis of Some Laboratory Testing and Analysis Variables for Input to Selection of Laboratory Tests for Asphalt Concrete*, Pacific Coast SHRP Superpave Facility, University of California at Berkeley, Institute of Transportation Studies, Pavement Research Center, November 1998.

22. Tayebali, A, Goodrich, Sousa, Monismith, "Relationships Between Modified Asphalt Binders Rheology And Binder-Aggregate Mixture Permanent Deformation Response", *Journal of the Association of Asphalt Paving Technologists*, Vol. 60, 1991.

23. Valkering, C.P., D.J.L. Lancon, E.deHilster and D.A. Stoker, Rutting Resistance of Asphalt Mixes Containing Non-Conventional and Polymer-Modified Binders, *Journal of the Association of Asphalt Paving Technologists*, Vol. 59, 1990.

24. Tanco, A.J., Permanent Deformation Response of Conventional and Modified Asphalt-Aggregate Mixes under Simple and Compound Shear Loading Conditions, Ph.D. Dissertation, University of California, Berkeley, 1992.

25. Tayebali, A.A., Influence of Rheological Properties of Modified Asphalt Binders on the Load-Deformation Characteristics of the Binder-Aggregate Mixtures, Ph.D. Dissertation, University of California, Berkeley, 1990.

26. California Department of Transportation, *Standard Test Methods,* Sacramento, January 1985.

27. Pavement Research Center, University of California, Berkeley, Mix Design and Analysis and Structural Section Design for Full Depth Pavement for Interstate Route 710, TM-UCB-PRC-99-2, June 1999.

28. Peattie, K.R., A Fundamental Approach to the Design of Flexible Pavements, *Proceedings,* International Conference on the Structural Design of Asphalt Pavements, University of Michigan, pp. 403-411, 1963.

29. Dorman, G. M., The Extension to Practice of a Fundamental Procedure for the Design of Flexible Pavements, *Proceedings,* International Conference on the Structural Design of Asphalt Pavements, University of Michigan, pp. 785–793, 1963.

30. Research and Development of the Asphalt Institute's Thickness Design Manual (MS-1), Ninth Edition, Research Report 82-2, The Asphalt Institute, College Park, Maryland, August 1982.

31. DeBeer, M., Developments in the failure criteria of the South African mechanistic design procedure for asphalt pavements", *Proceedings*, 7th International

Conference on the Structural Design of Asphalt Pavements, Nottingham, United Kingdom, August 1992.

32. Barksdale, R.D., Laboratory Evaluation of Rutting in Base Course Materials, *Proceedings, Third International Conference on the Structural Design of Asphalt Pavements*, Vol. 1, London, pp. 161-174, 1972.

33. Romain, J.E., Rut Depth Prediction in Asphalt Concrete Pavements, *Proceedings,* Third International Conference on the Structural Design of Asphalt Pavements, Vol. 1, London, 205-210, 1972.

34. Monismith, C.L., J.A. Deacon and J.T. Harvey, *Westrack: Performance Models for Permanent Deformation and Fatigue*, Pavement Research Center, CAL/APT Program, Institute of Transportation Studies, University of California, Berkeley, June, 2000.

35. Kenis, W.J., J.A. Sherwood, T.F. McMahon, Verification and Application of the VESYS Structural Subsystem, *Proceedings*, 5th International Conference on the Structural Design of Asphalt Pavements, The Netherlands, 1982.

36. Schapery, R.A., A Method of Viscoelastic Stress Analysis Using Elastic Solution, J. Franklin Institute, Volume 279.

37. Weissman, S.L. and J.L. Sackman, A Viscoplastic Constitutive Law for Asphalt Concrete Mixes at Elevated Temperatures; A Finite Deformation Formulation, Symplectic Engineering Corporation, June 2000.

38. Weissman, S.L. and J.L. Sackman, The Effect of Traffic Wander on Rut Evolution in Pavements with Asphalt Concrete Surface Layers, Symplectic Engineering Corporation, December 1999.

39. Schapery, R.A., Nonlinear Viscoelastic and Viscoplastic Constitutive Equations with Growing Damage, International Journal of Fracture, Volume 97, 1999.

40. Desai, C.S., Mechanics of Materials and Interfaces: the Disturbed State Concept, CRC Press, Boca Raton, Florida, 1999.

41. Harvey, J., N. Coetzee and L. Louw, *CAL/APT Program – Construction of the Goal 3 Overlays and Recommendations for Improved Overlay Performance in California*, Draft Report, Pavement Research Center, CAL/APT Program, Institute of Transportation Studies, University of California, Berkeley, November, 1999.

42. California Department of Transportation, *Standard Specifications*, Sacramento, July 1995.

43. American Association of State Highway and Transportation Officials (AASHTO), *Standard Specifications for Transportation Materials and Methods of Sampling and Testing, Part II Tests,* Eighteenth Edition, 1997.

44. Pavement Research Center (PRC), University of California, Berkeley, *Revision to AASHTO TP7 (TP7-00)*, Submitted to AASHTO for consideration, 2000.

45. American Association of State Highway and Transportation Officials (AASHTO). "Test Method for Determining the Permanent Deformation and Fatigue Cracking Characteristics of Hot Mix Asphalt (HMA) Using the Simple Shear Test (SST) Device, AASHTO TP7-94", *AASHTO Provisional Standards*, March 1995, pp. 164-186

46. Sousa, J. S. Weissman, J.L. Sackman, and C.L. Monismith, "Nonlinear Elastic Viscous with Damage Model to Predict Permanent Deformation of Asphalt Concrete Mixes", *Transportation Research Record 1384*, pp. 80-93, 1993.

47. Bronstein, M. and J.M.B. Sousa, *ATS™, A New Generation of Laboratory Testing Software*, Digital Control Systems, SHRP Equipment Corporation, Version 3.13, 1988.

48. Ferry, J.D., Viscoelastic Properties of Polymers, John Wiley & Sons, Inc.1961.

49. Wineman, A.S., and W.K. Waldron, Jr, Interaction of Nonhomogenous Shear, Nonlinear Viscoelasticity, and Yield of a Solid Polymer, *Polymer Engineering and Science*, Volume 33, Number 18, pp. 1217 – 1228, September 1993

50. Knauss, W.G., and I.J. Emri, Non-linear Viscoelasticity Based on Free Volume Consideration, *Computers and Structures*, Volume 13, pp. 123-128, 1981.

51. Knauss, W.G., and I.J. Emri, Volume Change and the Nonlinearly Thermo-Viscoelastic Constitution of Polymers, *Polymer Engineering and Science*, Volume 27, Number 1, pp. 86 – 100, January 1987.

52. Vinogradov, G.V., A. Ya. Malkin, *Rheology of Polymers*, Mir Publishers, Moscow, 1980.

53. Mark, J.E., B. Erman, F.R. Eirich, *Science and Technology of Rubber*, Second Edition, Academic Press, 1994.

54. O'Connell. P.A., and G.B. McKenna, Large Deformation Response of Polycarbonate: Time-Temperature, Time-Aging Time, and Time-Strain Superposition, *Polymer Engineering and Science*, Volume 37, Number 9, pp. 1485 – 1495, September 1997.

55. Molenaar, J.M.M., J.L.M. Voskuilen and J.J. Bothmer, "Effects of filler aggregate on rheological properies of mastic", Mechanical Tests for Bituminous Materials, *Proceedings of the Fifth International Rilem Syposium MTBM Lyon 97*, France, 14-16 May 1997.

56. Zorn, R., G.B. McKenna, L. Willner and D. Richter, Rheological Investigation of Polybutadienes Having Different Microstructures over a Large Temperature Range, *Macromolecules*, Volume 28, pp. 8552 – 8562, 1995

57. Lan, S.K, A.J. Giacomin and F. Ding, Dynamic Slip and Nonlinear Viscoelasticity, *Polymer Engineering and Science*, Volume 41, Number 2, pp. 507 – 524, February 2000

58. Laun, H.M., Description of the Non-linear Shear Behavior of a Low Density Polyethylene Melt by Means of an Experimentally Determined Strain Dependant Memory Function, *Rheologica Acta*, Volume 17, Number 1, pp. 1-15, January/February 1978.

59. Ozupek, S. and E.B. Becker, Constitutive Modeling of High-Elongation Solid Propellants, *Journal of Engineering Materials and Technology*, Volume 114, pp. 111 – 115, January 1992

60. Simo, J.C., On a Fully Three-Dimensional Finite-Strain Viscoelastic Damage Model: Formulation and Computational Aspects, *Computer Methods in Applied Mechanics and Engineering*, Volume 60, pp. 153-173, 1987.

61. Monismith, C.L., K. Inkabi, D.B. McLean, C.R. Freeme, *Design Considerations for Asphalt Pavements*, Office of Research Services, University of California, Berkeley, March 1977.

62. Krokosky. E.M., *Rheological Properties of Asphalt-Aggregate Compositions*, Massachusetts Institute of Technology, DSR 9547, June 1992.

63. Shames, I.H. and F.A. Cozzarelli, *Elastic and Inelastic Stress Analysis*, Prentice Hall, 1992.

64. Tschoegl, N.W., The Phenomenological Theory of Linear Viscoelasticity: An Introduction, Springer-Verlag, Berlin, 1989.

65. Govindjee, S., Lecture Notes, CE 234, *Computational Inelasticity*, University of California, Berkeley, Fall 1996.

66. Taylor, R.L., K. S. Pister and G.L. Goudreau, Thermomechanical Analysis of Viscoelastic Solids, *International Journal for Numerical Methods in Engineering*, Volume 2, pp 45-49, 1970

67. Taylor, R.L., Finite Element Analysis Program, University of California, Berkeley, 1999.

68. Cook, R.D., D.S. Malkus, M.E. Plesha, Concepts and Applications of Finite Element Analysis, Third Edition, John Wiley & Sons, 1989.

69. Baumgaertel, M., and H.H. Winter, Determination of Discrete Relaxation and Retardation Time Spectra from Dynamic Mechanical Data, *Rheologica Acta*, Vol. 28, pp 511-519, 1989.

70. Emri, I., and N.W. Tschoegl, Generating Line Spectra from Experimental Responses. Part I: Relaxation Modulus and Creep Compliance, *Rheologica Acta*, Vol. 32, pp 311-321, 1993.

71. Simhambhatla, M., and A.I Leonov, The Extended Pade-Laplace Method for Efficient Discretization of Linear Viscoelastic Spectra, *Rheologica Acta*, Vol. 32, pp 589-600, 1993.

72. *MATLAB Student Version*, Version 5.3, The Mathworks, Inc, August 1999.

73. Bejarano, M.E., *Rut Depth Definitions*, Internal Memorandum, Pavement Research Center, University of California, Berkeley, July 2000.

74. Harvey, J.T., Vallerga, B.A. and C.L. Monismith, "Mix Design Methodology for a Warrantied Pavement: A Case Study", *Transportation Research Record 1492*, pp. 184-192, 1995

75. Sokolnikoff, I.S, *Mathematical Theory of Elasticity*, Second Edition, New York, McGraw-Hill, 1956.

76. Timoshenko, S. and J.N. Goodier, *Theory of Elasticity*, New York, Third Edition, McGraw-Hill, 1970

APPENDIX 1

REPORTING OF LABORATORY DATA AND RANGES OF VALUES OF STORAGE AND LOSS MODULI

This Appendix discusses the data obtained from the shear frequency sweep tests described in Chapter 3. The raw data files were used to obtain an indication of the range or variability of the results calculated and reported from the ATS software *(47)*. Some of the problems with the raw data are discussed.

The ATS software processes the raw test data to determine the peak stresses and strains and the phase angle. The analysis is performed with a fast Fourier transform to represent the laboratory data with sine curves. After the data is transformed the peak values and phase angle are extracted.*(20)*

The ATS software reports one value for each parameter estimated per frequency, so it was not possible to determine some statistics for the estimates. However, the raw data files can be used to estimate the parameters, although this is a time consuming process.

Because some of the data is not smooth, determining the peak values, and especially, the phase angle can be difficult.

Good data was obtained from Specimen 87AF (57°C and 1.5% strain level). Therefore, this specimen was used to indicate the ranges of values for the parameters. The data was obtained from the original, unprocessed data file. The results are shown in Figures A1.1, A1.2, and A1.3. Figure A1.1 shows the strain values on the left hand side axis and the stress values on the right hand side axis. The stress data are plotted on a logarithmic scale.

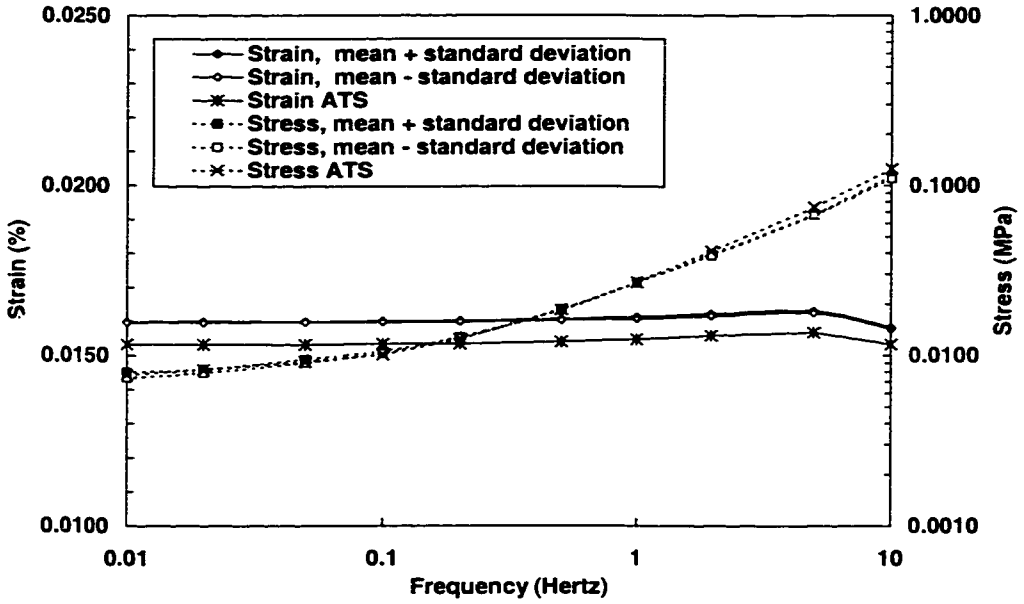

Figure A1.1 Mean and Standard Deviation of Stress and Strain with Frequency, from Raw Data and ATS processed Data

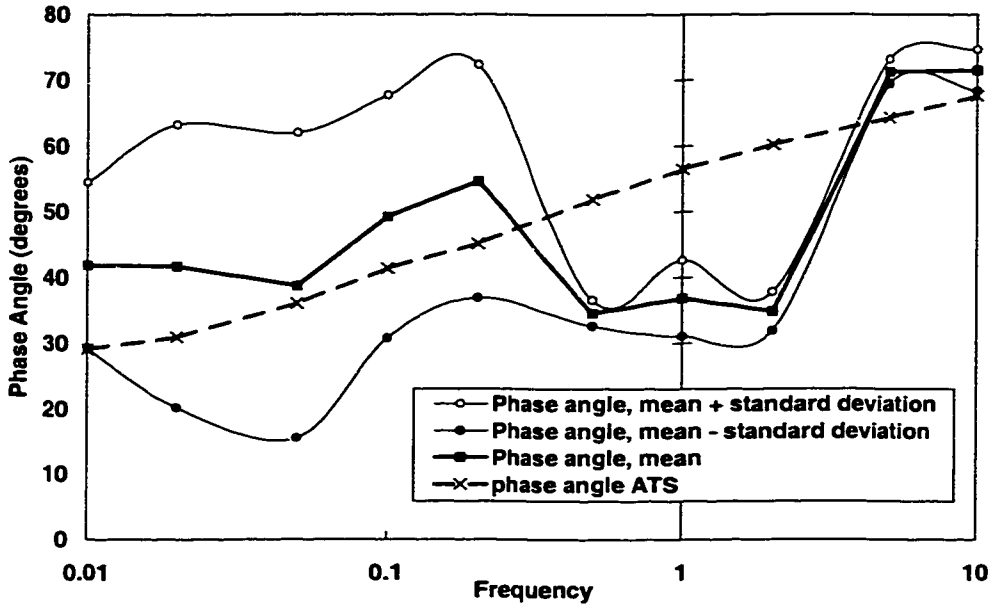

Figure A1.2 Mean and Standard Deviation of Phase Angle with Frequency from Raw Data and ATS Processed Data

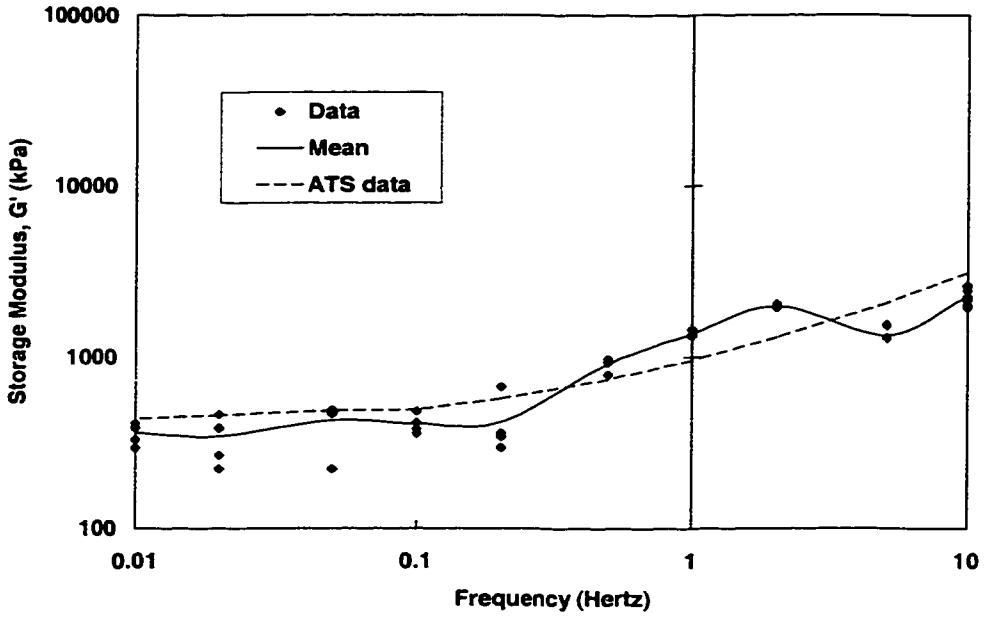

Figure A1.3 Storage Modulus, Data and Mean Values from Raw Data and ATS Processed Data

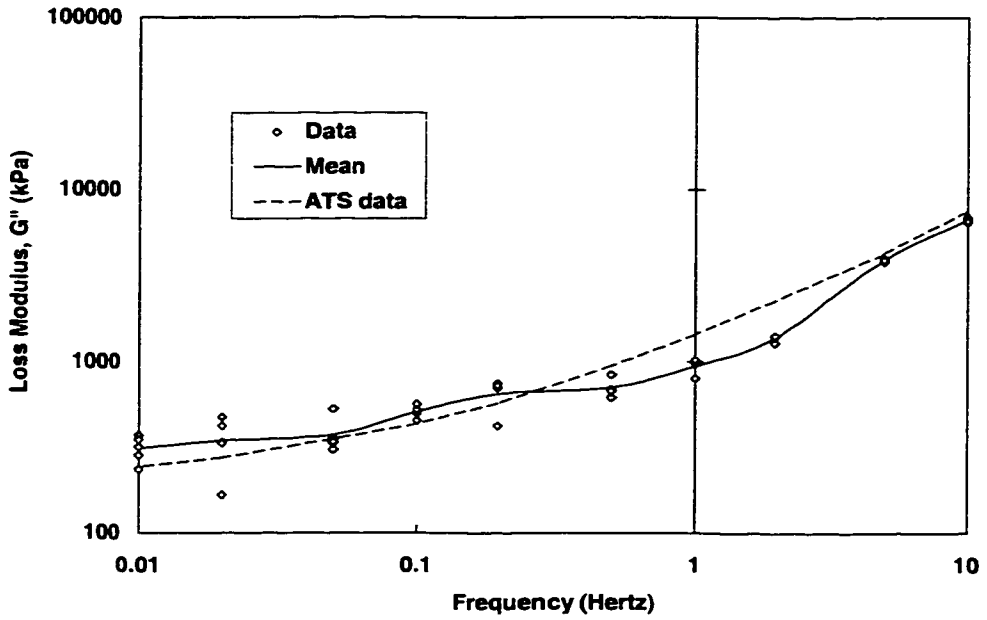

Figure A1.4 Loss Modulus, Data and Mean Values from Raw Data and ATS Processed Data

Figure A1.1 shows the stress and strain average values, plus and minus a standard deviation, and the values from the ATS data file. There is fairly good agreement, although the stress differs slightly at the higher frequencies, and the strain from the ATS software is consistently lower than the strain from the raw data.

Figure A1.2 shows a comparison of the phase angle average values, plus and minus the standard deviation, and the ATS data. There are large discrepancies in this data, which after examination of the raw data, is understandable. For example, Figure A1.5 for the 0.1 Hertz data shows how the peak values obtained from this data are probably reasonable. However, the variation in the data can significantly affect the reported value.

The data for this specimen had relatively few fluctuations at the peaks compared to other specimens.

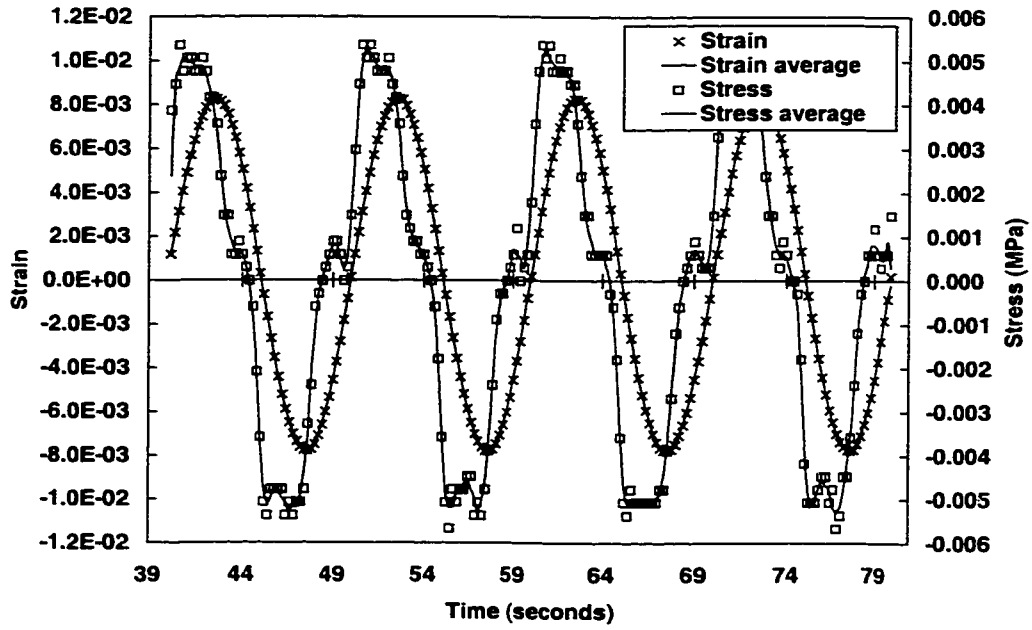

Figure A1.5 Variation in Peak Values of Stress and Strain

Figures A1.3 and A1.4 show the storage and loss moduli. The individual data points are the calculations from the raw data file, one per period, and the solid line represents the mean of these calculations. The dashed line represents the data from the ATS software. Although there are differences in the data, and the range of values per frequency is noticeable, given the variability always found in asphalt concrete mixes, this data is reasonable and acceptable.

For comparison purposes, the storage and loss moduli for each specimen tested at 1.5% strain are shown in Figures A1.6 and A1.7 respectively, using the same scale as Figures A1.3 and A1.4. The data for Specimen 87 is highlighted. The variance between specimens again appears reasonable. The effect of temperature on the moduli is evident, despite the variability within a given strain level.

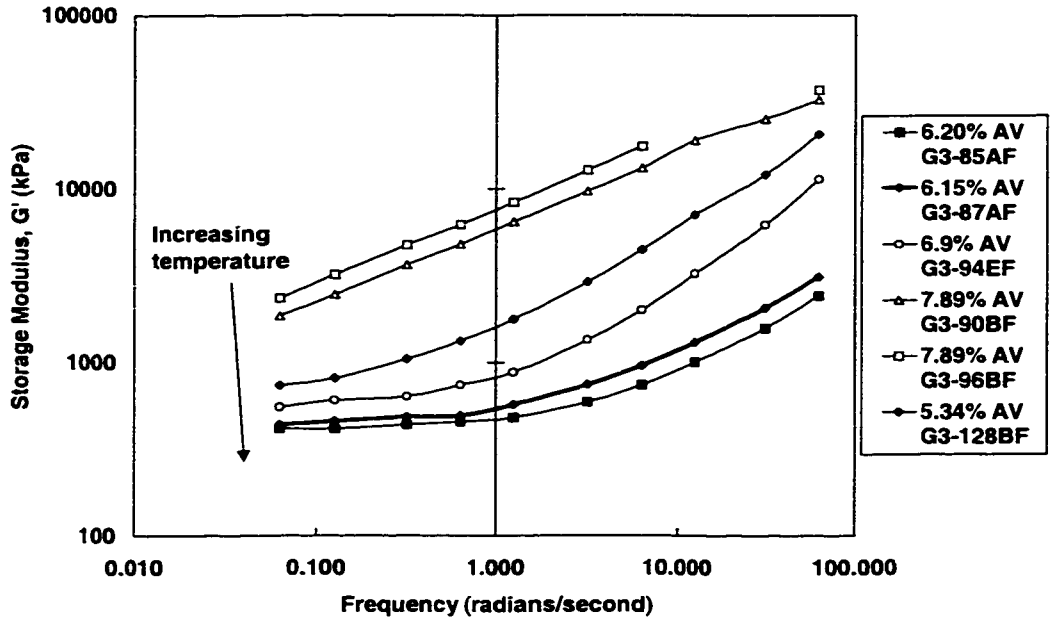

Figure A1.6 Storage Modulus for All Specimens Tested at 1.5 % Strain

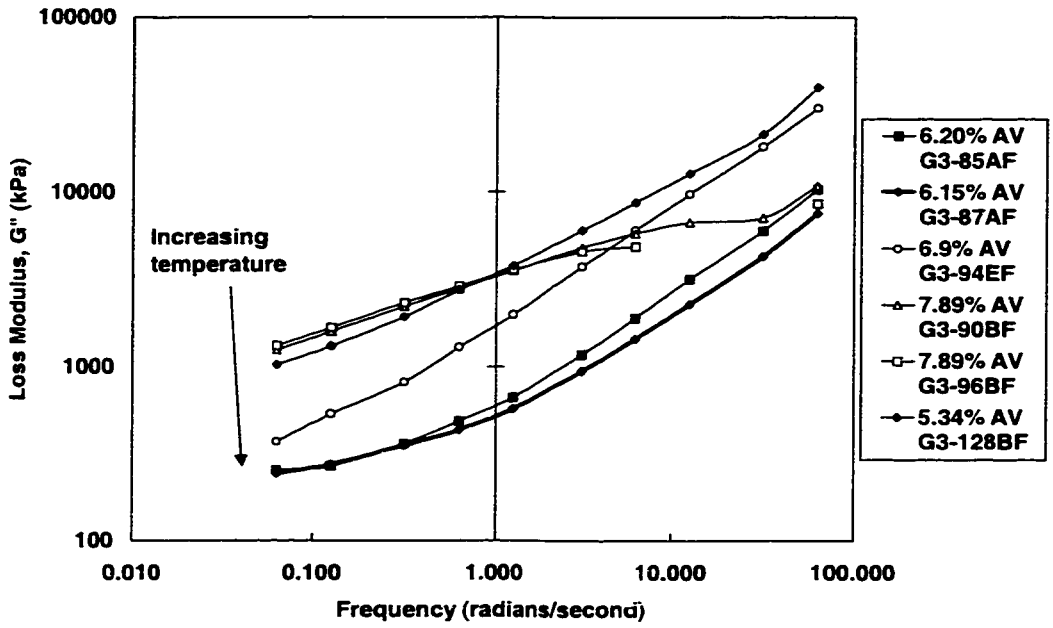

Figure A1.7 Loss Modulus for All Specimens Tested at 1.5 % Strain

APPENDIX 2

DERIVATION OF TIME CONTINUOUS CONSTITUTIVE MODEL AND ALGORITHM

In this Appendix the time continuous constitutive relationships for the nonlinear viscoelastic constitutive model and the time discretized algorithm are derived. The bulk component of the model is linear viscoelastic and accounts for the temperature effects with the reduced time concept using the Williams, Landel and Ferry (WLF) equation. The shear component is nonlinear viscoelastic and the temperature and strain dependencies are included through the horizontal and vertical shift factors, as described in Chapter 5.

The derivation for the bulk component is given first, followed by the shear component and finally the consistent tangent. The variables are defined in a list at the end of the Appendix.

In the finite element method the strain (ε) at time t is given and the stress (σ) is calculated. In this constitutive model the shear and volumetric deformation are separated using additive decomposition, shown in Equation (1.1) where p is the volumetric stress and **s** the deviatoric stress.

$$\boldsymbol{\sigma}(t) = p(t)\mathbf{1} + \mathbf{s}(t) \tag{1.1}$$

A2.1 Volumetric (Bulk) Component

The linear viscoelastic constitutive relationship is given by

$$p(t) = \int_{-\infty}^{t} K(t-s)\tfrac{d}{ds}[\theta(s)]ds \tag{1.2}$$

where

$$\begin{aligned} \theta &= \mathrm{tr}(\boldsymbol{\varepsilon}) \\ &= \varepsilon_{11} + \varepsilon_{22} + \varepsilon_{33} \end{aligned} \tag{1.3}$$

For simplicity, assume only one volumetric Maxwell element is used, N=1. The relaxation function can be written in a Prony series

$$K(t) = K^{\infty} + K^{1} e^{-\frac{t-s}{\lambda^{1}}} \tag{1.4}$$

Substitute (1.4) into (1.2) and separate the integral into $t \le 0$ and $t > 0$

$$p(t)=\int_{-\infty}^{t}\left(K^{\infty}+K^{1}e^{-\frac{t-s}{\lambda^{1}}}\right)\frac{d}{ds}\theta(s)ds \tag{1.5}$$
$$=\int_{-\infty}^{0}K^{\infty}\frac{d}{ds}\theta(s)ds+\int_{-\infty}^{0}\frac{d}{ds}\theta(s)ds+\int_{0^{-}}^{t}K^{\infty}\frac{d}{ds}\theta(s)ds+\int_{0^{-}}^{t}K^{1}e^{-\frac{t-s}{\lambda^{1}}}\frac{d}{ds}\theta(s)ds$$

Assuming no load is applied before $t=0$, $\theta(t)\equiv 0$ for $t<0$

$$p(t)=K^{\infty}\theta(0)+K^{1}e^{-\frac{t}{\lambda^{1}}}\theta(0)+\int_{0^{-}}^{t}K^{\infty}\frac{d}{ds}\theta(s)ds+\int_{0^{-}}^{t}K^{1}e^{-\frac{t-s}{\lambda^{1}}}\frac{d}{ds}\theta(s)ds$$
$$=K^{\infty}\theta(0)+K^{1}e^{-\frac{t}{\lambda^{1}}}\theta(0)+K^{\infty}\left[\theta(t)-\theta(0^{+})\right]+\int_{0^{-}}^{t}K^{1}e^{-\frac{t-s}{\lambda^{1}}}\frac{d}{ds}\theta(s)ds \tag{1.6}$$
$$=K^{\infty}\theta(t)+K^{1}e^{-\frac{t}{\lambda^{1}}}\left[\theta(0)+\int_{0^{-}}^{t}e^{\frac{s}{\lambda^{1}}}\frac{d}{ds}\theta(s)ds\right]$$

Define the volumetric history term, $q^{i}(t)$

$$q^{1}(t)=e^{-\frac{t}{\lambda^{1}}}\left[\theta(0)+\int_{0^{-}}^{t}e^{\frac{s}{\lambda^{1}}}\frac{d}{ds}\theta(s)ds\right] \tag{1.7}$$

Substitute (1.7) into (1.6)

$$p(t)=K^{\infty}\theta(t)+K^{1}q^{1}(t) \tag{1.8}$$

Generalize (1.8) for $N>1$

$$p(t)=K^{\infty}\theta(t)+\sum_{i=1}^{N}K^{i}q^{i}(t) \tag{1.9}$$

and (1.7) for $N>1$

$$q^i(t) = e^{-\frac{t}{\lambda^i}}\left[\theta(0) + \int_{0^-}^{t} e^{\frac{s}{\lambda^i}} \frac{d}{ds}\theta(s)ds\right] \tag{1.10}$$

Equations (1.9) and (1.10) give the time continuous constitutive relationship for the volumetric component. The next step is to time discretize these expressions to derive the algorithm for calculating the stress and calculating and storing the history terms. The time at the beginning of the time step is denoted t_n, at the end of the time step t_{n+1} and the time step duration

$$\Delta t = t_{n+1} - t_n \tag{1.11}$$

The subscripts n and n+1 reflect the applicable quantity evaluated at t_n and t_{n+1}, respectively.

At t_n (1.10) is

$$q_n^i = e^{-\frac{t_n}{\lambda^i}}\left[\theta(0) + \int_{0^-}^{t_n} e^{\frac{s}{\lambda^i}} \frac{d}{ds}\theta(s)ds\right] \tag{1.12}$$

and at t_{n+1}

$$\begin{aligned} q_{n+1}^i &= e^{-\frac{t_{n+1}}{\lambda^i}}\left[\theta(0) + \int_{0^-}^{t_{n+1}} e^{\frac{s}{\lambda^i}} \frac{d}{ds}\theta(s)ds\right] \\ &= e^{-\frac{t_n+\Delta t}{\lambda^i}}\left[\theta(0) + \int_{0^-}^{t_n} e^{\frac{s}{\lambda^i}} \frac{d}{ds}\theta(s)ds + \int_{t_n}^{t_{n+1}} e^{\frac{s}{\lambda^i}} \frac{d}{ds}\theta(s)ds\right] \\ &= e^{-\frac{\Delta t}{\lambda^i}} q_n^i + e^{-\frac{t_n+\Delta t}{\lambda^i}} \int_{t_n}^{t_{n+1}} e^{\frac{s}{\lambda^i}} \frac{d}{ds}\theta(s)ds \end{aligned} \tag{1.13}$$

To evaluate q^i_{n+1} the Taylor, Pister and Goudreau recursion assumption is used.*(66)* This assumes the rate of change of the strain during a time step is constant

$$\frac{d}{ds}\theta(t) = \frac{\Delta\theta}{\Delta t} \tag{1.14}$$

Reduce the integral in (1.13)

$$\begin{aligned}\int_{t_n}^{t_{n+1}} e^{\frac{s}{\lambda^i}} \frac{d}{ds}\theta(s)ds &= \frac{\Delta\theta}{\Delta t}\int_{t_n}^{t_{n+1}} e^{\frac{s}{\lambda^i}} ds \\ &= \frac{\Delta\theta}{\Delta t}\left[\lambda^i e^{\frac{s}{\lambda^i}}\right]_{t_n}^{t_{n+1}} \\ &= \Delta\theta e^{\frac{t_{n+1}}{\lambda^i}}\left(\frac{\lambda^i}{\Delta t}\right)\left[1-e^{\frac{\Delta t}{\lambda^i}}\right]\end{aligned} \tag{1.15}$$

Substitute (1.15) into (1.13)

$$q^i_{n+1} = e^{-\frac{\Delta t}{\lambda^i}} q^i_n + \Delta\theta\left(\frac{\lambda^i}{\Delta t}\right)\left(1-e^{\frac{\Delta t}{\lambda^i}}\right) \tag{1.16}$$

and evaluate (1.9) at t_{n+1}

$$p_{n+1} = K^\infty\theta_{n+1} + \sum_{i=1}^{N} K^i q^i_{n+1} \tag{1.17}$$

Equation (1.17) calculates the volumetric stress at time t_{n+1}. The derivation thus far has not included the temperature effects. This is included through the reduced time concept, where

$$\lambda(T_{ref}) = \frac{\lambda(T)}{a_T(T)} \tag{1.18}$$

The volumetric reduced time, $\chi(t)$, is defined as

$$\chi(t) = \int_{-\infty}^{t} \frac{1}{a_T(T(s))} ds \tag{1.19}$$

The reduced time is introduced into the constitutive relationships by replacing t with $\chi(t)$ and Δt with $\Delta\chi$ where

$$\begin{aligned} \Delta\chi &= \chi_{n+1} - \chi_n \\ &= \int_{-\infty}^{t_{n+1}} \frac{1}{a_T} ds - \int_{-\infty}^{t} \frac{1}{a_T} ds \\ &= \int_{t_n}^{t_{n+1}} \frac{1}{a_T} ds \\ &\approx \frac{1}{2}\Delta t\left[\frac{1}{a_{T_{n+1}}} + \frac{1}{a_{T_n}}\right] \end{aligned} \tag{1.20}$$

and the trapezoidal rule is used to evaluate the integral.

The shift factor is determined with the Williams, Landel and Ferry (WLF) equation, Equation (1.21).*(48)*

$$\log a_T = \frac{-C_{T1}(T - T_{ref})}{C_{T2} + T - T_{ref}} \tag{1.21}$$

Equation (1.16) becomes

$$q^i_{n+1} = e^{-\frac{\Delta\chi}{\lambda^i}} q^i_n + \Delta\theta\left(\frac{\lambda^i}{\Delta\chi}\right)\left(1 - e^{-\frac{\Delta\chi}{\lambda^i}}\right) \tag{1.22}$$

which is used in Equation (1.17) to calculate the volumetric stress.

A2.2 Shear (Deviatoric) Component

The shear component of the model contains the horizontal and vertical shift factors to account for the temperature and the nonlinearity in the strain. The shift factors are calculated with the norm of the maximum deviatoric strain that has occurred in the time history. In the discrete constitutive relationships the strain used to calculate the shift factors is the maximum deviatoric strain norm that has occurred up until the beginning of the time step, i.e., $\|\mathbf{e}_n\|$. During the time step Δt, the maximum strain may be increasing, but the model still uses the maximum at time t_n. This choice is explained and justified in Chapter 5, Section 5.3.2.

The derivation of the shear component initially ignores the horizontal shift factor.

The time continuous constitutive relationship for the deviatoric stress $(\mathbf{s})$ is shown in Equation (2.1), for M shear Maxwell elements

$$\mathbf{s}(t) = \sum_{i=0}^{M} \int_{-\infty}^{t} e^{-\frac{t-s}{\tau^i}} \frac{d}{ds}\left[\mathbf{s}^i(s)\right] ds \qquad (2.1)$$

where

$$\mathbf{s}^i(s) = \frac{2G^i}{a_V(s)}\mathbf{e}(s) \tag{2.2}$$

and,

$$a_V = 10^{\left[C_{V1}+C_{V2}\left(\log\frac{10^{-6}+\alpha}{10^{-6}+\|\mathbf{e}_{ref}\|}\right)+C_{V3}(T-T_{ref})\left(\log\frac{10^{-6}+\alpha}{10^{-6}+\|\mathbf{e}_{ref}\|}\right)\right]} \tag{2.3}$$

and,

$$\alpha = \max_{s\in(-\infty,t]}\|\mathbf{e}(t)\| \tag{2.4}$$

and the deviatoric strain is

$$\mathbf{e} = \boldsymbol{\varepsilon} - \tfrac{1}{3}\mathrm{tr}(\boldsymbol{\varepsilon})\mathbf{1} \tag{2.5}$$

Substituting (2.2) into (2.1) and pulling the constant G^i out of the derivative, (2.1) reduces to

$$\begin{aligned}
\mathbf{s}(t) &= \sum_{i=0}^{M}\left[\int_{-\infty}^{t} e^{-\frac{t-s}{\tau^i}}\frac{d}{ds}\left[\frac{2G^i}{a_V(s)}\mathbf{e}(s)\right]ds\right] \\
&= \int_{-\infty}^{t}\left(2G^{\infty}+\sum_{i=1}^{M}2G^i e^{-\frac{t-s}{\tau^i}}\right)\frac{d}{ds}\left[\frac{\mathbf{e}(s)}{a_V(s)}\right]ds \\
&= \int_{-\infty}^{t}2G^{\infty}\frac{d}{ds}\left[\frac{\mathbf{e}(s)}{a_V(s)}\right]ds+\sum_{i=1}^{M}\left[\int_{-\infty}^{t}\left(2G^i e^{-\frac{t-s}{\tau^i}}\right)\frac{d}{ds}\left[\frac{\mathbf{e}(s)}{a_V(s)}\right]ds\right]
\end{aligned} \tag{2.6}$$

Note that G^{∞} is the modulus of the free spring in the generalized standard linear solid. It is associated with an infinitely long relaxation time which results in the exponential term for G^{∞} reducing to a value of 1.

At time t_n (2.6) is

$$\mathbf{s}_n = \int_{-\infty}^{t_n} 2G^{\infty} \frac{d}{ds}\left[\frac{e(s)}{a_V(s)}\right] ds + \sum_{i=1}^{M}\left[\int_{-\infty}^{t_n}\left(2G^i e^{-\frac{t_n - s}{\tau^i}}\right)\frac{d}{ds}\left[\frac{e(s)}{a_V(s)}\right] ds\right] \tag{2.7}$$

Let the first term in (2.7) equal the shear history term for the free spring $\mathbf{h}_n^{\infty}$

$$\mathbf{h}_n^{\infty} = \int_{-\infty}^{t_n} 2G^{\infty} \frac{d}{ds}\left[\frac{e(s)}{a_V(s)}\right] ds \tag{2.8}$$

and the second term inside the summation equal the shear history term for the Maxwell element $\mathbf{h}_n^i$

$$\mathbf{h}_n^i = \int_{-\infty}^{t_n} 2G^i e^{-\frac{t_n - s}{\tau^i}} \frac{d}{ds}\left[\frac{e(s)}{a_V(s)}\right] ds \tag{2.9}$$

Substitute (2.8) and (2.9) into (2.7)

$$\mathbf{s}_n = \mathbf{h}_n^{\infty} + \sum_{i=1}^{M} \mathbf{h}_n^i \tag{2.10}$$

At time t_{n+1} (2.6) is

$$\mathbf{s}_{n+1} = \int_{-\infty}^{t_{n+1}} 2G^{\infty} \frac{d}{ds}\left[\frac{e(s)}{a_V(s)}\right] ds + \sum_{i=1}^{M}\left[\int_{-\infty}^{t_{n+1}}\left(2G^i e^{-\frac{t_{n+1} - s}{\tau^i}}\right)\frac{d}{ds}\left[\frac{e(s)}{a_V(s)}\right] ds\right] \tag{2.11}$$

Let the first term in (2.11) equal $\mathbf{h}_{n+1}^{\infty}$ and substitute (2.8) into (2.12)

$$\begin{aligned}\mathbf{h}_{n+1}^{\infty} &= \int_{-\infty}^{t_{n+1}} 2G^{\infty} \frac{d}{ds}\left[\frac{e(s)}{a_V(s)}\right] ds \\ &= \int_{-\infty}^{t_n} 2G^{\infty} \frac{d}{ds}\left(\frac{e(s)}{a_V(s)}\right) ds + \int_{t_n}^{t_{n+1}} 2G^{\infty} \frac{d}{ds}\left(\frac{e(s)}{a_V(s)}\right) ds \\ &= \mathbf{h}_n^{\infty} + 2G^{\infty} \int_{t_n}^{t_{n+1}} \frac{d}{ds}\left(\frac{e(s)}{a_V(s)}\right) ds\end{aligned} \tag{2.12}$$

The derivative in the integral in (2.12) is approximated by assuming the rate of change of the term is constant during a time step, which gives

$$\frac{d}{ds}\left(\frac{e(s)}{a_V(s)}\right) \approx \frac{\left(\frac{e_{n+1}}{a_{Vn}} - \frac{e_n}{a_{Vn-1}}\right)}{\Delta t} \tag{2.13}$$

Substituting (2.13) into (2.12), where the constant term from (2.13) is pulled out of integral gives

$$\begin{aligned}\mathbf{h}_{n+1}^{\infty} &= \mathbf{h}_n^{\infty} + 2G^{\infty} \int_{t_n}^{t_{n+1}} \frac{\left(\frac{e_{n+1}}{a_{Vn}} - \frac{e_n}{a_{Vn-1}}\right)}{\Delta t} ds \\ &= \mathbf{h}_n^{\infty} + 2G^{\infty} \frac{\left(\frac{e_{n+1}}{a_{Vn}} - \frac{e_n}{a_{Vn-1}}\right)}{\Delta t} \int_{t_n}^{t_{n+1}} ds \\ &= \mathbf{h}_n^{\infty} + 2G^{\infty}\left(\frac{\mathbf{e}_{n+1}}{a_{Vn}} - \frac{\mathbf{e}_n}{a_{Vn-1}}\right)\end{aligned} \tag{2.14}$$

Let the term inside the summation of the second term in (2.11) equal $\mathbf{h}_{n+1}^{i}$

$$\begin{aligned}\mathbf{h}_{n+1}^{i} &= \int_{-\infty}^{t_{n+1}} 2G^{i} e^{-\frac{t_{n+1}-s}{\tau^{i}}} \frac{d}{ds}\left(\frac{e(s)}{a_V(s)}\right) ds \\ &= \int_{-\infty}^{t_n} 2G^{i} e^{-\frac{t_{n+1}-s}{\tau^{i}}} \frac{d}{ds}\left(\frac{e(s)}{a_V(s)}\right) ds + \int_{t_n}^{t_{n+1}} 2G^{i} e^{-\frac{t_{n+1}-s}{\tau^{i}}} \frac{d}{ds}\left(\frac{e(s)}{a_V(s)}\right) ds \\ &= e^{-\frac{\Delta t}{\tau^{i}}} \int_{-\infty}^{t_n} 2G^{i} e^{-\frac{t_n-s}{\tau^{i}}} \frac{d}{ds}\left(\frac{e(s)}{a_V(s)}\right) ds + 2G^{i} \int_{t_n}^{t_{n+1}} e^{-\frac{t_{n+1}-s}{\tau^{i}}} \frac{d}{ds}\left(\frac{e(s)}{a_V(s)}\right) ds\end{aligned} \tag{2.15}$$

The integral in the first term of (2.15) is equal to $\mathbf{h}_n^i$. The derivative in the second term is again approximated with (2.13). Equation (2.15) reduces to

$$\begin{aligned}\mathbf{h}_{n+1}^i &\approx e^{-\frac{\Delta t}{\tau^i}}\mathbf{h}_n^i + 2G^i\int_{t_n}^{t_{n+1}} e^{-\frac{t_{n+1}-s}{\tau^i}}\left(\frac{\left(\frac{\mathbf{e}_{n+1}}{a_{Vn}}-\frac{\mathbf{e}_n}{a_{Vn-1}}\right)}{\Delta t}\right)ds \\ &= e^{-\frac{\Delta t}{\tau^i}}\mathbf{h}_n^i + 2G^i\left(\frac{\left(\frac{\mathbf{e}_{n+1}}{a_{Vn}}-\frac{\mathbf{e}_n}{a_{Vn-1}}\right)}{\Delta t}\right)\int_{t_n}^{t_{n+1}} e^{-\frac{t_{n+1}-s}{\tau^i}}ds \\ &= e^{-\frac{\Delta t}{\tau^i}}\mathbf{h}_n^i + 2G^i\left(\frac{\left(\frac{\mathbf{e}_{n+1}}{a_{Vn}}-\frac{\mathbf{e}_n}{a_{Vn-1}}\right)}{\Delta t}\right)e^{-\frac{t_{n+1}}{\tau^i}}\int_{t_n}^{t_{n+1}} e^{\frac{s}{\tau^i}}ds\end{aligned} \tag{2.16}$$

The integral in (2.16) is evaluated in (2.17)

$$\begin{aligned}\int_{t_n}^{t_{n+1}} e^{\frac{s}{\tau^i}}ds &= \left[\tau^i e^{\frac{s}{\tau^i}}\right]_{t_n}^{t_{n+1}} \\ &= \tau^i e^{\frac{t_{n+1}}{\tau^i}}\left(1-e^{-\frac{\Delta t}{\tau^i}}\right)\end{aligned} \tag{2.17}$$

Substituting (2.17) into (2.16) gives

$$\mathbf{h}_{n+1}^i = e^{-\frac{\Delta t}{\tau^i}}\mathbf{h}_n^i + 2G^i\left(\frac{\mathbf{e}_{n+1}}{a_{Vn}}-\frac{\mathbf{e}_n}{a_{Vn-1}}\right)\left(\frac{\tau^i}{\Delta t}\right)\left(1-e^{-\frac{\Delta t}{\tau^i}}\right) \tag{2.18}$$

Substituting (2.14) and (2.18) into (2.11) gives the deviatoric stress at t_{n+1}

$$\mathbf{s}_{n+1} = \mathbf{h}_{n+1}^{\infty} + \sum_{i=1}^{M}\mathbf{h}_{n+1}^i \tag{2.19}$$

The shear history terms are tensors, whereas the volumetric history term is a scalar due to the dependence on the tensor $\mathbf{e}$ and the scalar θ, respectively.

Thus far the horizontal shift for temperature and strain has been excluded. It is introduced through the reduced time concept where $\xi(t)$ is the shear reduced time, defined as

$$\xi(t) = \int_{-\infty}^{t} \frac{1}{a_H(T,\alpha)} ds \tag{2.20}$$

where

$$a_H = 10^{\left[C_{H1}+C_{H2}(T-T_{ref})+C_{H3}\left(\log\frac{10^{-6}+\alpha}{10^{-6}+|e_{ref}|}\right)+C_{H4}(T-T_{ref})\left(\log\frac{10^{-6}+\alpha}{10^{-6}+|e_{ref}|}\right)\right]} \tag{2.21}$$

and α was defined in (2.4).

The change in reduced time is calculated from (2.22)

$$\begin{aligned} \xi_{n+1} &= \xi_n + \Delta\xi \\ &= \xi_n + \int_{t_n}^{t_{n+1}} \frac{1}{a_H(s)} ds \end{aligned} \tag{2.22}$$

where $\Delta\xi$ is evaluated with the trapezoidal rule

$$\begin{aligned} \Delta\xi &= \int_{t_n}^{t_{n+1}} \frac{1}{a_H(s)} ds \\ &\approx \tfrac{1}{2}\Delta t\left(\frac{1}{a_{Hn}} + \frac{1}{a_{Hn-1}}\right) \end{aligned} \tag{2.23}$$

Replacing Δt with $\Delta\xi$ in (2.18) gives

$$\mathbf{h}^{i}_{n+1} = e^{-\frac{\Delta\xi}{\tau^{i}}}\mathbf{h}^{i}_{n} + 2G^{i}\left(\frac{\mathbf{e}_{n+1}}{a_{Vn}} - \frac{\mathbf{e}_{n}}{a_{Vn-1}}\right)\left(\frac{\tau^{i}}{\Delta\xi}\right)\left(1 - e^{-\frac{\Delta\xi}{\tau^{i}}}\right) \tag{2.24}$$

which is used in (2.19) to evaluate $\mathbf{s}_{n+1}$. With p_{n+1} from (1.17), the stress at time t_{n+1} can now be calculated using (1.1).

A2.3 Consistent Tangent

The consistent tangent, $\mathbf{C}$, is an important factor in the finite element code to ensure convergence, and is the partial derivative of the stress, $\boldsymbol{\sigma}$, with respect to the strain, $\boldsymbol{\varepsilon}$, at t_{n+1}, as shown in Equation (3.1). All terms that are functions of t_n are constant during the time step and therefore the derivative with respect to $\boldsymbol{\varepsilon}_{n+1}$ is zero.

$$\begin{aligned}\mathbf{C} &= \frac{\partial \boldsymbol{\sigma}_{n+1}}{\partial \boldsymbol{\varepsilon}_{n+1}} \\ &= \underbrace{\frac{\partial p_{n+1}}{\partial \boldsymbol{\varepsilon}_{n+1}} \otimes \mathbf{1}}_{\mathbf{C}^{vol}} + \underbrace{\frac{\partial \mathbf{s}_{n+1}}{\partial \boldsymbol{\varepsilon}_{n+1}}}_{\mathbf{C}^{dev}}\end{aligned} \tag{3.1}$$

The volumetric tangent term, $\mathbf{C}^{vol}$ is derived from (1.17)

$$\frac{\partial p_{n+1}}{\partial \boldsymbol{\varepsilon}_{n+1}} = K^{\infty}\frac{\partial \theta_{n+1}}{\partial \boldsymbol{\varepsilon}_{n+1}} + \sum_{i=1}^{N} K^{i}\frac{\partial q^{i}{}_{n+1}}{\partial \boldsymbol{\varepsilon}_{n+1}} \tag{3.2}$$

where

$$\frac{\partial \theta_{n+1}}{\partial \boldsymbol{\varepsilon}_{n+1}} = \frac{\partial \left(\varepsilon_{11} + \varepsilon_{22} + \varepsilon_{33}\right)_{n+1}}{\partial \boldsymbol{\varepsilon}_{n+1}} = \mathbf{1} \tag{3.3}$$

and,

$$\frac{\partial q^{i}{}_{n+1}}{\partial \boldsymbol{\varepsilon}_{n+1}} = \frac{\partial \left(e^{-\frac{\Delta\chi}{\lambda^{i}}} q_{n}^{i} + \Delta\theta \left(\frac{\lambda^{i}}{\Delta\chi} \right) \left(1 - e^{\frac{\Delta\chi}{\lambda^{i}}} \right) \right)}{\partial \boldsymbol{\varepsilon}_{n+1}} = \left(\frac{\lambda^{i}}{\Delta\chi} \right) \left(1 - e^{\frac{\Delta\chi}{\lambda^{i}}} \right) \frac{\partial \Delta\theta}{\partial \boldsymbol{\varepsilon}_{n+1}} \tag{3.4}$$

and

$$\frac{\partial \Delta\theta}{\partial \boldsymbol{\varepsilon}_{n+1}} = \frac{\partial \left(\theta_{n+1} - \theta_{n}\right)}{\partial \boldsymbol{\varepsilon}_{n+1}} = \mathbf{1} \tag{3.5}$$

Substitute (3.5) into (3.4)

$$\frac{\partial q^{i}{}_{n+1}}{\partial \boldsymbol{\varepsilon}_{n+1}} = \left(\frac{\lambda^{i}}{\Delta\chi} \right) \left(1 - e^{\frac{\Delta\chi}{\lambda^{i}}} \right) \mathbf{1} \tag{3.6}$$

and (3.3) and (3.6) into (3.2) to evaluate $\mathbf{C}^{vol}$

$$\mathbf{C}^{vol} = \frac{\partial p_{n+1}}{\partial \boldsymbol{\varepsilon}_{n+1}} \otimes \mathbf{1} = \left\{ K^{\infty} + \sum_{i=1}^{N} K^{i} \left(\frac{\lambda^{i}}{\Delta\chi} \right) \left(1 - e^{\frac{\Delta\chi}{\lambda^{i}}} \right) \right\} \mathbf{1} \otimes \mathbf{1} \tag{3.7}$$

Similarly, $\mathbf{C}^{dev}$ is calculated using the derivation in Section A2.2.

$$\begin{aligned}\mathbf{C}^{dev} &= \frac{\partial \mathbf{s}_{n+1}}{\partial \boldsymbol{\varepsilon}_{n+1}} \\ &= \frac{\partial \mathbf{h}^{\infty}_{n+1}}{\partial \boldsymbol{\varepsilon}_{n+1}} + \frac{\partial \mathbf{h}^{i}_{n+1}}{\partial \boldsymbol{\varepsilon}_{n+1}}\end{aligned} \tag{3.8}$$

where

$$\begin{aligned}\frac{\partial \mathbf{h}^{\infty}_{n+1}}{\partial \boldsymbol{\varepsilon}_{n+1}} &= \frac{\partial\left(\mathbf{h}^{\infty}_{n} + 2G^{\infty}\left(\frac{\mathbf{e}_{n+1}}{a_{Vn}} - \frac{\mathbf{e}_{n}}{a_{Vn-1}}\right)\right)}{\partial \boldsymbol{\varepsilon}_{n+1}} \\ &= \frac{2G^{\infty}}{a_{V}}\frac{\partial \mathbf{e}_{n+1}}{\partial \boldsymbol{\varepsilon}_{n+1}}\end{aligned} \tag{3.9}$$

and,

$$\begin{aligned}\frac{\partial \mathbf{h}^{i}_{n+1}}{\partial \boldsymbol{\varepsilon}_{n+1}} &= \frac{\partial\left(e^{-\frac{\Delta\xi}{\tau^{i}}}\mathbf{h}^{i}_{n} + 2G^{i}\left(\frac{\mathbf{e}_{n+1}}{a_{Vn}} - \frac{\mathbf{e}_{n}}{a_{Vn-1}}\right)\left(\frac{\tau^{i}}{\Delta\xi}\right)\left(1-e^{-\frac{\Delta\xi}{\tau^{i}}}\right)\right)}{\partial \boldsymbol{\varepsilon}_{n+1}} \\ &= \frac{2G^{i}}{a_{V}}\left(\frac{\tau^{i}}{\Delta\xi}\right)\left(1-e^{-\frac{\Delta\xi}{\tau^{i}}}\right)\frac{\partial \mathbf{e}_{n+1}}{\partial \boldsymbol{\varepsilon}_{n+1}}\end{aligned} \tag{3.10}$$

The derivative of the deviatoric strain with respect to the strain is

$$\begin{aligned}\frac{\partial \mathbf{e}_{n+1}}{\partial \boldsymbol{\varepsilon}_{n+1}} &= \frac{\partial\left(\boldsymbol{\varepsilon}_{n+1} - \frac{1}{3}\mathrm{tr}(\boldsymbol{\varepsilon}_{n+1})\mathbf{1}\right)}{\partial \boldsymbol{\varepsilon}_{n+1}} \\ &= \mathbf{I} - \tfrac{1}{3}\mathbf{1}\otimes\mathbf{1} \\ &= \mathbf{I}_{dev}\end{aligned} \tag{3.11}$$

Substitute (3.11) into (3.9) and (3.10), and (3.9) and (3.10) into (3.8) to evaluate $\mathbf{C}^{dev}$

$$\mathbf{C}^{dev} = \frac{2}{a_{V}}\left(G^{\infty} + \sum_{i=1}^{M} G^{i}\frac{\tau^{i}}{\Delta\xi}\left(1-e^{-\frac{\Delta\xi}{\tau^{i}}}\right)\right)\mathbf{I}_{dev} \tag{3.12}$$

This completes the derivation.

A4.4 List of Variables

$\mathbf{1}$ = second rank identity
$\otimes$ = tensor product
α = maximum deviatoric strain norm in time history
χ = bulk reduced time
$\boldsymbol{\varepsilon}$ = strain
λ^i = relaxation time of i^{th} bulk Maxwell element
θ = $\text{trace}(\boldsymbol{\varepsilon})$
$\boldsymbol{\sigma}$ = stress
ξ = shear reduced time
τ^i = relaxation time of i^{th} shear Maxwell element
$\Delta\chi$ = change in bulk reduced time
$\Delta\theta$ = $\text{trace}(\boldsymbol{\varepsilon}_{n+1}) - \text{trace}(\boldsymbol{\varepsilon}_n)$
$\Delta\xi$ = change in shear reduced time
Δt = time step duration
a_H = horizontal shift factor in shear component
a_T = temperature shift factor in bulk component
a_V = vertical shift factor in shear component
$\mathbf{e}$ = deviatoric strain
$\|\mathbf{e}\|$ = norm of deviatoric strain
$\|\mathbf{e}_{ref}\|$ = norm of reference deviatoric strain
$\mathbf{h}^\infty$ = history term for shear free spring
$\mathbf{h}^i$ = history term for i^{th} shear Maxwell element
p = volumetric stress
q^i = history term for i^{th} bulk Maxwell element
$\mathbf{s}$ = deviatoric stress
s = integration variable
t = time
$\mathbf{C}$ = consistent tangent
$\mathbf{C}^{dev}$ = shear term in consistent tangent
$\mathbf{C}^{vol}$ = bulk term in consistent tangent
$C_{H1} - C_{H4}$ = constants in horizontal shift factor in shear component
$C_{V1} - C_{V4}$ = constants in vertical shift factor in shear component
C_{T1}, C_{T2} = constant in temperature shift in bulk component
$G(t)$ = shear relaxation modulus

G^{∞} = shear modulus of free spring

G^{i} = shear modulus of i^{th} shear Maxwell element

$\mathbf{I}$ = fourth rank identity

$\mathbf{I}_{dev}$ = fourth rank deviatoric identity

$K(t)$ = bulk relaxation function

K^{∞} = bulk modulus of free spring

K^{i} = bulk modulus of i^{th} bulk Maxwell element

M = number of shear Maxwell elements

N = number of bulk Maxwell elements

T = temperature

T_{ref} = reference temperature

APPENDIX 3

COMPARISON OF 2D AND 3D SOLUTIONS

Simulations of the HVS test sections discussed in Chapter 6 were performed as both a three-dimensional (3D) and a two-dimensional (2D) plane strain representation of the pavement structure. Plane strain simulations take significantly less time to solve than 3D simulations, but the 3D simulation should be a more accurate representation of the pavement. Both 2D plane strain and 3D simulations were run to compare the results and check the appropriateness of reducing the 3D problem to an equivalent 2D problem.

Results from the simulations showed a large discrepancy between the 3D and 2D plane strain solutions. This is discussed in Section 6.2.3. The magnitude of the differences in the rutting profiles from the two simulations is evident in Figure 6.22. The deformation in the 3D simulations appears too small and the deformation in the 2D too large when compared to the HVS rutting study data. These results do not seem reasonable. An explanation for the differences is that the load is only applied to a specific point in the pavement when the tire is in contact it. In a pavement, when the tire is no longer in contact with the point but is in contact with an adjacent point some load is still being

imparted to the point. In the 3D simulations this is not accounted for, and the smaller amount of deformation is therefore expected. The equivalent strip load in the 2D plane strain simulations effectively applies the adjacent loads continuously. This is more aggressive than a real moving tire load and therefore results in more deformation.

To check whether there was an error in the material model, the same simulations were rerun using a linear elastic material. To check if the finite element code calculates the solutions correctly, the linear elastic solutions were also compared to the exact linear elastic solutions.

Pavement Simulations with Linear Elastic Material

The simulations used the same meshes shown in Figure 6.17 for the 2D simulation and Figure 6.18 for the 3D simulation, except that all three layers were reduced to a single layer. The linear elastic material had a Young's modulus of 1510 MPa and a Poisson's ratio of 0.48. These values were selected from the viscoelastic material properties of the DGAC fitted in Chapter 5. The high Poisson's ratio indicates a nearly incompressible material.

The boundary conditions in the 3D mesh differed from those shown in Figure 6.18 in that the x_1 planes on the boundary were fixed to restrict movement in the x_1 direction only. These boundary conditions are equivalent to the plane strain simulation. It was found

that the boundary conditions on these faces had little influence on the 3D solution. Two different load patterns were used in the 3D simulations: first, the tires shown in Figures 6R and 6S and; second, a strip load, with the load magnitudes used in the 2D simulation applied along the full x_1 length (Figure 6.20). The strip load replicates the loading in the 2D plane strain simulation.

Results of the finite element method (FEM) simulations again showed the same large discrepancies in the solutions, which indicates that an error in the material model is not responsible for the differences.

Comparison with Exact Solutions

To compare the elastic solutions with the exact solutions from the theory of elasticity, the tire and strip loads were replaced with a point and line load and the solutions were recalculated.*(75, 76)* A comparison of the vertical displacements from the 2D and 3D exact solutions and the finite element method (FEM) solutions are shown in Figure A3.1. The data were obtained on a ray at an angle of approximately 45° from the point of application of the load, away from the symmetry plane. The displacement was plotted as a function of the horizontal distance along this ray. Again, the differences in the magnitudes of the displacements are large. Comparisons of the stresses showed similar results.

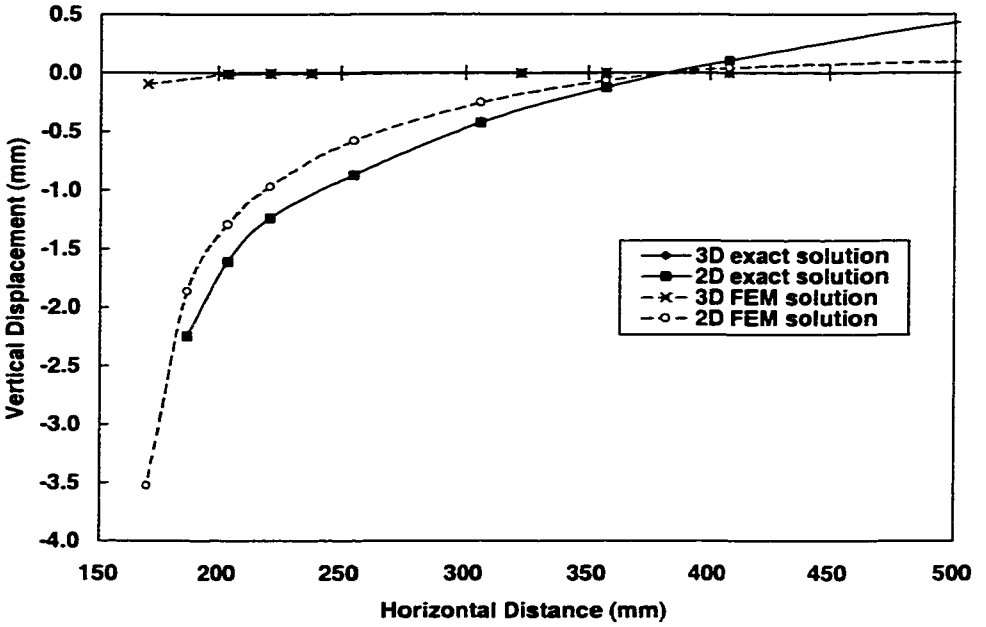

Figure A3.1 Comparison of Exact Solution and Finite Element Method Solutions for Linear Elastic Material in 2D and 3D Simulations

The results show that for the meshes, loading, and material properties used in the simulations the large differences in the displacements and stresses agree with the exact solutions from the theory of elasticity. Therefore, errors in either the material model or the finite element code are not responsible for these results.

Approach Selected to Determine Appropriate 2D Load

The problem remains, however, that there are significant differences in the 2D plane strain and 3D solutions. This is a modeling issue, which needs to be resolved. Essentially, the 3D loads need to be reduced to the plane strain problem to produce the

same deformation. Numerous simulations and comparisons are necessary to evaluate how to accurately reduce the loads in the 2D simulation to the "equivalent" 3D loads. In the time available for this dissertation research, it was not possible to perform this extensive evaluation. It was, therefore, decided to compare the residual vertical displacements from the 2D plane strain simulation with the measured permanent vertical deformation from the DGAC HVS test section (506RF) and arbitrarily reduce the 2D loads to obtain approximately similar results. This resulted in reducing the loads to one-third of their original values.